Modular Hybrid Architectures for Single Particle-based Analytical Assays

Dissertation

zur Erlangung des akademischen Grades

doctor rerum naturalium

(Dr. rer. nat.)

im Fach Chemie

eingereicht an der

Mathematisch-Naturwissenschaftlichen Fakultät

der Humboldt-Universität zu Berlin

von

Dipl. Chem. Dominik Arun Sarma

Präsidentin der Humboldt-Universität zu Berlin

Prof. Dr.-Ing. Dr. Sabine Kunst

Dekan der Mathematisch-Naturwissenschaftlichen Fakultät

Prof. Dr. Elmar Kulke

Gutachter/innen 1. Stefan Hecht

2. María Cruz Moreno Bondi

Tag der mündlichen Prüfung: 01.11.2019

For my grandpa Ramnath Sundaram Sarma

Abstract

Global megatrends such as demographic change, personalization, climate change or urbanization demand for increasingly flexible and mobile analytical measurement methods and assays. Especially in the environmental, agricultural, food and health sectors, chemical assays are a suitable choice. A large variety of such assays is available in the academic and industry area. However, their modification to measure new compounds is time-consuming and laborious, because they are typically designed to detect a specific single analyte.

A modular platform for chemical assay development is thus highly desirable. Such a system should include the possibility for fast, easy and flexible implementation of various recognition types towards emerging analytes and the possibility for multi-parameter (multiplexed) detection in a potentially portable fashion. Single particle-based assays have proven to be an adequate solution here.

In this work, I present hybrid polystyrene core-silica shell (SiO_2@PS) particles as new spherical substrates for the flexible configuration of single particle-based chemical assays. So far, it has mainly been the materials sciences that have employed this hybrid design. However, its tremendous and superior potential in contrast to plain polymer or silica particles as an assay platform has not yet been fully uncovered. Throughout the following chapters, I will show how to surpass the current state-of-the-art in bead-based chemical assay design and performance using core-shell (CS) particles.

First, a procedure to control the surface topology of the beads was developed, giving access to smooth, raspberry-like or multilayer-like CS structures. These particles were used for DNA detection down to the fmol-level (Chapter 2). A new tool to extract the roughness of the particles from electron microscopy images was developed next and applied to the wide range of CS beads prepared throughout the project (Chapter 3). This general protocol provides the basis for the comparability of future CS particle characterization. Finally, a multiplex assay with dye-encoded beads with non-fouling surfaces was developed to detect small molecules via immunochemical reactions in a wash-free procedure (Chapter 4). The latter ultimately proves that hybrid CS particles can combine high analytical performance and unmatched potential for flexible functionality.

Zusammenfassung

Globale Megatrends wie demografischer Wandel, Personalisierung, Klimawandel oder Urbanisierung erfordern immer flexiblere analytische Messmethoden und Assays. Insbesondere im Umwelt-, Agrar-, Lebensmittel- und Gesundheitssektor sind chemische Assays hier eine geeignete Wahl. Eine Vielzahl solcher Assays steht in akademischen und industriellen Bereichen zur Verfügung. Die Anpassung an neue Verbindungen hingegen ist oft schwierig zu realisieren, da der einzelne Test meist für einen spezifischen Analyten konzipiert ist.

Eine modulare, analytische Plattform für die Entwicklung chemischer Assays ist daher sehr wünschenswert. Ein solches System sollte die Möglichkeit einer schnellen und flexiblen Implementierung verschiedener Erkennungstypen für neue Analyten und die Möglichkeit einer Multiparameter-(Multiplex-)Bestimmung in einem robusten und portablen Auslesegerät beinhalten. Einzelpartikel-basierte, chemische Assays haben sich hier als geeignete Lösung erwiesen.

In dieser Arbeit stelle ich Polystyrol-Kern-Silikat-Schale (SiO_2@PS)-Partikel als modulare, hybride Plattform für die flexible Konfiguration von Einzelpartikel-basierten chemischen Assays vor. Bisher wurden solche Hybridpartikel hauptsächlich in den Materialwissenschaften eingesetzt. Das überlegene Potenzial als analytische Partikelplattform ist jedoch bei weitem noch nicht voll erschlossen. In dieser Arbeit werde ich dieses Potenzial anhand dreier Projektarbeiten aufzeigen.

Zunächst wurde ein Verfahren entwickelt, das den Zugang zu glatten, Himbeer- oder Mehrschicht-Partikelarchitekturen ermöglicht. Diese Partikel wurden für den DNA-Nachweis bis in den fmol-Bereich getestet (Kapitel 2). Ein neues Werkzeug zur Bestimmung der Rauheit der Partikel aus elektronenmikroskopischen Bildern wurde entwickelt und auf das breite Spektrum der im Projekt hergestellten SiO_2@PS-Partikel angewendet (Kapitel 3). Damit soll die Grundlage zur Vergleichbarkeit zwischen zukünftigen Partikelcharakterisierungen geschaffen werden. Schließlich wurde ein Multiplex-Assay mit farbstoffkodierten, Protein-abweisenden Partikeln entwickelt, um kleine Moleküle durch immunochemische Reaktionen in einem waschfreien Verfahren nachzuweisen (Kapitel 4). Letzteres verdeutlicht, dass eine hohe analytische Leistung mit neuem Potenzial an flexibler Funktionalität durch die Verwendung hybrider SiO_2@PS-Partikel kombiniert werden kann.

The experimental work of this thesis was done between the 1st of November 2012 and 30th of April 2016 under the project supervision of Dr. Knut Rurack in the Division 1.9 at the Federal Institute for Materials Research and Testing (BAM, Berlin) and the doctoral supervision of *Prof. Stefan Hecht* at the Chemistry Department of the *Humboldt-University of Berlin*. The work was funded by the MIS ("Menschen, Ideen und Strukturen") program (BAM/BMWi, Grant No. Ideen_2012_14).

Content

1 Introduction

Global megatrends (GMT) will govern not only economic decision-making but also guide global research in the natural sciences in the upcoming decades.[1-2] Trends like population growth, demographic change, personalization, climate change, and urbanization will inherently drive technological developments with a major impact also on the analytical sciences (Figure 1).

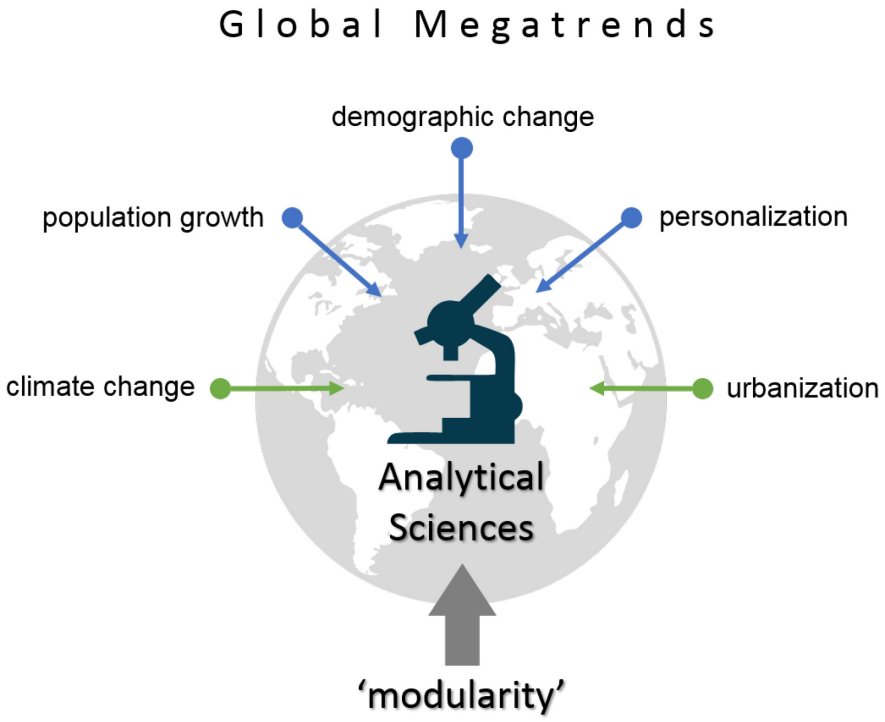

Figure 1. *Global megatrends within the context of analytical sciences development.*

For example, the less developed parts of the world will become the most significant contributors to global population growth. The increased population will need cheap and robust analytical assays on-site to measure basic human needs such as drinking water and foodstuff quality, given advanced analytical lab-testing with, for instance, liquid chromatography and mass spectrometry is not always a financially viable option or accessible in reasonable distance.

An aging society (demographic change) as another example is accompanied by an increasing demand for multi-parameter (multiplex) diagnostics due to increasing number of patients and emerging diseases. Recent trends in personalized medicine will moreover trigger the demand for point-of-care-testing (POCT) to reduce the sample-to-needle time.

The fight against climate change and for a clean environment to establish sustainability and improve resource efficiency is another major global mission. This inevitable challenge will boost the demand for miniaturized, portable assays to determine existing and emerging environmental and agricultural pollutants, especially in secluded areas.

Environmental conditions are also directly affected by other GMTs such as increasing anthropogenic emission (population growth and urbanization) and changing consumption patterns (personalization). As a consequence, food quality control and water management drive the development of (bio)analytical assays that can measure multiple parameters simultaneously outside of a dedicated chemical laboratory to provide the non-expert user with relevant results directly at the point-of-need.

In order to compete with the global trends and to address the associated challenges, modular platform solutions will be required which can (a) be quickly configured for emerging analytes, (b) be easily compiled to multiplex test-panels, and (c) allow for the integration in portable and at best automated devices. The envisioned tool should be simple and cheap in preparation and modification, avoiding costly instrumentation and sophisticated, time-consuming processing.

This work is dedicated to approaching modularity by way of a single analytical tool – a chemical assay platform – that can be tailored towards the multiplexed detection of chemical compounds in biologic, environmental, agricultural or food samples. A highly modular material should be designed, which allows the facile and fast adaption of the diverse and ever-changing analytical demands in a progressive global world.

1.1 Chemical assays

A chemical assay basically consists of three parts: (1) the recognition element, i.e., the receptor for a certain analyte, (2) the transducer, converting the binding event into a measurable signal and (3) the integration of the system in a suitable assay platform (Figure 2).

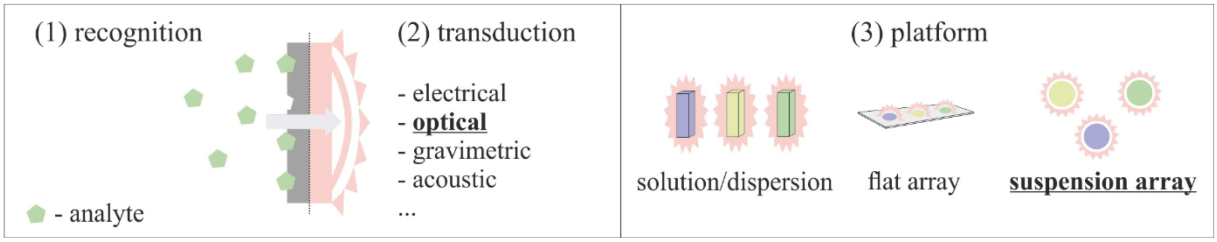

Figure 2. *Schematic illustration of the three main components of a chemical assay including the analyte recognition (1), the signal transduction (2), and the fluorescence assay platform (3).*

Within this thesis, the focus is laid on the development of a chemical assay platform (3) that can be equipped with many different types of recognition chemistries—nucleobase pairing, antibody-antigen binding, indicators for small-molecule or ion complexation—and uses a reliable and versatile transduction technique. Optical transduction (2) based on fluorescence seems particularly suitable for the desired system because it is highly sensitive with sub-microsecond temporal resolution.[3] Fluorescence-based chemical assays can also be easily miniaturized due to relatively low energy consumption, for instance, using a photodiode or LED technology.[4]

The fluorescence assay platform can be classified into solution- or dispersion-phase and solid-supported array formats such as flat arrays and suspension arrays. Fluorescence chemical assays in solution are powerful and modular tools for sensing in a controlled environment. When inorganic ionic species such as metal ions or inorganic anions as well as small organic molecules are targeted, fluorescent probes or indicators are a formidable choice. For this molecular strategy, analyte binding (i.e. recognition) in solution can be designed in silico and optical signaling pathways can directly be implemented in the probe development. Fluorescent indicators can translate analyte binding via intensity modulations (quenching, enhancement) or color changes based on electronic push-pull effects into a measurable signal.[5] Another

prominent class are fluorescent chemo-dosimeters, e.g., for the detection of metal ions through a reaction-based transformation of a non-fluorescent precursor into a highly fluorescent dye.[6] Biomacromolecules such as a single-stranded DNA or proteins, in contrast, are often indicated by dye- or fluorescently tagged or labeled complementary macromolecules.[7-8]

Dispersion-phase assays often rely on the use of nanoparticles (NPs) or beads as reporters, probes or supports in suspension. The single entity in this type of assay cannot or is not intended to be individually tracked. That is, the analytical signal is derived from the ensemble of particles within the dispersed phase.

Noble metal (NM) NPs such as gold NPs are often used in chemical sensing due to their intrinsic optical properties.[9] Upon binding of fluorophores to the surface, for example, energy- and electron-transfer processes commonly lead to fluorescence quenching which can be translated into a quantifiable optical signal.[10-11] Alternative techniques using NM NPs rely on surface-enhanced Raman scattering (SERS) effects or fluorescence modulation of coupled fluorophores for signal transduction.[12] Other NPs such as fluorescent dye-doped silica (SiO_2) NPs, polymeric NPs, semiconductor nanocrystals (quantum dots, QD) or rare-earth doped up-conversion NPs (UC-NPs) add more versatility to this field; each with distinct materials properties and application features as optical labels for assay design.[13-15] Typically, the size dimensions lie around 10 to 200 nm.

In solution- or dispersion-phase assays, single analytes are typically detected in each assay cavity as for instance single wells in a microtiter plate. The detection of multiple analytes in a single well (multiplex) is possible by using multicolor detection with different fluorophores or tuning of the NPs' optical properties.[16-18] Alternatively, the handling of solutions or dispersions and optical read-out can be done using microfluidic chips.[19-20] The flow generation can either be induced by pumps or electrophoretically.[21] The number of target analytes for solution- or dispersion phase assays, regardless of the handling and read-out method, is unfortunately limited to very low numbers and signal generation suffers from high cross-reactivity and cross talk because washing steps to remove loosely bound false analyte-receptor pairs is troublesome.

Solid-supported array formats represent a more suitable choice. The recognition and transduction elements in such arrays are coupled to solid surfaces which can either be flat (e.g. microchips, microtiter plate, membranes etc.) or spherical objects in the form of nano- or microparticles can constitute the solid carrier in suspension. In contrast to a solution or dispersion-phase assay, washing on solid-supported assays for cascade reactions or removal of

unbound analytes for improved assay response can be easily done manually or in an automated manner. An extremely cheap approach uses paper-based supports and capillary-flow energy for transport of solutions.[22]

Several label-free technologies also rely on solid supports which themselves act as the transduction element (integrated platform). Signaling, platform and read-out are combined within a single construction. Respective receptors or recognition elements capture the target analyte to the sensor surface. This is for example the case using acoustic, electric and gravimetric transduction on (mostly metallic) surfaces.[23-25] The transition from real solid supported formats to dispersed ones can be fluent which has been demonstrated for example with gold or graphene-based nanomaterials.[26] Label-free optical transduction can also be realized in an integrated platform using refractive index modulation via photonic crystals or microcavity resonators for example.[27]

Multiplexing on solid-supported platforms using fluorescence is enabled either using arrays of spotted probes on a surface via positional encoding or identification of individual particles as an array element in suspension by optical or physical encoding of the spherical carrier (suspension array). For both cases, in comparison to solution- or dispersion-phase assays, the array element must exceed the size of at least 200 nm for individual tracking and read-out with light-based methods. In real applications, bead-based systems can truly have sizes down to 200 nm while spots on surfaces commonly lie between 50 µm and 200 µm to ensure an unperturbed analytical performance.[28]

Both solid-supported formats are associated with analytical benefits and limitations: while optically encoded suspension arrays usually provide less multiplexing capacity with only up to 500 codes in commercially available systems, their analytical features such as sampling time, high-throughput capacities and required sample load are typically superior to flat arrays.[29]

Flat arrays, on the contrary, can be prepared with hundreds to thousands of array elements per chip depending on the preparation method and type of receptor (e.g. DNA, peptide, protein). While DNA microarrays have emerged as a powerful tool in DNA sequencing and more recently in FDA-approved clinical assays, a robust, consistent fabrication technology that survives multiple assay conditions and lab–lab variations for protein microarrays is still missing.[30]

Additionally, and key for the choice of the bead-based platform developed in this work, the preparation aspects from the bead to the final assay are superior in terms of cost, robustness, and modularity: Particles in suspension can be flexibly modified with the desired recognition elements using optimized coupling strategies in simple flask chemistry set-ups to address specific analytical needs. Billions of replicates are prepared in a single step using milligram level particle batches in the dispersion which greatly enhances reproducibility and stability of the array element. In contrast, flat arrays require costly spotting instrumentation which still suffers from spot inhomogeneity or drying effects. Moreover, libraries of optimized and individual single particle array elements can be created and modularly mixed to the desired test panels. Accordingly, bead-based arrays or suspension arrays promise to be an ideal modular basis for the development of the herein envisioned chemical assay platform.

1.2 Suspension arrays and FACS

The optical read-out of single beads in suspension arrays can be realized in different ways rendering the final integration of the chemical assay very flexible. The two most common and commercially advanced solutions are fluorescence microscopy and flow cytometric analysis (i.e. suspension array technologies, SAT). In this work, flow cytometric read-out as SAT was used because this established method is perfectly suited for bead-based multiplexed testing.[29] Additionally, FACS inherently serves as a model for further miniaturization in microfluidic devices (e.g. µflow cytometers) or other flow systems such as three-dimensional Labs-on-Valve to potentially address future POCT applications.[31-33] Besides, a fully developed bead-platform could easily be adapted for read-out with fluorescence microscopy if the particle density is sufficient for sedimentation within the test matrix.

In every case, the single particle must exceed the size of 200 nm for scattering-based read-out while being light-weighted to avoid sedimentation during analysis or analyte binding. This limits the choice of carrier material to basically polymers or silica (SiO_2).

Flow cytometry (or fluorescence-activated cell sorting, FACS. “FACS” is used in this work only because of simplicity; cells have not been analyzed.) was initially developed for the analysis of cells. The method allows to detect and analyze single objects in a fluidic stream using light excitation and correlated scattering and fluorescence detection (cf. section 2.3.2). This signal correlation allows discriminating between background fluorescence and particle-

correlated fluorescence and scattering. As an example, by using two different emitters in 10 intensities for encoding of a particle, a 2-dimensional array with 100 elements can be constructed (Figure 3).

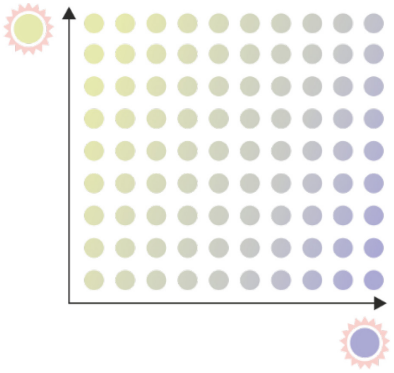

Figure 3. *2-dimensional suspension array with 100 encoded spheres.*

1.3 The spherical carrier – untapped potential

Having set the technical framework for the chemical assay platform development in this work, i.e. fluorescence transduction using single particle-based arrays, a major drawback was identified within the field when using cytometric read-out. So far, development of bead-based assays relied on optimization of the assay protocols using commercially available beads, often without specifically optimized materials and surface properties. In most cases, polystyrene (PS) or sol-gel silica (SiO_2) microparticles are used. Both materials are cheap and can be synthesized in high yields in the desired size range, for instance, using the classical Stöber method for SiO_2 or dispersion polymerization for PS particles.[34-35]

Commercial array platforms such as the BD™ cytometric bead array or the Luminex xMAP® technology preferably rely on PS beads. Their scattering properties with comparatively high refractive indices match well with the requirements on cytometric analysis and hydrophobic dyes can be easily incorporated for encoding.[36-37] Additionally, the density (~1.05 g mL^{-1}) matches well with the density of water, which ensures good dispersion stability.

The major drawback using PS beads is the limited flexibility for chemical surface modification. Functionalization is defined already by the choice of precursors during bead preparation in rather difficult two-stage or copolymerization procedures.[38] This strongly affects the outcome of the synthesis and limits batch preparation of the solid carrier for multi-purpose applications,

i.e. particles with identical sizes but different functionality. Moreover, the particle size has to be typically above 3 µm to offer the user straightforward handling properties.[39]

SiO_2 particles, on the other hand, can be post-functionalized with various functional groups using simple silane chemistry.[40] SiO_2 particles have higher densities (~2 g mL^{-1}) and lower refractive indices which make them less favorable for cytometric applications in comparison to PS (and more interesting for fluorescence microscopy).[41] Encoding with dyes for multiplex applications usually requires covalent integration of a silane derivative of the fluorophore during the synthesis step to prevent the dye from leaching in aqueous environments. Again, this limits batch preparation of differently encoded particles, since mixtures of different silanes will affect particle properties such as size, size distribution, and surface properties.

1.4 A hybrid approach for the platform design

To introduce modularity already at the stage of bead design and facilitate further preparation steps downstream, the concept of SiO_2 coated polymeric particles – core-shell (CS) particles in essence – as the solid support for bead-based applications was conceived in this work. The composites are built from a PS core, a SiO_2 shell (SiO_2@PS) and a layer of functional silanes (Figure 4). Thus, the flexible functionalization of a silica surface is combined with ideal materials properties of a polymeric PS core for cytometric read-out.[42] Moreover, straightforward synthesis routes for the preparation of highly monodisperse PS microparticles can be adapted.

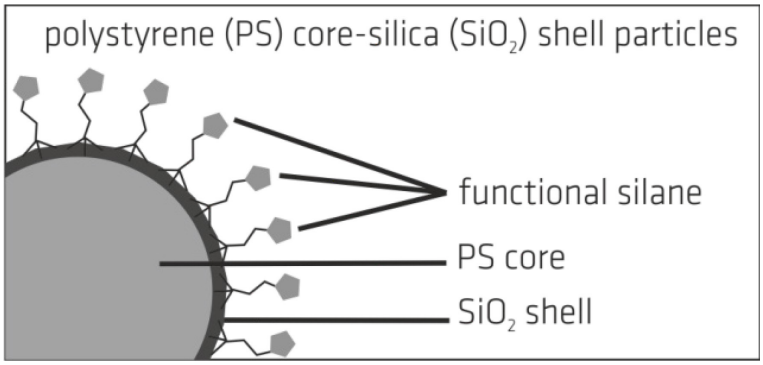

Figure 4. *Polystyrene core-silica shell (CS) particles modified with functional silanes on the particle's surface.*

SiO_2@PS particles have emerged at the end of the 1990s as novel building blocks for the development of new materials. Coating of the polymeric templates with a silica shell allowed to modulate the overall materials properties (e.g., mechanical, chemical, rheological) and opened doors for so-called silica hollow microspheres (SHMs).[43-44] Pioneering work was done here by the groups of Bamnolker et al., Graf et al. and Caruso et al..[45-47] Back then, the chemical modification features of a silica surface were already emphasized by the authors, however, the application in SAT was not yet considered. In the meantime, SAT entered the scientific world as a novel analytical tool around the turn of the millennium after the release of the first commercial multiplexed bead-assay by Luminex®.

Surprisingly, silica coatings on polymeric particles received attention almost exclusively for the fabrication of SHMs or the assembly of surface modified CS particles in colloidal crystals, on flat surfaces for surface coatings, i.e., super-hydrophobic, super-hydrophilic or anti-reflective surfaces, abrasive materials for mechanical polishing or their use in bulk for pollutant removal or chromatographic applications.[48-54] Accordingly, the vast majority of research in the field of CS microparticles focused on materials properties, while not aiming at SAT applications, to control the internal shell structure, the macroscopic surface structure or the shell thickness.[55-57]

Till today, only a few published works can be found which adopt SiO_2-coated polymeric particles for potential application in SAT.[58-63] These publications are more analytically oriented contributions, which provide only scarce details on general design rationales. They rely on rather individual and complicated architectures such as, e.g., sulfonation or the preassembly of gold NPs prior to coating.[59, 63]

Hence, an extensive survey covering the preparation, characterization, modification, and application of CS particles to explore the potential of this hybrid material as a chemical assay platform is missing and thus highly desirable. Such a general method should later also allow the integration of yet other particles (e.g., magnetic, luminescent) into or onto the hydrophobic core, the loading of small molecules into the core domain for encoding or the integration of highly porous entities such as mesoporous structures into both, core or shell, rendering the implementation of for example delivery functions feasible.[45, 64-65]

1.5 Synthetic pathways towards SiO_2@PS particles

Several synthetic strategies exist for the preparation of polymeric templates and their subsequent coating with silica, providing access to a wealth of size ranges and shell morphologies. The basic coating strategies can be categorized into divergent and convergent methods (Figure 5).

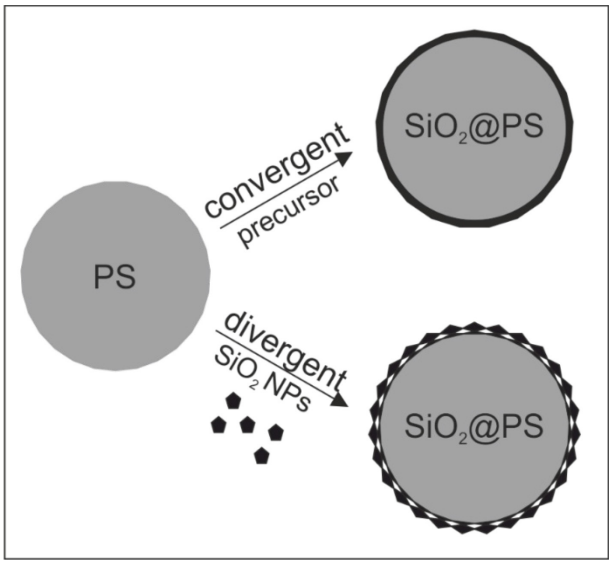

Figure 5. *Scheme of the two preparation pathways using either a convergent or divergent route. The precursor is a soluble monomer which precipitates upon polymerization on the surface of PS beads throughout the coating process.*

Divergent methods use pre-synthesized (or commercially available) colloidal SiO_2 NPs, which are attached to the PS core by chemical coupling, physical means such as layer-by-layer (LbL) or pickering emulsion techniques to form core-satellite assemblies.[47, 62, 66-67]

Apparently, divergent methods represent a straightforward synthetic approach to SAT-compatible CS beads, however, these methods are inherently limited to multilayer-like shell architectures. Moreover, it remains challenging to fix the architecture of such assembled composites to resist subsequent modification steps and exclude the detachment of the SiO_2 NP which could affect the analytical response.

Convergent methods, on the other hand, are based on the direct formation of stable and closed, yet chemically modifiable SiO_2 shells from soluble precursors in the presence of the PS cores during a sol-gel coating process. The cores must herein be chemically or physically tailored to promote the precipitation of SiO_2 onto the PS surface.

This can be achieved by using charged PS beads and electrostatic interactions. Water-based emulsifier-free emulsion techniques, for instance, can be used to prepare positively or negatively charged polymeric core templates.[68] Depending on the surface charge either smooth-appearing silica shells (on positive surfaces) or rough-appearing to raspberry-like structures (on negative surfaces) can subsequently be grown onto the cores. Such syntheses are limited to submicron-sized, monodisperse beads.[50, 55, 69-71]

Macromolecules such as polyvinylpyrrolidone (PVP) promote the precipitation of silica on the surface through acid-base or hydrogen bonding interactions.[46, 72-74] Decoration of the beads' surface with PVP can either be realized via adsorption or dispersion polymerization in organic solvents using PVP directly as the stabilizing surfactant.[74-75] Dispersion polymerization will give access also to larger beads with very good monodispersity for cytometric read-out, making this technique perfectly suitable for the preparation of the polymeric cores in this study.

Along with that route, organic initiators such as the most commonly used azobisisobutyronitril (AIBN) are employed in conjunction with the surfactant to tailor the surface chemistry of the core. Other initiators such as dibenzoylperoxide or 4,4'-azobis(4-cyanopentanoic acid) (ACPA) add more flexibility to this approach. They permit to vary the radical initiation mechanism or to introduce additional functional groups on the surface.[44-45]

1.6 Scope of the thesis

The development of hybrid core-shell (CS) particles as a modular single particle-based chemical assay platform in SAT were the scope of my dissertation project. Flow cytometry for signal read-out was used as a technology that is established for all potentially relevant scenarios, i.e., routine lab-bound analysis, robust field measurements and adaption for further miniaturization. Signal transduction was based on fluorescence which is not only intrinsically highly sensitive and indispensable for flow cytometry, but also compatible with various recognition chemistries and signaling pathways.

The next chapter presents the systematic investigation of CS particle preparation, characterization, and application as SAT array elements for DNA detection. The development of a flexible and robust synthesis method for the CS carriers with access to a wide range of particle surface topologies from smooth to raspberry- and multilayer-like will be outlined. Special focus will be laid on fit-for-purpose characterization methodologies: nitrogen adsorption can serve to elucidate the true morphology of CS particles using t-plot analysis and micropore studies. A novel method to measure the mass and density of the microparticles – resonant mass measurement (RMM) – is further introduced to determine the density of the composites.

Electron microscopy (EM) is a standard method to visualize and characterize plain and hybrid particles. However, a methodological approach to extract key topological parameters from image analysis has not been fully exploited so far. Accordingly, chapter three is devoted to a methodological survey with a focus on (1) the comparison between SEM and TSEM and (2) a novel method to determine the contour roughness of the beads. CS particles with varying size and architecture were prepared and used as the specimen in this study.

The fourth chapter covers the encoding of the CS particles with organic dyes and their application in an immunochemical model assay targeting small molecules in a competitive detection scheme. Emphasis will also be laid on chemical surface design using mixed silane layers with amino-silane and polyethylene glycol- (PEG) silane to reduce non-specific binding. This chapter highlights a key flexibility feature of chemically tailored SiO_2 surfaces and concludes with a first successful realization of an immunochemical multiplex bead array that can be used for the sensitive and selective analysis of four small-molecule target compounds of environmental concern in parallel in a simple mix-and-read fashion.

1.7 Preliminary remarks on the conception of this thesis

The results of my doctoral thesis are grouped into three consecutive chapters as outlined in section 1.6, reflecting the phases of my Ph.D. project. All three subprojects have in common that they are based on the use of hybrid CS architectures, consisting of SiO_2-coated PS microparticles. The scientific outcomes detailed in chapters two to four led to scientific output in the form of three research articles and/or a series of presentations at national and international conferences.

Every chapter, i.e. subproject, contains a specific introduction/motivation, followed by the presentation and discussion of the results and the corresponding experimental details. Written text is largely inspired by the publications yet was adapted to guarantee readability of the thesis and comparability between chapters. Unpublished experiments complement the studies and add more hands-on-results for the reader.

The concluding chapter five reviews key results in a complementary manner. A SWOT analysis subsequently discusses also weaknesses and threats of the CS-based assays to allow for a better evaluation of a potential breakthrough of the platform in the field. This leads to a future projection of opportunities using CS particles in chemical assay development. Ultimately, the CS-particle-based approach will be placed within the bigger context of available and emerging analytical assay technologies.

2 Polystyrene Core–Silica Shell Particles with Defined Architectures

a versatile platform for suspension array technologies

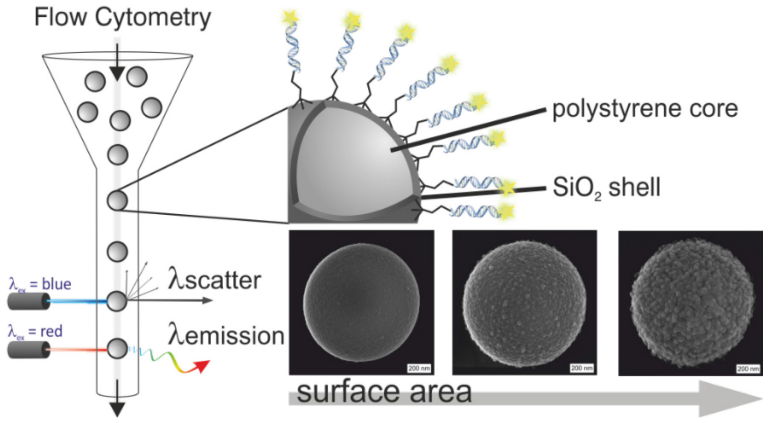

2.1 Abstract

The need for rapid and multiplexed screening in analytical laboratories has led to significant growth in interest in suspension array technologies. In this chapter, a straightforward synthetic route to highly monodisperse SiO_2-coated PS core–shell beads as a novel platform for SAT using cytometric read-out is presented. The particles have controlled surface topologies from smooth to raspberry- and multilayer-like shells. This is made possible by varying the molecular weight of PVP, which was used as the stabilizer of the cores. The particles were thoroughly characterized and comprehensive information on the composition, size, structure, and surface area of the particles is provided. All particles show ideal cytometric detection patterns and convenient handling properties due to the material composition. The beads are endowed with straightforward modification possibilities through the SiO_2 shells. The particles were successfully implemented in cytometric SAT model assays, illustrating the benefits of tailored surface area and structure which is readily available for small-molecule anchoring. Very promising assay performance was shown for DNA hybridization with quantification limits down to 8 fmol.

2.2 Introduction

SAT plays an increasingly important role in various fields of the analytical sciences.[76-78] Due to the requirement of only small amounts of sample, fast reaction kinetics, facile array preparation and the recent availability of user-friendly, robust and reasonably priced flow cytometers, bead-based SAT is an attractive alternative to classical flat arrays or ELISA techniques.[79-81] One crucial advantage of cytometry is its ability to correlate light-scattering signals from the individual beads with fluorescence. Discrimination of the background and unwanted aggregates is thus possible and single particles can be analyzed.

Pure PS or SiO_2 beads are conventionally used as the spherical support. The employment of hybrid CS particles in SAT applications represents a versatile alternative because the favorable properties of a polymeric core and a rigid, yet chemically modifiable silica shell are combined.

This chapter describes a PVP-mediated convergent preparation method for SiO_2@PS particles and their application in DNA detection using flow cytometry. The use of PVP as stabilizer already at the stage of core formation was initially applied by Bamnolker et al. and further investigated and exploited by several others.[45, 74, 82] A closer look at the SEM images which are shown in the relevant papers reveals significant changes in the shell structures when varying the average PVP chain length. Surprisingly, a direct correlation between the molecular weight of PVP as the stabilizer and the resulting shell structure has not yet been investigated.

This strategy seemed particularly straightforward and versatile for a systematic investigation of generating monodisperse SiO_2@PS particles in a structurally controlled fashion. As will be detailed in the subsequent sections, the structure of the SiO_2 coatings on PS beads in basic ethanol/water mixtures can be precisely tuned without changing the coating protocol or using additives. Native SiO_2 shell structures of monolayer- to multilayer-like architecture can be obtained with PVP of increasing molecular weight by this approach. In addition, a prototype SAT application was realized. A correlation between structure and reactivity in cytometric proof-of-principle DNA hybridization assays could be found.

2.3 Results and discussion

2.3.1 Preparation of polystyrene core particles

A straightforward preparation method for polystyrene core particles possessing appropriate anchors for growing a SiO_2 shell must be developed for simple and reliable synthesis of CS particles. I opted here for dispersion polymerization as the most suitable method with PVP as the stabilizer. This approach is well-suited for subsequent SiO_2 shell growth by a convergent method as the latter can take advantage of the readily available PVP chains on the surface of the particles, able to interact with the silica sources through hydrogen bonds.[83] Compared to existing techniques, the preparation of PS core particles using dispersion polymerization was exploited and refined in two ways.

1. ACVA was used as the initiator, which is less hazardous and inflammable than other commonly used thermal initiators such as BPO or AIBN.[45, 74]
2. a systematical evaluation of the structure-directing effect of the stabilizer PVP with different molecular weight on SiO_2 shell formation was done for the first time.

Various studies have been performed by Paine et al., revealing the mechanism of formation, the influence of reaction parameters on the size and size distribution as well as a detailed view on the particle structure during dispersion polymerization with PVP as the stabilizer.[84-85] They found that an increase in the molecular weight of PVP leads to decreased particle sizes due to improved stabilization of the polymer seed particles. Hence, the amount of styrene must be carefully adjusted for the preparation of similarly sized PS particles when identical amounts of PVP are used for subsequent unequivocal comparison like in this study.

Three different commercially available PVP stabilizers were employed: PVP10, PVP40 and PVP360, respectively, resulting in three different beads termed PS-PVP10, PS-PVP40, and PS-PVP360. The amount of styrene was varied between 4.8 and 19.2 wt.-% to total weight of solvent used. TSEM overview images of the obtained PS particles are shown in Figure 6.

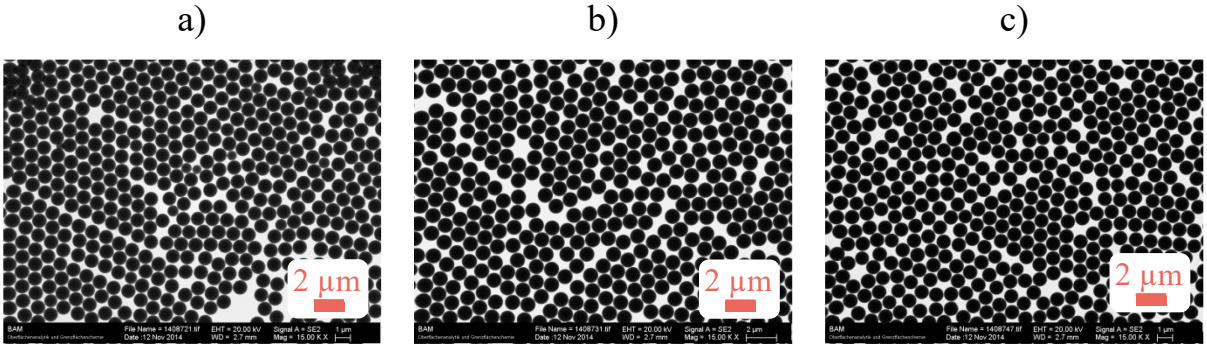

Figure 6. *TSEM images of the PS core particles: a) – PS-PVP10; b) – PS-PVP40; c) – PS-PVP360.*

The particles are nicely distributed on the carbon film and partly form 2-dimensional packings, indicating good monodispersity. To verify this result, the size and size distribution of the particles were determined. A convenient and well-known approach for size analysis of spherical objects is to measure the projection area of the individual specimen in such electron microscopy images and to extract the equivalent circular diameter (*ecd*).

Images can be processed in ImageJ, a freely available open source software, using a proper threshold to obtain binary images of accurately identified particles and applying a watershed algorithm to separate touching particles.[86] The setting of the proper threshold has been tested on certified reference materials of well-known dimensions.[86-87] Then, the projection area of individual particles can be determined using ImageJ's built-in analysis tool.

The distribution plots were obtained after counting 180 beads in 12 nm particle size bins. Peak analysis using Gaussian fit (eq. I, black dashed line, Figure 7) of the major bead populations revealed an average equivalent circular diameter *ecd* ≈ 912 nm across all batches (Table 1).

eq. I. $$y = y_0 + A * e^{-\frac{(x-xc)^2}{2w^2}}$$

Additionally, statistical analysis of all counted particles was done to calculate the mean diameter as well as the standard deviation (σ) assuming circles of same areas as those of the identified particles. The coefficient of variation (c_v) is then given as the ratio of standard deviation to mean size. The c_v is a measure for monodispersity and represents an important quality factor of the particle batches.

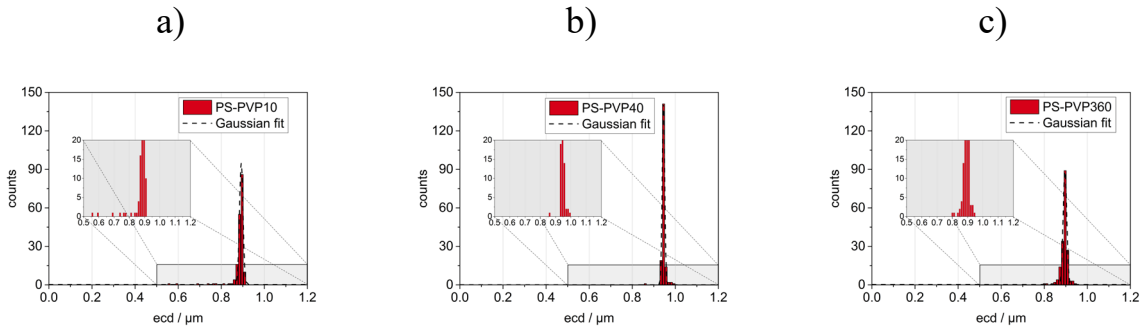

Figure 7. *Diameters (ecd) determined from TSEM image analysis with ImageJ software using Gaussian fit of main peak from distribution plots: a) – PS-PVP10; b) – PS-PVP40; c) – PS-PVP360.*

The c_υ listed in Table 1 amounts to <5% and indicates good monodispersity across the entire particle batches. With regard to application and performance evaluation of these particles as platform elements in SAT, monodispersity and similarity in size are of great importance for comparability and data interpretation.[88]

Table 1. *Equivalent circular diameter (ecd), coefficient of variation (c_υ), the theoretical surface area per particle as well as BET surface area determined from nitrogen adsorption including the C-Value obtained from BET analysis.*

sample	*ecd* [a] / nm	c_υ [b]	A_s [c] / µm² particle^{-1}	BET [d] / m² g^{-1}	C-Value [d]
PS-PVP10	893.0	4.7	2.51	n.d.	n.d.
PS-PVP40	945.0	1.0	2.81	n.d.	n.d.
PS-PVP360	896.2	1.9	2.52	6.05	50.8

[a] Determined with TSEM image analysis. [b] c_υ determined from statistical analysis of all counted particles. [c] Surface area was calculated assuming an ideal sphere model. n.d. - not determined. [d] Analysis was performed with the built-in software after data acquisition with the ASAP 2020 instrument (Micrometrics).

Grafted PVP chains usually form patches on the surface of PS particles, especially for higher molecular weight stabilizers.[89] Determination of the specific surface area (A_s) with nitrogen adsorption still showed a value of ~6 m² g^{-1} for PS-PVP360, which matches with the calculated surface of ideal spheres (assuming a density of 1.05 for polystyrene), without an indication of

micropore formation, i.e., high C-values in the BET analysis (Table 1).[90] The experimental raw data plot can be found in Annex 6.1.

All polymeric core particles are therefore considered to be spherical, non-porous and smooth. Determination of the surface area of the bare cores to 2.51, 2.81 and 2.52 µm² per particle for PS-PVP10, PS-PVP40 and PS-PVP360 can be calculated assuming an ideal sphere model.

2.3.2 Flow automated cell sorting (FACS)

The particles were next characterized by flow cytometry (FACS). This laser-based method collects scattering and fluorescence information from individual particles in a hydrodynamically focused fluidic stream, making it highly suitable for single particle read-out in SAT (Figure 8).

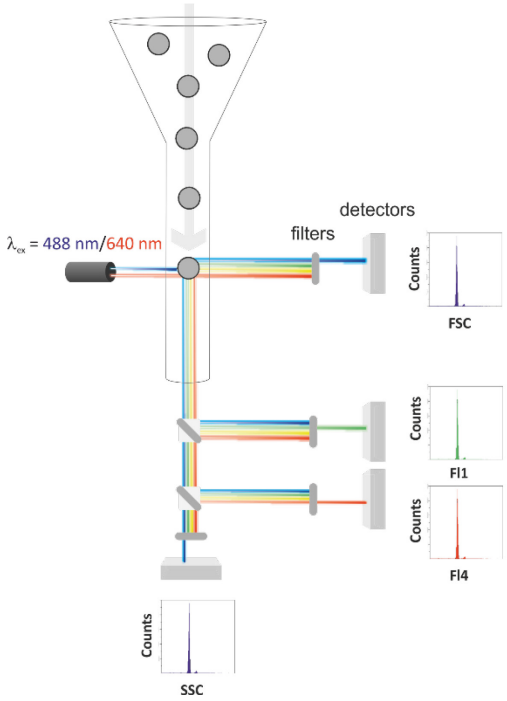

Figure 8. *FACS principle with two laser sources (λ_{ex} = 488 nm and 640 nm), detection of scattered light at 180° (FSC) and 90° (SSC), as well as two fluorescence detectors at 90° with a green-light bandpass filter FL1 and a red-light bandpass filter FL4.*

Light scattering after irradiation with a 488-nm laser source is recorded at 180° (FSC, forward scattering) or 90° (SSC, sideward scattering) using a detector (typically a photomultiplier or

photodiode) and suitable optical filters. Particles must typically be larger than 200 nm to scatter enough light so that they can be detected with typical benchtop FACS instruments. The intensity of scattering is directly correlated to the size of the particles. Counting rates of a few hundred or thousand particles per second are common with FACS.

Hence, FACS provides qualitative information to track the most important particle properties such as size, size distribution, and presence of secondary particles with high statistic numbers in very short times. The FSC signal is commonly used for size measurements since it is less affected by the structure (or granularity) of the particles. The results obtained with FACS measurements of the three particle batches are summarized in Figure 9. The signal is plotted in "mean channel intensity" (MCI, linear scale).

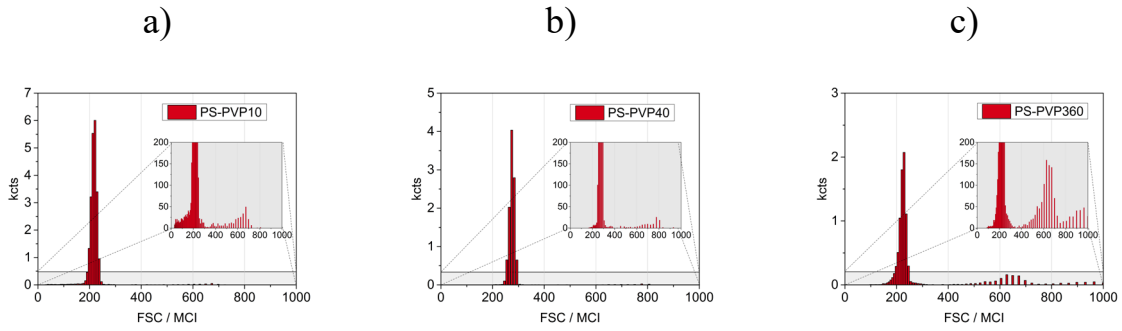

Figure 9. *Forward scattering (FSC) analysis of PS particles using FACS: a) – PS-PVP10; b) – PS-PVP40; c) – PS-PVP360. Histograms are resolved in "kilo counts" (kcts) per "mean channel intensity" (MCI). The inset shows a magnified section to visualize secondary particles (left from main peak) and dimers (right from main peak).*

Three different regions can be identified; the main peak centered at the peak maximum ($x_m \pm 3\sigma$, derived from Gaussian fit analysis), secondary particles at lower values and aggregated particles at higher values. In the case of PS10, a slightly left-skewed distribution was observed with an increased number of counts of approximately 4.7% to lower values ($< x_m - 3\sigma$). This is consistent with image analysis which revealed a certain amount of smaller secondary particles (cf. Figure 6a). For PS-PVP40 and PS-PVP360, a bell-shaped distribution was found, lacking any hint for smaller secondary particles.

Furthermore, FACS analysis provides information about the stability and aggregation behavior of the particles in dispersion derived from counts at higher values ($> x_m+3\sigma$). As can be seen in the insets in Figure 9, additional counts were observed for all particles. In agreement with reports in the literature, these peaks are ascribed to a low number of aggregated particles (dimers, trimers, etc.).[91] PS-PVP360 shows significantly more aggregation, approximately 15% in comparison to only 1–2% for PS-PVP10 and PS-PVP40, which presumably stems from the entanglement of long PVP chains occurring during the drying step in the preparation procedure. Such entanglement complicates complete separation of the particles prior to FACS analysis. This was supported by an experimental observation: Whereas dispersions from PS-PVP10 and PS-PVP 40 can be readily prepared in water, PS-PVP360 requires extensive ultra-sonication.

Finally, Gaussian fit analysis of the main peaks in the FACS histograms revealed c_v of ca. 4.9% for PS-PVP10 and PS-PVP360 and 3.6% for PS-PVP40, showing that the major bead populations are monodisperse in terms of an actual SAT application.

2.3.3 Preparation of CS particles: SiO_2-coating of polymeric core

Formation of the hydrophilic SiO_2 shell on the PS particles was performed in an ammonia-catalyzed sol-gel process in ethanol with tetraethoxysilane (TEOS) as the precursor. Identical synthetic conditions were used for all core particles to investigate only the effect of PVP with different molecular weight on the coating process.

An increase of the particle size after coating can be determined by TSEM image analysis which primarily indicates a successful coating of the particles (Table 2). A first difference in the coating performance between the different core particles becomes obvious, because the shell thickness (t_{shell}), which was derived from the difference of CS and core diameter divided by two, increases gradually when stabilizers with a higher molecular weight are used.

Additionally, the SiO_2 content of the different batches was determined by thermogravimetric analysis (TGA, a more detailed discussion of the data can be found in section 2.3.4). The SiO_2 content increases from 16.0 wt.-% to 28.7 wt.-%. However, a linear correlation between SiO_2 content and shell thickness was not found, strongly indicating structural changes of the shell.

Table 2. *Diameters (ecd), coefficient of variation (c_v) and shell thickness (t_{shell}) of the SiO_2@PS particles and shell forming SiO_2-NPs ($ecd_{SiO2\ NPs}$).*

sample	*ecd* [a] / nm	c_v [b]	t_{shell} [c] /nm	SiO_2 [d] / wt.-%	$ecd_{SiO2\ NPs}$ [e] / nm
SiO_2@PS-PVP10	935.0	1.5	21.0	16.0	~20
SiO_2@PS-PVP40	1017.5	1.0	36.2	20.2	~32
SiO_2@PS-PVP360	1006.5	3.4	55.2	28.7	~35

[a] Determined with TSEM image analysis. [b] Determined from statistical analysis of all counted particles. [c] Calculated by subtracting the ecd of CS particles from ecd of neat core particles divided by two. [d] Determined with TGA. [e] Size was estimated with image analysis, measuring at least 15 NPs visible on the surface of the shell.

A detailed view of the shell topology was possible with SEM (Figure 10). The In-Lens detector of the instrument enabled high-resolution imaging of the surface due to its ability to collect selectively only the high-resolution SE1 electrons, emitted locally at the point of impact of the primary electron beam onto the specimen's surface.

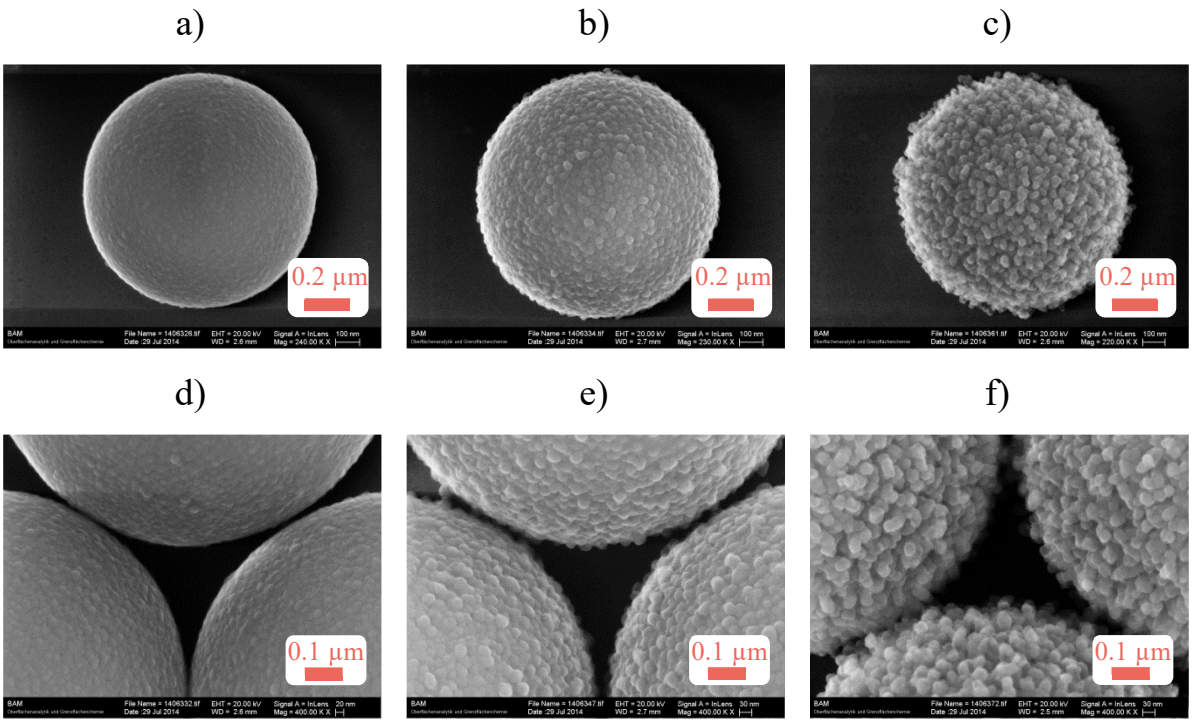

Figure 10. *SEM images of SiO_2@PS particles: a), d) – SiO_2@PS-PVP10; b), e) – SiO_2@PS-PVP40; c), f) – SiO_2@PS-PVP360.*

Smooth appearing (SiO_2@PS-PVP10), raspberry-like (SiO_2@PS-PVP40) and multilayer-like (SiO_2@PS-PVP360) structures can be distinguished on the surfaces of the particle batches with high reproducibility within a single batch. All shells are assembled from small SiO_2 NPs, which have fused together in different degrees to form the shell.

Inspection of the SiO_2 NPs assembled on the core particles' surfaces allowed to deduce the average size of the SiO_2 NPs (Table 2) by manually drawing circles or ellipses ($N > 15$) and calculating the equivalent circular diameter ($ecd_{SiO2\ NP}$). Images in higher magnifications were recorded for this purpose (Figure 11).

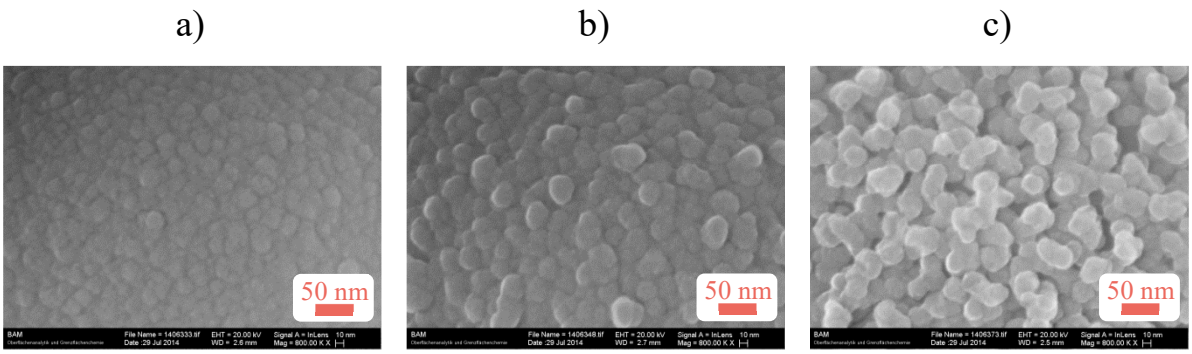

Figure 11. *SEM images of SiO_2@PS particles: a) – SiO_2@PS-PVP10; b) – SiO_2@PS-PVP40; c) – SiO_2@PS-PVP360.*

Although the boundaries of the NPs of SiO_2@PS-PVP10 were not as distinct as those of SiO_2@PS-PVP40 and SiO_2@PS-PVP360, the visual comparison suggested slightly smaller SiO_2 NP sizes of ca. 20 nm for SiO_2@PS-PVP10, reflecting well the theoretical value of a silica shell formed by a smooth monolayer of fused SiO_2 NPs. For SiO_2@PS-PVP40 and SiO_2@PS-PVP360, on the contrary, shell thickness exceeds SiO_2 NP size by factors of approximately 1.1 and 1.6, respectively, suggesting an increasingly looser assembly.

TEM images confirm the CS structure of the particles (Figure 12). A darker appearing shell domain can be seen for all particles which account for the silicon with higher atomic number and hence stronger contrast generation.

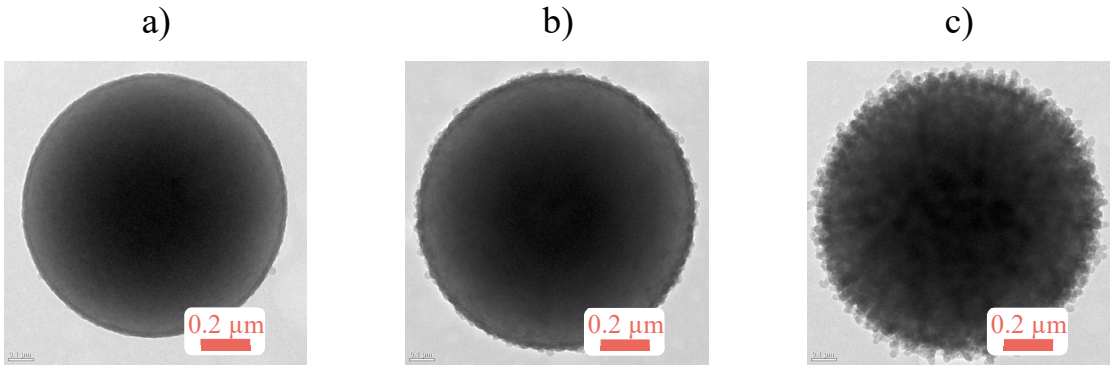

Figure 12. *Representative TEM images taken from the SiO_2@PS particles: a) – SiO_2@PS-PVP10; b) – SiO_2@PS-PVP40; c) – SiO_2@PS-PVP360.*

2.3.4 Thermogravimetric analysis

A detailed interpretation of TGA curves adds more insight into the microscopic structure of the particles (Figure 13, left). Basically, three phases were noticed during runs in synthetic air and can be assigned to the following processes: until 280°C, water desorption takes place (phase 1) followed by core burning until 400 C° (phase 2).[74] In the third phase, condensation reactions and removal of organic residues from the silica domain take place until only inorganic, dehydrated SiO_2 remains.[92]

During the whole process of thermal degradation, a coupled mass spectrometer recorded the amount of the major thermal degradation product CO_2 (Figure 13, right).

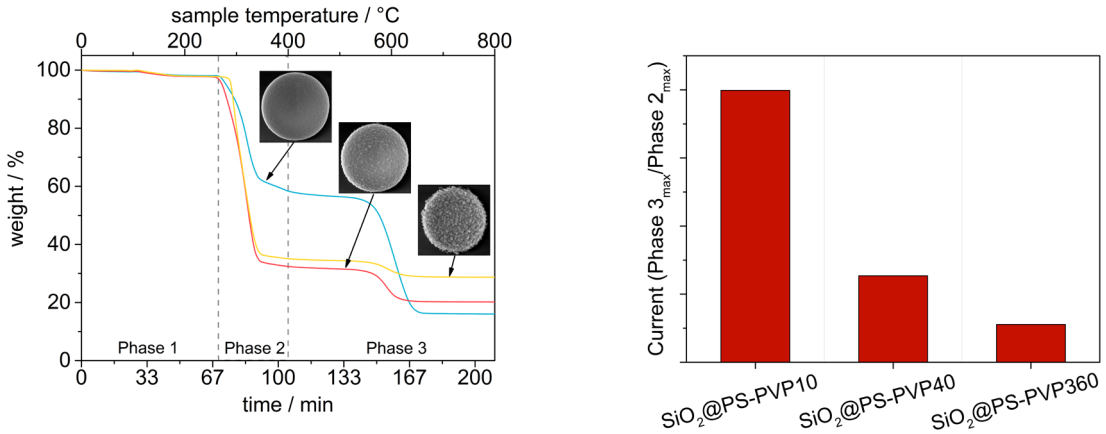

Figure 13. *Left – TGA curves for SiO_2@PS-PVP10, SiO_2@PS-PVP40 and SiO_2@PS-PVP360. Right – ratiometric amount of released CO_2 during phases 2 and 3 of combustion.*

For SiO_2@PS-PVP10, a significantly higher amount of CO_2 was released only during the third phase. At the same time, almost 50 % of the polymeric core was retained until temperatures as high as 500 °C for the smoothest CS particles.

The TGA data suggest that the short PVP10 chains lead to a closed, non-porous silica shell whereas longer PVP40 chains penetrate the shell domain and produce micropores during the thermal process as suggested by Chou et al. or Li et al. for PVP-mediated silica coating of inorganic nanoparticles.[93-94] TSEM/SEM measurements of the silica residues after TGA analysis revealed hollow structures for all particles, so-called silica hollow microparticles (SHMs), and confirmed the complete thermal removal of the core (Figure 14).

Moreover, only for SHMs generated from SiO_2@PS-PVP10, an increased number of cracked particles is observed (Figure 14d, red circles); the structures of the other particles remain largely intact (Figure 14e,f). It is worth noting that the macroscopic shell structure does not change during thermal treatment. Use of PVP should thus also allow for control over the surface structure of intact SHMs with raspberry- or multilayer-like structure.

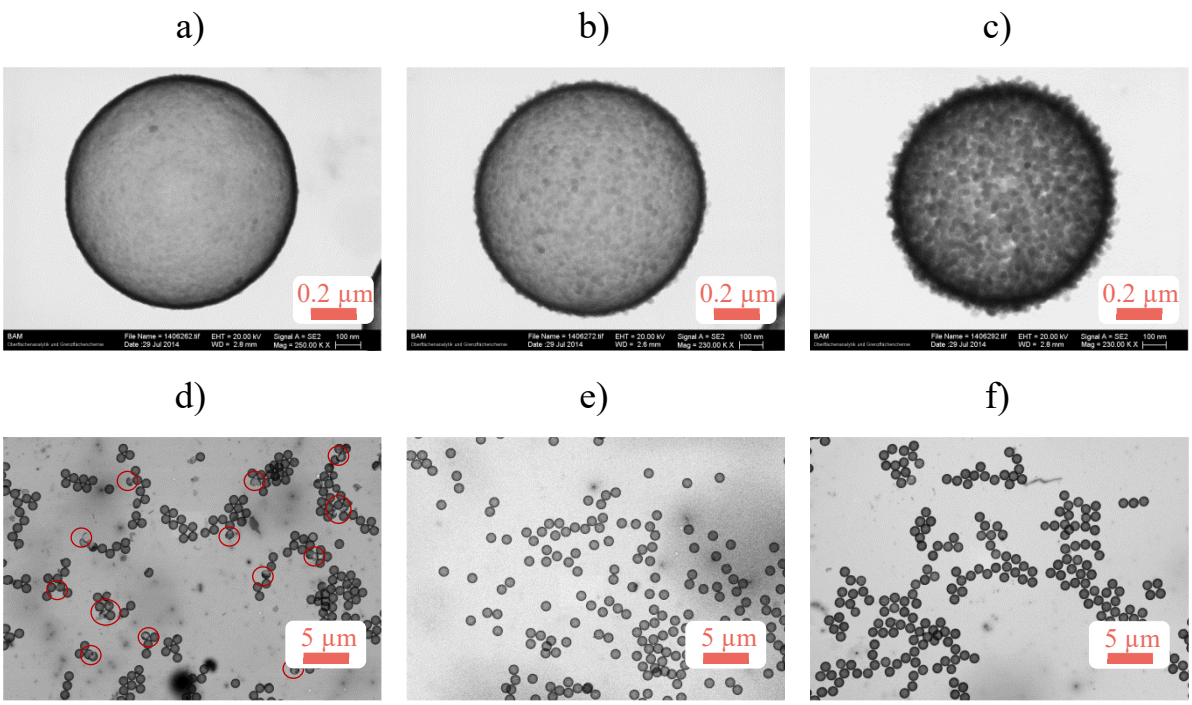

Figure 14. *TSEM images of SHMs resulting from TGA treatment, i.e. thermal combustion of the polymeric core: a), d) – smooth SHMs from SiO_2@PS-PVP10; b), e) – raspberry-like SHMs from SiO_2@PS-PVP40; c), f) – multilayer-like SHMs from SiO_2@PS-PVP360.*

In agreement with the conclusions from TGA analysis, many of the non-porous and smooth SiO_2@PS-PVP10 particles release their combustion products only after the shell has cracked because of the increasing pressure inside the core. In the case of SiO_2@PS-PVP40, decomposition of shell-penetrating PVP results in pores within the silica shell which are big enough to release CO_2 continuously. The macroporous multilayer-like structure of SiO_2@PS-PVP360 further facilitates the release of combustion products, which is evident from the lowest amount of released CO_2 in the third stage.

Investigation of cracked SHMs provided further insight into the gradual change of the shell structure from smooth to raspberry- and multilayer-like (Figure 15). The cracked shells additionally permitted to estimate a value for the average shell thickness, yielding ca. 20 and 30 nm for SiO_2@PS-PVP10 and SiO_2@PS-PVP40, respectively, agreeing well with those determined by image analysis.

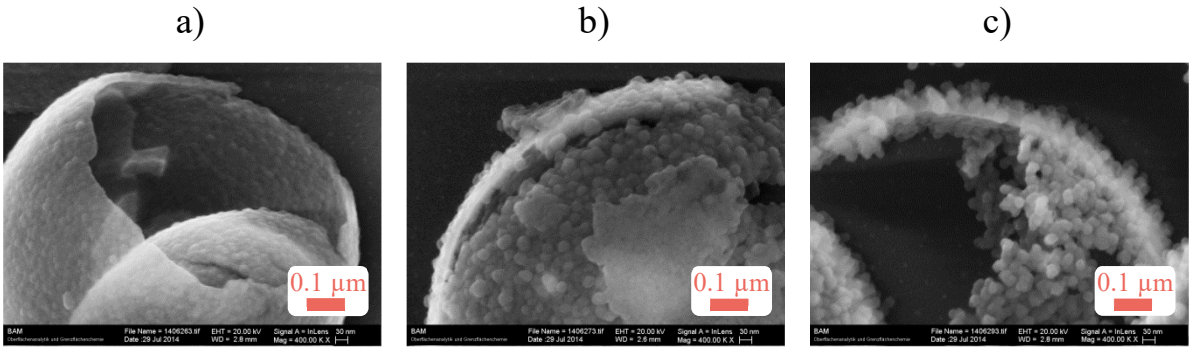

Figure 15. *SEM images of cracked shells from SHMs after thermal removal of the polymeric core: a) – SiO_2@PS-PVP10; b) – SiO_2@PS-PVP40; c) – SiO_2@PS-PVP360.*

2.3.5 The mechanism of CS particle formation

Although the exact mechanism of shell formation could not fully be unraveled, several observations were made during the studies which hint at a decisive influence of (i) the degree of shielding of the charges on the involved particles by and (ii) the structural conformation of PVP with different molecular weight.

The size of the excess SiO_2 NPs, present in the supernatant of all the three hybrids directly after the coating process (prior to washing or further processing), amounted to similar hydrodynamic radii R_h of 21–24 nm as determined by dynamic light scattering (Table 3).

Table 3. *Size determinations and zeta potential (ZP) of SiO_2 NPs, which are formed during the coating process, with DLS using a Zetasizer Nano XS (Malvern).*

sample	R_h, SiO2-NP[a] / nm	$ZP_{\text{in coating medium}}$ / mV	$ZP_{\text{in water}}$ / mV
PS-PVP10	23.9	-5.26±2.85	-57.0±7.7
PS-PVP40	20.7	-1.52±2.93	-39.5±6.2
PS-PVP360	23.9	-1.98±3.10	-42.9±5.5
SiO_2 NPs	23.8	-3.52±3.50	-40 to -50 [95]

[a] Hydrodynamic radius.

These findings suggest that under the reaction conditions employed (ethanol/water (50:1), c_{NH3} ~ 0.5M), silica seeds will unperturbedly grow in solution regardless of the PVP chain length on the PS beads present in the mixture. This was confirmed by carrying out the sol-gel reaction in the absence of PS beads, again yielding SiO_2 NPs of R_h = 24 nm. If one further considers that at basic pH not only the carboxylated PS core particles possess a net negative surface charge but also the silica particles (zeta potentials in coating medium, cf. Table 3), the adsorption of SiO_2 NPs onto the cores primarily depends on the attenuation of the cores' surface charge density by the PVP mediators. Note that for SiO_2 NPs, surface charge density decreases with increasing particles size, with particles of ca. 50 nm approaching the value of flat SiO_2 surfaces.[96]

For PVP, commonly the higher the molecular weight is the more efficient is the shielding effect of the net charge of PS beads with this effect depending strongly on molecular weight below ca. 40 kDa and only weakly on molecular weight above ca. 40 kDa.[97] This was confirmed by ZP measurements of the cores in water where PS10 possesses a ZP of –57 mV while those for PS40 and PS360 lay around –40 mV.

Taking further into account that a considerably large number of ammonium ions is present in the system, the association of smaller SiO_2 NPs (with a higher net surface charge) onto the more negatively charged PS10 is tentatively ascribed to a higher concentration of NH_4^+ ions in the interlayer between PS/PVP beads and SiO_2 NPs, in accordance with findings by Fuji's group.[70] As a result, smaller SiO_2 NPs assemble on PS10 due to surface charge effects, forming a more densely packed monolayer and hence smoother coating.

For PVP40 and PVP360, on the contrary, the longer PVP chains form larger patches on the surface in conjunction with the more strongly shielded negative charges of PS40 and PS360 leading to a looser assembly of larger SiO_2 NPs on these two cores. Here, the different chain lengths of PVP40 and PVP360 presumably contribute to the differences seen for SiO_2@PS-PVP40 and SiO_2@PS-PVP360: adsorption due to hydrogen bonding of SiO_2 NPs to PVP in different distances from the surfaces rather than electrostatic effects are expected to be decisive here.

When the synthesis is carried out with lower concentrations of TEOS for example, similar SiO_2 NP sizes are found on the surfaces. However, in comparison to SiO_2@PS-PVP10, the coating of for instance the PS360 core by SiO_2 NPs is by far not surface area-wide (Figure 16).

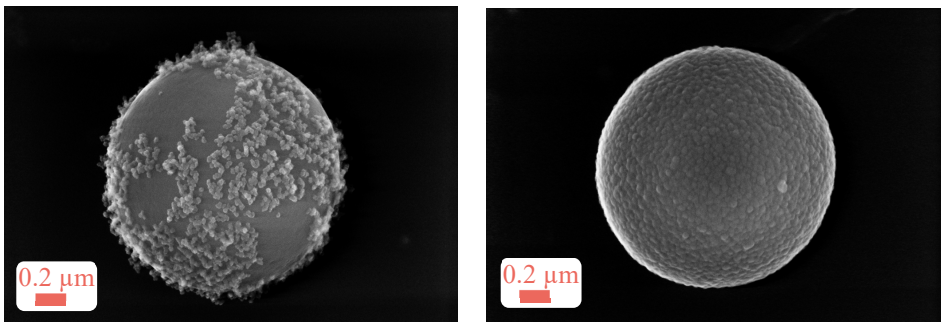

Figure 16. *SEM images of SiO_2@PS-PVP360 (left) and SiO_2@PS-PVP10 (right) with lower amount of TEOS during the coating process (0.5 mL instead of 1.5 mL).*

This, in turn, correlates with a lower amount of protonated Si-OH groups (corresponding to a higher surface charge) being available on the smaller particles for hydrogen-bonding interactions with PVP at pH ~ 11, reflecting well the loose binding of the NPs onto PS360.[98]

In summary, considerations of the interplay of electrostatic effects as the primary and hydrogen bonding as the secondary driving forces in conjunction with the molecular weight-specific properties of PVP permit the tailoring of desired CS architectures.

2.3.6 Particle density with resonant mass measurement

The core particles and CS particles were further characterized by resonant mass measurement (RMM). The aim was to investigate if mass-related information of individual beads would allow

the calculation of the core or core-shell particle size and density as well as shell density and thickness.

The working principle of this rather new methodology relies on a resonant frequency shift which is induced by individual particles passing a suspended microchannel resonator. This detection scheme allows mass changes to be measured down to the femtogram level.[99] The construction of the microfluidic chip is shown in Figure 17 (left).

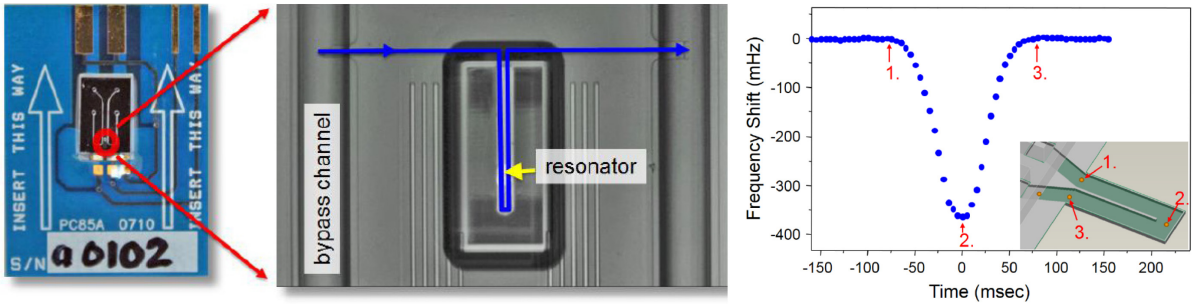

Figure 17. *Left – photograph of a MEMS sensor chip, and a microscope view of the resonator. Right – frequency shift induced by transition of crossing particles.*

The frequency shift is recorded using optical-based detection (Figure 17, right) and the signal is proportional to the mass of the displaced fluid.[99] By calibration with a particle standard with a known volume and density, the frequency shift can be converted to the buoyant mass according to the Archimedes principle (eq. II).

eq. II. $$m_{buoyant} = m_{standard} - m_{displaced\ fluid}$$

For particles with known density ($\rho_{particle}$), the buoyant mass can then be converted to the dry mass (m_{dry}) and equivalent spherical diameter ($esd_{particle}$) using eq. III and eq. IV.

eq. III. $$m_{dry} = \frac{m_{buoyant}}{\left(1 - \frac{\rho_{fluid}}{\rho_{particle}}\right)}$$

eq. IV. $$esd_{particle} = \left(\frac{6 * m_{dry}}{\pi * \rho_{particle}}\right)^{\frac{1}{3}}$$

The particle density can be calculated with a convolution method developed by Malvern Instruments Ltd. Here, the buoyant mass of the sample is measured in two fluids with different densities. Assuming a constant volume in both fluids, the density can be determined by maximizing the convolution between the dry mass distributions when altering the densities (Figure 18).

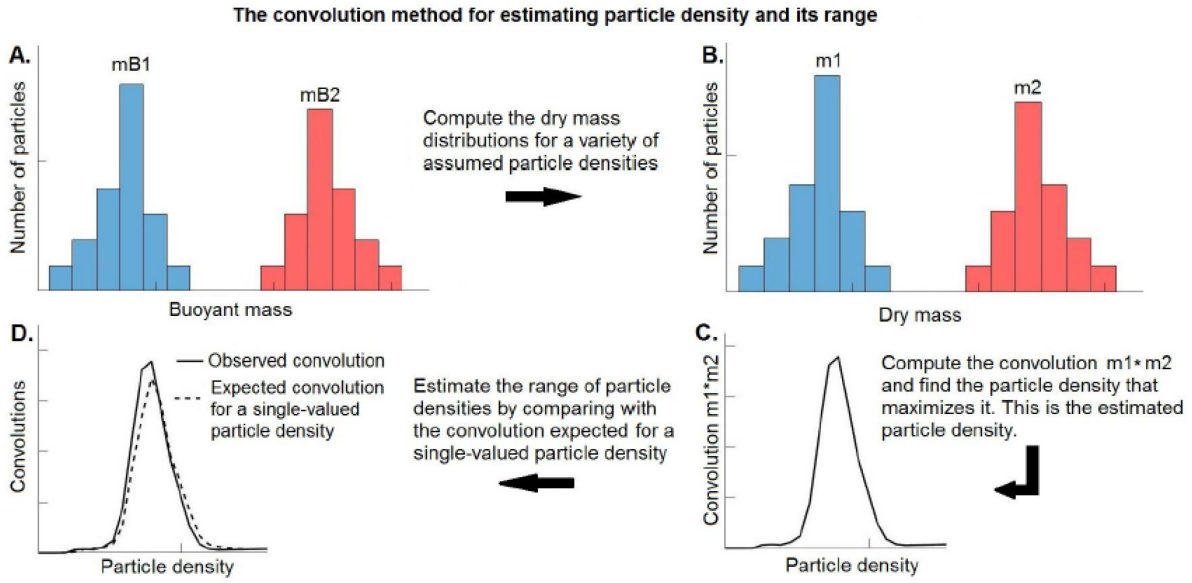

Figure 18. *Convolution method for density determinations: A – the buoyant mass distributions in two different fluids; B – dry mass distributions using a variety of assumed particle densities; C – the convolution of the two distributions for each particle density. The estimated particle density is the value that maximizes the convolution; D – Estimate the range of particle densities by comparing with the convolution expected for a single valued density. Figure reprinted from* [100].

The densities are listed in Table 4. The density of the pure PS particles matches well the density of pure polystyrene with 1.05 g mL^{-1} and the densities of CS particles increase from PS-PVP10 to PS-PVP40 and PS-PVP360.

In fact, the densities fit well with the sum of the mass fraction and density of the core and the shell (determined with TGA, cf. Table 2), assuming a density of silica of 1.62 g mL^{-1}. This is in good accordance with theoretical densities of particles with a one-level pore-system (ρ ~

1.644 g mL^{-1}), i.e. silica particles which are themselves constructed of smaller closely packed nanospheres.[101]

Table 4. *Calculated densities for core and CS particles using the convolution method.*

sample	ρ_{core} / g mL^{-1}	σ	ρ_{CS} / g mL^{-1}	σ
PS-PVP10	1.057	0.003	1.146	0.035
PS-PVP40	1.058	0.002	1.173	0.003
PS-PVP360	1.054	0.002	1.201	0.002

With the densities in hand, the mass and size distributions can now be measured and calculated with eq. III and eq. IV. Figure 19 shows an exemplary histogram plot of PS-PVP10 and Si@PS-PVP10 with 500 measured particles counted in 20 fg bins. The plots for the other particle batches are shown in Annex 6.2.

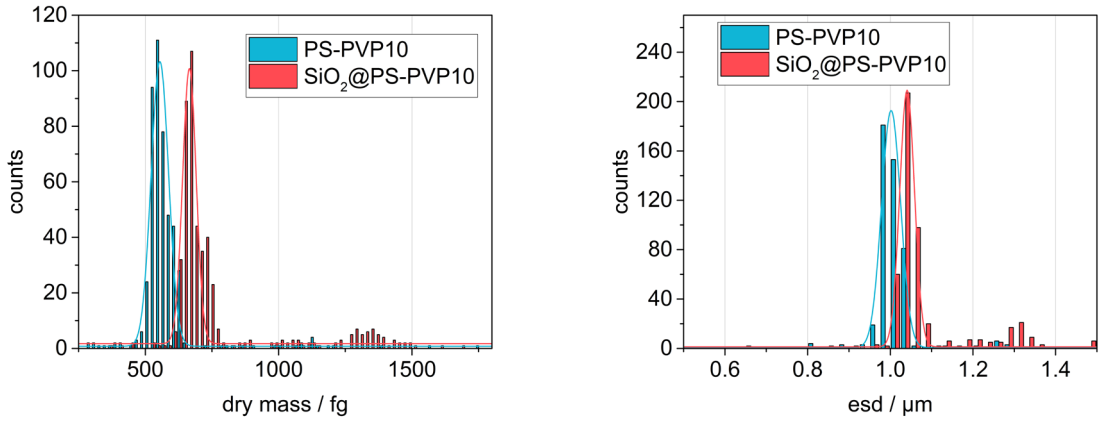

Figure 19. *Exemplary plot of dry mass (left) and size distributions (right) for PS-PVP10 (blue) and SiO_2@PS-PVP10 (red) particles. Distribution plots of the other four particle batches can be found in Annex 6.2.*

There is a clear increase in mass and size due to the addition of a silica shell. This trend can further be analyzed using Gaussian fit analysis of the plots. This allows extracting the mean

values for mass and the equivalent spherical diameter (*esd*) for all particles. The results are listed in Table 5.

The results from shell thickness calculation by subtracting the diameter of the coated and uncoated sphere divided by two is comparable to the values determined from TSEM image analysis, validating the equivalent spherical diameter *(esd)* determined in the wet state using RMM as a reliable measure for bead characterization.

Table 5. *Summary of the equivalent spherical diameter (esd), calculated mass (m_{dry}), and corresponding coefficient of variation (c_υ) for all particles derived from the RMM measurements. Additionally, the mass (m_{shell}) and thickness of the shell (t_{shell}) was calculated by subtraction the CS and core particle size (divided by two for shell thickness).*

	esd / nm	c_υ	m_{dry} / fg	c_υ	t_{shell} / nm	m_{shell} / fg
PS-PVP10	1002.0	2.3	554.7	5.9	-	-
PS-PVP40	1071.8	1.3	682.4	4.9	-	-
PS-PVP360	1022.0	1.8	590.6	4.9	-	-
SiO_2@PS-PVP10	1040.7	1.7	665.4	3.8	19.3	110.7
SiO_2@PS-PVP40	1127.5	1.6	880.0	4.3	27.9	197.6
SiO_2@PS-PVP360	1137.8	2.5	926.2	7.0	57.9	335.6

In this regard, another interesting finding with RMM can be extracted from the dry mass distribution. Next to the main population of SiO_2@PS-PVP10, a secondary population can be identified with doubled dry masses (Figure 19, left) – an argument supporting the assumption that the aggregates found with FACS are particle dimers (section 2.3.2).

2.3.7 Surface area with nitrogen adsorption

Regarding the choice of a particle platform for an analytical assay, surface area, porosity, and accessibility of surface functional groups are of paramount importance. The different CS particles were thus also analyzed by nitrogen adsorption/desorption. Figure 20 shows the adsorption against the relative pressure for all particles.

Apparently, no mesopores were formed in the shell of any of the CS particles, see the typical type II desorption isotherms (Figure 20a–c, red curves). The initial sharp adsorption of N_2 in the isotherm of SiO_2@PS-PVP360 (Figure 20c, black curve) and a C-value of ~370 derived from the BET fitting rather indicate the presence of micropores (Table 6). Usually, C-values between 80 and 150 are found for non-porous materials.[102]

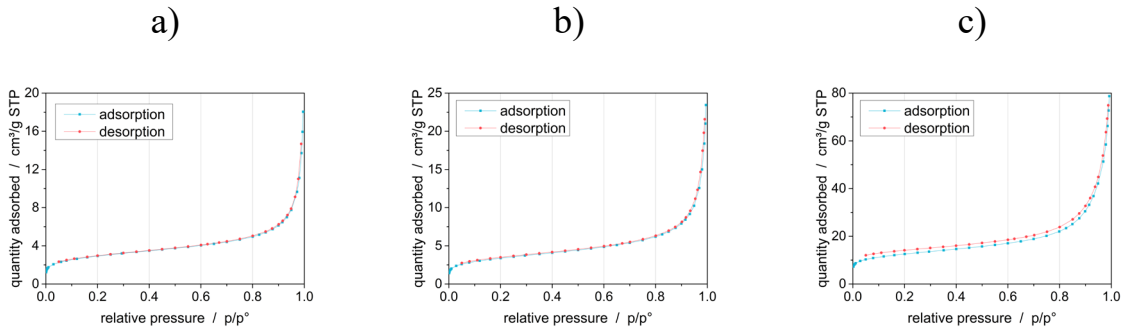

Figure 20. *Nitrogen adsorption/desorption curves: a) – SiO_2@PS-PVP10; b) – SiO_2@PS-PVP40; c) – SiO_2@PS-PVP360.*

Table 6. *C-Values extracted from BET-Analysis.*

	Si@PS-PVP10	Si@PS-PVP40	Si@PS-PVP360
C-Value	159.6	157.8	368.8

Hence, the external surface area was determined with the t-method developed by Lippens and de Boer.[103] The adsorption data are plotted against the layer thickness (t-plot), which is calculated using the Harkins and Jura correlation using eq. V. The linear regression between 3.5 and 5 Å, which correlates to the range between monolayer formation and capillary condensation, allows the separation of micropore and external surface area through the slope of the fit using eq. VI (Figure 21).[104]

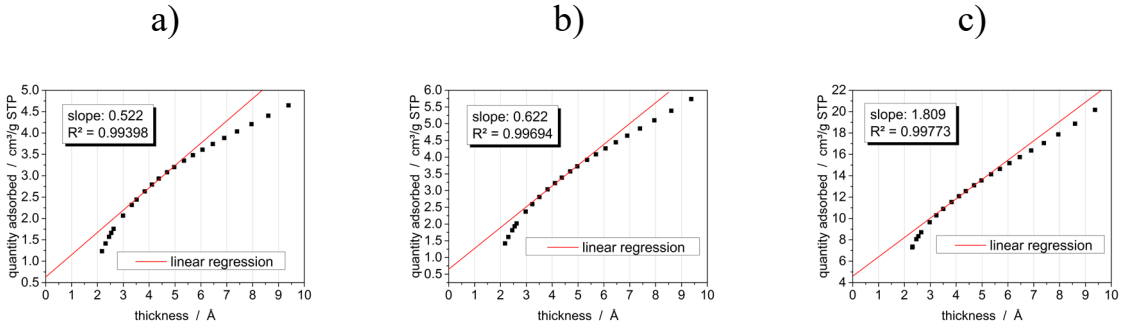

Figure 21. *T-plot of the nitrogen adsorption data: a) – SiO_2@PS-PVP10; b) – SiO_2@PS-PVP40; c) – SiO_2@PS-PVP360.*

The results are collected in Table 7. In comparison to the BET derived surface area, micropore area for SiO_2@PS-PVP360 accounts for roughly 38%. In contrast, the fraction of micropore area accounts for approximately 20% in the case of SiO_2@PS-PVP10 and SiO_2@PS-PVP40.

eq. V. $$t\,(\text{Å}) = \sqrt{\frac{13.99}{0.034 - \log\left(\frac{p}{p_0}\right)}}$$ (Harkins and Jura)

eq. VI. $$A_{t-plot} = (slope \times 15.468)$$

In the next step, a value for the "surface per particle" was determined which will allow the comparison of cytometric data, i.e., signals related to individual particles. The number of particles per gram was thus derived from TGA data under the assumption that the beads are perfect spheres (eq. VII – eq. X).

eq. VII. $$V_{core} = \left(\frac{4}{3}\right) \times \pi \times \left(\frac{d}{2}\right)^3$$

eq. VIII. $$m_{core} = \frac{V_{core}}{10^{18}} \times \rho_{PS}$$

eq. IX. $$m_{TGA} = 1 - \left(1g * \left(\frac{SiO2\ (\%)}{100}\right)\right)$$

eq. X. $$N^{\,TGA}_{particles} \times g^{-1} = \frac{m_{TGA}}{m_{core}}$$

To account for the smaller secondary particles, which contribute to the surface and increase the total number of particles, the size and standard deviation determined from statistical analysis of the full TSEM data set were used here. The surface area per particle was then calculated from the ratio of $N^{TGA}_{particles}$ to the external surface area per gram (Table 7).

Compared to non-porous spheres, an increase in surface area with an increasing molecular weight of PVP can be observed. For smooth CS particles, a slight increase of surface area with a factor of ~1.5 in line with the model of a rather smooth and dense SiO_2 coating on PS10 with only little bulging of SiO_2 NPs can be found. For the raspberry-like particles, an almost doubled surface can be calculated, which correlates well with an increased bulging of SiO_2 NPs. Finally, for the multilayer-like particles a significantly larger increase of surface can be found with a factor of ~6 due to the macroporous network of SiO_2 NPs.

Table 7. *Calculated surface area (A_{CS}) per gram from BET and t-plot analysis. Mean diameters and deviations are determined from the statistics of all counted particles with TSEM image analysis. Particle number per gram and corresponding surface area (A_{CS}) per particle are also included.*

	SiO_2@PS-PVP10	SiO_2@PS-PVP40	SiO_2@PS-PVP360
$A_{CS\ (BET)}$[a] / $m^2\ g^{-1}$	10.5	12.1	45.0
$A_{CS\ (t\text{-}plot)}$ / $m^2\ g^{-1}$	8.1	9.6	28.0
ecd_{CS}[b] / nm	937.4 ± 13.9	1018.0 ± 9.8	1002.3 ± 34.2
$N_{particles}^{TGA}$ / $\times 10^{12}\ g^{-1}$	2.3 ± 0.3	1.7 ± 0.1	1.8 ± 0.1
$A_{CS\ (t\text{-}plot)}$ / μm^2 $particle^{-1}$	3.7 ± 0.5	5.6 ± 0.2	15.4 ± 0.9

[a]Analysis was performed with the built-in software after data acquisition with the ASAP 2020 instrument (Micrometrics). [b] Diameter determined from size analysis using the full T-SEM data set.

2.3.8 Investigation of particle microporosity

Nitrogen adsorption helped to further understand the architecture of CS particles. As mentioned in section 2.3.3, it is believed that PVP lies flat at the intersection between polymer core and SiO_2 shell for SiO_2@PS-PVP10 particles. Conclusively, stepwise heat treatment of the particles should not result in significant differences of the surface area unless the shell cracks or topologically deforms. CS particles prepared with PVP40 or PVP360 on the contrary, are probably composed of a hybrid shell structure where PVP is intercalated within the SiO_2 shell domain. Heat treatment might lead to internal changes, especially in the 100 °C range, because PVP degradation begins and water desorption takes place.[105]

A novel set of particles was prepared for this study with isopropanol as polymerization medium (core particles labeled as “PS/IPro”). Particle size distribution, mean size (*ecd*) and coefficient

of variation (c_v) are listed in Annex 6.3. Adjusted amounts of styrene for the preparation of similarly sized particles using PVP with different MW were used in analogy to the previously applied synthetic method in ethanol. Due to the more hydrophobic solvent, the particles are slightly bigger (1.3 – 1.4 µm) than particles prepared in ethanol but reveal the same surface topology appearance after silica coating, ruling out significant influence of the solvent (Figure 22).

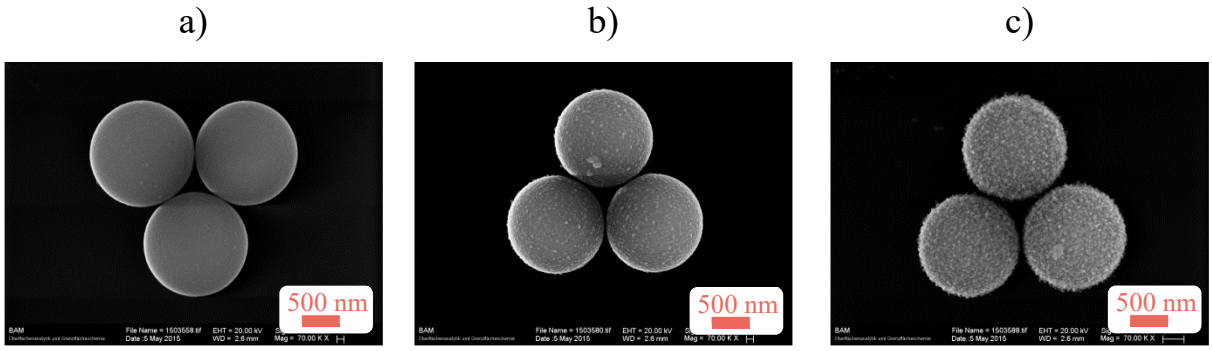

Figure 22. *SEM images in the same FOV: a) – of SiO_2@PS/IPro-PVP10; b) – SiO_2@PS/IPro-PVP40; c) – SiO_2@PS/IPro-PVP360.*

For this study, CS particles were heated under nitrogen to 60°C, 100 °C and 200°C for 5 h, respectively. The analysis was performed after the sample cooled down to room temperature. In Figure 23, the BET surface area as well as the external surface area, derived from t-plot analysis, is plotted against the heating temperature.

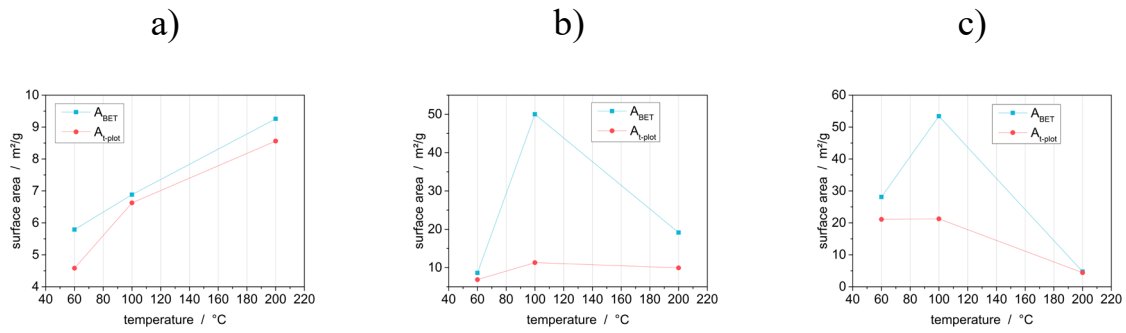

Figure 23. *Surface area from BET and t-plot analysis vs temperatures used for heating: a) – SiO_2@PS/IPro-PVP10; b) – SiO_2@PS/IPro-PVP40; c) – SiO_2@PS/IPro-PVP360.*

A gradual increase can be seen for SiO_2@PS/IPro-PVP10 for both, the BET as well as the external surface area, making a change of the internal structure of the shell unlikely. In contrast, the other two CS particles show a significant BET increase at 100 °C. The amount of external area remains rather low here, indicating the formation of micropores which account for approximately 77% and 60% of the surface area of SiO_2@PS/IPro-PVP40 and SiO_2@PS/IPro-PVP360, respectively, when the particles are treated at 100 °C.

Micropore analysis with adsorption data down to p/p_0=0.01 was performed for SiO_2@PS/IPro -PVP40 treated at 100 °C to gain more insight into the micropore size and distribution (Figure 24).

The BET surface area was determined to 47.1 ± 0.5 $m^2\ g^{-1}$. This fits well with the value determined in the previous run. Porosity distribution analysis from the micropore experiment by density functional theory (Model: N_2@77K, Cylindrical Pores in an Oxide Surface) complemented this information and revealed two major pore fractions at 0.9 and 1.1 nm (Figure 24, right). The area of these two micropore populations accounts for approximately 95% of the total area underlining the large impact of micropore formation upon heating. Note that due to the different analytical methods (BET vs. DFT) the total amount of surface area differs significantly. Looking at the results from t-plot analysis, the surface area from micropores accounts for approximately 77% of the total surface area.

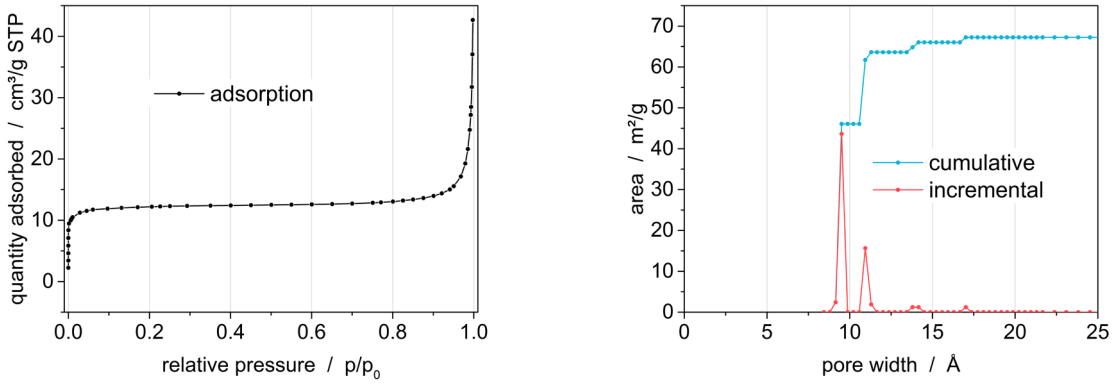

Figure 24. *Adsorption isotherm (left) and pore width distribution by volume (right) of SiO_2@PS/IPro-PVP40 treated at 100 °C.*

Further interesting information can be derived from the pore width distribution, enabling a detailed look into the shell structure. Szczerba et al. calculated a PVP layer thickness on silicate surfaces of around 5 – 6 Å.[106] A PVP double layer seem to be the prevalent architecture which hints at the intercalation of PVP loops within the shell. Such loops are typical for PVP either adsorbed or covalently attached to polymeric microparticles or silica substrates.[97, 107-108] Upon heating to 100 °C, the micropores are formed due to evaporation of water which results in the surface increase.

Interestingly, upon further heating to 200°C a decreasing BET surface area as well as a decreasing micropore contribution is observed for coated particles prepared with PS/IPro-PVP40 and PS/IPro-PVP360. SEM images taken from the particles heated to 200°C give more insight here (Figure 25).

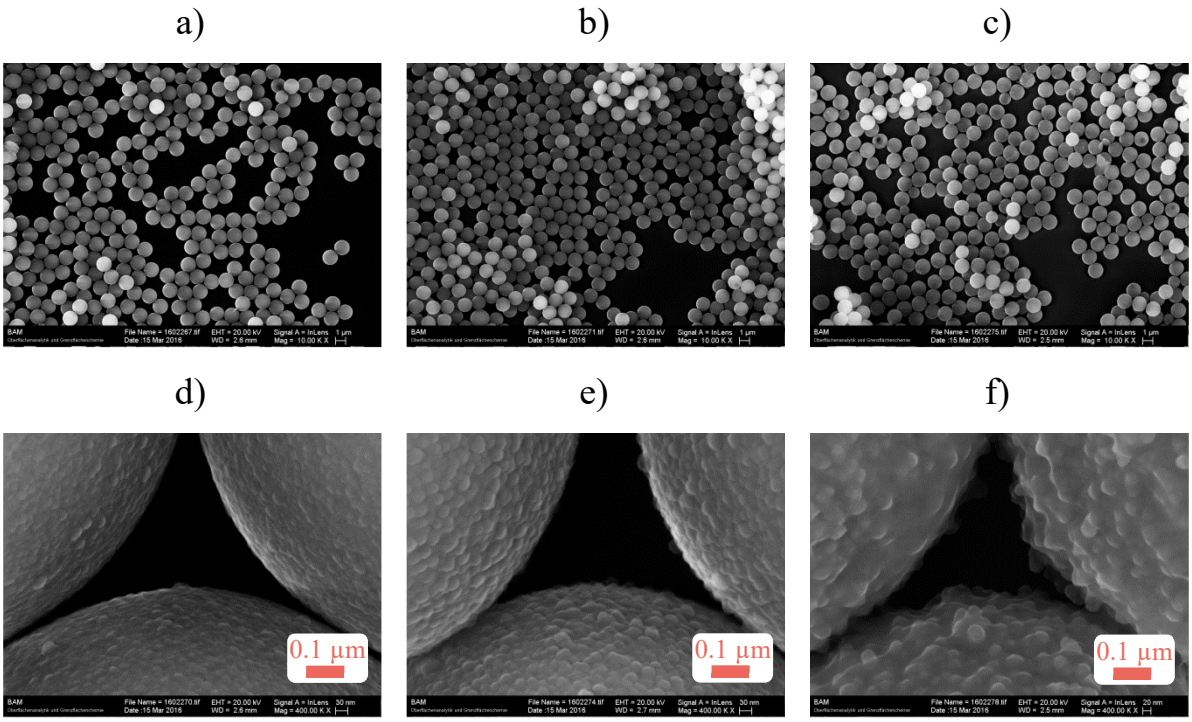

Figure 25. *SEM images taken from the CS particles after heating to 200°C. Images show different FOV for the corresponding particles: a), d) – SiO_2@PS/IPro-PVP10, b), e) – SiO_2@PS/IPro-PVP40, c), f) – SiO_2@PS/IPro-PVP360.*

The images strongly suggest the subsequent filling of micropores with either melted PVP (melting temperature (T_m) between 130 – 180 °C) or by thermally reinitiated sol-gel-reactions,

leading to aging/ripening which usually consumes smaller particles, as can clearly be seen for thermally treated SiO_2@PS/Ipro-PVP360.

In the case of a reinitiated sol-gel-reaction, “smearing” of the silica shell should be noticed for all hybrids, i.e., also SiO_2@PS/IPro-PVP10 and SiO_2@PS/IPro-PVP40. However, their structural integrity remains largely intact. EDX-mapping of silicon on an exemplary image of SiO_2@PS/Ipro-PVP360 further proves that the underlying shell structure remains unaffected after thermal treatment (Figure 26) proving that filling of the micropores occurs with melting polymer.

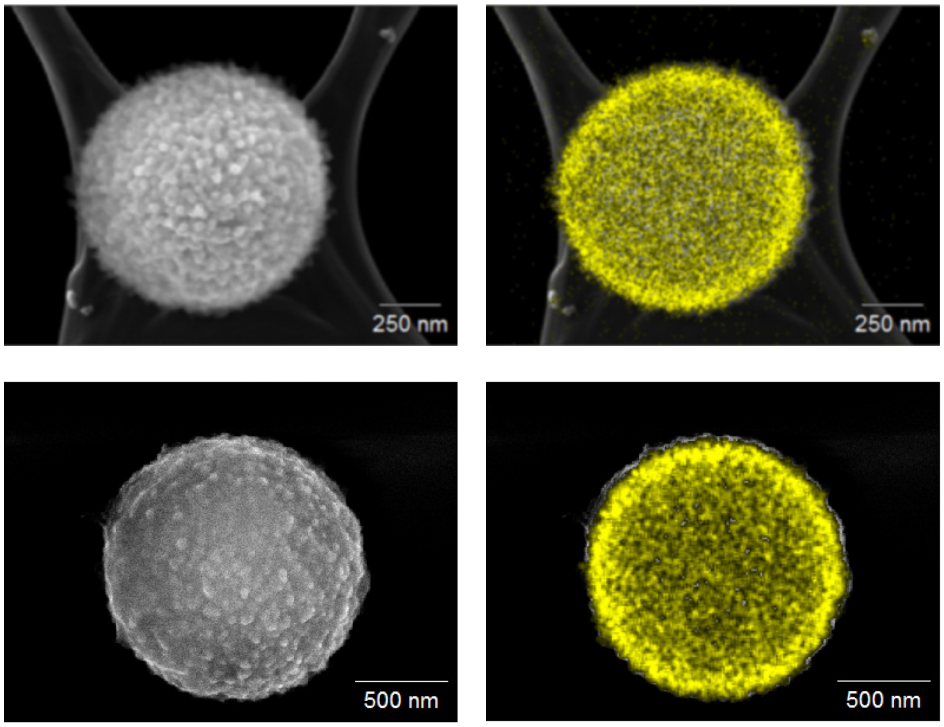

Figure 26. *Exemplary image of SiO_2@PS/Ipro-PVP360 (left) and elemental mapping of silicon (yellow) via EDX (right) before (top-row) and after (bottom-row) thermal treatment.*

Surprisingly, the melting is obviously not gravity driven since this would have led to flow into one direction and finally to the coalescence of the particles. A possible explanation can be found in the capillary forces of the SiO_2 NPs which are acting on the polymer chains.[68] It is reasonable to believe that this induces a homogeneous leakage into every direction, finally leading to the particle structures obtained.

Further analysis of the images shown in Figure 25e reveals no significant changes of the shell appearance in SiO_2@PS/IPro-PVP40, proving that micropores are not formed due to cracking of the shell but due to the evacuation of the microcores.

A cracked particle would probably tear and thus show clearly visible craters or holes in the shell. As an example, part of the CS particle batch SiO_2@PS/IPro-PVP40 was dissolved in 20% (v/v) THF/water mixture, inducing swelling of the core. The resulting particles are shown in Figure 27. There, the increasing pressure from swollen polymeric cores leads to cracking and further tearing of the shell resulting in “pacman”-like particles.

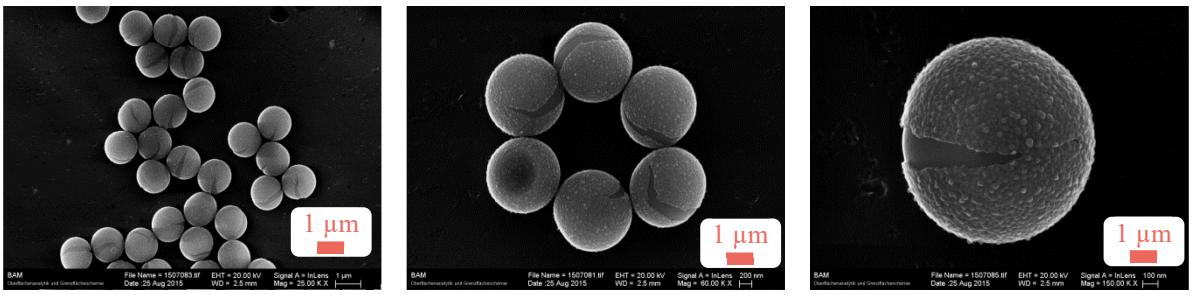

Figure 27. *SEM images of SiO_2@PS/Ipro-PVP40 particles which were treated with a 20% (v/v) THF/water mixture.*

2.3.9 CS particles and FACS

To investigate the potential use of SiO_2@PS particles as suspension array elements, their scattering properties were first compared to the bare core particles because suitable detection patterns are the major requirements for successful detection in cytometry. Figure 28 shows that the maximum signal of the forward scattering shifted slightly to higher intensities after coating which indicates the successful growth of a shell.

Comparison of c_υ values before and after coating show increasing monodispersity for SiO_2@PS-PVP10 and SiO_2@PS-PVP40 with c_υ of 4.5 and 2.8 and worse monodispersity for SiO_2@PS-PVP360 with $c_\upsilon = 6.1$. The latter can be attributed to a less homogeneous distribution of architectures due to less stable structures.

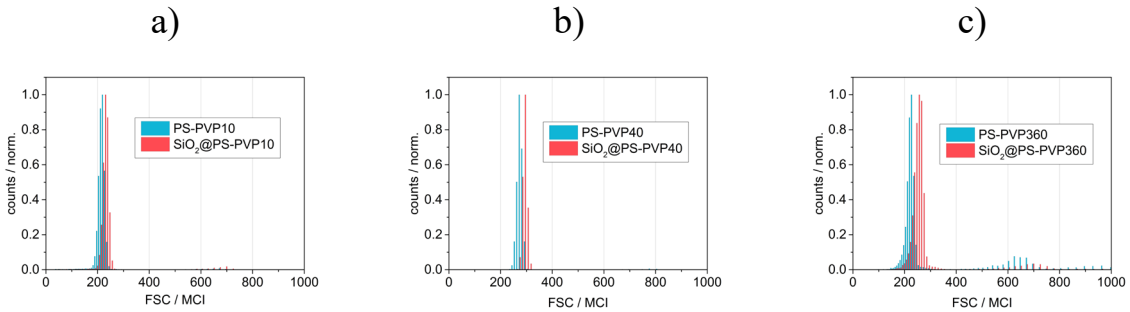

Figure 28. *Normalized FACS histograms obtained in FSC before (blue) and after (red) coating of the particles: a) – SiO_2@PS-PVP10; b) – SiO_2@PS-PVP40; c) – SiO_2@PS-PVP360. Peaks were normalized for better visualization of the signal shift.*

Despite their CS nature, the polystyrene core predominantly defines the scattering properties, related to its refractive index, which is advantageous for cytometric SAT applications. At the same time, the overall density of the SiO_2@PS particles also suits the requirements on applicability in suspension arrays, proven by tracking the sedimentation of the core particles in comparison to the CS particles and bare SiO_2 microparticles (Figure 29).

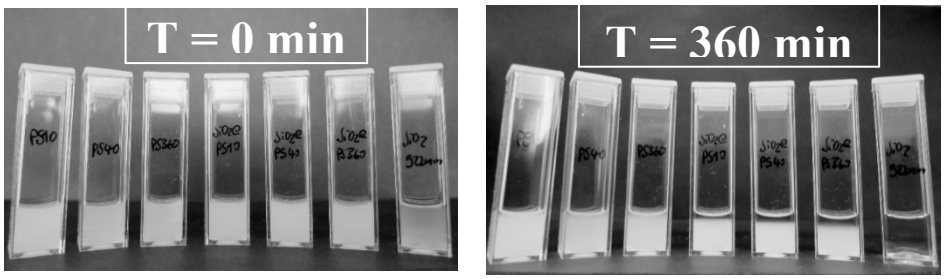

Figure 29. *Investigation of sedimentation behavior of the particles (PS-PVP10, PS-PVP40, PS-PVP360, SiO_2@PS-PVP10, SiO_2@PS-PVP40 and SiO_2@PS-PVP360, from left to right) in aqueous dispersion (0.1% w/v) after 0 min (left) and 360 min (right). Plain silica microparticles (922 ± 30 nm, MicroParticles GmbH, Germany) were used for comparison (cuvette on the right).*

While a suspension of PS particles remained stable over a period of 360 min, full sedimentation of the SiO_2 microparticles can be observed. The CS particles showed intermediate sedimentation behavior with an increasing tendency of sedimentation speed from PS10 to

PS360, reflecting well the increasing amount of SiO_2 as determined for instance by TGA and a corresponding increase in density as was shown with RMM.

Practically, this fine-tuning of density is very advantageous because it makes particle handling in cytometric SAT feasible also for such rather small beads. Some silica particles such as mercaptosilane microparticles or bare SiO_2 beads have also been employed in cytometric applications. However, their practical handling properties are less advantageous in SAT using fluidic instrumentation due to fast sedimentation. During long-term measurements, the particles would settle to the ground and/or the local particle concentration would change over time, significantly affecting characterization or assay outcome. Moreover, such particles are usually less monodispersed.[88, 109] Thus, silica microparticles are preferably used in SAT-based on fluorescence microscopic techniques, where sedimentation and attachment to the flat surface are desired and monodispersity is not a critical quality factor.

2.3.10 Surface modification of the SiO_2 shell

A major advantage of SiO_2-coated polymer particles is the facile and flexible modification of their surface with silanes that are commercially available with a large variety of functional groups. Functionalization with organosilanes is widely known in the field of assay design and applications.[13, 42] In this study, 3-aminopropyltriethoxysilane (APTES) was employed to decorate the surface with amino groups. Modification with basic APTES does not require any additional catalyst or reagent and thus represents a straightforward and controllable method for functionalization. Moreover, APTES can catalyze the co-condensation of other monomers with different functional groups for the preparation of mixed silane surfaces.[110] For example, mixed APTES/TMOS silane layers show increasing abilities to bind biomolecules and the stability of particles can be increased by co-condensation of phosphonate silanes on the surfaces.[111-112] As another example, polyethylene glycol silanes (PEGS) can co-condense on the surface to introduce anti-fouling properties as will be shown in chapter 4. These examples illustrate the enormous potential the CS structure harbors for specifically tailored suspension array elements. Quantification of the amino groups on the particles was done with a ninhydrin test (Figure 30).[113]

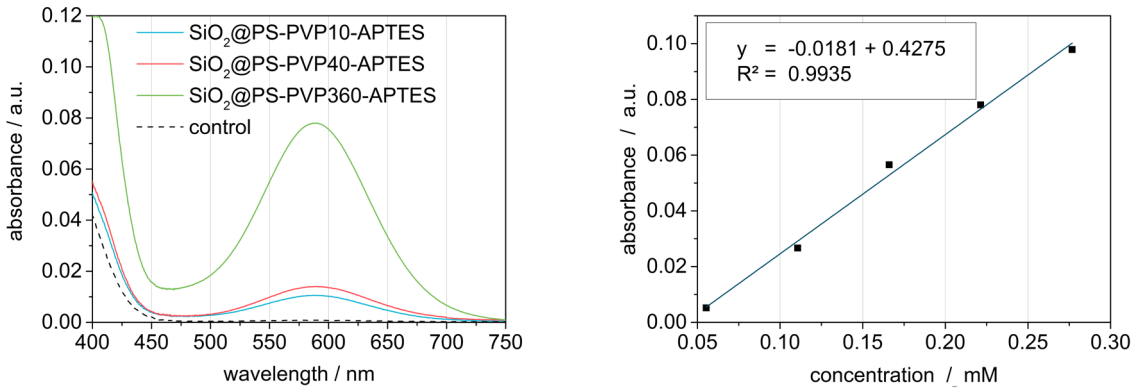

Figure 30. *Left – Absorption spectra of the supernatant after reaction with ninhydrin. Right – calibration curve of ninhydrin test using pentylamine as a standard.*

In a control experiment, unmodified SiO_2@PS-PVP40 was used to show that remaining ammonium from the coating procedure does not affect the results. The ninhydrin test revealed a similar functional group density with approximately 6 amino groups per nm² for all particles considering the surface area determined from t-plot analysis. The amino group density lies close to an expected value of approximately five amino groups per nm² for APTES-modified SiO_2 surfaces reported in the literature.[114]

2.3.11 Small-molecule binding

To prove successful modification and highlight possible fields of application for such CS particles in SAT, FITC as a small model molecule was coupled to the amino group-modified surface. The isothiocyanate group of this popular dye label readily reacts with the nucleophilic amino group on the surface. The fluorescence signal was collected upon irradiation with a 488-nm laser source and detection in the FITC-Channel (FL1 – 520/20 nm) with flow cytometry. This enables the qualitative comparison of labeling density on individual beads. Using SpheroTech calibration beads and a calibration curve for the determination of "molecules of equivalent fluorochrome" (MEF), the labeling results could moreover be semi-quantified. The calibration curve and FACS histograms are shown in Figure 31a,b. Relevant correlation plots and gates for data handling are specified in Annex 6.4.

A comparison between the MEF values obtained after binding of FITC and the external surface area show a proportional signal increase from SiO_2@PS-PVP10 to SiO_2@PS-PVP360 (Figure

31c). Hence, the accessibility of the increasing external surface area for small organic molecules is not modulated by the change in structure.

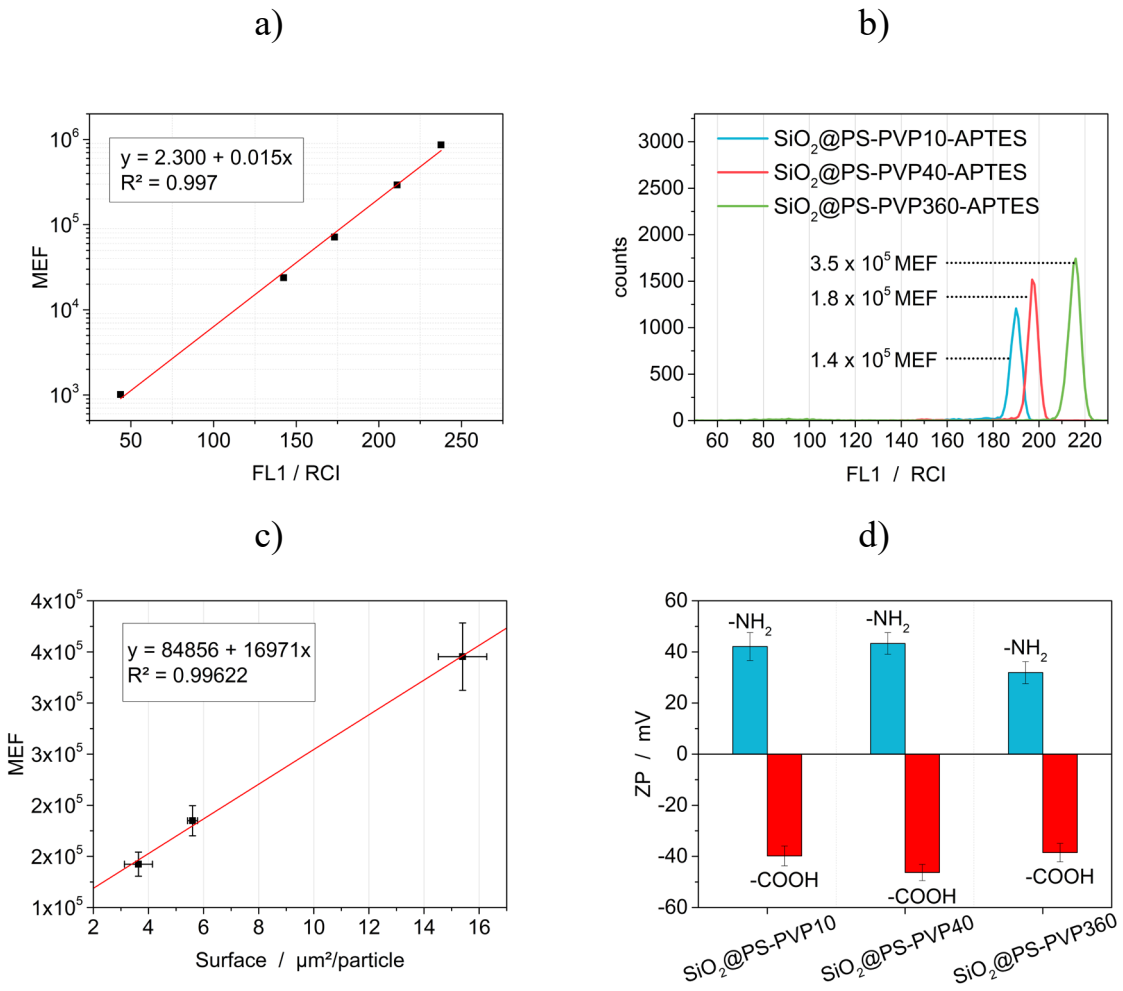

Figure 31. *a) – Calibration plot for SpheroTech calibration beads which was used to calculate MEF from RCI values; b) – gated FACS analysis of FITC-modified particles; c) – MEF values plotted against the surface per particle; d) – zeta potentials of particles before (-NH₂) and after (-COOH) carboxylation using 5% anhydride stock solution.*

At this point it is worth mentioning, that the results obtained from the ninhydrin method and the FITC coupling support the validity of surface area values obtained from t-plot analysis in two ways: first, it is reasonable to expect a comparable APTES functional group density of the external area for all SiO_2 shells, because APTES would not be able to penetrate the micropores. Second, the FITC coupling is a complementary technique that verifies the calculated increase

from SiO_2@PS-PVP10 to SiO_2@PS-PVP360. Nevertheless, further improvements in this direction, i.e. determination of the external or accessible area of CS particles could be made if certified non-porous reference materials would be available. This would give a more reliable reference curve to convert the relative pressure from the BET plot to the statistical thickness required for the t-plot.

In the next step, succinic anhydride was used in a ring opening reaction with the amino groups on the surface to form free carboxylic acid groups for subsequent coupling of DNA.[115] Fast conversion of amino groups is desired, if not used for coupling because degradation of the amino silane layer can occur.[116] The reaction was performed in ethanol instead of DMF to prevent dissolution of the core. It can be found that 5% anhydride stock solution in DMF (2% final volume concentration DMF during the reaction) was enough for efficient conversion. After the reaction, all particles showed negative zeta potentials due to the presence of carboxylate groups on the surface (Figure 31d).

2.3.12 DNA hybridization

The DNA assay was performed using an 18-mer amino group modified c-DNA, which was attached to the carboxylated particles through EDC-mediated coupling. Initially, the c-DNA functionalized CS beads were tested toward different moles of fluorescein (FAM)-labeled target DNA (t-DNA with 15 complementary base pairs) in a direct 1:1 mix-and-read hybridization assay and the signal response was calculated in terms of MEF (Figure 32).

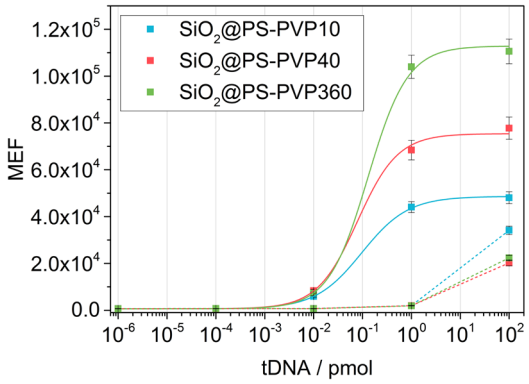

Figure 32. *Dose–response curve for the hybridization of complementary FAM-labeled t-DNA towards c-DNA-modified and unmodified (control) core-shell beads recorded on the Partec CyFlow space©. Signal response was converted to MEF using SpheroTech calibration beads.*

For the determination of standard deviations, five measurements were averaged. All particles display a uniform logistic dose-response behavior towards t-DNA, while control particles without c-DNA show non-specific adsorption at concentrations >1 pmol t-DNA. The probe density of DNA on the particles can be derived from the logistic fit maximum (Table 8).

Table 8. *Summary of SAT relevant properties of the CS particles.*

	SiO_2@PS-PVP10	SiO_2@PS-PVP40	SiO_2@PS-PVP360
APTES [a] / $-NH_2$ nm^{-2}	~6.7	~6.3	~6.5
FITC [b] / MEF $particle^{-1}$	1.4×10^5	1.8×10^5	3.5×10^5
ZP_{-NH2} / mV	42.1	43.3	31.9
ZP_{-COOH} / mV	-39.8	-46.3	-38.5
t-DNA [c] / N $particle^{-1}$	4.9×10^4	7.6×10^4	11.3×10^4
LOQ / fmol	8.0	12.8	18.9
dynamic range / fmol	48	95	225

[a] Density of amino groups determined with Ninhydrin test. [b] Total amount of small molecules per particle derived from FITC coupling test. [c]Density of DNA per particle derived from the logistic fit from dose-response curve (Figure 32). [d]LOQ and dynamic range was determined from an 8-point calibration (Figure 33).

In comparison to small-molecule binding, lower binding densities per bead for all particles were observed which is primarily ascribed to the sterically more demanding DNA molecules. Still, the density of hybridized DNA of approximately 1×10^4 dsDNA μm^{-2} is comparable to that of hybridization efficiencies on carboxylic acid group-modified PS beads of 1 µm with 14–16 base pair matches and lies close to an ideal density of $\sim2\times10^4$ probes μm^{-2} for efficient hybridization.[117-118]

Another experiment was performed and eight t-DNA concentrations in three repetitions were measured (Figure 33, left). The sensitivities of the model assays using CS particles can be compared to existing techniques through the limit of detection (LOD) in analogy to for instance Horejsh et al. They derived LODs as the background signal plus 10SD and found values of ~30 fmol for a molecular beacon-based, amplification-free direct binding assay without washing.[119] Thiollet et al. used quantum dot-encoded microspheres and determined similar detection limits but had to perform several washing steps after hybridization.[120] In both cases, polymer beads

with diameters larger than 3 µm were used as spherical substrates. In this direct experiment, avoiding time-consuming washing steps by a simple and fast mix-and-read assay, less than 1 fmol, i.e., ca. 0.1–0.2 fmol, could be detected.

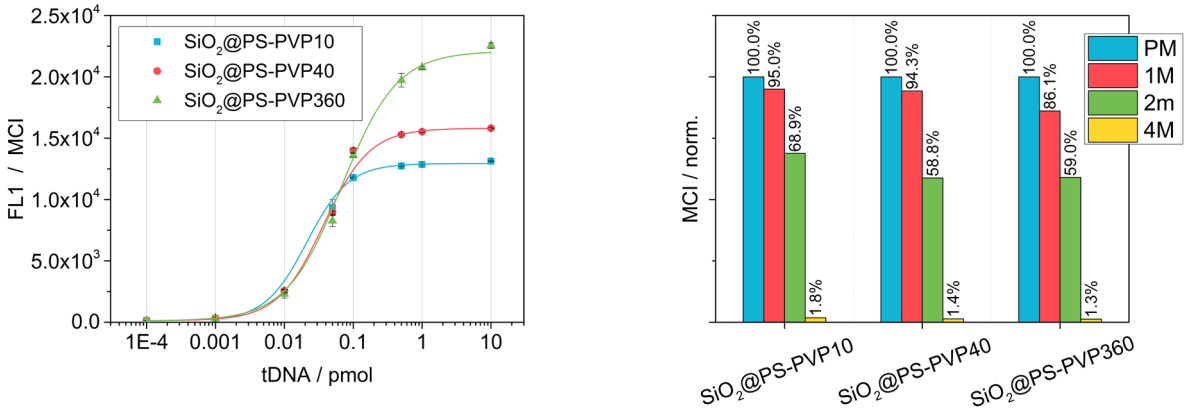

Figure 33. *Left – calibration curves for the hybridization of complementary FAM-labeled t-DNA towards c-DNA-modified CS beads using eight concentrations. A logistic function was used to fit the data and to extract the linear range (EC20 to EC80) as well as the limit of quantification (LOQ, EC20). Right – signal intensities in normalized MCI with complementary and non-complementary (four adenosine units were stepwise exchanged by cytosine) t-DNA.*

Especially when using logistic regression, the EC20 (or limit of quantification, LOQ) and EC80 values, defining the linear range, are more adequate to describe the hybridization assay performance. Here, LOQs of 8.0 fmol for SiO_2@PS-PVP-PVP10, 12.8 fmol for SiO_2@PS-PVP40 and 18.9 fmol for SiO_2@PS-PVP360 were found which are still lower than the published values mentioned above. The detection ranges of the assays were determined to 48, 95 and 225 fmol for SiO_2@PS-PVP10, SiO_2@PS-PVP40 and SiO_2@PS-PVP360, respectively. All data is collected in Table 8.

It is apparent that despite the highest number of receptors per bead, the lowest sensitivity is observed for SiO_2@PS-PVP360 particles. This is probably due to the sterically demanding DNA molecules and hints at reduced SAT performance for multilayer-like particles and sterically demanding targets.

Smooth SiO_2 coatings are obviously more advantageous for sensitive assays using bigger sized targets (proteins, large DNA etc.), while multilayer-like beads are preferably used for small-

molecule immobilization or shorter DNA receptors. Looking at the dynamic range, the larger surface area provides a broader detection range. It is thus likely that bigger sized beads with smooth or raspberry-like structures will show superior performance.

Additionally, control experiments with 50 fmol of non-complementary tDNA with one (M1), two (M2) and four mismatches (M4, in all cases substituting cytosines for adenines) were done (Figure 33, right). All particles show only minor non-specific adsorption with less than 2% of signal intensity when four mismatches are present in the tDNA strand. A slightly higher discrimination capability can be found for rougher CS particles (SiO_2@PS-PVP360 and SiO_2@PS-PVP40) in contrast to the smooth CS particles with approximately 60% signal intensity versus 70% signal intensity, respectively.

2.3.13 Effect of coating conditions

To further explore possible coating scenarios on the polymer beads, different conditions were tested. For these studies, the PS-PVP40 particles were used. Four parameters were investigated and evaluated by SEM images of the obtained particles.

Parameter 1: Influence of the solvent.

Stöber sol-gel routes and silica coatings on polystyrene cores (anionic, cationic or PVP-stabilized) are typically performed in ethanol. Here, the solvent was varied to more polar methanol and less polar isopropanol. Surprisingly, solvent effects on silica coatings have not been discussed in the literature so far.

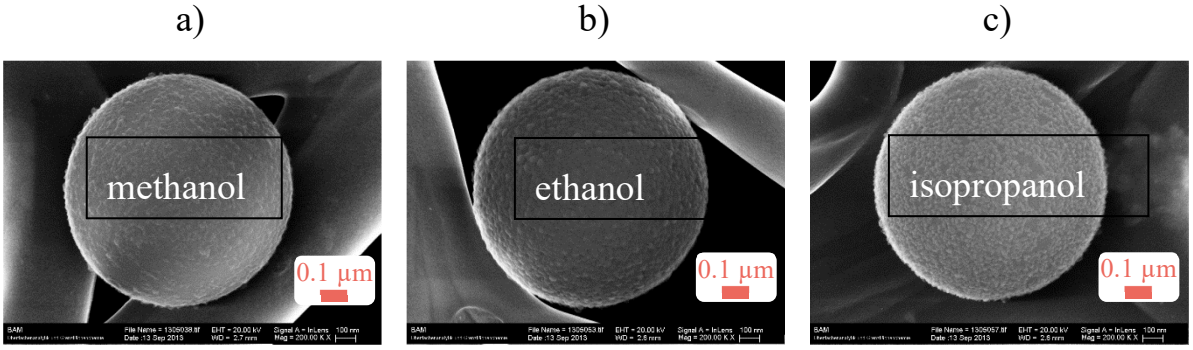

Figure 34. *Influence of the solvent on silica coating: a) – in methanol; b) – in ethanol; c) in isopropanol. 0.5 mL TEOS (TEOS/PS ratio of 1/1) and 1.5 mL ammonium hydroxide were used. 500 mg core particles were present, resulting in a TEOS/PS ratio (v/w) of 1.*

Figure 34 shows the SEM-images of the resulting particles after washing and drying. A closed shell is only observed for coatings conducted in ethanol. Incomplete silica shells can be seen for particles prepared in methanol and isopropanol, while SiO_2 NPs being smaller ($ecd_{SiO2\ NP}$ in methanol < $ecd_{SiO2\ NP}$ in isopropanol) in comparison to the shell forming SiO_2 NPs prepared in ethanol. As solvents with increasing size and polarity have rather unusual and unordered effects on the sol-gel process, a conclusive explanation is difficult.[121]

Parameter 2: Influence of TEOS/PS ratio.

Increasing TEOS concentration on anionic and cationic particles typically induces thicker silica shells.[72, 122] The effect of TEOS in terms of its ratio to the amount of PS core particles was therefore also investigated here.

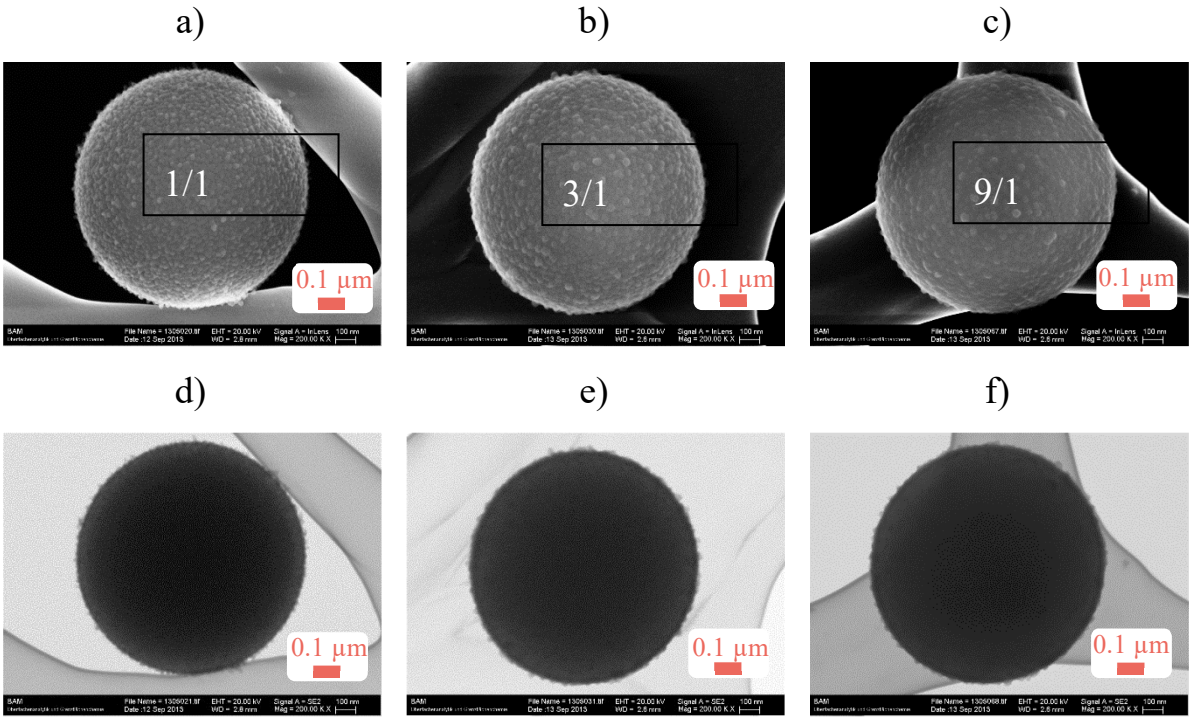

Figure 35. *Influence of the TEOS/PS ratio on silica coating: a,d) – 1/1; b,e) – 3/1; c,f) – 9/1. 1.5 mL ammonium hydroxide were used. 500 mg core particles were present.*

SEM images reveal an increasing shell thickness only from 1/1 to 3/1 ratio. In the case of PVP-stabilized anionic beads like in this case, the shell thickness seems to reach a maximum thickness as indicated by the TSEM images (Figure 35d-f).

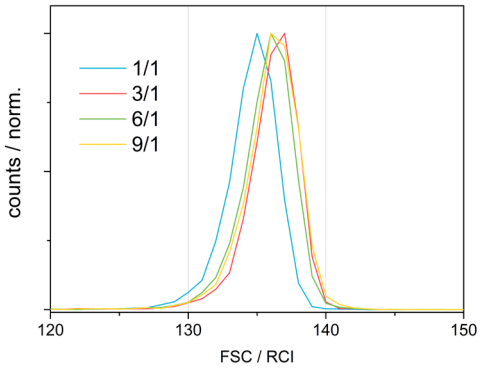

Figure 36. *FACS analysis of CS particles prepared with different TEOS/PS ratio.*

These results were confirmed by FACS analysis (a fourth batch was included with a ratio 6/1 – no SEM images available for these particles) which revealed no significant further particle growth above a TEOS/PS ratio of 3/1 (Figure *36*).

Parameter 3: Influence of ammonium hydroxide concentration.

The amount of ammonium hydroxide typically has a significant effect on the coating. In this study, the concentration was varied to lower (~0.2 M) and higher concentrations (~1.5 M).

As can be seen in Figure 37, a lower ammonium hydroxide amount led to small SiO_2 NPs attached to the surface forming a homogenous but incomplete shell coating. For higher base concentrations, no coating and only loosely bound, bigger SiO_2 NPs were observed in the particle batch. These results are in good agreement with the results by Kobayashi et al..[75] They found that an increasing shell thickness was observed within a range of 0.2–0.8 M of ammonium hydroxide for PS beads with adsorbed PVP. At concentrations as high as 1.2 M, only secondary SiO_2 NPs were generated due to accelerated sol-gel reactions: initially formed SiO_2 NP growth is faster than the diffusion of monomer and nuclei to the particles' surface.

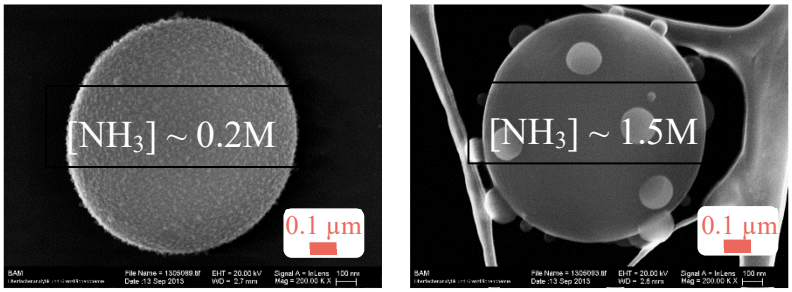

Figure 37. *Influence of the ammonium hydroxide concentration using lower (~0.2 M, left) and higher (~1.5 M, right) amounts. 0.5 mL TEOS were used. 500 mg core particles were present, resulting in a TEOS/PS ratio (v/w) of 1/1.*

Parameter 4: Effect of the catalyst.

Lastly, two different catalysts were used to test the applicable range of pH during coating. The practical reason here is to avoid harsh basic conditions if doping of the shell with organic molecules or NPs is envisaged. A neutral route was chosen with phosphate buffer (pH = 7) using NaOH for neutralization and a 0.1M HCl solution was used in an acidic route. The neutral route was inspired by a He et al. who formed mesoporous silica materials under these conditions.[123]

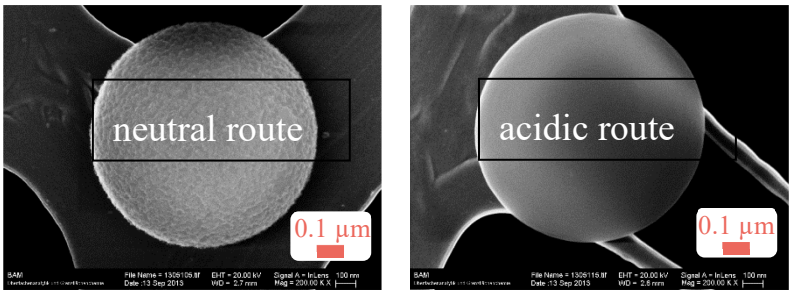

Figure 38. *Effect of catalyst using phosphate buffer (pH = 7 with NaOH, left) and HCl (0.1M, right). 0.5 mL TEOS was used. 500 mg core particles were present, resulting in a TEOS/PS ratio (v/w) of 1/1.*

While the acidic route yielded no coating at all (it cannot be ruled out that silica seeds or particles were formed, because the particles were washed before SEM images were taken), the neutral route surprisingly showed some degree of coating. The silica material appears as very small clusters on the surface.

2.3.14 Silica shell re-growth under neutral conditions

To investigate further particle engineering aspects and inspired by the promising coating results under neutral conditions, a shell re-growth was examined at room temperature and 50°C using a 1/1 ratio of TEOS and CS particles.

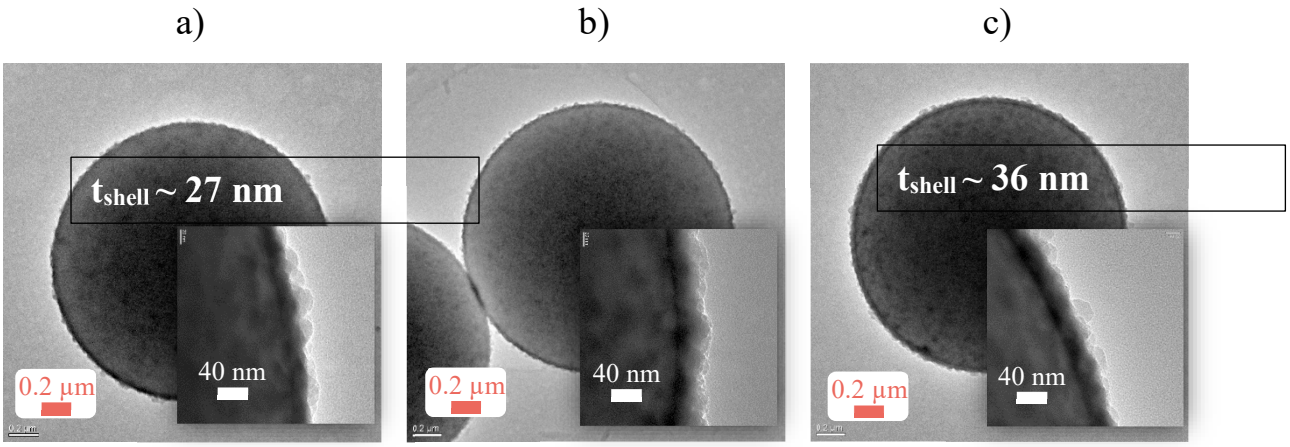

Figure 39. *TEM images of CS particles before and after re-growth of the silica shell: a) – before re-growth; b) – after re-growth at room temperature; c) – after re-growth at 50°C.*

The effect of temperature can be nicely visualized in TEM images of the obtained particles (Figure 39). While re-growth at room temperature leads to deposition of ultra-small SiO_2 NPs (~1−5 nm), the silica shell can be nicely continued to grow at elevated temperatures. A total increase of shell thickness of ~9 nm was achieved in this case (note that the thickness was derived from a single image).

2.3.15 Effect of the core size

To demonstrate the possibility to prepare also larger CS beads and study the effect of size on the shell architecture, another two PS particles were prepared for PVP10-, PVP40- and PVP-360-mediated beads each, varying the amount of styrene: 9.6 and 19.2 wt.-% for PVP10; 4.8 and 19.2 wt.-% for PVP40; 4.8 and 9.6 wt.-% for PVP360).

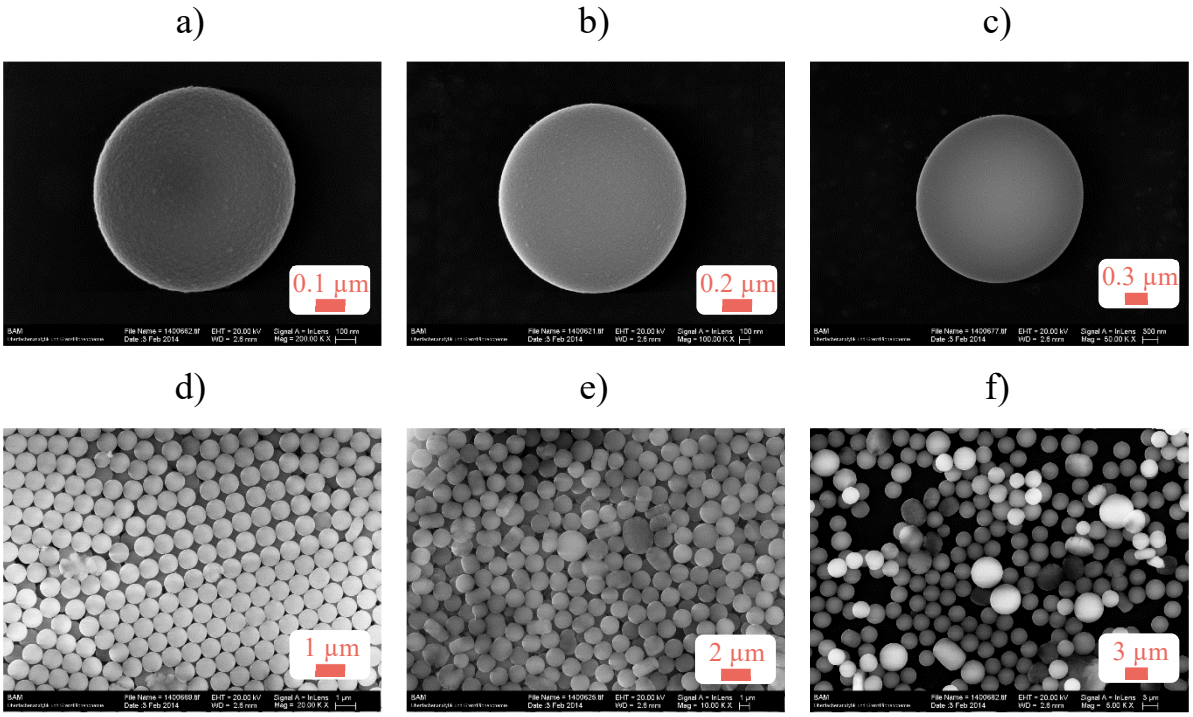

Figure 40. *SEM images of SiO_2@PS-PVP10 particles using different amount of styrene during PS core synthesis: a,d) – 4.8 wt.-% styrene; b,e) – 9.6 wt.-% styrene; c,f) – 19.2 wt.-% styrene.*

Monodisperse particle batches for PVP10-mediated PS core synthesis can only be observed with the lowest concentration of styrene (note that this is the batch used in the previous section as PS@PS-PVP10, *ecd* = 935 nm). Different populations of particle size were found for particles with the highest concentration of styrene used. The intermediate concentration results in somewhat similar sized but deformed particles. Interestingly the smooth shell architecture can be found even on the largest beads found in the batch using the highest amount of styrene.

Particles with good monodispersity can be found for all batches prepared with PVP40 as can be derived from Figure 41 (evaluated by visual inspection of overview images shown in the bottom row). Within the range of styrene amounts used here, a smooth control over size between 611 – 1313 nm can be achieved. Also, the shell architecture with raspberry-like appearance is comparable.

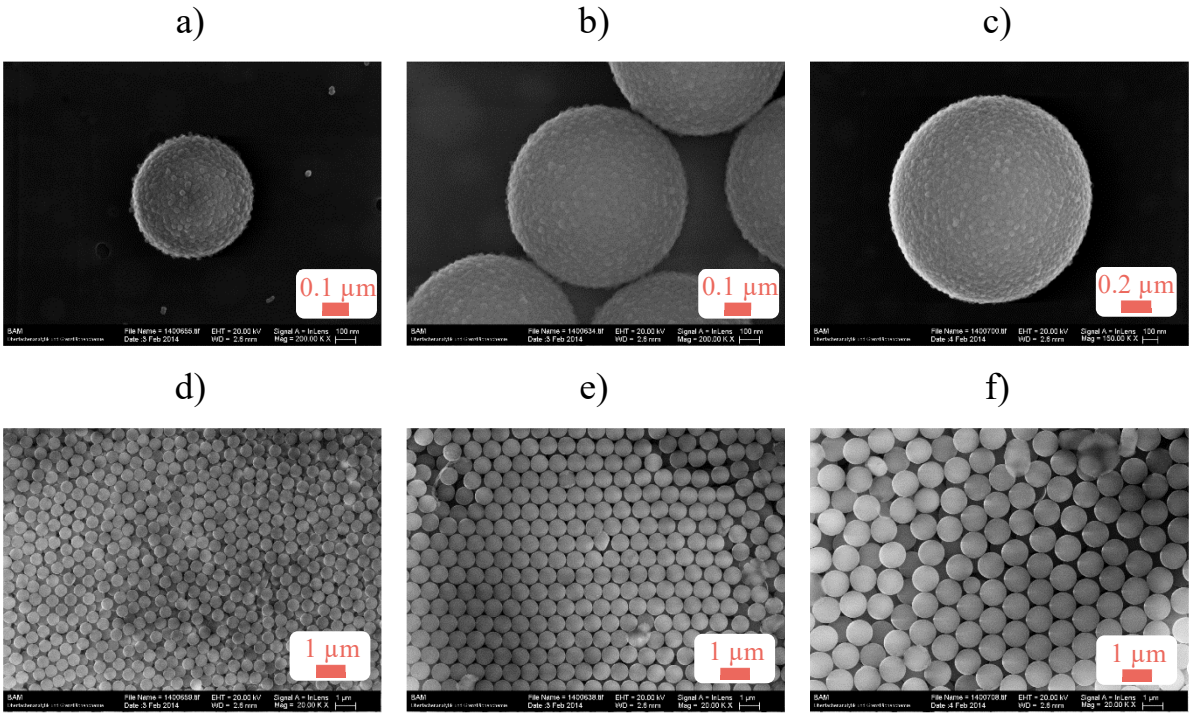

Figure 41. *SEM images of SiO_2@PS-PVP40 particles using different amount of styrene during PS core synthesis: a,d) – 4.8 wt.-% styrene; b,e) – 9.6 wt.-% styrene; c,f) – 19.2 wt.-% styrene.*

Particles prepared with PVP360 also show good batch quality with monodisperse size distributions (Figure 42). The size varies between 575 and 1036 nm. Again, the same shell architecture is obtained for all batches regardless of the core size. This does not only hold for the overall appearance, but also for the SiO_2 NP.

Since PVP40- and PVP360-mediated PS bead synthesis results in monodisperse particles for all styrene contents used, and all other parameters were kept constant, the lower batch quality for particles prepared with PVP10 is ascribed to a reduced stabilization effect of shorter PVP-chains on growing spheres.[84] The same trend was by Tseng et al. who found dropping batch quality with PVP10-stabilized PS-beads when using a styrene content above 12.5 wt.-%.[124]

The results from visual inspection of the SEM-images are summarized in Table 9. It becomes evident, that the core size has no effect on the architecture-directing effect of PVP. The herein presented strategy for surface control can be applied to a wide range of bead sizes and architectures.

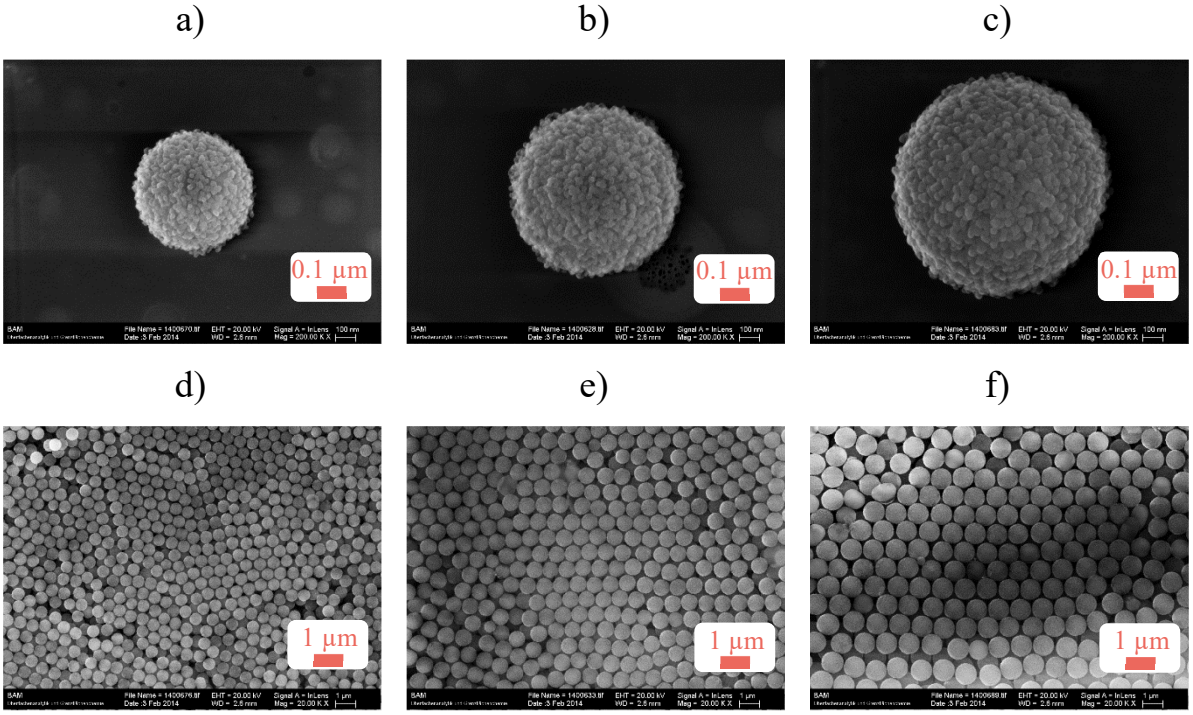

Figure 42. *SEM images of SiO_2@PS-PVP360 particles using different amount of styrene during PS core synthesis: a,d) – 4.8 wt.-% styrene; b,e) – 9.6 wt.-% styrene; c,f) – 19.2 wt.-% styrene.*

Table 9. *Summary of visual inspection of SEM images recorded for SiO_2@PS particles using PVP10, PVP40 and PVP360 with varying amounts of styrene.*

sample	MW_{PVP} / Da	styrene / weight-%	*ecd* / nm	batch quality [a]	architecture
Figure 40a	10	4.8	935	monodisperse	smooth
Figure 40b	10	9.6	1739	polydisperse	smooth
Figure 40c	10	19.2	< 3000	polydisperse	smooth
Figure 41a	40	4.8	611	monodisperse	raspberry
Figure 41b	40	9.6	1018	monodisperse	raspberry
Figure 41c	40	19.2	1313	monodisperse	raspberry
Figure 42a	360	4.8	575	monodisperse	multilayer-like
Figure 42b	360	9.6	802	monodisperse	multilayer-like
Figure 42c	360	19.2	1036	monodisperse	multilayer-like

[a] determined by visual inspection of the respective overview SEM image.

2.4 Conclusion

In this chapter, monodisperse SiO_2@PS CS particles with diameters of roughly 1 µm as suspension array elements were prepared. The surface topology and surface area of the composites could be precisely controlled using a PVP-mediated convergent coating method.

The key for architectural control is the use of PVP with different MW with a gradual increase of available surface area from PVP10- to PVP40- and PVP360-mediated SiO_2@PS-particles, which corresponds well to SiO_2 NPs forming a mono- to a multilayer-like shell. The different CS structures were characterized with TGA and nitrogen adsorption revealing flat PVP chains between the intersection of the polymeric core and SiO_2 shell in the case for PVP10-mediated coatings and shell structures with intercalated PVP for PVP40- and PVP360-mediated coatings. Additionally, the particles were characterized with resonant mass measurements to determine the density of the core, the core-shell, and the silica shell domain.

All particles are compatible with SAT, showing ideal scattering profiles using cytometry. FACS, in turn, was also used to obtain in-depth information about particle size, size distribution, and coating in a rapid and potentially automatable manner. The SiO_2 shell moreover allows to precisely tune the density of the hybrid particles, making also these smaller CS particles accessible for cytometric read-out due to optimized sedimentation speed. The CS particles could be facilely decorated with amino and carboxylate groups taking advantage of the native SiO_2 surface and were tested in simple but representative SAT model assays: whereas small-molecule probes can readily take advantage of the defined amount of surface functional groups provided, DNA hybridization performance does not correlate with functional group density for larger biomolecules. In contrast, smooth SiO_2 coatings show the best sensitivity, indicating steric hindrance on raspberry- or multilayer-like coatings. The hybridization experiments showed promising results for all particles with quantification limits down to 8 femtomoles.

An SEM survey of CS particles was conducted varying several coating parameters such as the solvent, the TEOS/PS ratio, the concentration of ammonium hydroxide, the catalyst and PS core size to investigate the robustness of the protocol. A potential shell re-growth strategy under neutral conditions and at elevated temperature adds more versatility for CS particle engineering.

2.5 Experimental

2.5.1 Materials

Poly(vinylpyrrolidone) (PVP10 with ~10 kDa, PVP40 with ~40 kDa and PVP360 with ~360 kDa, Sigma), styrene (ReagentPlus, <99%, Sigma) basic alumina (Al_2O_3, Brockmann I, Acros) and 4,4'-azobis(4-cyanovaleric acid) (ACVA, MP Biomedicals) were used for the PVP-coated polystyrene core synthesis. Ammonium hydroxide (32% in water, Merck) and tetraethoxyorthosilicate (TEOS, <99%, Merck) were used for the silica coating and hydrochloric acid (HCl, 37%, Merck), fluorescein isothiocyanate isomer I (FITC, ≥90%, Sigma), aminopropyltriethoxysilane (APTES, 97%, ABCR) and succinic anhydride (97%, Sigma) were used for surface modification. FAM- (6-carboxyfluorescein) labeled oligonucleotides (5'- C6 Amino-TTT CAT CCA TC -6-FAM -3') were purchased from Metabion (Steinkirchen, Germany) and coupled with *N*-(3-dimethylaminopropyl)-*N*-ethylcarbodiimide hydrochloride (EDC, BioXtra grade, Sigma). MES buffer (10 mM, pH = 4.5, 2-(*N*-morpholino)ethanesulfonic acid) and TRIS buffer (10 mM, pH = 8.0, TRIS/SDS (0.05 %SDS), TRIS/TE (1mM TE), tris(hydroxymethyl)aminomethane (TRIS), sodium dodecyl sulfate (SDS), ethylenediaminetetraacetic acid (TE) were used for coupling and washing, respectively. Hybridization to c-DNA- (5'-C6–NH_2-TTT ATG TCG TTT GCT GTA-3', Metabion GmbH, Germany) modified particles was performed with FAM-labeled t-DNA (3'-TAC AGC AAA CGA CAT-5', Metabion GmbH, Germany) in TMAC (tetramethyl ammonium chloride) buffer, which was prepared according to Luminex Corp. protocols. Phosphate Buffer (PB, 0.1M, pH = 7.4) was used for cytometric analysis. Methanol (Alfa Aesar, Germany), ethanol (abs. 99% and 96%, ChemSolute), isopropanol (Extra Pure, >99%, Fisher Scientific) and water of MilliQ grade (BAM) were used as solvents and for washing. All reagents were used without any further treatment.

2.5.2 Polystyrene core synthesis

PVP-stabilized microparticles were synthesized by dispersion polymerization with ACVA as the initiator. First, 1.7 g (1.8 wt.-% of total solvent weight) of the stabilizer (PVP10, PVP40 and PVP360) were dissolved in 100 mL ethanol in a 250 mL 3-necked round-bottom flask with a magnetic stirrer. The solution was then heated to 75 °C in an oil bath. ACVA was weighed separately (2.1% (w/v) to volume of the monomer) and dissolved in 20 mL ethanol. Styrene

was filtered through a basic alumina column to remove the stabilizer and then added to the ACVA solution. 4.8, 9.6 or 19.2 wt.-% (weight of styrene to total weight of solvent) for the preparation of PS-PVP10, PS-PVP40 or PS-PVP360, were added, respectively. Both solutions were then degassed simultaneously with an argon stream for 30 min. Afterwards, the solution containing ACVA and styrene was directly transferred to the preheated PVP solution and the mixture was stirred for 24 h at 500 rpm. The particles were subsequently separated from the solution by centrifugation and washed three times with methanol in centrifugation/redispersion cycles. The microparticles were obtained as white solid after drying overnight in a vacuum oven. The product was stored at room temperature without any further treatment.

For particles employed in the porosity studies (section 2.3.8), isopropanol was used for the preparation of the PVP solution. The ACVA solution was prepared with EtOH because of the low solubility of the initiator in organic solvents.

The yield (in g product per mL added styrene) accounted to approximately 10% for PVP10-, and 50% for PVP40- and PVP360-mediated synthesis. The particles prepared in iso-propanol showed slightly better yields. A more precise determination of yield was not done due to product losses throughout the washing procedure with repeated centrifugation and redispersion cycles.

2.5.3 SiO_2 coating of polymeric core

Formation of the shell on PS particles was performed in an ammonia-catalyzed sol-gel process with TEOS as the precursor. First, a 1% (w/v) dispersion of PS core particles was prepared in 50 mL ethanol in a round-bottom glass equipped with a magnetic stirrer. After addition of 1 mL Milli-Q water, the dispersion was treated in an ultrasonic bath to remove air bubbles and to promote homogeneous distribution of the particles. 1.5 mL TEOS and 1.5 mL ammonium hydroxide were subsequently added. The particles were separated from the dispersion medium by centrifugation after 24 h of reaction at room temperature and washed twice with water and once with ethanol in centrifugation/redispersion cycles. The particles were dried in a vacuum for 4 h and stored at room temperature.

2.5.4 SiO_2 shell functionalization

2.5% (w/v) stock dispersions of CS particles were prepared in 800 µL water. 400 µL of a mixture of methanol and $HCl_{37\%}$ (9/1) were subsequently added for surface activation in an ultrasonic bath for 5 min. Afterwards, the dispersion medium was exchanged twice with 400 µL absolute EtOH, respectively. Then, 4 µL (in case of SiO_2@PS10 and SiO_2@PS40) or 15 µL (in case of SiO_2@PS360) APTES were added to the dispersion for amino modification. The mixtures were agitated for 20 h at 800 rpm and 40 °C. Finally, the particles were washed three times with an EtOH/H_2O mixture (1/1) in centrifugation/redispersion cycles. After drying in a vacuum for 2 h, the particles were dispersed in water as a 1% stock solution and stored in the refrigerator until further use.

For modification of the CS particles with carboxylic acid groups, 0.1% (w/v) dispersions of amino group-modified particles in 1.5 mL ethanol were prepared (Scheme 1). 30 µL of succinic anhydride in DMF were added and the mixture was left to react in a thermomixer (800 rpm) at 40°C overnight. Then, the particles were washed three times with an EtOH/H_2O mixture (1/1) in centrifugation/redispersion cycles. After drying in a vacuum for 2 h, the particles were dispersed in water as a 1% (w/v) stock solution and stored in the refrigerator until further use.

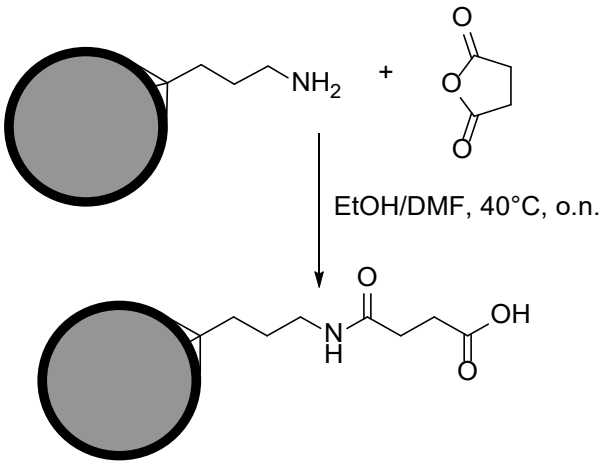

Scheme 1. *Ring-opening reaction between the amine group from the APTES modification and succinic anhydride.*

2.5.5 Ninhydrin test

The ninhydrin test following the protocol of Soto Cantu et al. was used for the quantification of amino groups.[113] In this case, pentylamine instead of hexylamine was used for the recording of a calibration curve between 0.05 and 0.28 mM. 5 mg of functionalized particles were dispersed in 1.4 mL absolute ethanol and 0.4 mL ninhydrin stock solution (0.35%) with ultrasonication. After stirring in a thermomixer (500 rpm) at 65°C for 30 min, the dispersion was cooled down in the refrigerator before centrifugation. 0.5 mL of supernatant was then mixed with 1.5 mL absolute ethanol in a quartz cuvette for recording the absorption spectrum.

2.5.6 Small-molecule coupling to amino modified particles

FITC was coupled to the APTES-modified particles through a simple addition reaction of isothiocyanate to amino groups (Scheme 2). 2.5 µL of the 1% (w/v) amino-modified particle stock solution was mixed with 97.5 µL EtOH and 300 pmol of FITC, freshly prepared in abs. EtOH. After 20 h the particles were washed three times with EtOH in centrifugation/redispersion cycles.

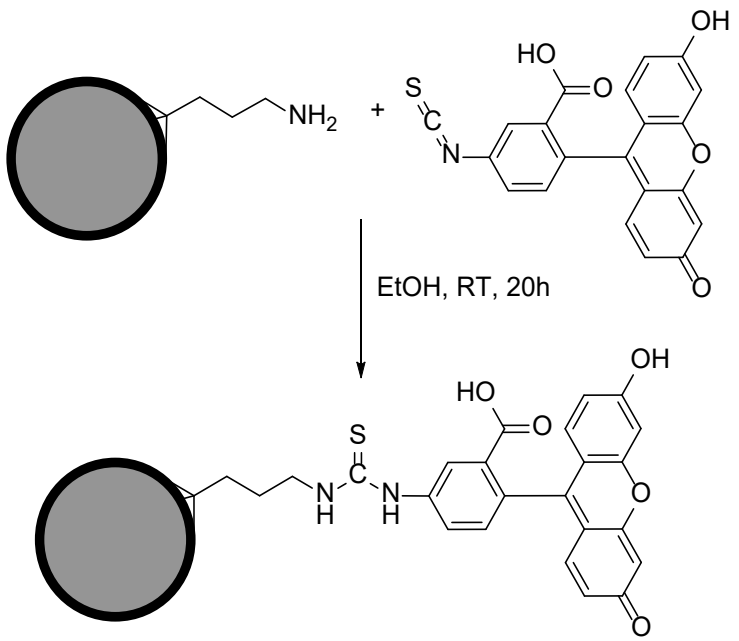

Scheme 2. *Reaction between the amine group from the APTES modification and FITC.*

Amino-modified DNA complementary (c-DNA) to the target sequence (t-DNA) was bound through a C6- and TTT-spacer to carboxylate-modified particles by EDC-mediated coupling. 2.5 µL of the 1% (w/v) amino-modified particle stock solution were mixed with 97.5 µL coupling buffer. Then, 10 and 20 µL of freshly prepared solutions of EDC and Sulfo-NHS (10 mg mL^{-1}) were pipetted to the particles. After activation for 15 min at room temperature, 300 pmol of DNA were added. DNA was allowed to couple for 2 h during agitation at 1000 rpm at room temperature. Finally, the particles were washed twice with TRIS/SDS in centrifugation/redispersion cycles and re-dispersed in 100 µL TRIS/TE, yielding a 0.025% (w/v) stock solution of c-DNA-modified particles.

2.5.7 Hybridization of FAM-labeled t-DNA

TMAC buffer was used for hybridization experiments. The proportions were adapted from Luminex' hybridization protocols. In a typical experiment, 5 µL of c-DNA-modified particle stock solution were mixed with 95 µL hybridization buffer. Then, labeled t-DNA solutions (5 – 10 µL) in hybridization buffer were added. After 30 min of incubation at 25°C, the particles were analyzed with flow cytometry either directly, with an Accuri C6 from BD, or after 20-fold dilution with 1 mL PB buffer with a CyFlow Space (Partec).

2.5.8 Methods and instrumentation

High-resolution scanning electron microscopy (SEM) as well as transmission mode imaging SEM (TSEM) were performed on a Zeiss Supra 40 equipped with a high-resolution cathode (Schottky field emitter), an In-Lens SE secondary electron detector used in the high-resolution mode and single unit transmission set-up. Energy dispersive X-ray spectroscopy (EDX) has been performed with a large-area SDD EDS detector (Thermo Fisher Scientific). Transmission electron microscopy (TEM) was conducted with a FEI Tecnai G2 20 S-TWIN microscope operating at 200 kV. Samples for SEM, TSEM and TEM were prepared on carbon thin film-modified copper grids (200 mesh) by drying 3 µL of a 0.1% (w/v) dispersion in water. ImageJ software analysis is outlined in chapter 3.

TGA (thermogravimetric analysis) measurements were performed with a TGA 24 from Setaram Instrumentation (Caluire) with a coupled MS to collect the information on the CO_2 release during combustion.

Flow cytometric analysis was performed on a CyFlow space (Partec) equipped with a $\lambda = 488$ nm argon laser for excitation. Forward scattered (FSC) and sideward scattered light (SSC) was detected at 0° and 90°, respectively, with 488 nm band pass filters and gains of 137 and 180. Fluorescence (FL1) was detected at 90° with a 520-50 band pass filter and a gain of 650. All samples were measured in dispersion using PB or water at a concentration of 5×10^{-4} % (w/v). Each run was performed under the same instrumental settings with a run time of 60 s (30 s for hybridization experiments). Results are reported by respective gating and after data export to Origin 9.1 (OriginLab) for further data handling. Correlation plots of FSC and SSC were used to set gates (Figure 82) for all experiments.

Zeta potential and dynamic light scattering experiments were performed with a Zetasizer Nano ZS using 1×10^{-3}% (w/v) particle concentration in water. Instrument settings were set automatically with minimum 30 repetitions.

External surface areas were determined by N_2-adsorption/desorption according to the t-plot method of de Boer using the Harkins and Jura correlation on an ASAP 2010 instrument (Micromeritics).

For resonant mass measurements (Archimedes. Malvern Instruments), the particles were diluted in deionized water and sonicated for 5 minutes. Then the particles were diluted in the respective fluids to a concentration of approx. 10^6–10^7 beads mL^{-1} before injecting and running the measurement. For particles density determinations using the convolution method, sucrose and ethanol solution with densities between 0.8 and 1.2 g cm^{-3} were used. DI water was used for size measurements.

2.5.9 Responsibility assignment

The project was designed, planned and executed (including synthesis, experiments, data and image analysis) by Dominik Sarma unless otherwise stated. SEM instrument was operated by S. Benemann (BAM, Div. 6.1). A. Zimathies and C. Prinz (BAM, Div. 1.3) performed N_2 adsorption/desorption measurements. S. Reinsch (BAM, Div. 5.6) conducted the TGA measurements. The TEM was operated by S. Selve (TU Berlin). RMM measurements were conducted by Malvern Instruments (UK, Worcester) under the supervision of H. Jankevics.

3 Characterization of CS Particles Using Dual-mode TSEM/SEM Set-up

introducing a new tool for the quantification of roughness

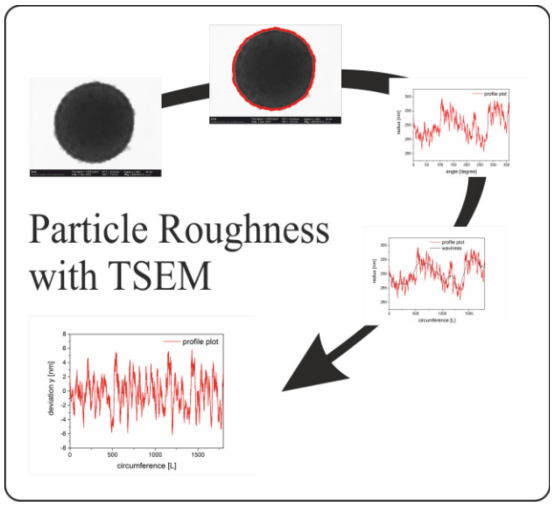

3.1 Abstract

Comprehensive particle characterization of CS particles is essential for batch-to-batch reproducibility and objective performance assessment across architectures, protocols, and laboratories. Particle characterization with respect to size, size distribution, shell thickness and texture, surface area and roughness or materials composition is commonly conducted with different analytical methods, often on different samples. In this chapter, a dual-mode TSEM/SEM set-up with an EDX detector is presented to obtain a complementary data set with sufficient statistical confidence of one and the same sample on a single instrument.

An image analysis tool was developed to derive and quantify the profile roughness of CS particles from individual beads. Comparison with surface roughness data from AFM showed a similar trend in roughness across the series of particles. Reliable classification into *smooth* and *rough* particles is proposed and roughness changes within different particle batches were tracked systematically.[125]

3.2 Introduction

Given the wide range of accessible CS particle architectures, the demand for a reliable characterization method that allows comparing results of all the available synthetic approaches in an objective manner is high. This is especially relevant when applications of CS particles are envisaged in which the morphology of the silica shell plays a key role. In surface coatings with CS particles, for example, the effect of the hydrophilicity/hydrophobicity or anti-reflection properties of the surface strongly depends on the hierarchical dimensions of the hybrid as well as on the roughness of the particles.[53, 126] Adhesion can also strongly differ as a function of deviations of the roughness at the nanoscopic scale.[127] Moreover, as proven in the previous chapter, the assay performance as well rely on the surface topology of the beads.

In this regard, three main parameters have been identified which comprise a thorough characterization of CS particles: (1) the size and size distribution of the core particle and the final composite, (2) the shell morphology including the thickness, size of shell-building blocks (e.g., SiO_2 NPs) and their assembly on the core bead's surface, and (3) the resulting roughness of the shell of the CS bead.

Several methods have been well established for the reliable determination of (core) particle size and mono/polydispersity, whether in the native suspension or in dried states, such as counting (including imaging), fractionating, spectroscopic ensemble and integrating methods.[128] However, because the morphology of CS particles is of special interest, microscopic techniques are the methods of choice here. Methods measuring in suspension cannot reveal these features in a reliable fashion; morphologies are smeared by the particle's motion and an apparent shell thickness, derived for instance from the size difference of a particle prior to and after shell growth in suspension, can differ simply because the chemical nature of the CS particle is altered after shell growth.

From the well-established microscopy techniques, transmission electron microscopy (TEM) is commonly employed for (nano)particle size and shell thickness determination, scanning electron microscopy (SEM) for obtaining a detailed view of the particle shell surface texture and, to a lesser extent, atomic force microscopy (AFM) for retrieving information on the roughness.

Problematic here is on one hand that two or three different instruments must be used, this often resulting in the fact that different areas or even different parts of a sample are being analyzed.

AFM will suffer from extensive experimental runtimes to analyze a larger number of particles. On the other hand, no reliable methodology exists for the evaluation of a bead's *roughness* or *smoothness* using SEM or TEM. Here, images are commonly analyzed visually so that the imaged beads are classified into *rough* or *smooth* depending on the operator's perception or interpretation.

In this part of the project, these issues were addressed by elucidating whether a reliable characterization of CS particles can be performed with a single instrument and how an image analysis procedure can yield a reliable parameter for a particle's roughness, potentially allowing for a standardized classification into *smooth* and *rough*. A dual mode SEM set-up was opted for which permits the imaging of particles of the same sample area in the high-resolution, surface-sensitive, so-called *InLens*® mode as well as in the transmission mode (TSEM), virtually at the same time. The method has been successfully applied recently for the accurate characterization of other types of (nano)particles.[87, 129]

A systematic investigation of the parameters size and size distribution, shell thickness, composition, and texture, as well as the profile roughness, was performed on exemplary CS materials, which were all synthesized using the synthetic procedures presented in chapter 2.

Special focus was laid on the comparison of the *InLens*® (SEM) and TSEM modes, to evaluate the strengths and limitations of both methods for the corresponding analysis and parameters derived. AFM measurements were further invoked for analysis by an independent morphology-resolving technique. Finally, a procedure was developed to reliably assess the root mean squared (RMS) profile roughness (R_Q) of a particle by analyzing its contour in a standardized manner, yielding a thorough set of morphological data of CS particles.

3.3 Results and discussion

3.3.1 Particle size and size distribution

The first parameter of this investigation was the size and size distribution of the core particles. To assess the outcome of *InLens*® SEM and TSEM images, three differently sized polystyrene beads termed PS5-PVP40 (cf. section 2.3.15), PS20-PVP40 and PS30-PVP40 were used. In all cases, PVP40 was used as the stabilizer during the convergent polymerization. Images were taken from samples of each batch with an identical field of view (FOV), i.e., magnification, using both operation modes (Figure 43).

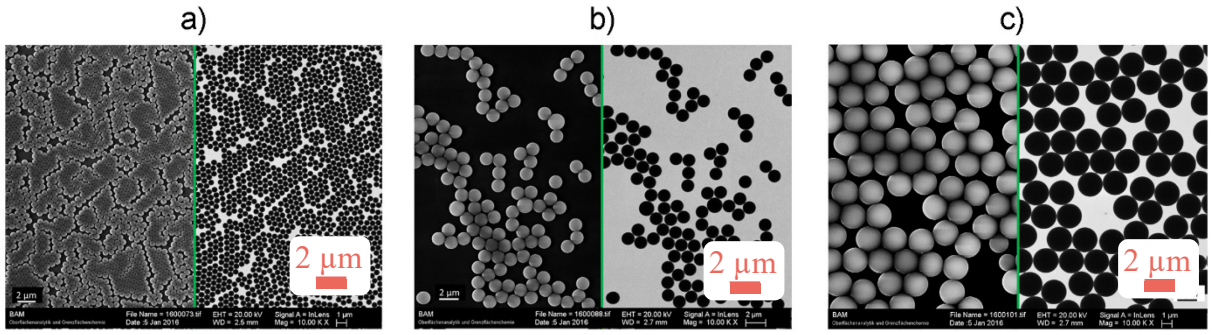

Figure 43. *SEM (left from green line) and TSEM (right from green line) images taken from the same sample areas with 0.03 pixel nm^{-1} resolution: a) – PS5-PVP40; b) – PS20-PVP40; c) – PS30-PVP40.*

The size data obtained for the different ensembles of particles are presented in Table 10. Analyses of images taken in *InLens*® SEM mode yield beads which are 20–30 nm larger than determined via TSEM. This effect of saturation of the (surface sensitive) *InLens*® signal at the particle boundaries is well-known and eventually results in a slight overestimation of the true size in the dry state as shown by Hodoroaba and co-workers.[128] From a qualitative point of view, both methods agree reasonably well (below 4% relative deviation).

Note, that the PS20-PVP40 batch is virtually identical to the previously prepared PS-PVP40 particles. The major difference here is the increased amount of styrene used (18.1 wt.-% in contrast to 9.6 wt.-%) which leads to particles with larger diameters (1.3 µm in contrast to 0.9 µm).

Table 10. *Size data (ecd, and c_v) of polystyrene core particles obtained from SEM and TSEM image analysis of N particles.*

	SEM			TSEM		
	N	*ecd* / nm	c_v	*N*	*ecd* [a] / nm	c_v
PS5-PVP40	780	564.7	2.2	1343	543.4	2.4
PS20-PVP40	105	1300.1	3.9	106	1274.0	3.8
PS30-PVP40	58	2459.7	5.7	58	2430.7	5.8

The difference between the two imaging modes becomes more obvious after image processing. An example is given for the PS5-PVP40 batch (Figure 43a). The TSEM image, contrary to the *InLens*® SEM image, can be easily processed with an automated threshold based on the IsoData algorithm.[130] This will give more user-independent results since transmission contrast levels between particles and the supporting carbon film are significantly larger. Additionally, TSEM will result in a significantly higher number of particles meeting the given requirements of a 0.8 minimum circularity, defined as (eq. XI)

eq. XI. $$4 * \pi * \left(\frac{area}{perimeter^2}\right)$$

and a minimum size of 100 nm. These two parameters were set to exclude agglomerates and small artifacts. For the *InLens*® SEM image, on the other hand, individual thresholds had to be set because an automated threshold will not sufficiently differentiate between particles and background (Figure 44). Even with manually adjusted thresholds, the analysis accounts for only 58% of matching particles for the *InLens*® SEM image, significantly increasing the measurement time to gather enough particles for a representative analysis (Figure 45). Moreover, as highlighted before, a slight overestimation of the particle size is induced by using the conventional SEM images.

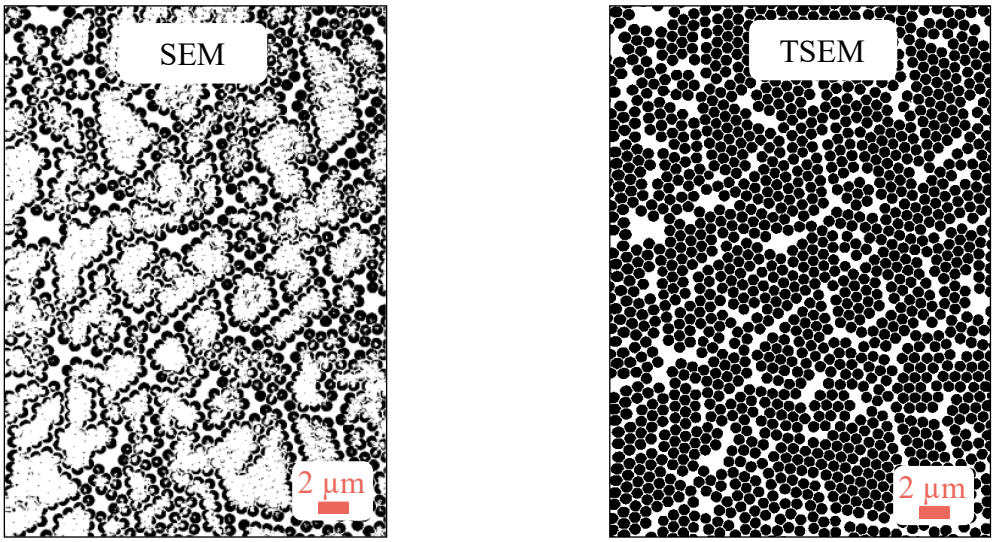

Figure 44. *Binarized images from SEM (left) and TSEM (right) of the bead batch PS5-PVP40 after an automated threshold setting based on IsoData and watershed algorithm applied with ImageJ.*

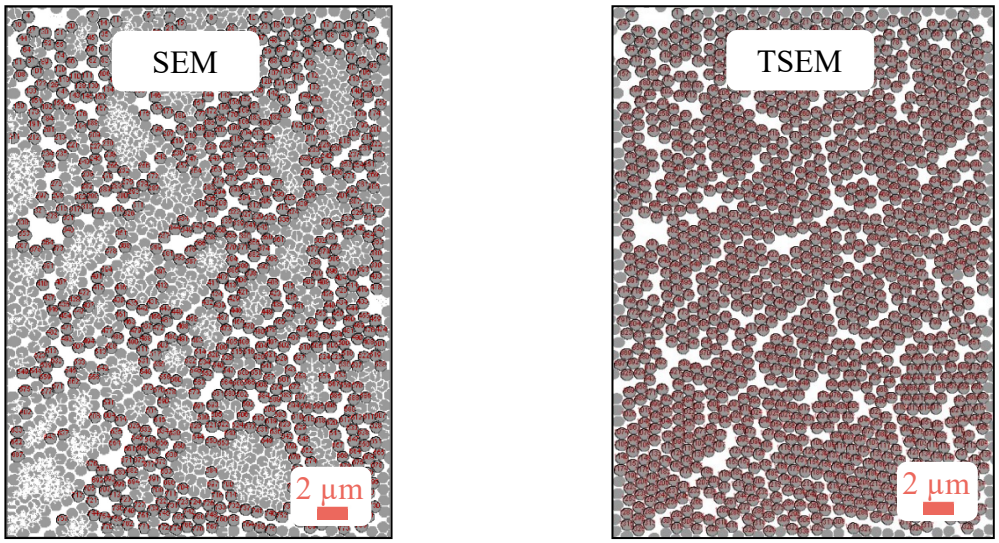

Figure 45. *SEM (left) and TSEM (right) image of PS5-PVP40 after image processing using an adjusted threshold for SEM images and an automated threshold (IsoData algorithm) for TSEM. Using SEM images, only 776 of possible 1343 particles fulfill the requirements of a minimum circularity of 0.8 and a minimum size of 100 nm.*

Conclusively, analysis of TSEM images will yield better results in terms of true particle size in the dry state with higher numbers of particles which meet the dimensional requirements in comparison to SEM image analysis of the same sample area. Based on this, particle sizes were derived subsequently only from TSEM image analysis.

3.3.2 Shell morphology of CS beads with SEM and TSEM

To examine the performance of EM for the morphological characterization of CS particles using *InLens*® SEM and TSEM modes, the beads were coated with a silica shell. These particles were termed SiO_2@PS5-PVP40, SiO_2@PS20-PVP40 and SiO_2@PS30-PVP40.

Images of differently sized CS particles were recorded in the *InLens*® SEM mode (Figure 46) in a suitable FOV to show sets of three particles. In all cases, small SiO_2 NPs assemble on the larger core particles and fuse to form a shell with a raspberry-like appearance of the particles. This is in good accordance with previous results found with SiO_2@PS-PVP40 particles, underlying the robust fabrication method of PVP40-mediated synthesis of raspberry-like particles, also in different sizes (cf. Figure 10b).

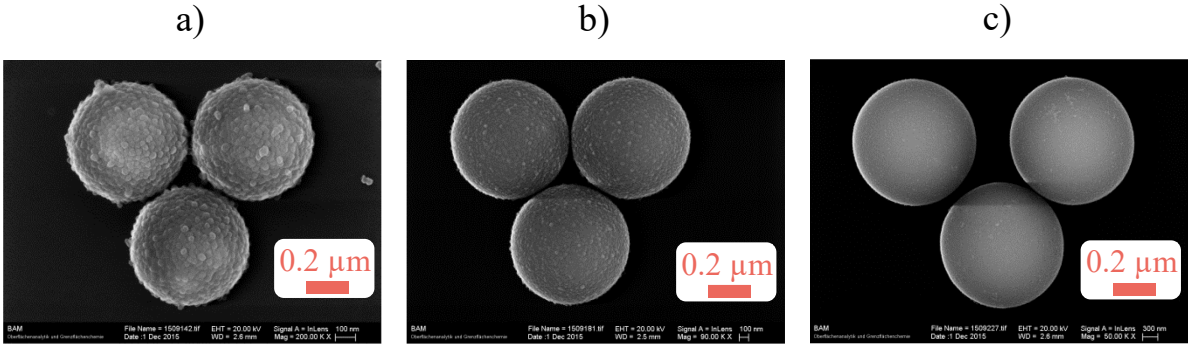

Figure 46. *SEM images within different FOV with corresponding resolution of 0.55, 0.25 and 0.14 pixel* nm^{-1}*: a) –* SiO_2*@PS5-PVP40; b) –* SiO_2*@PS20-PVP40; c) –* SiO_2*@PS30-PVP40.*

Characterization of the CS particles was complemented by EDX elemental maps and line scans, tracking the elements silicon and carbon (Figure 47a–c). The core-shell structure of all particle types can be clearly resolved in the mapping mode with a silicon-rich outer layer and a carbon-rich core, representing the SiO_2 shell and the polymeric template, respectively. Looking at the

EDX line scans, the amount of silicon in the outer shell domain is highest for the smallest particles SiO_2@PS5-PVP40. The considerably high carbon content in the shell of particles SiO_2@PS20-PVP40 and SiO_2@PS30-PVP40 can be explained by diffusion of PVP chains and/or polystyrene into the shell layer via capillary forces which are induced by small SiO_2 NPs in these cases.[68] This phenomenon was also observed during the microporosity study in section 2.3.8.

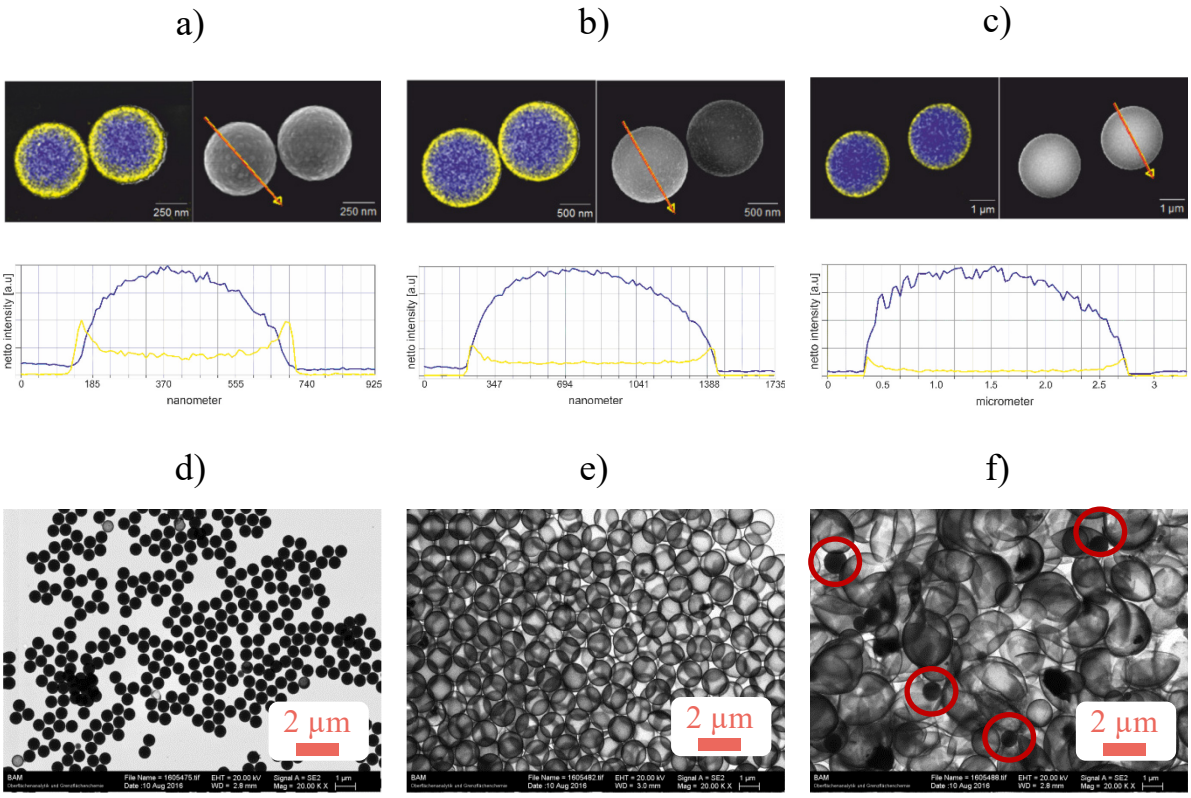

Figure 47. *EDX analysis for SiO_2@PS5-PVP40 (a), SiO_2@PS20-PVP40 (b), and SiO_2@PS530-PVP40 (c) including silicon (yellow) as well a carbon (blue) signals. For each particle, a representative EDX mapping (top row, left images) and line scan (middle row) are shown together with the corresponding SEM image (top row, right images) where the line scan trace is visualized. TSEM images after dispersing the CS particles in THF overnight: d) – SiO_2@PS5-PVP40; e) – SiO_2@PS20-PVP40; f) – SiO_2@PS530-PVP40 (the red circles highlight smaller intact particles in the batch).*

Intrigued by these findings, the stability of the ensembles was assessed by dispersing the particles in pure THF to induce swelling and dissolution of the core for silica hollow

microsphere (SHM) formation. In Figure 47d–f, TSEM images are shown for the CS particles after overnight treatment. The transmission mode enables a direct investigation of hollow sphere formation since particles appear more transparent if the core material is absent.[129] Only bigger sized particles result in SHMs, while the smaller CS particles remain largely intact, this reflecting well the increased stability due to the fully covering SiO_2 shell domain. Interestingly, this does not only hold for SiO_2@PS5-PVP40 particles, but also for smaller microparticles found in the SiO_2@PS30-PVP40 batch observed in Figure 47f, see red circles. These results also show that medium-sized SHM particles made from PVP40-mediated CS particles can either be prepared by dissolution or thermal treatment as was shown in section 2.3.4.

The shell morphology can be further examined from images recorded with the same FOV in higher magnification for the three different particle batches, revealing the size of the shell-forming SiO_2 subunits (Figure 48 and Table 11). These will give information on shell thickness assuming a monolayer arrangement like previously found for SiO_2@PS-PVP40.

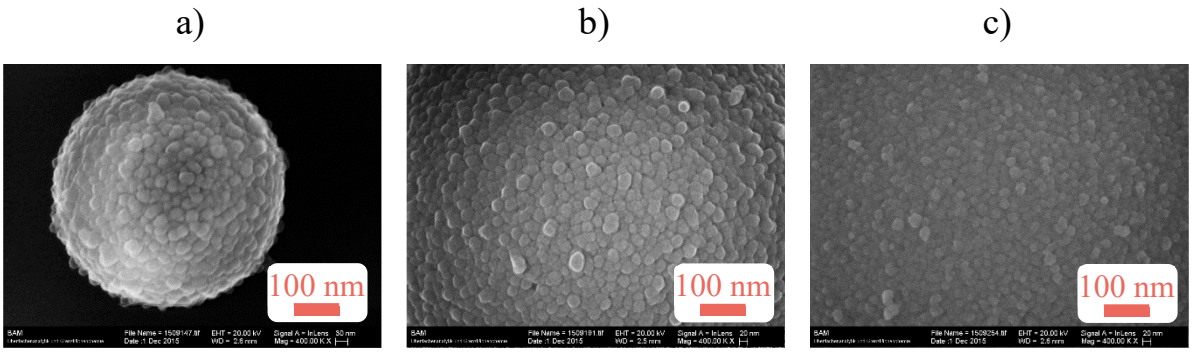

Figure 48. *SEM images of the CS particles in identical FOV with resolution of 1.09 pixel nm^{-1}: a) – SiO_2@PS5-PVP40; b) – SiO_2@PS20-PVP40; c) – SiO_2@PS30-PVP40. Size determination of SiO_2 NPs was performed with ImageJ, measuring the area of 30 manually drawn circles or ellipses and calculating the equivalent circular diameter (ecd).*

Shell thicknesses (t_{shell}) were additionally analyzed with TSEM by measuring the overall size of CS beads, then subtracting the size of the pure PS particles, and finally dividing by two. For this analysis, the sizes of 250 particles (pure PS and CS particles) were measured and distribution plots with 7 nm bins were created (Figure 49).

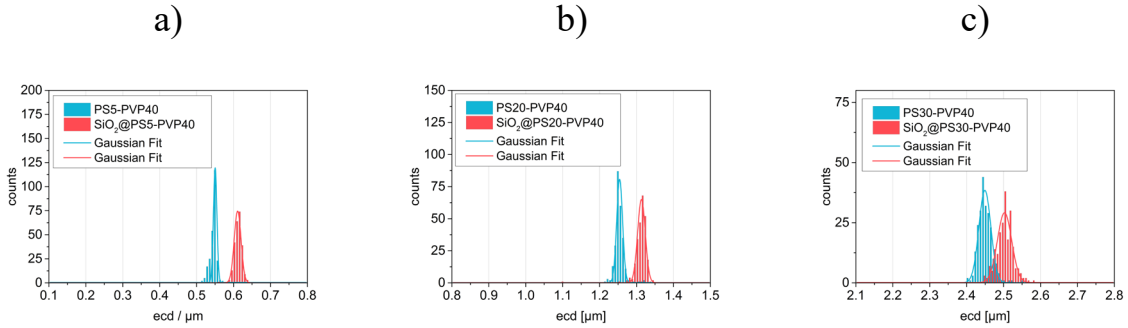

Figure 49. *Size distribution plots for the beads derived from TSEM image analysis: a) – PS5 and SiO_2@PS5-PVP40; c) – PS20 and SiO_2@PS20-PVP40; c) – PS30 and SiO_2@PS30-PVP40.*

The results of the size analysis of the core and CS beads together with the corresponding calculated shell thicknesses via subtraction as well as SiO_2 NP size determination are given in Table 11. The coefficient of determination R^2 for all Gaussian fits is above 0.9 indicating a basically bell-shaped distribution for all particles. Again, an excellent correlation between the shell thickness obtained by CS/core particle size difference in TSEM mode and via direct sizing of the SiO_2 NPs in the conventional SEM mode is observed.

Table 11. *Diameter of the main mode of core (ecd_{core}) and CS particles (ecd_{CS}), coefficient of determination* R^2*, coefficient of variation (c_v) obtained from full data set (N = 250), shell thickness (t_{shell}) as well as diameters of shell-forming SiO_2 NPs ($ecd_{SiO2\ NPs}$).*

	ecd_{core} [a] / nm	R^2	c_v [b]	ecd_{CS} [a] / nm	R^2	c_v [b]	t_{shell} / nm[c]	$ecd_{SiO2\ NPs}$ [d] / nm
SiO_2@PS5-PVP40	550.2	0.95	1.7	611.1	0.99	2.2	30.4	31.4
SiO_2@PS20-PVP40	1254.2	0.97	2.2	1313.0	0.98	2.5	29.4	29.5
SiO_2@PS30-PVP40	2449.3	0.98	12.9	2502.5	0.92	18.3	26.6	24.6

[a] *ecd* was determined from Gaussian fit analysis of the main size mode by TSEM. [b] c_v was determined from statistical data of full data set (N = 250).[c] t_{shell} was derived by subtracting ecd_{core} from ecd_{CS} divided by two. [d] $d_{SiO2\ NPs}$ was determined from 30 analyzed SiO_2 NPs on the surface of CS beads using high-resolution SEM images (Figure 48).

The c_v for PS5-PVP40 and PS20-PVP40 increases slightly after shell formation but remains below 5% which shows that the overall size distribution and monodispersity is retained. PS30-PVP40 in contrast results in significantly higher c_v. This rather high value differs from the c_v measured in the previous section (cf. Table 10) and corresponds to secondary microparticles which were already found in TSEM images after core dissolution (Figure 47) and identified in images of different sample areas recorded on this sample.

The importance of a Gaussian fit analysis of main populations to determine shell thicknesses via subtraction becomes clear because the number of particles from different size fractions in polydisperse samples can differ for core and CS particles in the respective imaged sampling areas. This can have a differing influence on the statistical mean size which in turn would result in less reliable values for the shell thickness.

3.3.3 Roughness of CS particles

The images of the CS particles with an adequate FOV shown in Figure 46 strongly suggest a change of the surface texture from rough to smooth. Scrutinizing the published literature on SiO_2-coated materials, however, it became apparent that a standardized method for quantifying the roughness of surfaces is lacking; utmost works simply evaluate the roughness by visual inspection of EM images.[131-132] Moreover, terms like *smooth* or *rough* in the literature, exemplified by the work of Lu et al., are often not related to objective parameters or referenced to the respective FOV, but depend significantly on visual perception of an individual operator and image resolution.[72]

AFM was already introduced as an analytical method to obtain data on the roughness of surfaces also for spherical substrates. In AFM, commonly area profiles composed of successive line profiles (eq. XII) of the specimens' surface are recorded, from which the root mean square surface roughness (S_Q) is determined:

eq. XII. $$S_Q = \sqrt{\frac{1}{l} * \int_0^l z(l)^2 dl}$$

Here, S_Q is defined as the square root of the mean squared deviation of successive height profile plots (z) divided by the length of the entire profile (l). An example of an S_Q determination of CS beads by AFM can be found in Zhang et al.[122] However, the number of examples in this field given in the literature is considerably small. The latter is presumably due to the fact that

AFM measurements of spherical surfaces cannot usually be done in compliance with standardized procedures and generally suffer from an unavoidable correlation to the FOV.[133] For instance, when the diameters of the beads differ or when the surface roughness is like the height of the spherical calotte within the FOV, the curvature must be corrected, whereby the correction itself depends on surface roughness. A comparison of the surface roughness on spherical particles can be made if bead diameters and FOVs can be kept identical as in this present case.

SEM or TEM, on the other hand, are routine characterization methods for CS beads of different sizes and surface morphologies. To provide a solid base for the characterization of the roughness, a simple procedure to track the contour of the particles and obtain a line profile of the particles' surface topography was developed. The profile data can then be used for further data derivation such as R_Q. In analogy to AFM, the profile roughness R_Q in EM is defined as in eq. XIII, with y denoting the lateral profile, read from a 2D projection image.

eq. XIII. $$R_Q = \sqrt{\frac{1}{l} * \int_0^l y(l)^2 dl}$$

In fact, this concept of roughness characterization from contour lines was initially proposed by Jacobs in the context of theoretically predicting the role of atomic-scale roughness on the adhesion properties of few nanometer-sized diamond tips to surfaces as measured by TEM.[127] This model was adopted here and transferred to hybrid particles consisting of a micron-sized core and nano-sized particles fusing into a shell which, in combination with TSEM images, allows deriving a more standardized parameter for the roughness of such widely employed core-shell particles.

3.3.4 Contour analysis for the determination of RMS profile roughness (R_Q)

The steps of the procedure of R_Q calculation from TSEM micrographs are visualized in Figure 50, with the example of SiO_2@PS5-PVP40. For the analysis, a raw EM micrograph showing one bead in adequate FOV was first loaded into ImageJ. After calibrating the scale of the image, the analyzed area was reduced to an 8-bit image.

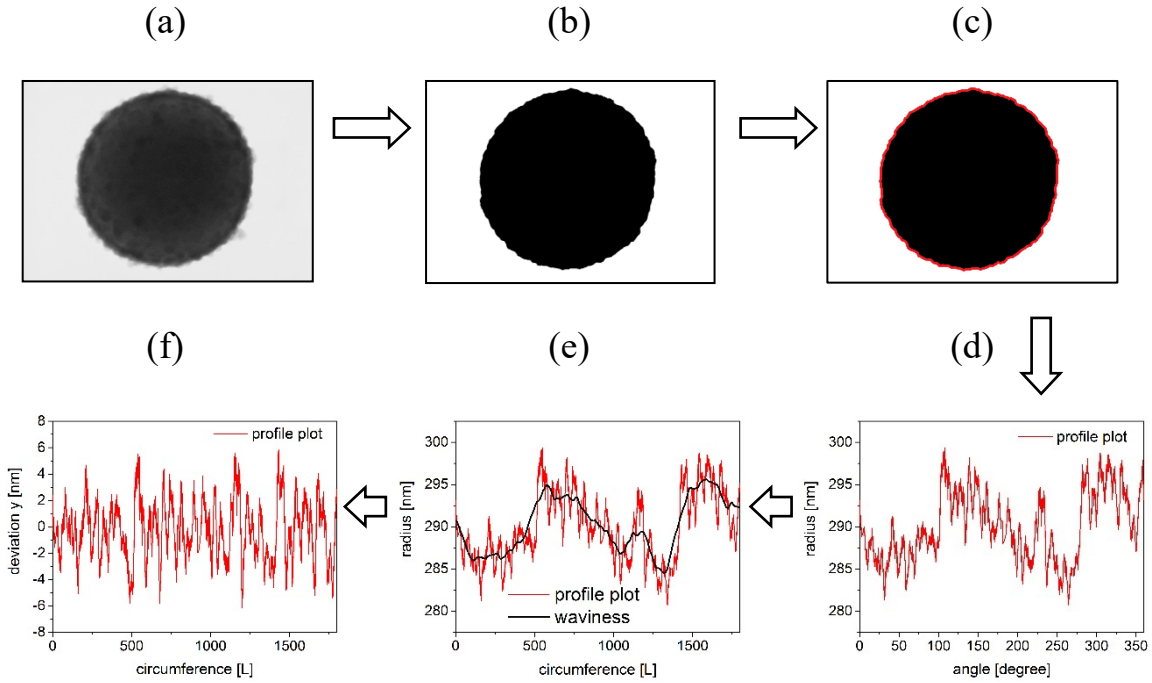

Figure 50. *Exemplary image processing starting from the 8-bit TSEM image of SiO_2@PS5-PVP40 (a) which was next reduced to a binary projection image (b) from which a contour (red line) was derived (c). Then the profile was plotted against the angle at constant radius (d). After data processing using a moving average to subtract waviness (black line) from the profile (e), the small-scale deviation or nano-roughness plotted against the circumference (L) was obtained (f).*

Next, an automatic threshold based on the IsoData algorithm was set to delimitate particle boundaries, creating a projection image of the particle (Figure 50b).[130] If there were voids visible within the projection image, they were manually filled with black color since a complete filling of the analyzed object was necessary for further analysis. The contour of the particle projection was then analyzed with a self-written software package, which estimates the particle center by reducing the root mean square of the angle-resolved radius until a minimum is reached. From this apparent center, the respective radii were exported (Figure 50c,d) into the software Origin (OriginLab Co., Northampton, MA) for further data analysis. Afterward, the profile length (l) of the circle was calculated using the particle's angle and the optimized radius. As almost all particles tend to appear slightly elliptical in the TSEM images, either because they have truly such a shape or because of a small residual drift or deformation during SEM measurement, the change in radius tends to be dominated by this feature rather than by the true surface. To remove this influence of waviness from the profile, the raw data were smoothed

with a moving average using a bandwidth of 50% of the particles' radius, corresponding to a range within an angle of 30° (Figure 50e). Subsequently, the smoothed data were subtracted from the raw data, to derive only the information on small-scale radius deviations (Figure 50f). Finally, R_Q was calculated from these net line profiles using eq. XIII.

3.3.5 Determination of R_Q: SEM vs. TSEM

To test the procedure on CS beads, PS5-PVP40 was coated with five different concentrations of TEOS (SiO_2@PS5-PVP40-C1 to SiO_2@PS5-PVP40-C5, Table 12).

Table 12. *Concentrations of TEOS used for the coating of PS5*

SiO_2@PS5-PVP40	-C1	-C2	-C3	-C4	-C5
TEOS / mM	23	45	135	271	406

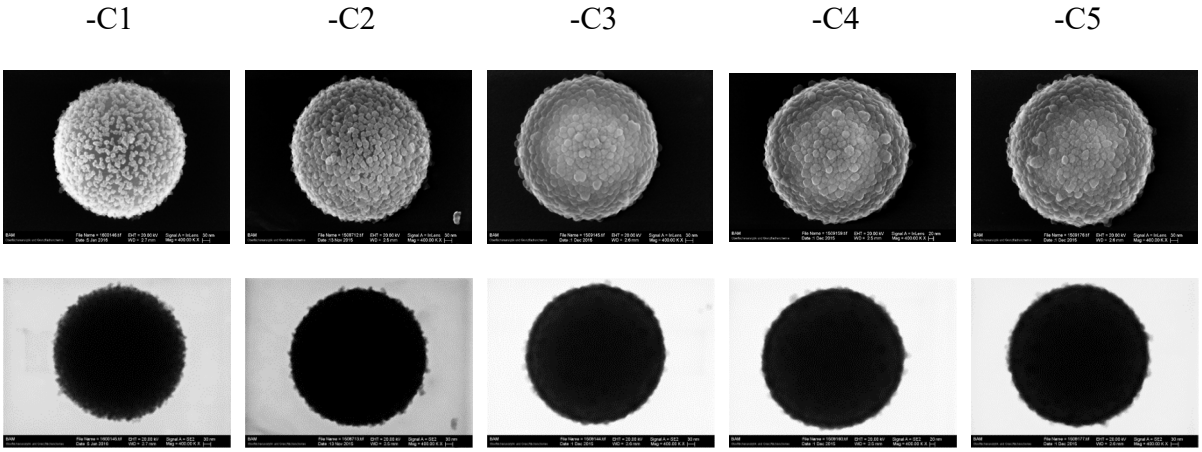

Figure 51. *Representative SEM (top) and TSEM (bottom) images of SiO_2@PS5-PVP40 particles prepared with varying TEOS concentration during SiO_2 coating. Identical FOV was used here for all images, with 1.09 pixel nm^{-1} resolution.*

Using this sample set, the difference between SEM and TSEM image processing was investigated. The profile roughness R_Q was determined from the contour analysis as outlined above from images recorded in both modes of identical areas. Representative images of the CS particles within identical FOV are shown in Figure 51 to provide a visual guide.

In Figure 52a, the R_Q calculated from both modes is plotted against the TEOS concentration used. Two zones could be identified that match well with the visual inspection of the beads: (i) fully covering shells (closed) for which no subjacent polymer surface is visible (SiO_2@PS5-PVP40-C3, -C4 and -C5), and (ii) perforated shell structures (open) for which lose assemblies of particles on the surface of the template (SiO_2@PS5-PVP40-C1 and –C2) are observed. The particles with a perforated shell and the lowest density of SiO_2 NPs on their surface (SiO_2@PS5-PVP40-C1) showed similar R_Q values when calculated from *InLens*® SEM and TSEM images.

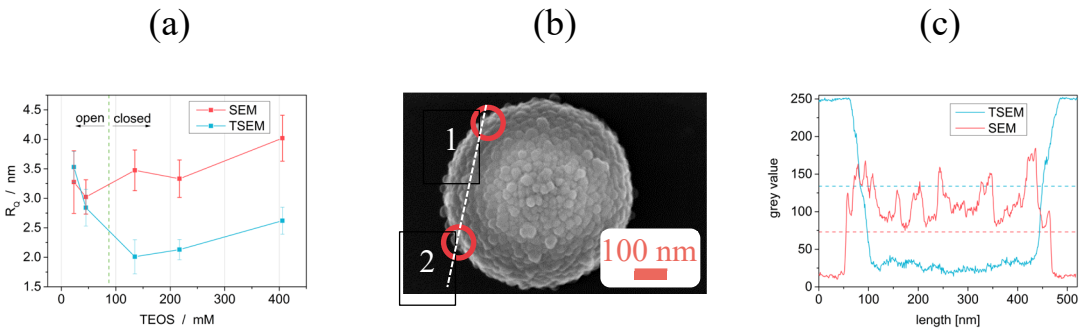

Figure 52. *a) – R_Q obtained from SEM (blue) and TSEM (red) plotted against the initial TEOS concentration used during SiO_2 coating. Standard deviations were determined from analysis of three particles; b) – SEM image showing one representative SiO_2@PS5-PVP40 particle. Two SiO_2 NPs which are present in the rear level of the particle are highlighted with orange circles; c) – respective SiO_2 NPs are highlighted in the profile scan (red line for SEM and blue line for TSEM) showing the grey levels corresponding to a line drawn with ImageJ as shown in b).*

For SiO_2@PS5-PVP40-C2, only a TSEM-based analysis reflected the change toward a smoother surface with a significant reduction of R_Q from 3.5 ± 0.3 to 2.8 ± 0.3 nm. The difference is probably correlated to the effect of saturation of the *InLens*® signal in SEM mode at the particle boundaries which masks the exposed polymer surface (or open voids within the shell) in the projection. The same trend was visible upon stepping to fully covering shells for which *InLens*® SEM-based analysis resulted in even larger R_Q values even though further densification and merging of SiO_2 NPs should result in a smoother surface. TSEM-based analysis again showed better performance here with a further reduced R_Q value.

This large difference of R_Q derived from either *InLens*® SEM or TSEM image analysis for fully covering shells is a direct consequence of the corresponding contrast (and grey levels) of SiO_2

NPs on the surface of the CS beads. An example is illustrated in Figure 52b in which two SiO_2 NPs that are present at the rear side of the bead are highlighted in red circles. The grey levels corresponding to a line drawn in ImageJ, which crosses both highlighted regions, were tracked in both SEM and TSEM images and the resulting profile scans are shown in Figure 52c. The IsoData algorithm[130] has set thresholds of 73 for the *InLens*® SEM image and 134 for the TSEM image based on the mean value built from the average grey levels of background and image. Both threshold values are also plotted in the profile scans in Figure 52c.

It becomes clear that the threshold setting for *InLens*® SEM images includes unwanted asperities (all objects above the threshold), finally resulting in a higher profile roughness. TSEM on the other hand automatically excludes these artifacts and thus results in more reliable R_Q values and hence a smoother surface. This more accurate description directly improves the discrimination between closed and open shells. To visualize the outcome after setting the threshold, exemplary binary TSEM and SEM images of the same SiO_2@PS5-PVP40-C3 particle are shown in Figure 53.

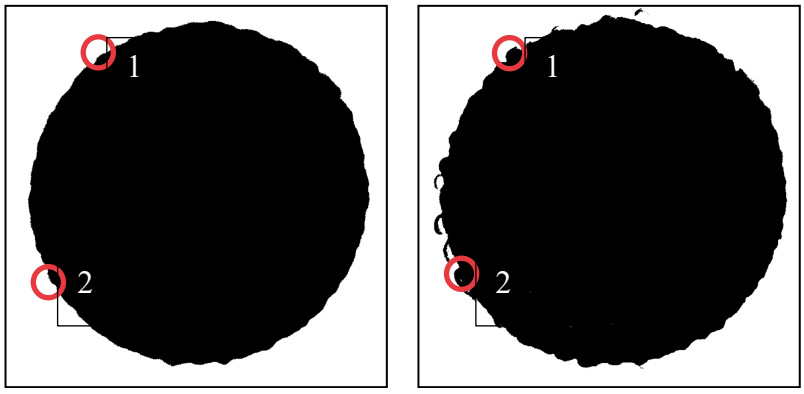

Figure 53. *Binary projection images of the SiO_2@PS5-PVP40-C3 particle from Figure 5a after setting an automated threshold in TSEM (left) and SEM images (right).*

In fact, the R_Q of 2.0 ± 0.3 nm for this CS particle derived from TSEM image analysis is close to the value determined by Zhang et al. with AFM on comparable CS beads, i.e., an S_Q of 1.7 nm for 800 nm sized PS beads coated with a SiO_2 NP shell of up to ca. 40 nm in thickness (see also section 3.3.8 for a direct comparison of TSEM and AFM results on samples from the same batch of CS particles).[122]

It is important to point out that the contour analysis approach is semi-quantitative in the sense that it strongly depends on the scale. Reliable R_Q data can therefore only be determined and compared for CS particles recorded in the same FOV. Nonetheless, whenever approaches to 'roughness controlled' coatings are proposed in which the increase or decrease of roughness is evaluated by visual inspection of CS beads using EM imaging with identical FOV, such as for instance in the work published by Li and coworkers, the contour analysis proposed here could significantly enhance the validity of the analysis, providing more accurate data that describe the actual profile roughness.[56]

3.3.6 Classification of profile roughness using R_Q at different FOV

Having established an optimized procedure for the contour analysis based on TSEM images, it was of major interest to elucidate whether profile roughness threshold values would allow for more consistent classification of CS particle morphologies into *smooth* and *rough*. First, looking at (artificially created, i.e., computer-drawn) ideal circles in varying FOV, a strong dependence of the calculated noise and corresponding R_Q is evident, because of changing pixel size (Figure 54, left).

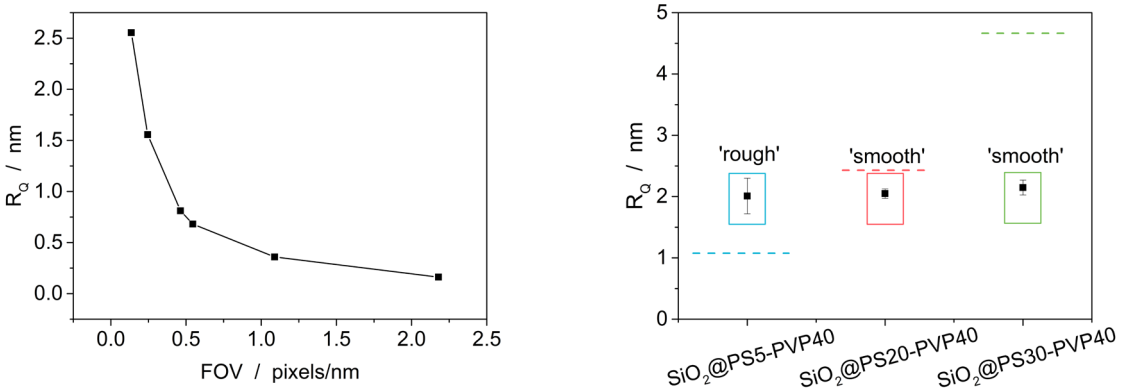

Figure 54. *Left – profile roughness, R_Q, of simulated drawn circles plotted as a function of the respective image resolutions. Right – classification of SiO_2@PS5-PVP40 (blue), SiO_2@PS20-PVP40 (red) and SiO_2@PS30-PVP40 (green) according to the corresponding threshold represented as dashed line in the respective color. Standard deviation for R_Q was determined from analysis of three different TSEM images.*

These R_Q values times three ($3\times R_Q$) were set as an adequate roughness threshold (T) above which a reliable characterization of R_Q values is feasible for the FOV used. In other words, below T, surfaces are referred to as *smooth* because asperities cannot be resolved anymore at the FOV used (the roughness is hence masked by the noise), while above T deviations can be measured at the nanoscale above the noise, classifying a surface as *rough*.

To check whether T in conjunction with the FOV qualifies as an objective parameter for the classification of CS beads into *rough* and *smooth*, R_Q was calculated from TSEM images of SiO_2@PS5-PVP40, SiO_2@PS20-PVP40 and SiO_2@PS30 -PVP40. The results are shown in Figure 54 (right) in which the dashed colored lines indicate the thresholds for the respective particle and FOV used. In this case, only SiO_2@PS5 can be termed *rough*, since only its calculated R_Q lies well above T determined from a FOV with a respective resolution of 1.09 pixel nm^{-1}.

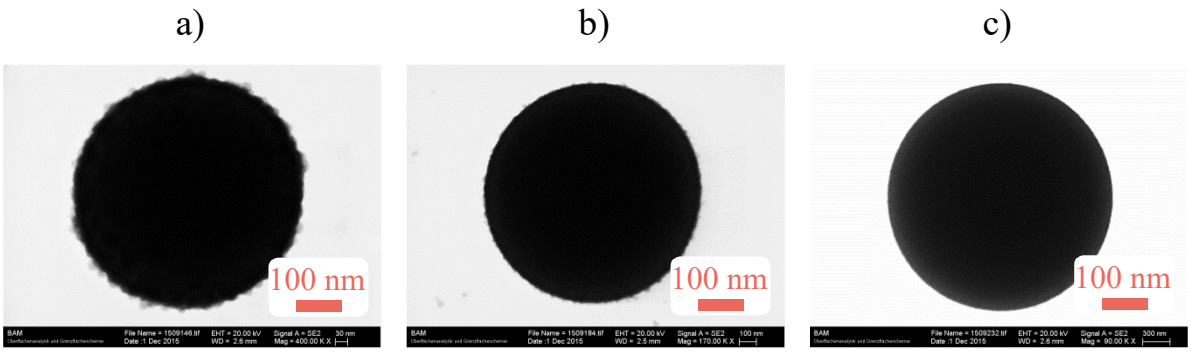

Figure 55. *Representative TSEM images in adequate FOV with corresponding resolution of 1.09, 0.46 and 0.25 pixel nm^{-1}: a) – SiO_2@PS5-PVP40; b) – SiO_2@PS20-PVP40; c) – SiO_2@PS30-PVP40.*

This classification fits well to the visual inspection of TSEM images recorded for the particles shown in Figure 55: while PS5 clearly reveals a rough surface, PS20 and PS30 are classified as smooth in the FOV used.

It is worth noting that smooth surfaces could eventually bear smaller nano-sized surface textures which are not resolved with the contour plot from the TSEM images. Hybrid materials with a mesoporous shell on a polystyrene core, for example, promising candidate materials for improved chemical mechanical polishing of surfaces, have narrow pores with diameters frequently as small as 3 nm.[134] In contrast to the materials for which SiO_2 NPs with sizes of 20–

30 nm constitute the shell and create surface structures with distinct roughness, the periodically repeating pores in mesoporous materials rather define the inner structure of an overall smooth and evenly thick shell.

3.3.7 Classification of profile roughness using R_Q at identical FOV

Like reported in chapter 2, micron-sized polystyrene cores for SiO_2@PS beads with controlled surface topology can be prepared in a facile way by dispersion polymerization using PVP with different MW as a stabilizer. For this purpose, PVP10, PVP40, and PVP360 with ~10 kDa, ~40 kDa, and ~360 kDa, respectively, were employed to control the subsequent shell formation from a monolayer to multilayer-like shells. In the present study, an additional batch with a stabilizer of intermediate molecular weight, i.e., PVP160 (MW ~ 160 kDa) was prepared. The CS beads are termed SiO_2@PS-PVP10, SiO_2@PS-PVP40, SiO_2@PS-PVP160 and SiO_2@PS-PVP360 corresponding to the PVP used for the core preparation. Respective TSEM images of the series of beads are shown in Figure 56.

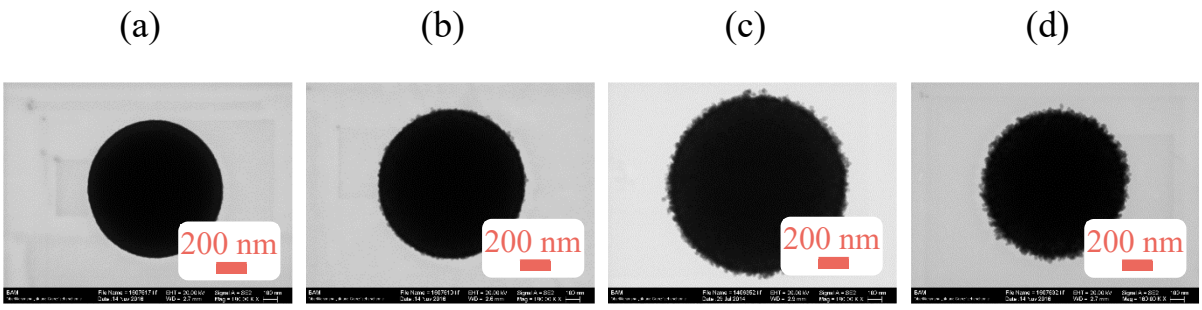

Figure 56. *Representative TSEM images in same FOV with a resolution of 0.49 pixel nm^{-1}: a) – SiO_2@PS-PVP10; b) – SiO_2@PS-PVP40; c) – SiO_2@PS-PVP160; d) – SiO_2@PS-PVP360.*

The determined R_Q values from TSEM images are plotted in Figure 57 (left) together with the corresponding threshold set for analysis. The particles obtained with PVP10 as the stabilizer can be classified as possessing a smooth surface, i.e. roughness cannot be resolved, whereas PVP with higher MW result in rough surfaces, matching well the visual inspection from TSEM images. Moreover, a gradual increase of R_Q from ~3 to ~8 nm was noticed for PVP40, PVP160 and PVP360, reflecting well the structural change from shells fully covered by SiO_2 NP monolayers to rougher, multilayer-like shell architectures.

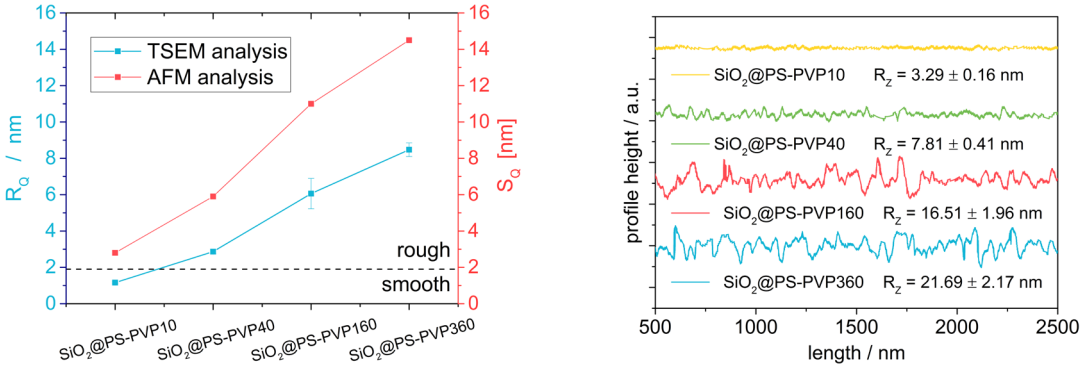

Figure 57. *Left* – R_Q *calculated by TSEM analysis and* S_Q *from AFM image analysis of CS beads with different shell architecture and the corresponding threshold (dashed line) for 0.49 pixel nm*$^{-1}$ *FOV. Standard deviations were determined from analysis of three different particles. Right – exemplary roughness profiles extracted from 2D projection TSEM images and corresponding calculated* R_z *values.*

The difference observed can already result in significant variations of materials properties such as increased adhesion, modified anti-fogging or super-hydrophobic properties as well as differences in the adsorption behavior of biomolecules or toxicological effects. While investigations in this field so far mostly relied on visual and purely qualitative perception of the beads' outer surface, the contour analysis now provides a facile and transparent quantitative tool to obtain objective and comparable data, rendering the correlation of profile smoothness/roughness with other functions or properties more reliable.

Next to the R_Q as a primary value for profile roughness, the profile plots can further be used for the determination of other roughness parameters. As an example, the peak-to-valley height (R_Z) was calculated from the profile plot by subtracting the height average of the five lowest peaks from the average of the five highest peaks using the smoothed roughness profile data. Figure 57 (right) shows sections of the profile plots with corresponding R_Z values.

A relative correlation of R_Q with R_Z is observed which indicates a roughness increase due to an increasing difference of height averages of the profile plot. This is consistent with a model for which SiO_2 NPs of the same size assemble either in monolayer-like (e.g., for PVP10) or as multilayer-like structures (e.g., for PVP160 and PVP360). PVP40 leads to a state for which first NPs are protruding from the SiO_2 NP monolayer, i.e., the onset of a multilayer-like structure which can be observed clearly from SEM images (Figure 58). This structural change is also well reflected in a gradual increase in the shell thickness (Table 13).

The size distribution plots, which were used for the shell calculation of PS-PVP160 and SiO_2@PS-PVP160, are shown in Annex 6.5.

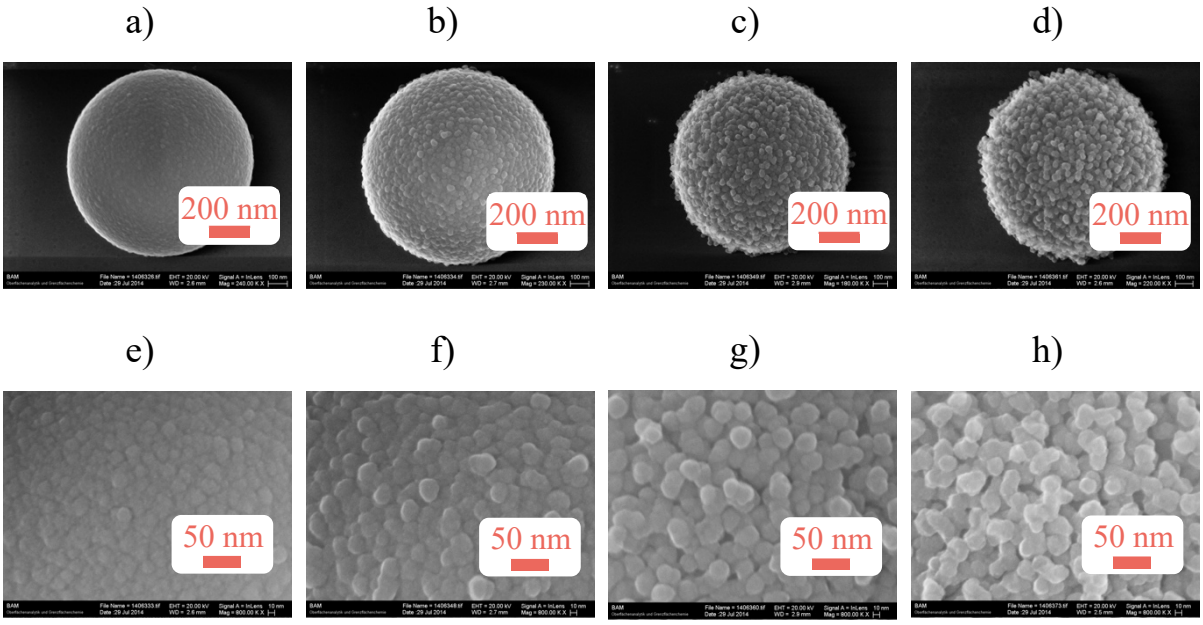

Figure 58. *SEM images from CS particles: a), e) – SiO_2@PS-PVP10; b), f) – SiO_2@PS-PVP40; c), g) – SiO_2@PS-PVP160 and d), h) – SiO_2@PS-PVP360.*

Additionally, the surface area per particle was determined as a mean value of 13.53 µm² for SiO_2@PS-PVP160 using t-plot analysis (cf. section 2.3.7 and 2.5.8, for experimental details Annex 6.6). The number of particles per gram was calculated considering a silica content of 26.0 mass-% (determined by thermogravimetric analysis, cf. Annex 6.6). Because SiO_2@PS-PVP160 particles with an average diameter of 1.20 µm are slightly bigger than the other particles of ~0.91 µm size, the ratio of measured surface area to the calculated surface area of the ideal sphere, i.e., the external surface relative increase, was used to compare the data (Table 13). Again, a correlation between the increase of surface area and profile roughness was found, supporting further the proposed model.

Table 13. *Shell thickness and ratio of measured to calculated surface area of an ideal circle for CS particles prepared with PVP10, PVP40, PVP160 and PVP360. Data for -PVP10, -PVP40 and -PVP360 are derived from the previous section.*

SiO_2@PS	-PVP10	-PVP40	-PVP160	-PVP360
t_{shell} / nm	21.0	36.2	45.6	55.2
$A_{CS}/A_{ideal\ sphere}$	1.6	2.0	4.1	6.1

3.3.8 Comparison of profile roughness (TSEM) and surface roughness (AFM)

For a better reliability assessment of the derived roughness data, the TSEM results of the previous section were compared with results obtained by AFM imaging. Since the surface roughness S_Q determined by AFM strongly depends on a variety of parameters, utmost attention was devoted to consistent data acquisition.

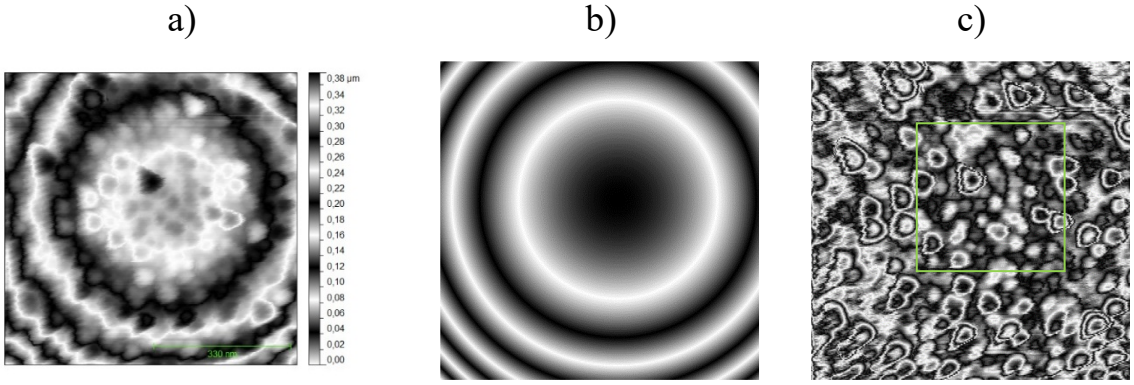

Figure 59. *AFM surface roughness S_Q on the example of SiO_2@PS-PVP40: a) – image raw data (height mode); b) – spherical fit for subtraction; c) – frame with the field of analysis (FOA)*

Figure 59 exemplarily provides the imaging and S_Q calculation strategy from raw data (Figure 59a), spherical fit subtraction (Figure 59b) and the field of analysis (FOA, Figure 59c). The analysis has been carried out with the free software tool Gwyddion (http://gwyddion.net/) and the various parameters derived for the different CS particles are collected in Table 14. Regarding the reliability of the data, not only are the AFM results in themselves consistent, but good comparability between S_Q derived from AFM measurements and R_Q from the contour analysis by TSEM imaging can be found (Figure 57 left).

Table 14. *Topographic AFM data for distinct particles.*

sample		peak to valley height, R_Z / nm	surface roughness, S_Q / nm
SiO_2@PS-PVP10, #1		9.9	2.6
SiO_2@PS-PVP10, #2		20.3	3.3
SiO_2@PS-PVP10, #3		10.3	2.5
SiO_2@PS-PVP10	median	13.5	2.8
SiO_2@PS-PVP10	standard deviation	5.9	0.4
SiO_2@PS-PVP40		28.4	5.9
SiO_2@PS-PVP160		33.6	11.0
SiO_2@PS-PVP360		40.7	14.5

Despite different measurement conditions of TSEM and AFM, the absolute roughness, standard deviation and the trend among different particle architectures show good comparability. Accordingly, the classification *rough*/*smooth* for all four sample types by means of TSEM is well supported by AFM. This verification by an independent method clearly demonstrates the validity of the TSEM imaging procedure proposed here for evaluation of CS particle roughness.

It should be noted that the two imaging methods measure physically different roughness. TSEM refers to the envelope of the 2D projection of a particle as a transmission image. This means that also asperities shortly before and immediately beyond the plane of the largest section through the particle contribute to the overall ‘envelope’ profile. Relative to the roughness as determined by AFM, where the AFM tip accesses better the valleys between asperities by sensing a real 2D surface by means of successive line profiles, the roughness determined from 2D projection TSEM images is somewhat underestimated. Nevertheless, this unavoidable difference between the two measurands does not impede the application of the quantitative approaches presented above either with the TSEM methodology or with the AFM one.

3.4 Conclusion

A comprehensive characterization, using SEM and TSEM operation modes and image analysis, was carried out in this study which results in reliable quantitative data about the architecture and roughness of CS particles. Suitable test materials for this investigation were synthesized using dispersion polymerization for the core preparation and a subsequent SiO_2 coating procedure based on ammonia catalyzed sol-gel process with an alkoxysilane as the precursor.

Starting from the determination of size and size distribution of the particle's core, where transmission mode images of particles in the dry state offer more reliable dimensional data and straightforward image processing including automated thresholds, a next step was undertaken to characterize the shell architecture and elemental composition using high-resolution SEM imaging and EDX analysis. An increasing trend of diffusion of core material into the shell was observed for bigger sized particles by using EDX elemental line scans. This is accompanied by a decreasing core protection capability of the shell. Thus, only the core of the smaller particles with silica-only shells was protected, while the dissolution of the bigger particles led to the formation of SHMs. Gaussian fits with mean size determination and extraction of the respective differences between the CS and core particles divided by two gave reliable results for the shell thickness, which fit well with the size of shell-forming SiO_2 NPs. These were directly measured by high-resolution SEM imaging of the particles' surface.

A contour analysis tool was introduced to obtain roughness profiles from particle projection images using TSEM or SEM from which the RMS profile roughness of the particles' surfaces was calculated. The R_Q (noise) of drawn reference circles sets an objective threshold (defined as three times the noise) for the classification of smooth and rough surfaces depending on the FOV used: surfaces are classified as *smooth* if the roughness is smaller than the threshold. Above the threshold, the roughness can sufficiently be discriminated from the noise and, hence, the surface is classified as *rough*. In this range, if recorded with identical FOV, the R_Q of particles of the same batch can also be analyzed continuously to track batch homogeneity or between different batches to evaluate obvious or subtle changes of roughness. For a practical illustration of the procedure, the R_Q was determined from two sets of CS beads. While the R_Q of the approximately 600 nm sized CS beads could be fine-tuned in the range from 2 to 3.5 nm, the roughness for ~1 µm beads was controlled over the full range from smooth to rough surfaces, with a maximum roughness of approximately 8 nm.

In addition to a comprehensive characterization of CS beads using SEM/TSEM imaging as well as EDX analysis, this research aimed at a more consistent methodological approach for data handling in terms of size and shell thickness determination from image analysis. Moreover, a reliable yet accessible parameter, i.e. the RMS profile roughness R_Q, using SEM or TSEM profile plots derived from particle projection images, adds valuable and reliable information. Further evaluation of roughness can be performed using additional parameters derivable from the profile plot. Exemplarily, the peak-to-valley height R_Z was determined to evaluate quantitatively a general architecture description of CS particles prepared with PS cores with different MW of PVP stabilizer.

Future work is directed at expanding the applicability of the procedure proposed here to image analysis in transmission electron microscopy (conventional TEM as well as at an SEM being equipped with the transmission mode option), to provide a standard contour analysis tool for this popular analytical technique. This would allow end-users to post-analyze images of CS particles quantitatively and to compare and classify them in an objective manner.

3.5 Experimental

3.5.1 Materials

Poly(vinylpyrrolidone) (PVP10 with ~10 kDa, PVP40 with ~40 kDa, PVP-K160 with ~160 kDa (45% in water) and PVP360 with ~360 kDa, Sigma), styrene (ReagentPlus, <99%, Sigma) basic alumina (Al_2O_3, Brockmann I, Acros) and azo-bis-cyanovaleric acid (ACVA, MP Biomedicals) were used for the PVP-coated polystyrene core synthesis. Ammonium hydroxide (32% in water, Merck) and tetraethylorthosilicate (TEOS, <99%, Merck) were used for the silica coating. Methanol (Alfa Aesar, Germany), ethanol (abs. 99% and 96%, ChemSolute), THF and water of MilliQ grade (BAM) were used as solvents and for washing. All reagents were used without any further treatment.

3.5.2 Polystyrene core synthesis

PS5-PVP40 and PS-PVP160 were synthesized in a round-bottomed glass flask by dispersion polymerization as described in chapter 2. For larger microparticles (PS20-PVP40 and PS30-PVP40), a reaction carousel from Radleys® was used and the reaction volume was scaled down to ca. 1/10th to reduce monomer consumption. For the lower volume procedure, styrene was added together with an ACVA solution directly into the reaction tube. Then, the mixture was degassed for 30 min and placed in a pre-heated station. The reaction was conducted for 24 hours at 500 rpm mixing speed.

The particles were left to cool down after the reaction. Then they were transferred to falcon tubes and separated from the solution by centrifugation. The particles were washed three times with methanol in centrifugation/redispersion cycles. The microparticles were finally obtained as white solid after drying them overnight in a vacuum oven. The product was stored at room temperature without any further treatment. Detailed recipes for all batches are given in Table 15.

Table 15. *Recipes for the preparation of polystyrene (PS) particles by dispersion polymerization using ACVA as initiator and different MW stabilizer PVP.*

name	V^a / mL	V_{St} / mL	ACVA[b] / % (w/v)	PVP[c] / wt.-%	MW_{PVP} / kDa	$t_{reaction}$ / °C
PS-PVP160	120.0	15.0	2.0	1.8[d]	160	75
PS5-PVP40	120.0	4.55	2.0	1.8	40	75
PS20-PVP40	12.0[e]	1.89	1.8	1.8	40	70
PS30-PVP40	8.1[e]	3.00	2.0[f]	3.1	40	70

[a] Total volume (V) of reaction. [b] With regard to volume of monomer. [c] With regard to total weight of solvent. [d] Absolute ethanol was used and water was added to obtain a 96% percent ethanol solution, because the PVP160 itself is delivered as 45% solution in water. [e] Smaller reaction volumes were conducted in a reaction station from Radleys®. [f] MeOH instead of EtOH was used here for the preparation of the ACVA stock solution.

3.5.3 SiO_2 coating of polymeric core

The reactions were performed according to the procedure described in section 2.5.3 with the only difference that the reaction volume was scaled down by $1/10^{th}$ for the preparation of SiO_2@PS particles with fixed amount of TEOS (SiO_2@PS20-PVP40, SiO_2@PS30-PVP40, SiO_2@PS-PVP160), and by $1/100^{th}$ for the particles with varying amount of TEOS (SiO_2@PS5-PVP40, cf. Table 12). For the latter, the reaction was performed in 2 mL tubes without magnetic stirrer and a Thermomixer (Eppendorf®) with a mixing speed of 500 rpm was used.

3.5.4 Methods and instrumentation

A SEM (Zeiss Supra40, Oberkochen) with a Schottky field emitter has been used for the experiments in the present study. The SEM is equipped with an *InLens*® detector able to collect selectively the high-resolution secondary electrons ('SE1'). This type of detection is especially valuable when sample surface morphology with nanometer resolution is required, i.e., as for the purposes here.

The transmission mode at this SEM instrument (TSEM) was operated by using a sample holder dedicated to this purpose. In this way, no additional STEM detector for transmission is necessary, but the preparation of the particulate sample on electron transparent substrates, i.e., on TEM grids as typically for TEM. Further details on this instrumentation can be found in [87, 129]. This relatively new methodological approach complements the advantages of the two

different imaging modes for the same rasterized area on the sample: high surface sensitivity by *InLens*® and accurate in-depth and lateral dimensional information by TSEM.

Energy dispersive X-ray spectroscopy (EDX) has been performed with a large-area SDD EDS detector (Thermo Fisher Scientific) having a nominal area of 100 mm^2. This high-sensitivity EDX applied in combination with transmission arrangement of the samples for TSEM mode results in high-resolution EDX imaging well suited for qualitative elemental analysis of (nano)particles with a spatial resolution down to 10 nm.[135-136]

AFM measurements were performed on a closed-loop type AFM (Dimension 3100S, Digital Instruments/Veeco) in tapping mode imaging. The topometrical analysis was carried out with a Pointprobe-Plus (Nanosensors; Silicon, cantilever length 225 µm, resonance frequency 160 kHz, nominal tip radius of curvature 10 nm, tip cone angle 35°). The measured area (FOV) was (700 × 700) nm^2 with 512 (fast scan axis) × 256 data points. The analyzed area (field of analysis) was (330 × 330) nm^2 to limit the angular deviation of scan plane to values lower than the half-cone angle of the tip (17.5°) and to ensure inclusion of a statistically relevant number of SiO_2 NPs even for the largest size (SiO_2@PS-PVP360). The Marquardt-Levenberg fitting routine was used to perform the spherical fitting in Gwyddion. It shall be noted that the software is treating the data as a geometrical summation of all the 512 measured distances, in contrast to a true (x,y) area measurement, thus resulting in eq. VII (see above) that slightly differs from the respective equation in [133].

3.5.5 Responsibility assignment

The project was designed, planned and executed (including synthesis, experiments, data and image analysis) by Dominik Sarma unless otherwise stated. SEM/TSEM instrument was operated by S. Benemann (BAM, Div. 6.1). J. Mielke (BAM, Div. 6.1) developed the image analysis tool. AFM measurements and image analyses were performed by M. Sahre and supported by U. Beck (BAM, Div. 6.7).

4 Multifunctional Polystyrene Core–Silica Shell Microparticles

a bead-based platform with anti-fouling properties for multiplexed and quantitative detection of small molecules.

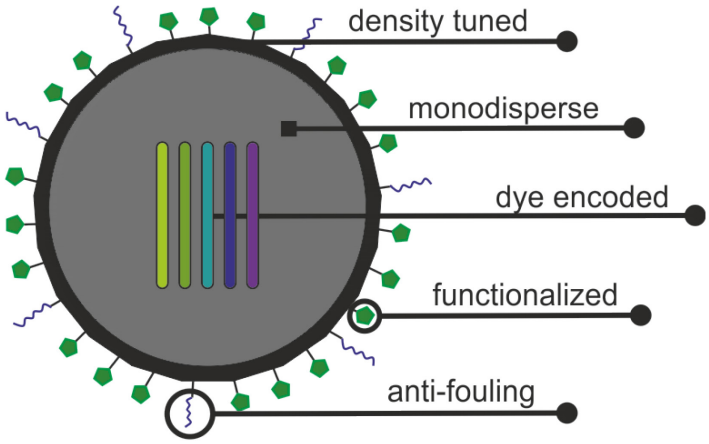

4.1 Abstract

A general requirement for spherical carriers in bead-based assays is the ability of dye-encoding. In this chapter, two different hydrophobic BODIPY dyes, a green light emitting dye and a red light emitting, were encapsulated inside the polystyrene spheres using a swelling method. The homogeneous and unperturbed growing of the SiO_2 shell allowed the formation of encoded CS particles with high monodispersity and convenient handling properties. 5-plex arrays were created using different dye concentrations with well-resolved signal patterns in cytometric read-out.

A subsequent modification of the silica shell with an equimolar APTES/PEG silane blend results in a modified surface with multifunctional properties. The APTES provides amine groups for the attachment of a caffeine derivative (hapten) to create antigen-coupled microspheres for the application in multiplex suspension array fluorescence immunoassay. The PEG moiety effectively suppresses the non-specific binding of antibodies on the surface. Based on these multifunctional properties, a highly selective assay for the detection of caffeine in beverages was developed.[137]

4.2 Introduction

The use of encoded spherical microparticles as the solid carrier in (bio)analytical cytometric assays is well-suited for the quantitative detection of multiple analytes with fast reaction kinetics and the handling of samples with low volume.[138-141] These features contributed to their increasing popularity in biomedical diagnostics and drug development, applications in which short assay processing times are essential and only limited amounts of sample material are available.[142] More recently, the immunochemical detection of small-molecule analytes for which the corresponding mono- or polyclonal antibodies are available became increasingly popular in food and environmental analysis with special focus on wastewater and agricultural samples.[143-145] Today, commercial bead-based platforms such as the Luminex xMAP® or the BD™ Cytometric Bead Array represent the most commonly employed systems for cytometric SAT. Here, the beads are provided in the form of functionalized and dye-encoded polystyrene (PS) particles with diameters of 5.5 and 7 µm.[146-147] The successful establishment of SAT led to other suppliers also offering encoded beads in various sizes for open platform integration in cytometric or fluorescence imaging formats, e.g., the Plex Red4 kit from PolyAn GmbH, Berlin, Germany or Quantumplex™ from Bangs Laboratories, Inc., Fishers, IN, USA. However, three major drawbacks using polystyrene carriers in multiplexed bead arrays can be identified.

(i) Beads of comparatively large sizes with diameters > 3 µm are required to guarantee acceptable processing times when using centrifugation during washing or functionalization steps.[39]

(ii) The encoding with organic dyes is limited to low- (number of parameters < 5) or medium-plex panels (number of parameters < 500), because dyes tend to aggregate at higher concentrations and/or if different dyes are used, their spectral overlap in typical detection windows precludes higher-order multiplexing.[148]

(iii) The beads often show a strong tendency for non-specific binding of biomacromolecules, potentially leading to low signal-to-noise (S/N) ratios or the generation of false-positive signals.[149]

Most of the published work on novel particle designs for cytometric applications focused on drawback (ii), i.e., they aim at an extension of the multiplexing capacity. For example, Gu, Xu et al. prepared a 100-code library based on a complex host-guest assembly approach to overcome spectral interferences from multiple dyes incorporated in the same domain.[66, 150] Lu et al. reported lifetime encoding and on-the-fly decoding in scanning cytometry.[151] Whether such an approach has a 'significant multiplexing capacity' despite the considerable computation time that the decoding of higher-plex lifetime encoded arrays would require, remains to be shown.

An alternative to organic fluorophores for encoding are quantum dots (QDs). These semiconductor nanocrystals possess advantageous fluorescence properties such as high quantum yields and narrow emission bands while being excitable in a broad spectral window.[152] Despite these promising features, the use of QDs is still waiting for a breakthrough. Recent research that promoted QD encoding stayed with tri-plexing, revealing no substantial benefit.[153] Besides fluorescence, other approaches such as Raman spectral encoding or graphically encoded microcarriers have been proposed to propel SAT beyond the current limit of 500 codes.[79] Whereas Raman encoding is still in its infancy, lithographic codes cannot be decoded with conventional flow cytometry.[154-156]

It is obvious that many attempts so far showed only moderate success to surpass the 500-codes limit. They will thus hardly replace well-plate formats or microarray technologies as the classical 'workhorses' in qualitative screening applications such as early drug discovery or genome-related screening (microRNA profiling, DNA sequencing). With respect to quantitative analysis, on the other hand, multiplexed systems are limited to the detection of a few analytes in parallel in either well-plate formats or microarray technologies, mainly because of cross- and shared reactivity issues.[157-158] Consequently, the strengths of many of the low- to medium-plex bead arrays proposed so far can perhaps be much better exploited in quantitative assays. This was the main reason to address aspects related to drawback (iii) in this work: non-specific binding.

Non-specific binding can be reduced by using additives such as polyvinyl alcohol or commercial blocking formulations when simple polystyrene beads are employed. However, further washing steps are required during assay processing.[149, 159] A more convenient route to suppress non-specific binding on beads is to endow their surface with antifouling properties. This can be achieved through the attachment of hydrophilic polyethylene glycol (PEG) or

zwitterionic moieties such as sulfobetaines.[160] However, because commercial beads usually express a single functional group on their surface, mostly an amino or a carboxylic acid group, multistep procedures, hetero-bifunctional linkers or partial functionalization routes are commonly needed for introducing a second (antifouling) function to the microparticles' surface.[161-163] In-situ formation of PEGylated polymer beads using PEG comonomers during polymerization has been reported in methodological articles, but their application features were not studied.[164] A straightforward, single-step and modular synthesis protocol to equip encoded beads with a bi- or multifunctional surface, offering functional groups for coupling and against fouling, is thus highly desirable.

This chapter uncovers how access to all these features is possible when polystyrene (PS) core/silica (SiO_2) shell (SiO_2@PS) particles are used. Such hybrids allow to combine the material's features of PS as a core and provide a defined silica shell for controlled post-modification using silane chemistry. APTES provides amino groups for the attachment of a caffeine hapten derivative to create antigen-coupled microspheres; PEGS introduces polyethylene glycol-moieties, endowing the surface with antifouling properties to suppress non-specific binding.

Surprisingly, published work on SiO_2@PS beads did not yet make full use of the chemical flexibility offered by a silica surface. Concerning the dedicated surface functionalization of encoded beads, for instance, Wu et al. prepared silica-coated melamine-formaldehyde resins for bead-based assays. They focused on the preparation of colored beads and functionalized the surface only with APTES as the single silane.[58, 60-61] Jun et al. used PS beads decorated with silver NPs that were encapsulated into a silica shell containing Raman reporter molecules for SERS encoding. Again, APTES was used as the sole silane for surface functionalization.[59] Also in the case of PS cores doped with QDs for SAT, Cao and co-workers only implemented a single functional group after encapsulation of the microparticle cores with a silica shell.[63] Based on the layer-by-layer approach to core/shell particles, Wilson et al. encoded PS beads with layers of QDs before assembling a final layer of SiO_2 NPs. This layer was also only modified with APTES.[62]

To elucidate the possibilities lying dormant with silica surface modification, expertise in SiO_2@PS particle design, mixed silane surfaces and dye-doped polymer particles were combined to develop APTES- and polyethylene glycol silane- (PEGS) expressing encoded beads that constitute the basis of a straightforward 5-plex array. [48, 64, 125, 165-166] The beads were

employed in an exemplary mix-&-read competitive immunoassay for the psychoactive compound caffeine (CAF). The determination of CAF in beverages such as energy drinks is under the legislation of the European Union.[167] Quantitative, fast and simple methods for the monitoring of CAF contents in such foodstuffs are thus required. Quantitative determination of CAF in beverages was realized, using a wash-free protocol with flow cytometry read-out with negligible non-specific binding due to the antifouling properties of the beads' silica surface.

4.3 Results and discussion

4.3.1 The core-shell (CS) platform

The hybrid CS particle architecture are ideally suited to build up composite systems that provide unique and novel features for multifunctional particles. The surface of a silica shell enables facile chemical tailoring with conventional silane chemistry.[42] The polymeric bead carrier defines the general properties (e.g., size, refractive index, and density) ideally required for handling and optical read-out as outlined in chapter 2. As core material, two batches of similarly sized monodisperse PS particles, obtained by dispersion polymerization with PVP40 as the stabilizer, were used. One batch (PS20-PVP40) was synthesized on a smaller scale, as described in section 3.5.2. The surface modification studies were performed with this batch. Since larger amounts of beads were required for encoding and immunoassay studies, the batch prepared in isopropanol was used (PS/IPro-PVP40, cf. section 2.5.2). TSEM overview images of both particles are shown in Figure 60.

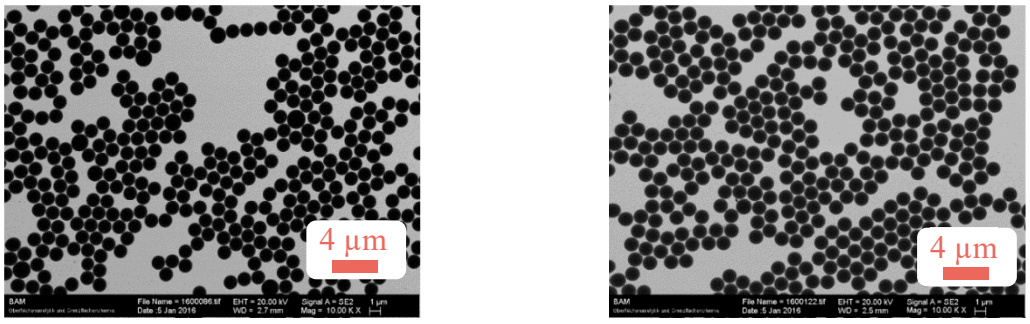

Figure 60. *TSEM images of PS/IPro-PVP40 (left) and PS20-PVP40 (right) in the same field of view (FOV).*

Both beads show diameters (*ecd*) of ca. 1.3 µm, possessing ideal sizes for bead-based applications (cf. Annex 6.8). To get additional information on the particle size distribution of the samples for the intended FACS application, cytometric measurements were run and the forward scatter (FSC) plots analyzed. Figure 61 shows that both particle batches are highly monodisperse with $c_v < 5$ %.

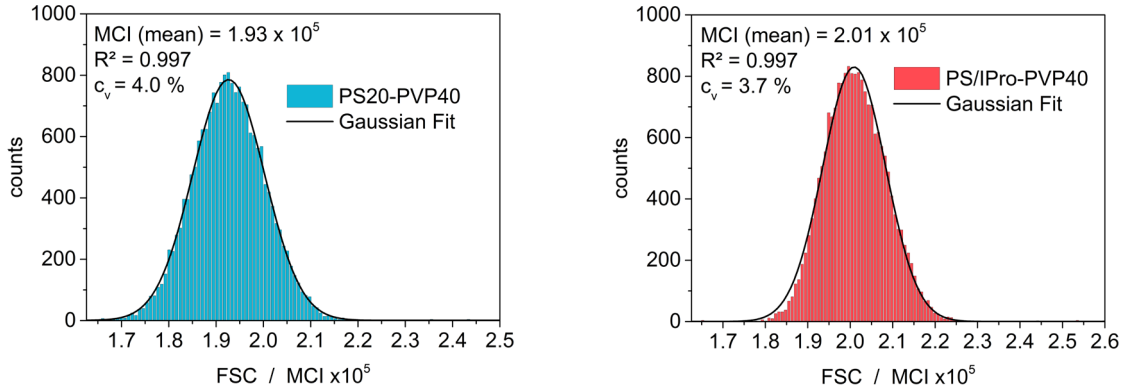

Figure 61. *Distribution plots and mean signal intensities from the gated cytometric signals in the forward scattering (FSC) channels, shown together with the Gaussian fit and corresponding c_v, for PS20-PVP40 (left) and PS/IPro-PVP40 (right).*

After silica-coating, both particles reveal the typical raspberry-like surface topology (cf. Figure 48 for PS20-PVP40 and Figure 25 for PS/IPro-PVP40). Characterization data of both plain and CS-particle batches are summarized in Table 16.

Table 16. *Characterization data (diameter as equivalent circular diameter, ecd; coefficient of variation, cv; surface area, A, and SiO_2 content in %) of representative particles used in this study.*

	PS20 -PVP40	PS/IPro -PVP40	SiO_2@PS20-PVP40	SiO_2@PS/IPro-PVP40
ecd / nm	1254.2[a]	1282.6[d]	1313.0[a]	1371.0[e]
c_v	2.2[a]	3.3[d]	2.5[a]	1.2[e]
$A_{C/CS}$ / µm²	4.95[b]	5.17[b]	9.53[c]	9.95
SiO_2 / wt.-%	–	–	n.d.	19.8

[a] cf. Table 11. [b] Surface area of plain beads was calculated assuming an ideal sphere model. [c] Surface area (A) was calculated using a factor of 1.92 (obtained from PS/IPro-PVP40 and SiO_2@ PS/IPro-PVP40 data) and multiplying with surface area of plain beads. [d]Annex 6.3. [e] Determined according to the method described in section 2.5.8.

An external surface area of for instance 9.95 µm² ± 0.98 µm² per particle was calculated for SiO_2@PS/Ipro-PVP40 by N_2 adsorption/desorption according to the t-method of Lippens and de Boer using the Harkins and Jura correlation as described in section 2.3.7. These values

exceed the theoretical surface area of an (ideal) PS sphere of similar size (e.g., 5.17 µm² for PS/IPro-PVP40) by a factor of ca. 1.9. This increase in the surface area reflects the formation of the raspberry-like shell structure. Assuming an equivalent surface increase for SiO_2@PS-PVP40 with similar shell structure, the surface area for this particle batch was estimated as 9.53 µm². Data from nitrogen adsorption and thermogravimetric analysis are shown in Figure 62.

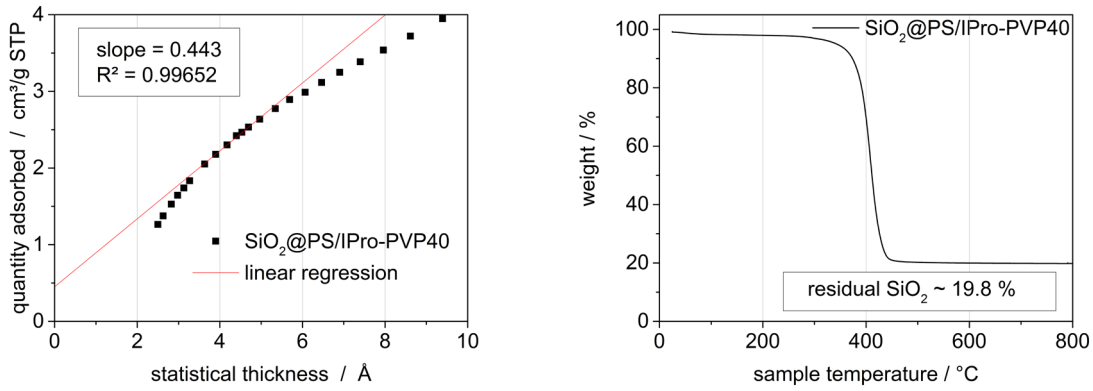

Figure 62. *Left – t-plot of the nitrogen adsorption isotherm of SiO_2@PS/IPro-PVP40 using Harkins and Jura correlation. Right – TGA curve for the combustion of CS particles SiO_2@ PS/IPro-PVP40 with a heating rate of 5K min^{-1} from 30°C to 800°C.*

4.3.2 Optical encoding of the polymeric core

An essential requirement for beads to be applicable in multiplexed cytometric assays is their encoding. There are numerous possibilities to integrate unique identification features such as physical parameters (size, refractive index, shape) or optical codes.[168-169] The latter commonly rely on fluorescence properties immanent to the embedded luminophores such as QDs, UC NPs or fluorescent dyes.[39, 79, 148] The optical code is used for identification of a specific type of bead equipped with a specific receptor unit or, as in this case, a specific analyte surrogate (hapten). The focus of this work lies on the possibility to simultaneously detect and quantify a comparably low number of analytes. This approach is most often sufficient in the monitoring of environmental compartments, agricultural processes or the production of foodstuff. Because key problems usually encountered when trying to use dyes for the generation of a larger library of codes such as spectral cross-talk or concentration quenching can be neglected here, simplicity led the way, i.e., steric loading of organic dyes into the core by swelling.[64, 170] Moreover, since bright and photostable BODIPY dyes are excellent candidates for such purposes and my

workgroup has long-standing experience with BODIPY dyes, two suitable dyes **1** and **2** were employed.[64, 171-174]

1 emits green and **2** red fluorescence that perfectly matches with the optical layout of the conventional benchtop cytometer used here. Figure 63 depicts exemplary fluorescence excitation and emission spectra of encoded polymer beads PS/IPro-PVP40 (initial dye concentration of 2×10^{-4} M).

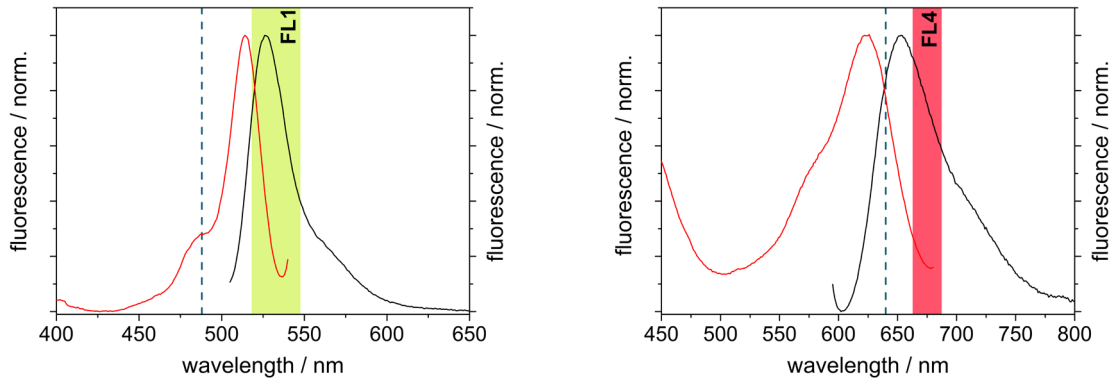

Figure 63. *Emission (black, λ_{ex} = 489 nm and 580 nm) and excitation (red, λ_{obs} = 550 nm and 700 nm) spectra for green (left) and red (right) encoded polymer particles containing dyes **1** and **2** (cf.* Scheme 3*). Vertical dashed lines denote the two laser wavelengths available in the cytometer, green and red areas the spectral windows of the bandpass filters in the fluorescence channels FL1 and FL4 used here.*

The use of **2**, a dye with a strongly solvatochromic emission, additionally provided insight into the polarity of the polystyrene matrix.[173] The emission maximum of 653 nm resembles closely that of **2** in diethyl ether, reflecting well the hydrophobic environment inside the PS core particles.

4.3.3 Optimizing the dye-encoding procedure

Suitable staining conditions were tested using three different particle concentrations (0.5%, 2.5%, and 5% (w/v)) in conjunction with three different total contents of THF, while initially fixing the dye concentration to 2×10^{-4} M using **2** as the dye. The one-to-one ratio of pre-swelling and swelling volume was maintained constant. Results are shown in Table 17.

Ideal homogeneous encapsulation, i.e., lowest $c_υ$ within one particle concentration run, were found for a pre-swelling with 65 µL THF (9% (v/v)) and a subsequent doping with the same amount of THF (total amount of THF is 16.7% (v/v)), regardless of the initial concentration of particles (see Index A03, A06 and A09). Looking at the signal intensities from A03, A06, and A09, a reduction in code fluorescence can be observed when using higher particle concentration, i.e., lower dye-to-particle ratios. Because MCI (mean channel intensity) values of 20,000–30,000 are still entirely sufficient for conventional flow cytometers, the highest particle concentrations (A09) was used to obtain as many beads with a minimum amount of dye.

Table 17. *Set of samples used for optimization of the swelling procedure, including the mean channel intensity (MCI) and $c_υ$ of the respective (gated) signal in the FL4 detector equipped with a 675/25 nm bandpass filter.*

Index	concentration / % (w/v)	THF / µL	FL4 / MCI	$c_υ$
A01	0.5	35/35	97,343.45	171.5
A02	0.5	50/50	161,521.58	30.1
A03	0.5	65/65	211,820.82	6.1
A04	2.5	35/35	27,091.84	23.8
A05	2.5	50/50	35,566.83	73.9
A06	2.5	65/65	46,819.04	13.1
A07	5	35/35	12,701.20	258.7
A08	5	50/50	17,208.52	117.3
A09	5	65/65	23,858.00	48.4

4.3.4 Creating a 5-plex array

After adaption of the dye-encoding procedure for PVP-stabilized PS cores, different concentrations of initial dye solution using green dye **1** (green; prefix ‘G’) and red dye **2** (red; prefix ‘R’) were employed to create five different codes (codes G1–G5 and codes R1–R5, using 4, 2, 1, 0.5, and 0.25×10^{-4} M dye stock solutions, respectively). The spectral properties of the encoded particles were investigated by fluorometry. The emission maximum of the green particles remained constant over all five concentrations, indicating unperturbed encapsulation

of **1** without aggregation or the occurrence of re-absorption effects (Figure 64, left). In the case of the red particles, only the batch doped with the highest concentration of **2** (code R1) showed a slightly red-shifted emission band, indicative of minor re-absorption effects due to the high loading of the dye in the polymer matrix (Figure 64, right). However, this effect is negligible for the aspired application and the entire set of beads was used in further steps.

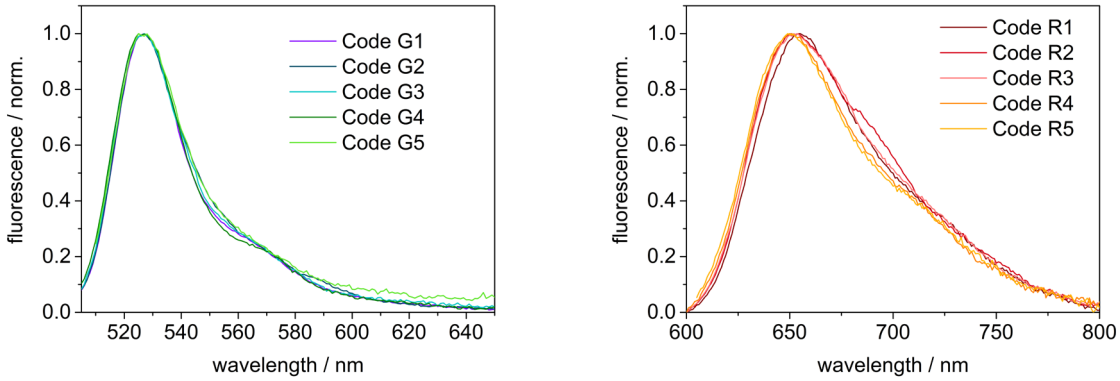

Figure 64. *Normalized emission spectra of doped particle dispersions in water with different concentrations of dyes* ***1*** *(green-encoded,* λ_{ex} *= 489 nm, left) and* ***2*** *(red-encoded,* λ_{ex} *= 580 nm, right).*

As Figure 65 shows, coating the doped PS core particles with silica has no detrimental effect and the green-encoded 5-plex CS particle array can be detected using flow cytometry. All particle populations can be well resolved in the fluorescence histogram plots (FL1-H and FL4-H) as well as in the correlation plot between FL1-H and FSC-H. For the red-encoded CS particles, slightly skewed profiles were observed with < 4% of the events having been counted in the neighboring gate to lower intensities (Figure 65c,d). Although population separation is slightly worse than for the green beads, > 95% of correct binning, i.e., decoding enables to use also the red beads for further studies.

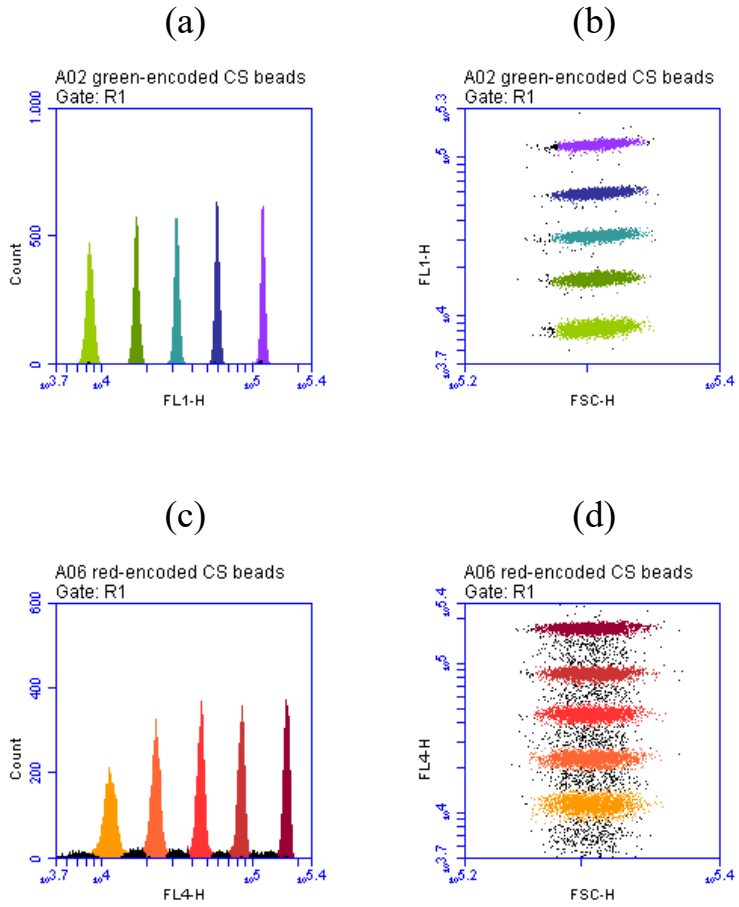

Figure 65. *Gated and colored histograms and scatter plots for functionalized green-encoded (a,b) and red-encoded (c,d) CS beads in the respective decoding channel. Note that the functionalized encoded beads (cf. subsequent section) yield virtually identical patterns.*

For both plex-sets, cross-talk between channels is negligible as evidenced by the only very low background fluorescence readings if, for instance, green-encoded beads were recorded in FL4-H and red-encoded beads in FL1-H (Figure 66). Although background signals up to ca. 1000 a.u. are measured, crosstalk is virtually absent because valid signals are always larger than ca. 7000 a.u., see panels a,c in Figure 65.

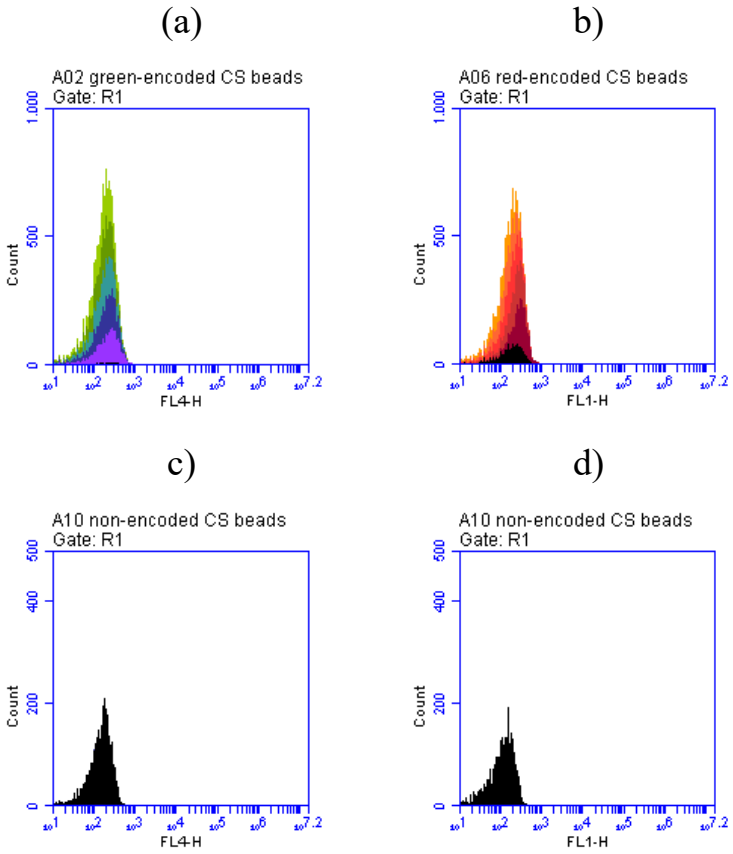

Figure 66. *Gated and colored (for color code, see* Figure 65*) histograms for functionalized green-encoded CS beads measured in the red detection channel (FL4-H, a), for the respective red-encoded CS beads measured in the green detection channel (FL1-H, b) and for non-encoded beads measured in green and red detection channels (c, d).*

Excitation and emission spectra were recorded for encoded polymer and SiO_2-coated CS beads (codes G2, R2) to assess in more detail whether the coating influences the fluorescence properties of the embedded dyes (Figure 67). The overall spectral characteristics such as bandwidth and major band shape do not change, indicating that the dye remains intact during the silica coating process with its highly alkaline conditions.

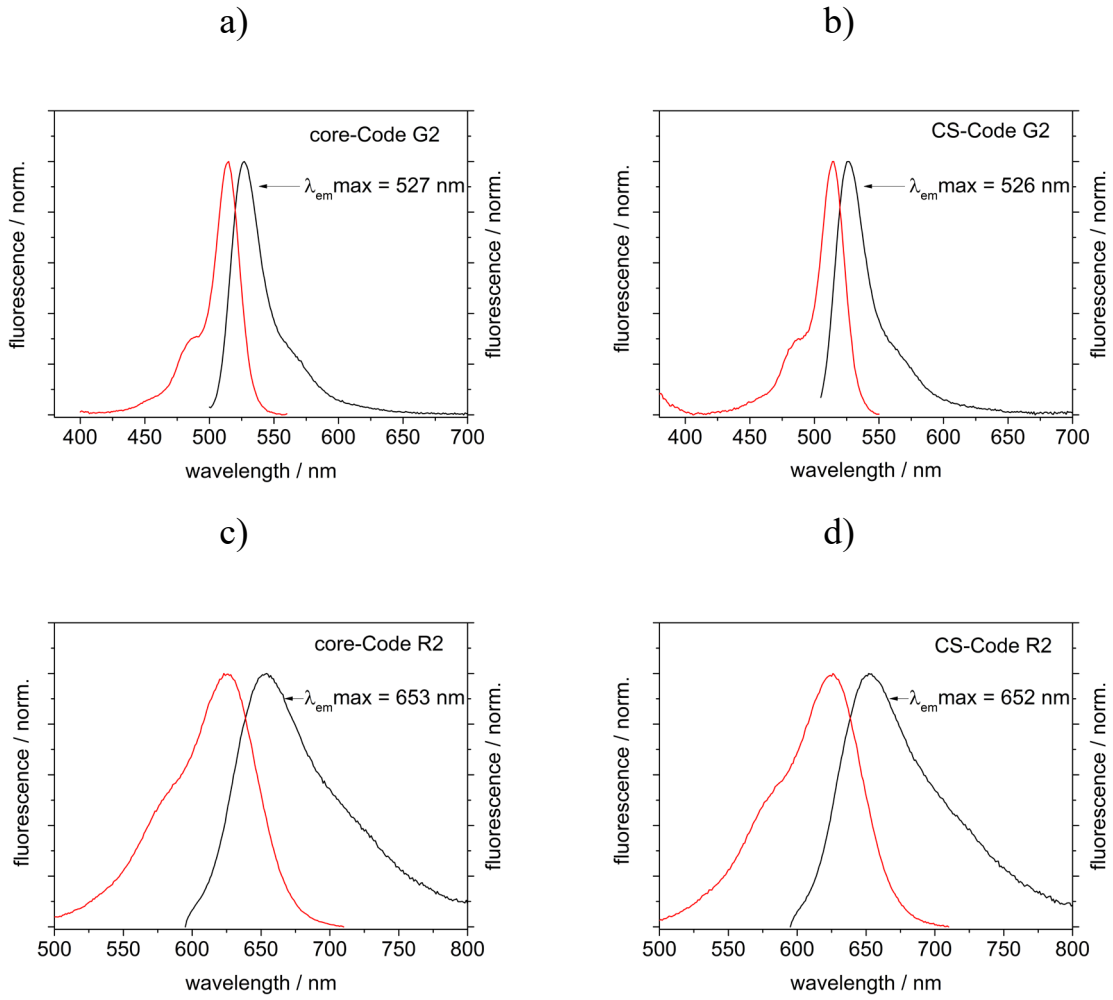

Figure 67. *Fluorescence spectra for G2/R2-core (before coating) and G2/R2-CS (after coating) particles. Excitation spectra were recorded with λ_{obs} = 570 nm (a) and λ_{obs} = 730 nm (c) and emission spectra were recorded with λ_{ex} = 489 nm (b) and λ_{ex} = 580 nm (d) for green and red encoded particles, respectively.*

The structural integrity of the CS particle 5-plex array was characterized by SEM. Particles of each plex-set were mixed, including also non-doped CS beads, and SEM images were recorded. Figure 68 reveals that there is no significant difference between the green and the red 5-plex nor within one 5-plex set. This proves that a SiO_2 shell can successfully be grown onto pristine as well as dye-encoded particles without perturbing their features.

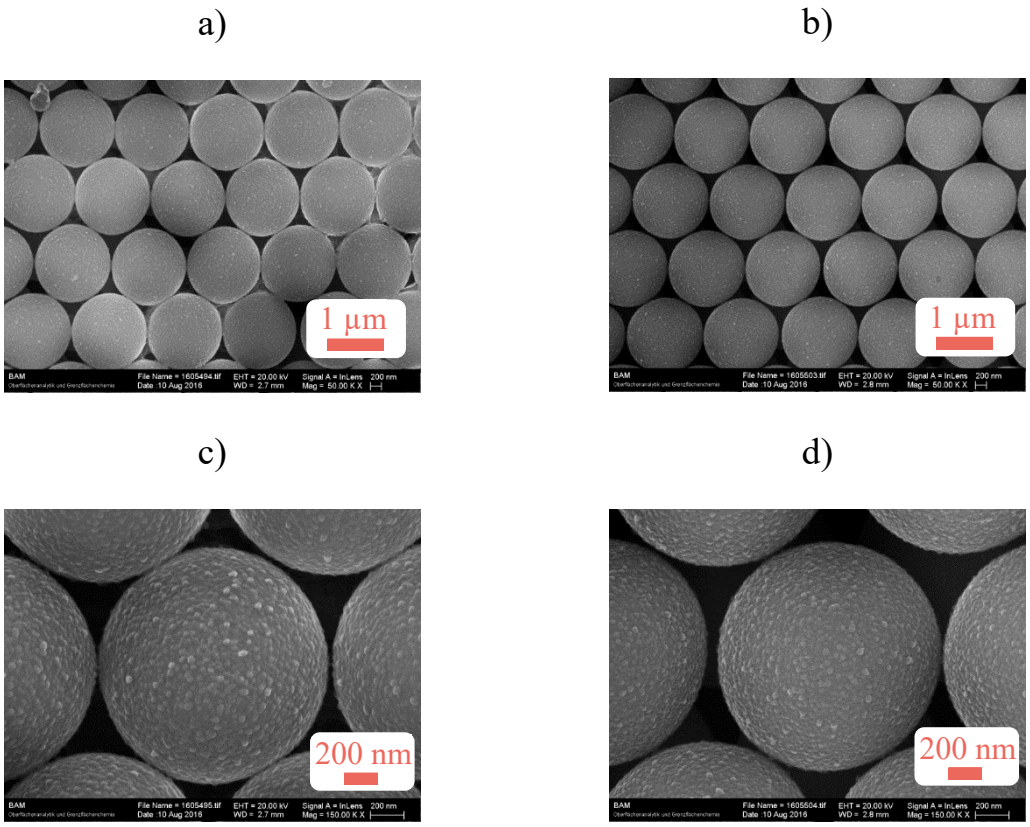

Figure 68. *SEM images of the green (a,c) and red (b,d) 5-plex array. All five coded particles were mixed together including non-coded spheres.*

4.3.5 Dual surface functionalization of CS beads and CAFH-coupling

To exploit the potential of a rational surface design of CS beads, mixed silane surfaces using equimolar blends of APTES and PEG silane (PEGS) were prepared. PEG is widely known to suppress non-specific binding of antibodies or other biomolecules because PEG moieties increase the hydrophilicity of flat or spherical surfaces.[175-176] In particular, APTES (unary surface as control, CS1) or an equimolar APTES/PEGS blend (binary surface, CS2) were simply added to pre-activated CS beads in different solvents for functionalization without any additional catalyst. CAFH coupling was performed similarly for both particles CS1 and CS2 in a subsequent step, yielding CS1-CAFH and CS2-CAFH (Figure 69). SiO_2@PS20-PVP40 beads were employed for the surface functionalization studies.

Because the PS cores are not cross-linked (this applies to all particle batches prepared for this thesis), special attention must be paid to the silanization medium. Hydrophobic organic solvents will swell or even dissolve the polymeric core. Functionalization reactions are thus limited to

either low MW alcohols or water as the solvent. Consequently, two sets of particles with unary and binary surfaces were prepared in water at room temperature, ethanol at room temperature and ethanol at 40°C (EtOH40) to identify the best suitable functionalization conditions. Pre-activation of the silica shell was carried out in a 9:1 methanol/HCl mixture, keeping the HCl content as low as possible to avoid etching of SiO_2.[177-178]

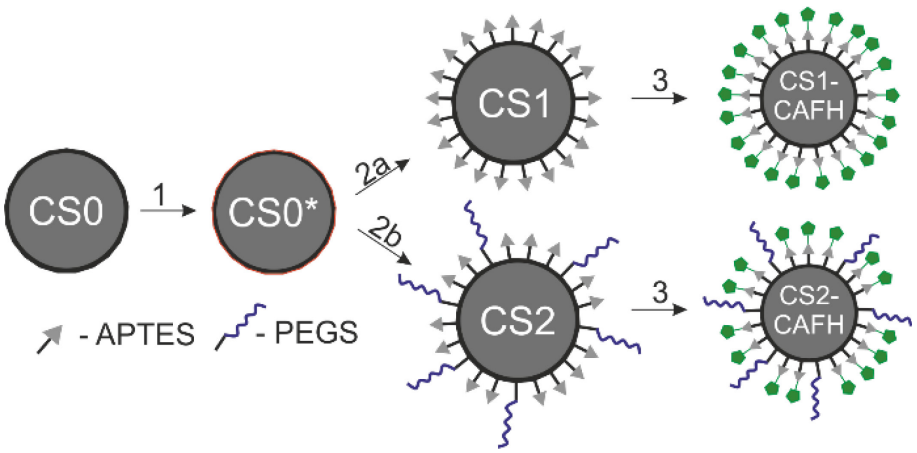

Figure 69. *Schematic representation of particle activation (1) in MeOH/HCl, functionalization with unary APTES only (2a) as well as binary APTES/PEGS blend (2b) and coupling of CAFH (3).*

Mixed surfaces on silica shelled particles have so far only been prepared on silica-encapsulated inorganic NPs (e.g., QDs and iron oxide NPs).[179-180] This approach to mixed APTES/PEGS silane layers on dye-encoded SiO_2@PS particles for application in cytometric assays is thus original. In this study, an equimolar ratio of APTES/PEGS was employed, because preliminary tests with varying ratios and mixtures of silanes (including other organo-silanes in ternary mixtures) showed no decisive influence on the antifouling properties. Future in-depth screening studies might lead to even better-tailored beads, but as is evident from the results presented in the subsequent sections, the equimolar mixture yields already highly potent objects.

4.3.6 Characterization of the mixed surfaces

All silane-functionalized particles possess positive zeta potentials, proving successful modification with APTES. In contrast, CS0 shows the characteristic negative zeta potential of a neat silica surface (Table 18, top row). The number of amino groups on the CS particles was

determined with a modified ninhydrin test (cf. section 2.5.5). Considering the calculated surface area of 9.53 µm² particle^{-1}, the amino group density was determined to ~11 APTES molecules per nm^2 for unary surfaces (Table 18, 2nd row, entries for CS1). Such densities are typically found on spherical substrates due to the ability for denser packing or the formation of silane multilayers.[113]

Table 18. *Zeta potential (ZP), amino content and density, anti-PEG-AB-binding and CAFH coupling efficiency for unary (CS1) and binary (CS2) functionalized particles using EtOH at 40°C, EtOH and pure water as reaction medium.*

	CS0	CS1-			CS2-		
		EtOH40	EtOH	Water	EtOH40	EtOH	Water
ZP / mV	–28.6 ± 4.0	7.7 ± 0.8	10.4 ± 0.7	13.9 ± 0.5	10.1 ± 0.5	9.5 ± 0.9	8.5 ± 1.2
NH_2 / nm^{-2} [a]	– [b]	11.5	10.5	12.1	9.4	8.5	12.9
NH_2 / mmol g^{-1}	– [b]	0.132	0.120	0.139	0.108	0.098	0.148
MCI / FL1 [c]	4183 ± 942	n.d.	1654 ± 74	604 ± 43	n.d.	101769 ± 2717	98707 ± 2831
CAFH-coupl. / % [d]	–	n.d.	90	87	n.d.	90	78

[a] Ninhydrin test with a rel. uncertainty ±7 %. [b] Below LOD, ref [48]. [c] Anti-PEG-AB. [d] Indirect Ninhydrin test.

The difference with respect to the amino group densities of a batch prepared in the same way and presented in section 2.5.4, ~6 functional groups per nm² could not be satisfactorily resolved during the time frame of this thesis. The most probable explanation seems to be that the ninhydrin test is less tolerant of environmental conditions than the literature suggests.[113] An overview including the results from chapter 2 and one intermediate result from an initial experiment for this study clearly show this trend (Table 19). Hence, analysis and comparison of data points is rational only when the measurements were conducted on the same day.

Table 19. *Overview of APTES-modified particles (SiO_2@PS-PVP40) and corresponding amino group density determined with the ninhydrin method.*

	13.08.2014	15.02.2016	12.07.2016
$-NH_2$ / nm² particle^{-1}	6.3	8.9	11.5
calibration function	y = -0.018 + 0.428x	y = -0.012 + 0.356x	y = -0.012 + 0.405x
R^2	0.9938	0.9799	0.9827

For binary surfaces prepared in ethanol, the total amino content per g of particles determined with the ninhydrin test is 22% lower compared to the unary surfaces (Table 18, 3rd row, entries "EtOH40" and "EtOH" for CS2). For functionalization in water, the number of amino groups is even slightly higher for binary surfaces (Table 18, 2nd/3rd row, last column).

The quantitation of PEG on particle surfaces is challenging, especially when hybrid microparticles are under study.[181] This is why a qualitative assessment of successful PEG grafting to the particles using an anti-PEG-AB in an indirect immunochemical test was opted for. Remarkably, the primary antibody (pAB) bound to the rather short PEG chains immobilized on a hard sphere, rendering this method suitable for comparative assessment of grafting ratios. The assay results indicate that almost the same number of PEG groups are present on particles prepared in ethanol and water. This can be seen in Table 18, 4th row and in the very similar titration curves of the anti-PEG-AB with CS1 and CS2 particles prepared in either EtOH or water (Figure 70).

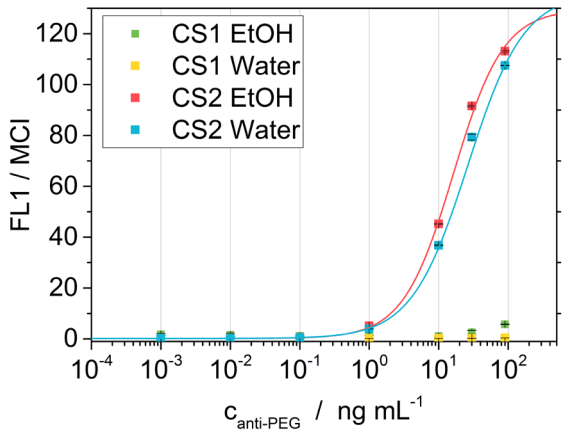

Figure 70. *Titration curve of the anti-PEG-AB with unary (CS1) and binary (CS2) functionalized particles using EtOH and pure water as reaction medium.*

Subsequent CAFH grafting to both types of particles, i.e., those with single- and mixed-silane surfaces, yields comparably high conversion rates of amino groups, with coupling efficiencies between 78% and 90% (Table 18, bottom row). An indirect approach was chosen here, i.e., determination of the difference in amino group content prior to and after the reaction of the beads with CAFH by ninhydrin tests as described above. Note that due to the qualitative examination of data derived from the Ninhydrin test, an actual amount of CAFH cannot be deduced.

4.3.7 Inhibition of nonspecific binding using mixed silane layers

The effect of PEGS and/or APTES present on the surface of the CS1/CS2 particles and their influence on the non-specific binding of non-targeted antibodies was evaluated in a fit-for-purpose experiment. Therefore, a general model system was established: Positive and negative controls were carried out in a direct and indirect fashion for CAF-coupled particles and non-functionalized CS particles in cytometric immunoassays. The signals were detected after mixing the beads with a corresponding dye-labeled anti-CAF-AB (anti-caffeine antibody; direct) or anti-CAF-AB and dye-labeled sAB (secondary antibody; indirect). No washing steps were included because a mix-&-read assay was envisaged. Negative control responses were tested toward dye-labeled anti-BSA-AB (direct-negative) as well as with polyclonal bovine-IgG together with dye-labeled sAB (indirect-negative).

In Figure 71 (left), the four different immunochemical reactions are assigned to color codes and the signal responses in the green channel FL1 are plotted in the lower part (for intensities, see Table 20). Note, that the antibodies used here differ in clonality (mono- and polyclonal—anti-CAF-AB vs. anti-BSA-AB) as well as in their origin (mouse and bovine—anti-CAF-AB vs. bovine-IgG), to represent different classes of antibodies which are commonly used in immunoassays. The results are shown in Figure 71 (right).

First, the control particles (CS0) with a neat silica surface show only weak signals in the direct and the indirect test, which proves the absence of non-specific binding on native CS beads with an unmodified silica surface. The highest background signal of the CS0 series (indirect-negative test), plus ten times the standard deviation of triplicate runs, was used as a threshold for false-positive signals in the other cases. Thus, signals from samples whose negative control exceeded an MCI of 962 (indicated as dashed red line) were classified as false-positive. To investigate the effect of silane functionalization on the non-specific binding, particles without CAFH

modification were also tested. All responses are clearly below the false-positive benchmark, indicating that the zeta potential and therefore electrostatic interactions should have a minor influence on non-specific binding (cf. Table 18, top row and Table 20, entries 2-5).

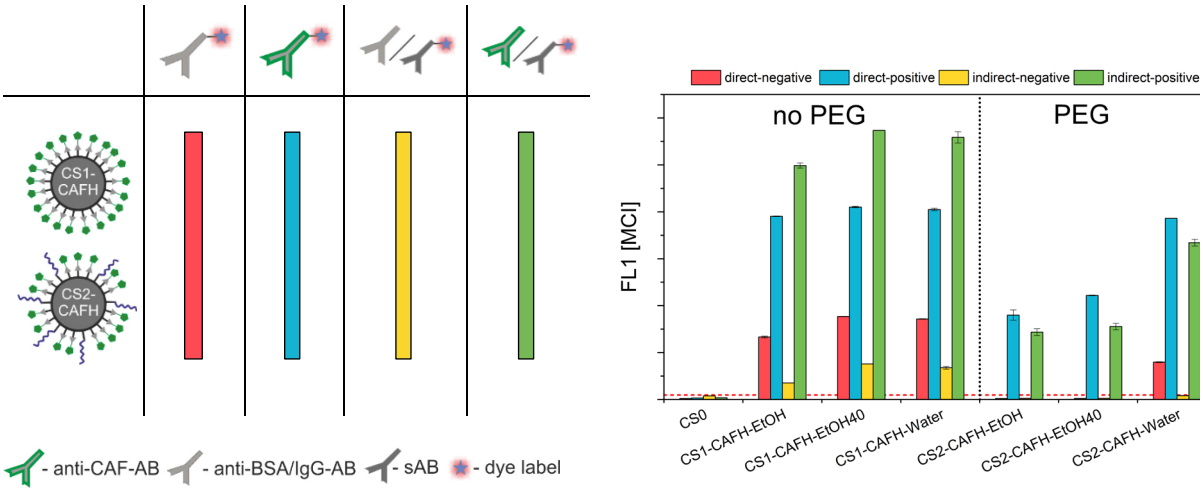

Figure 71. *Left – Color code for the four different immunochemical reactions. Right – Cytometric assay results for CS0 as well as CS1 and CS2 after functionalization under different reaction conditions. The signal was recorded in FL1 and the standard deviations were obtained from triplicate measurements.*

CS1-CAFH beads with unary surfaces in contrast, regardless of the functionalization conditions used, resulted in false-positive readings as well as high signal responses towards the respective pAB (anti-CAF-AB, anti-BSA-AB or bovine-IgG) for direct and indirect assays. The lowest false-positive signal (indirect negative, CS1-CAFH-EtOH) is still significantly higher than the background threshold. All other negative controls exceeded this value. Paired *t*-test analysis was used as a statistical hypothesis test and yielded a *t*-score $|t_{calc}| = 45.6$ and a probability $p = 1.4 \times 10^{-6}$ for 4 degrees of freedom, DF. The coupling of caffeine obviously leads to binding of the designated pAB, whether labeled or not. For non-labeled pAB, tandem binding of sAB occurs readily as well. For both scenarios, non-specific binding of non-targeted pABs is also considerably high (yellow and red bars in Figure 71, left panel “no PEG”). These data indicate that functionalization with CAFH is responsible for non-specific binding, presumably due to the general reduction in polarity and hydrophilicity of the beads’ surfaces when going from an APTES to a predominantly CAFH-coated surface.

Table 20. *Assay performance of the beads are given in MCI (FL1) from positive and negative assays for unary APTES only (CS1) and binary APTES/PEG (CS2) functionalized particles using EtOH at 40°C, EtOH and pure water as the reaction medium.*

		direct signaling		indirect signaling	
		negative	positive	negative	positive
1	CS0	213.8 ± 5.7	214.7 ± 6.1	776.9 ± 18.5	368.2 ± 30.9
2	CS1-EtOH	136.7 ± 2.1	139.7 ± 2.3	175.7 ± 2.1	242.0 ± 11.3
3	CS1-Water	144.7 ± 1.5	142.3 ± 0.6	189.3 ± 2.5	239.0 ± 3.5
4	CS2-EtOH	135.7 ± 2.3	136.7 ± 0.6	170.7 ± 5.9	240.7 ±7.5
5	CS2-Water	142.0 ± 8.0	149.0 ± 10.5	177.3 ± 2.1	243.7 ± 2.1
6	CS1-CAFH-EtOH40	17688.8 ± 46.3	41032.6 ± 169.2	7568.1 ± 34.6	57353.6 ± 13.1
7	CS1-CAFH - EtOH	13319.9 ± 92.6	39044.9 ± 76.6	3522.7 ± 14.7	49858.1 ± 542.0
8	CS1-CAFH - Water	17151.1 ± 66.2	40495.9 ± 275.0	6749.6 ± 309.7	55866.4 ± 1206.2
9	CS2-CAFH - EtOH40	214.0 ± 37.0	17987.0 ± 1090.1	243.2 ± 1.8	14344.7 ± 740.8
10	CS2-CAFH - EtOH	225.1 ± 7.0	22173.1 ± 69.8	252.4 ± 10.4	15555.6 ± 701.9
11	CS2-Water	7956.1 ± 93.7	38605.6 ± 7.1	821.8 ± 3.2	33439.2 ± 717.4

The positive effect of PEGS can be deduced from binary CS2-CAFH beads functionalized in ethanol. Non-specific binding, i.e., weak to none false-positive signals, was virtually absent for both, the direct and the indirect test (yellow and red bars in Figure 71, right panel "PEG"). The highest signal observed for negative controls (indirect negative, CS2-CAFH-EtOH40) was even significantly lower than the indirect negative test for neat silica surfaces, CS0 ($|t_{calc}| = 18.3$, $p = 5.2 \times 10^{-5}$, DF = 4). This indicates that the suppression on non-specific interactions is distinctly higher for CS2-CAFH than for neat silica (CS0) and unary APTES-functionalized CS1-CAFH particles, the different CS1-CAFH showing signals above the pre-assigned threshold**.** Positive tests with 60- to 90-times higher signal intensities compared to the corresponding negative controls were found when the particles were functionalized in ethanol (Table 20, lines 9 and 10).

When functionalization of CS2 beads was carried out in water (Table 20, line 11), the presence of PEG still suppresses non-specific binding in the indirect assay, yet the signal gain is lower (only ca. 40-fold) and a number of false-positive responses were registered in the direct assay. This indicates worse selectivity against non-targeted polyclonal anti-BSA-AB. This finding is remarkable since the PEG content of these particles is comparable to that of the particles prepared in ethanol.

The adsorption behavior of APTES on silica surfaces might provide an explanation here. In aqueous solutions, as for CS1/C2-Water, APTES tends to form monolayers due to the electrostatic interaction between protonated amino groups and the negatively charged silanol-expressing surface.[182] Thus, shielding of the surface will perhaps prevent condensation of a less reactive second silane such as PEGS in the direct vicinity of the amino groups. Moreover, partial protonation of the amino groups in water would suppress their catalytic effect on the condensation of neighboring silanes. Instead, PEGS might preferentially condense at additional multilayer sites or in islands, leaving the total number of amino groups largely unchanged. As a result, the PEG chains might not be distributed homogeneously to evenly unfold their antifouling properties on the surface. On the other hand, for the CS particles functionalized in ethanol, the results show that non-specific binding is suppressed. A more homogeneous mixture through APTES-catalyzed condensation of PEGS as proposed by Blitz et al. might be the reason here.[110] Surface-bound APTES leads to the condensation of organo-silanes in its proximity to form more homogeneous mixed silane layers.[110] In this case, PEG chains are evenly distributed within the silane layer—which is supported by the lower amount of APTES found on CS2 beads prepared in ethanol.

4.3.8 Encoded CS particles with dual surface functionalization.

Ultimately, the best performing functionalization protocol, relying on ethanol, was adopted for the 5-plex bead set using SiO_2@PS/IPro-PVP40 to prepare multifunctional particles with a color code and functional groups for coupling and antifouling properties. It is worth mentioning that modifications of commercially available dye-encoded beads in ethanol would result in significant dye loss and destruction of the optical code. This would strongly limit the possibilities for chemical surface modification, because only reactions that can be conducted in neat aqueous media could be applied for the commercial beads.

To assess the robustness of the title beads, dye leakage was tracked over the course of coating, functionalization and hapten coupling along the optimized route with ethanol at room temperature (Figure 72a).

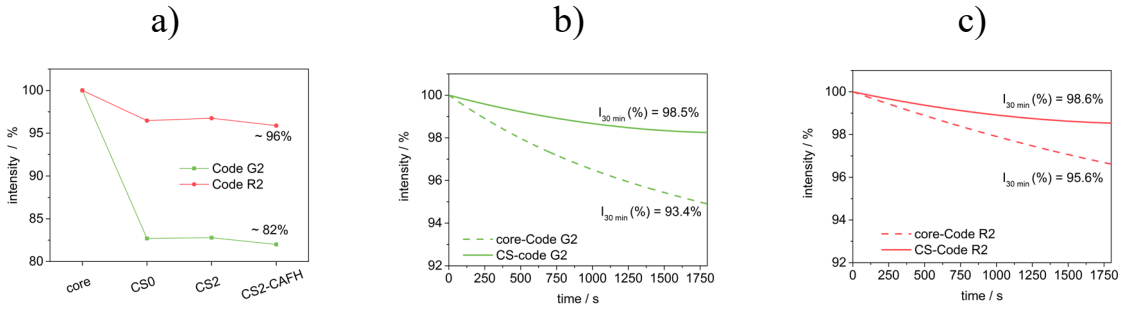

Figure 72. *a) Signal intensity (mean, FL1-H for green and FL4-H for red codes) over the course of bead preparation. Dye stability of green (b) and red (c) codes upon excitation with a Xenon lamp (green code: λ_{ex} = 489 nm, λ_{em} = 525 nm, bandpass 3.5 nm; red code: λ_{ex} = 580 nm, λ_{em} = 650 nm, bandpass 6.5 nm) in the fluorescence spectrometer for 30 minutes (1s intervals) for G2/R2 polymer and CS particles. Smoothed data are plotted in b) and c) to visualize signal decrease over time.*

A significant dye loss is only observed in the coating step, and the fluorescence code remains surprisingly stable during subsequent functionalization and hapten coupling steps in ethanol. The loss is therefore ascribed to hydrophobic TEOS acting as a swelling agent for the beads before its hydrolysis and the formation of the silica shell. This was confirmed by using a higher amount of TEOS (450 mM instead of 135 mM) during the coating of green-encoded beads, which led to a significant loss of dye/fluorescence intensity of ca. 98%. It is also important to note that storage of beads in ethanol for > 220 d led to only minor signal losses and still allowed for unequivocal resolution of the 5-plex in both cases, emphasizing the outstanding stability of the particles.

The photostability of codes G2 and R2 was also exemplarily investigated by tracking the fluorescence over time upon irradiation at 489 nm and 580 nm for green- and red-encoded beads (Figure 72b,c). A stabilizing effect of the silica shell was observed which is ascribed to limited diffusion of oxygen into the beads, avoiding photo-oxidation.[75]

4.3.9 Feasibility study: assay design

The working principle of the bead-based immunoassay devised here is shown in Figure 73. It is a simple mix-&-read procedure based on CS beads and cytometric read-out.

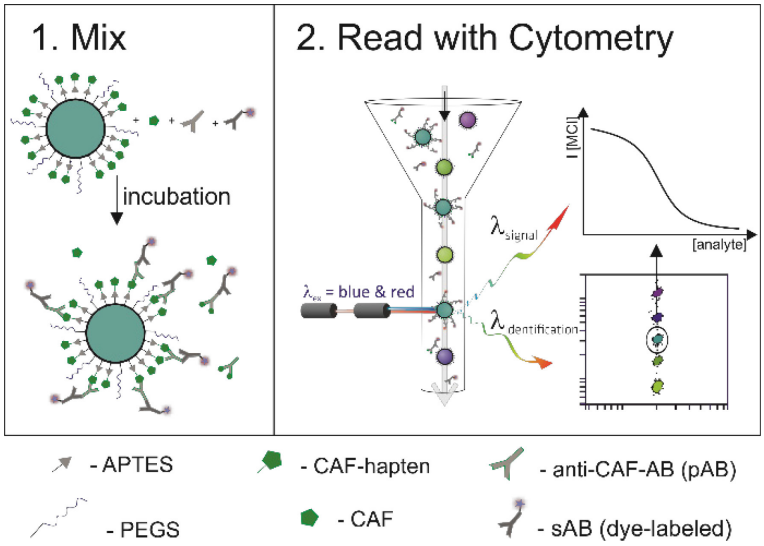

Figure 73. *Principle of the CS particle-based assay using dye-encoded microbeads and indirect signal generation. 1. Mixing and incubation. 2. Reading and bead decoding by flow cytometry.*

The signal is generated on one particle (shown in bluish-green) in a mixture of differently encoded beads. Because each of the differently encoded beads can be associated with a specific immunoassay, the approach shall be perfectly suitable for multiplexing and the simultaneous detection of different small molecule analytes. This approach is a combination of the suspension array technology (SAT) and a fluorescence immunoassay (FIA). It is a simple, wash-free and potentially multiplexable immunochemical test.

The signal generation relies on a competitive reaction between CAFH-bearing CS beads and the analyte present in the sample for the respective pAB. Because the indirect assay format was applied, a dye-labeled sAB is added which binds to the pAB on the beads. All reagents are mixed in one compartment without additional washing steps and result in a competitive assay response. Using flow cytometry for signal read-out, bead-correlated fluorescence can be intrinsically discriminated from the background signal, i.e., from unbound labeled sAB. In this way, the analytical response can be detected without washing because non-specific binding of

proteins such as primary or detection antibodies on the designed bead surface carrying APTES/PEGS is efficiently suppressed.

4.3.10 Feasibility study: caffeine detection in beverages

Assay performance was tested with caffeine as a model analyte. First, a calibration curve was generated from the plex-set, mixing CAF-conjugated CS2 particles (G3, R3) together with the four other non-conjugated CS particles. Eight fixed concentrations of CAF were then added together with pAB in triplicates. The signal response in detection channels FL1/FL4, stemming from the equivalent number of bound sABs, was recorded after incubation without washing. Figure 74 shows a representative data set generated by gating on the G3/R3 bead population.

All signal responses remained below the 10σ threshold for non-labeled beads, i.e., codes G1, G2, G4, and G5. Non-specific binding is thus absent also within a mixture of all five encoded beads (Figure 74b). The residual black signal at higher intensities in Figure 74b was tentatively attributed to aggregates which are not inside the gate R1. These data will therefore not be considered in the subsequent analysis as can be seen in Figure 74c.

A logistic fit function ($R^2 = 0.998$) was used for analysis of the dose-response data (Figure 75, left). Working ranges (EC20–EC80) of 1.2–9.3 and 1.8–24 µg L^{-1} were determined for green- and red-encoded particles, respectively (Table 21). These are well suitable for the detection of caffeine at low concentrations, for example in beverages.

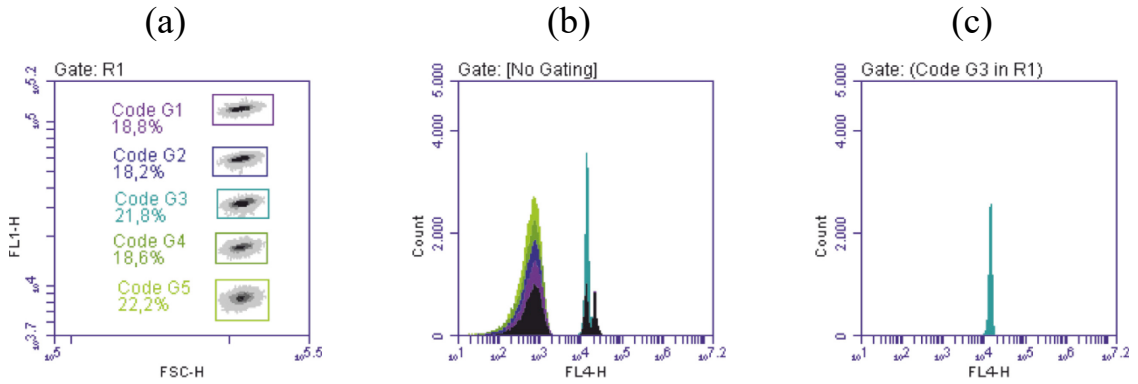

Figure 74. *a) Color gates in the FSC-H vs. FL1-H scatter plot (R1 gated); b) and c) – Ungated and gated FL4-H detection channel readings for the lowest concentration of caffeine in the calibration measurement. The mean signal intensity from the gated plot (c) was used as signal response of CS2 beads in the competitive assay.*

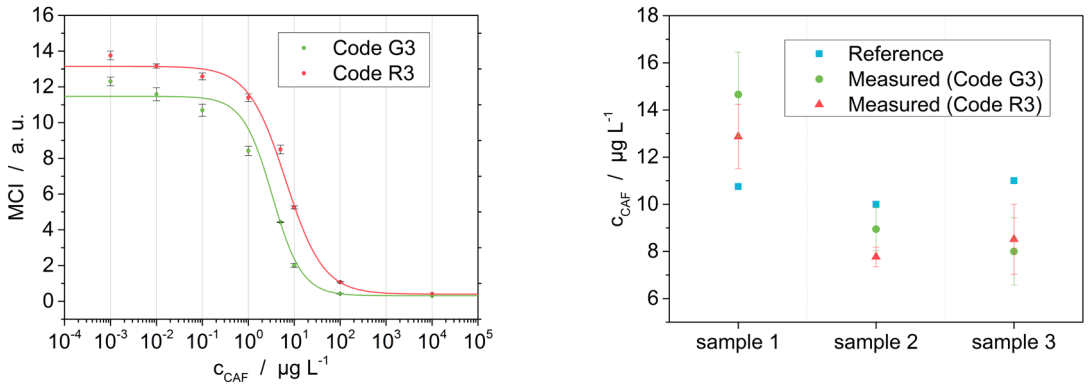

Figure 75. *Left - Calibration curve using a logistic fit function for analysis. Right - CAF detection in 5-plex array with codes G3 and R3 in beverages (dilution factor: 1:20.000) with reference value shown in yellow.*

As a proof of concept for a wash-free detection of small molecules in real samples, the content of CAF was measured in three different beverages (sample 1–Maya Mate, sample 2–Club Mate and sample 3–Club Mate IceTea). The assay was performed without washing steps after a 1:20,000 dilution of the beverage in Milli-Q water and the results are shown in Figure 75 (right). The data presented in Table 21 show that the CAF content could be determined with a mean recovery rate of 98 ± 31 %, spanning from 68–146 %, which is good for a simple, wash-free assay. Typically, SAT-based immunoassays yield recovery rates between 70–130 %.[183-185] Most likely, fine-tuning of the incubation time, antibody concentrations and buffer composition, hence classical immunoassay optimization loops, can further improve the assay performance of this format.

Table 21. *Data (EC20, EC50 and EC80) obtained from logistic fitting of dose-response data and recovery rate (RR) for the detection of CAF in beverages.*

	EC20	EC50	EC80	$RR_{sample\ 1}$ / %	$RR_{sample\ 2}$ / %	$RR_{sample\ 3}$ / %
Code R3	1.2 ± 0.2	3.3 ± 0.3	9.3 ± 0.8	120 ± 13	78 ± 4	68 ± 9
Code G3	1.8 ± 0.3	6.5 ± 0.5	24.1 ± 1.8	146 ± 21	90 ± 9	73 ± 3

A factor which can influence the analytical result in wash-free assays is the incubation time associated with the detection delay when automated sample injection is utilized, for instance, from a 96-well plate as the multiple sample reservoir. In this model assay, a gradual increase of the signal response was indeed observed throughout the experiments, probably due to adsorption of sAB to the surface with progressing time or a non-equilibrium state. This effect can also be seen in the low-concentration response (Figure 75, left) where the signal does not reach saturation. Such kinetically induced shifts can be overcome using step-by-step sampling and measurement of each data point.

4.3.11 Feasibility study: multiplexed detection using CS bead-arrays

To examine the full potential for multiplexed testing, a 4-plex array was developed for the simultaneous mix-and-read detection and quantification of caffeine (CAF), isolithocholic acid (ILA), carbamazepine (CBZ) and diclofenac (DCF) in wastewater (Figure 76).

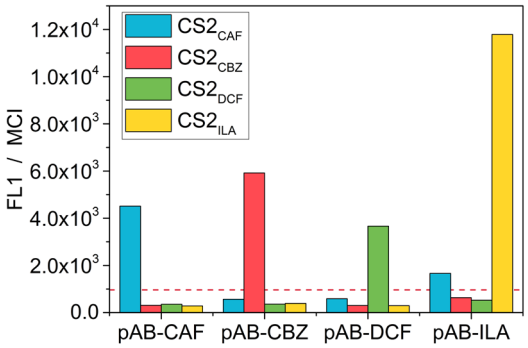

Figure 76. *CS2 red-encoded beads coupled with different haptens for multiplexed detection of anthropogenic markers in wastewater.*

All pABs bind specifically to the respective hapten-coupled CS bead, proving that the prepared particles are ideal candidates for an immunochemical multiplex assay. A threshold was set using 10σ above the highest background signal. Only for CAF-coupled beads, a slightly increased signal was found with anti-ILA-AB. Because the polyclonal pAB was employed directly from sera, reduction of this false-positive can be most likely achieved with monoclonal and purified AB.

4.4 Conclusion

Rationally designed CS particles were successfully employed in the immunochemical detection of a low molecular weight analyte molecule, using competitive binding of analyte and hapten-coupled microparticles to a primary antibody. The analytical signal was generated with a labeled secondary antibody and detected using a benchtop cytometer.

The CS particles as solid supports have ideal material properties for cytometric detection and signal read-out. At the same time, the core acts as a matrix for encoding by doping with fluorescent dyes. Here, BODIPY dyes with different spectral properties were introduced to create 5 different optical codes each in the green and red detection channel. The polymeric core is thus fully compatible with classical encoding strategies while it still allows for an unperturbed growth of a silica shell on these dyed cores. Because of the versatility of BODIPY chemistry,[186] flexible color tuning can be realized in a straightforward manner.

The silica shell then adds unique benefit to the system because the surface can be precisely tuned using silane chemistry. In this study, simple silane blends with an equimolar ratio of APTES and PEGS were employed in an optimized functionalization procedure to prepare amino-functionalized mixed surfaces with antifouling properties. It was found, that functionalization in ethanol gave superior performance over water. The procedure is a simple one-step co-condensation of an equimolar silane blend without requiring an additional catalyst. The presence of PEGS significantly reduced non-specific binding to the particles, facilitating quantification of the model analyte caffeine in a wash-free procedure.

Remarkably, only the stable encapsulation of dyes in CS particles which resist subsequent treatments and post-modification in ethanol solutions allowed to adopt the optimized protocol. Commercially available polymeric beads usually suffer from dye leaching when the particles are handled in ethanol. In future, other silanes could be tested in blends with APTES to tailor chemical or physical properties such as adhesion, biocompatibility, charge, hydrophilicity/hydrophobicity of the particles or introduce multiple functionalities on the surface.

This study shows the tremendous potential that resides with the solid support itself when using robust, easy-to-prepare hybrid particles consisting of polymeric cores with silica shells. Another major difference in this system to commercial platforms is the size. The CS particles with approximately 1.3 µm circular diameter are rather small in comparison to conventional beads

with usually more than 3 µm. Nonetheless, their performance in a prototype assay was readily acceptable. Whereas for plain polystyrene beads of this size, particle handling would be cumbersome due to slow sedimentation speed, the title beads allowed for straightforward handling. Fast pelleting times (< 2 min at 6.000 rpm) for washing and slow sedimentation for automated sampling (up to 2 h) are enabled due to the increased density of the hybrid material. Additionally, if using the same mass concentration, approximately 75-times more particles are present in the reaction chamber which results in either less sample consumption to acquire the same number of beads or gives access to higher statistical numbers.

A first feasibility study for the detection of four anthropogenic wastewater markers showed high specificity of the bead array, proving its potential as a modular platform for the multiplexed analysis of real samples. This potential could already be exploited in a subsequent study, where an optimized multiplex assay towards CBZ, ILA, CAF, and DCF was successfully applied in real wastewater samples from Berlin.

4.5 Experimental

4.5.1 Materials

Poly(vinylpyrrolidone) (PVP40 with ~40 kDa, Sigma), styrene (ReagentPlus, <99%, Sigma) basic alumina (Al_2O_3, Brockmann I, Acros) and 4,4'-azobis(4-cyanovaleric acid) (ACVA, MP Biomedicals) were used for the PVP-coated polystyrene core synthesis. Ammonium hydroxide (32% in water, Merck) and tetraethylorthosilicate (TEOS, >99%, Merck) were used for the silica coating and hydrochloric acid (HCl, 37%, Merck), fluorescein isothiocyanate isomer I (FITC, ≥90%, Sigma), aminopropyltriethoxysilane (APTES, 97%, ABCR), PEG silane (PEGS, 2-[(methoxy(polyethyleneoxy)$_{6–9}$propyl]trimethoxysilane with 6–9 PE units, CAS 65994-07-2, 90%, ABCR) and succinic anhydride (97%, Sigma) were used for surface modification. Acetate buffer (0.02 M, pH 5.0) was used for zeta potential measurements. Tris-buffered saline (TBS; 10 mM tris(hydroxymethyl)aminomethane, 150 mM NaCl, pH = 8.5) was employed in all immunochemical assays as reaction medium. Methanol (Alfa Aesar, Germany), ethanol (abs. 99% and 96%, ChemSolute), isopropanol (Extra Pure, >99%, Fisher Scientific), *N*,*N*-dimethylforamide and tetrahydrofuran (DMF and THF; 99.8%, Acros Organics) and water of Milli-Q grade were used as solvents and for washing. All reagents were used without any further treatment.

4.5.2 Polystyrene core synthesis

Two batches of PVP-stabilized polystyrene core particles were prepared, a small-scale batch in ethanol (PS20-PVP40) as described in section 3.5.2 and a larger-scale batch prepared in isopropanol (PS/IPro-PVP40) as described in section 2.5.2. Whereas PS20-PVP40 served as starting material for the surface modification experiments, PS/IPro-PVP40 was used for the encoding and immunoassay studies where higher amounts of material were necessary.

4.5.3 Dye-encoding of the PS core

PS/IPro-PVP40 particles were encoded with hydrophobic BODIPY (boron–dipyrromethene) dyes (Scheme 3) through an optimized two-step swelling technique in water/THF mixtures. The two BODIPY dyes **1** and **2** (Scheme 3) were prepared according to published protocols.[173, 187] First, 650 µL of particle stock dispersion (5% (w/v)) were mixed with 65 µL pure THF for pre-

swelling. After 1 h incubation at room temperature and gentle mixing using a rotator (40 rpm), 65 µL of the dye solution of the respective initial concentrations in THF were added and the combined solutions were further mixed for 2 h under identical conditions. Afterwards, the beads were centrifuged and washed twice with water and once with ethanol (96%) in dispersion/centrifugation cycles. Finally, the beads were dried in a vacuum oven for 4 h and then stored in the dark at T < 10 °C. To create the 5-plex array, five different initial dye concentrations with 4, 2, 1, 0.5 and 0.25 × 10^{-4} M were used.

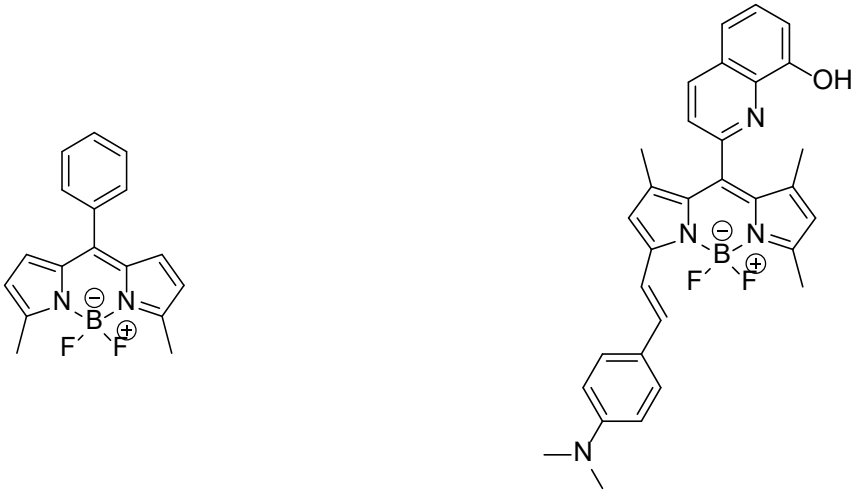

1 **2**

Scheme 3. *Molecular structures of dyes **1** and **2**.*

4.5.4 SiO_2 coating of polymeric core

Details on the preparation procedure for SiO_2@PS20-PVP40 and SiO_2@PS/IPro-PVP40 can be found in section 2.5.3. Dye-doped particles were coated in an Eppendorf tube, scaling down the volume of PS core dispersion to 1 mL (10 mg particles) - cf. section 3.5.3. Note that avoiding a magnetic stirrer and using vertical or overhead shaking is crucial to prevent destruction of the particles.

4.5.5 SiO_2 shell functionalization

Functionalization of the CS particles was performed after activation of the SiO_2 shell. Activation was done by ultrasonication of the particles for 5 min in a 1% (w/v) concentration using a 9:1 volume ratio of methanol and concentrated hydrochloric acid (HCl) as dispersion medium. After washing the particles two times with ethanol in dispersion/centrifugation cycles, the beads were re-dispersed in the functionalization medium (either ethanol or water) to a stock

concentration of 1% (w/v) for dye-encoded beads. Subsequently, the silane was added to the activated bead dispersion as a 1/10 diluted solution of APTES in ethanol (20 µL per 10 mg particles) to prepare unary surfaces. For binary surfaces, a 1/10 diluted solution of APTES in ethanol and a 1/5 diluted solution of PEGS in ethanol were subsequently added to the activated bead dispersion (20 µL per 10 mg particles each). Since the molecular weight of PEGS with ~459 to ~591 g mol^{-1} is almost twice as high as the MW of APTES with ~ 221 g mol^{-1}, the mixture of the differently diluted silane solutions is quasi equimolar. The mixture was left to react at room temperature in a rotator (40 rpm) or at 40 °C in a thermomixer at 500 rpm. After 20 h reaction time, the particles were centrifuged and washed three times with ethanol in centrifugation/redispersion cycles and then left to dry in a vacuum oven for 3 h.

4.5.6 Caffeine hapten (CAFH) coupling

0.1% (w/v) particle dispersions of CS beads were first prepared in 1.5 mL abs. ethanol. Then, 50 µL of a 93 mM solution of NHS-activated esters of CAFH (7-(5-carboxypentyl)-1,3-dimethylxanthine) in dimethylformamide (DMF) were added and the mixture was left to react for 20 h in a thermomixer at room temperature at 500 rpm. The NHS activation of CAFH was done as reported by Carvalho et. al.[188] After the reaction, the particles were centrifuged and washed three times with abs. ethanol in centrifugation/redispersion cycles. Finally, the particles were re-dispersed in 150 µL $ethanol_{70\%}$ (~1% (w/v)) and stored until further use as array element in the bead-based immunoassay.

4.5.7 Particle characterization

A Schottky field emitter SEM (Zeiss Supra40, Oberkochen, Germany) was used for electron microscopy. The transmission mode at this SEM instrument (TSEM) was operated by using a sample holder dedicated to this purpose. In this way, no additional TSEM detector for transmission is necessary, but only preparation of the particulate sample on electron transparent substrates, i. e., on typical TEM grids. Samples were diluted to 0.1% (w/v) prior to pipetting 2–3 µL on a 200-mesh copper grid covered with a carbon film.

ImageJ software was used for statistical TSEM image analysis of at least 200 particles (full data set) to determine the size of the PS and CS beads as well as the size of the SiO_2 NPs (manually drawn circles). For PS and CS particles, automated threshold and watershed features were used

for image processing. Analyses exclude particles with circularity smaller then 0.8 and sizes 100 nm. Distribution plots for Gaussian peak analysis were generated by counting populations between 500 and 2000 nm with a bin width of 15 nm. The equivalent circular diameter (*ecd*) and coefficient of variation (c_υ) were determined according to 3.5.4.

BET isotherm data was acquired by N_2 adsorption/desorption on an ASAP 2010 instrument (Micromeritics). The external surface area was calculated according to the t-plot method of de Boer using the Harkins and Jura correlation (cf. section 2.3.7). TGA (thermogravimetric analysis) measurements were performed with an instrument from Mettler Toledo (Gießen, Germany).

Zeta potential experiments were performed with a Zetasizer Nano ZS using 1×10^{-3}% (w/v) particle concentration in acetic acid buffer (pH = 5). Particles were incubated for 24 hours before measurement. Instrument settings were set automatically with minimum 30 repetitions and standard deviation was determined from triplicate measurements.

4.5.8 Fluorescence spectroscopy

Fluorescence spectra (emission and excitation) of dye-encoded particles were recorded on a Fluoromax-4 spectrofluorometer (Horiba Scientific) with 0.05% (w/v) particle dispersion in water. Kinetic measurements were conducted with a sample holder equipped with a magnetic stirring bar (operated with 200 rpm) in order avoid particle sedimentation during measurements.

4.5.9 Flow cytometry and signal analysis

The fluorescence signals in both channels can be derived from two parameters which are accessible through cytometric analysis. First, the signal intensity provides information on the efficiency of dye incorporation via swelling. Second, the c_υ from the signal, obtained from the respective signal analysis using built-in software tools such as gating, provides information about the homogeneity of incorporation via swelling. An example is given in Figure 77, showing the results for the experimental runs A01–A03 (cf. Table 17).

Data processing is visualized to gather the desired information. The correlation plot of forward (FSC-H) and sideward (SSC-H) scattering marks the particle populations. Next to the main mode (Gate R1), aggregates are found at higher intensities in the SSC-H and FSC-H detector. Respective gating (R1) will exclude these aggregates in the further data processing. In Figure

77 (right) the gate-correlated fluorescence, i.e., the optical code, is shown as a histogram. An additionally set gate (M2) provides statistical data such as mean intensity as well as the c_v of the signal. Histograms or correlation plots of the 5-plex arrays were generated in the same way.

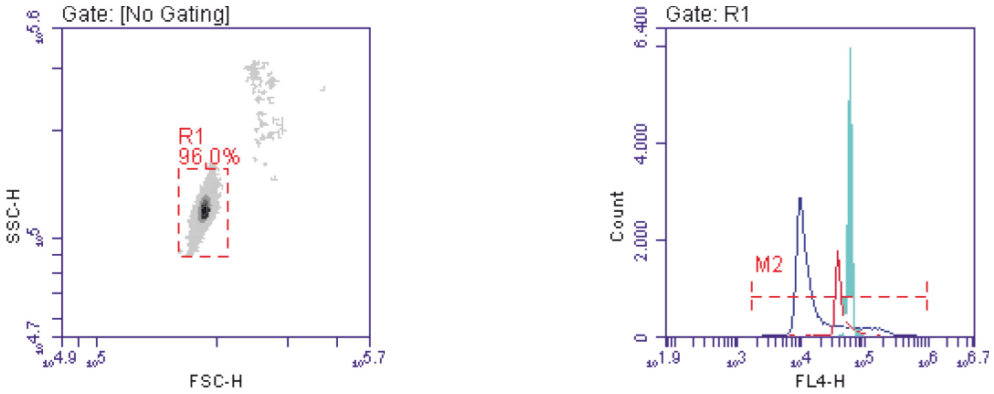

Figure 77. *Left - Correlation plot of FSC-H and SSC-H showing the respective scattering patterns for the CS particles. A gate R1 on the main mode was set for further analysis. Right - FL4-H histogram showing the fluorescence which is correlated to the gated scattering signals, i.e., fluorescence from encoded core particles. The M2 gate was set manually to derive statistical information from the signal distribution of A01 (blue), A02 (red) and A03 (cyan).*

4.5.10 Immunochemical detection of PEG surface functionalization

For a first qualitative assessment of PEG moieties on the particles' surface, 100 µL of the primary anti-PEG antibodies (monoclonal rabbit IgG, clone PEG-B-47, abcam, 182 ng mL^{-1}) were incubated with 20 µL of a 0.0015% (w/v) suspension of CS particles for 5 min. After adding 100 µL of AlexaFluor®488-labeled sAB (goat-anti-rabbit IgG, polyclonal, Thermo-Fisher Scientific, LOT: 1745855, 2.0 µg mL^{-1}) and incubation for 25 min, the particles were analyzed by flow cytometry. Second, a seven-point titration curve of the anti-PEG-AB spanning from 90 to 0.001 ng mL^{-1}, using the same protocol, was recorded. Each point of the curve was measured in triplicate for unary (CS1) and binary (CS2) functionalized CS particles using EtOH and pure water as reaction medium.

4.5.11 General immunoassay procedures

Immunoassays were performed in non-binding, black microtiter plates (Greiner Bio-One). For dilution of the beads and biochemical reagents, TBS (10 mM tris(hydroxymethyl)aminomethane, 150 mM NaCl, pH = 8.5) was used. The incubation time for each step was set to 5 min, if not stated otherwise, and the plate was shaken at 750 rpm on an orbital shaker during incubation. Signal read-out was performed by flow cytometry, equipped with an auto-sampler for microtiter plates. A volume of 7 µL of each well was analyzed, using a flow rate of 14 µL min^{-1}. Beverage samples were degassed by ultra-sonication and diluted 1:20,000 in ultrapure water (Milli-Q) prior to measurement.

4.5.12 Studies on non-specific binding

100 µL of the pAB were incubated with 20 µL of a 0.00625% (w/v) suspension of CS particles for 5 min. For the indirect detection, 100 µL of AlexaFluor®488-labeled sAB were additionally added and incubated for 25 min. A pair of an anti-CAF-AB (monoclonal mouse immunoglobulin G2b or IgG2B, clone 1.BB.877, LOT: L2051502 M, US Biological c = 0.14 µg mL^{-1}) and a goat-anti-mouse IgG (H+L)-AlexaFluor®488-sAB (polyclonal, Thermo-Fisher Scientific, LOT: 1745855, 2.0 µg mL^{-1}) served as a positive control for indirect detection. For direct detection, the FITC-anti-CAF-AB was used in a concentration of 1.0 µg mL^{-1} and incubated with the beads for 30 min. In contrast, a FITC-labeled anti-bovine serum albumin-AB (anti-BSA-AB, polyclonal, sheep, Thermo-Fisher Scientific, 1.0 µg mL^{-1}) as well as a bovine-IgG (Sigma-Aldrich, 0.1 µg mL^{-1}) and an anti-bovine IgG (H+L)-AlexaFluor488-sAB (polyclonal, goat, Jackson immunoResearch, LOT:118210, 1.5 µg mL^{-1}) pair were used as negative control for CAF-coupled beads.

4.5.13 Calibration curves and sample measurements

50 µL of either CAF standards in Milli-Q water or sample were incubated with 50 µL of anti-CAF-AB for 5 min. Then, 20 µL of a 0.00625% (w/v) suspension of differently encoded CS particles were added, before 100 µL of secondary, dye-labeled antibodies were added at a concentration of 2 µg mL^{-1}, followed by a 25 min incubation period. Depending on the dye used for encoding, either goat-anti-mouse IgG (H+L)-AlexaFluor®488-AB (for coding with red dye **2**) or goat-anti-mouse IgG (H+L)-AlexaFluor®647-AB (polyclonal, Thermo-Fisher

Scientific, LOT: 1705800) (for coding with green dye **1**) were employed. Samples were measured in quadruplicate.

4.5.14 Multiplex array

100 µL of primary anti-CAF (272 µg/L), anti-CBZ (350 µg/L), anti-DCF (20 µg/L) and anti-ILA (dilution of polyclonal serum 1:100000) ABs were shaken on an orbital shaker. Then, 20 µL of a 0.00625% (w/v) suspension of encoded and hapten-coupled CS particles (CBZ hapten was provided by Div. 1.8, BAM, and coupling was done according to the procedure in section 4.5.6) were added and mixed for 5 min, before 100 µL of secondary, AlexaFluor®488-labeled antibodies were added at a concentration of 2 µg mL^{-1}, followed by a 5 min incubation period. Goat-anti-mouse IgG (H+L)-AlexaFluor®488-AB were employed.

4.5.15 Responsibility assignment

The project was designed, planned and executed (including synthesis, experiments, data and image analysis) by Dominik Sarma unless otherwise stated. Immunoassay protocols, non-specific binding studies, generation of calibration curves and sample measurements, synthesis of hapten, FITC-labeling of pABs, and the anti-PEG-AB study were supported by P. Carl (Div. 1.8, BAM).

5 Summary

The aim of this work was to develop a modular chemical assay platform using CS microparticles consisting of a PS core and a SiO_2 shell. The exploration was realized in three phases.

The first phase covered the fundamental preparation and characterization aspects of CS particles and proposed these particles with different architecture as carrier platform for cytometric SATs. The preparation method developed here is surpassing the state of the art with a novel strategy to flexibly control the topology of particles' surface on the nanoscale with opportunities to assess different structures such as smooth (i.e. SiO_2@PS-PVP10), rough (i.e. SiO_2@PS-PVP40) and multilayer-like CS particles (i.e. SiO_2@PS-PVP360) via one method. Several synthetic parameters were investigated, highlighting engineering aspects that rely on the herein presented CS particles.

Having in mind the future application of these CS particles as suspension array elements, important characterization techniques such N_2 adsorption to determine the external surface area or to investigate the internal composition of the hybrid as well as cytometry for particle characterization were introduced and improved as compared to the existing literature. The experiments successfully resolved an in-depth view of the particles' structure and revealed crucial information on important analytical features such as the accessible surface area "per particle" and particle handling properties for SAT purposes.

RMM was introduced as a novel characterization method for CS particles. The density could be determined and information about the size of the core CS particle and silica shell was confirmed. The formation of doublets in FACS was verified with this method.

Proof-of-principle studies showed that CS particles are very practical array elements for small-molecule attachment and DNA hybridization assays with ideal handling properties. Differences in the assay performances between particle architectures were investigated: while the multilayer-like particles are very promising candidates for small-molecule attachment, for instance, for coupling fluorescent probes or indicators for metal ion, anion or small organic molecule detection, the closed shell architectures (i.e. SiO_2@PS-PVP10 or SiO_2@PS-PVP40) can preferably be employed in proteomic or genomic assays in which analytes and reporters have comparatively large sizes. The DNA assay performance using CS particles was superior in comparison to published cases using bigger sized microspheres.

The second phase was built on further investigations about synthetic factors (the influence of core size, the influence of TEOS concentration during coating, additional MW of PVP with 160 kDa) allowing to address different process parameters and, accordingly, CS architectures with subtler differences in composition, structure, and size. SEM and TSEM imaging were employed as standard techniques for particle characterization throughout the whole project. However, the development of improved and standardized analysis procedures was essential for a more comprehensive comparison of the prepared particles.

First, a methodological approach for a more consistent data acquisition and analysis of CS particles from TSEM/SEM image analysis, including for instance derisions of size and size distribution as well as the shell thickness, was done. Additionally, the shell composition which was outlined already in chapter two was verified by EDX analysis.

Second, a method was developed based on a self-written software to track the contour of the particles and derive the particle roughness as a novel quantitative descriptor of the particle structure. This enabled an objective classification of *rough/smooth* for the first time. Moreover, using the synthetic approach developed in this thesis, the roughness could be fine-tuned on the sub-10 nm scale.

Together, the two chapters 2 and 3 resulted in a comprehensive data set of the particles, and the information is summarized in Table 22.

The addressable size range and corresponding density can only be reliably given for CS particles prepared from PVP40-stabilized cores, see also the collective data of polystyrene particles highlighted in this work in Annex 6.7. The reason for this is the synthetic accessibility of differently sized cores for a PVP of such MW (cf. section 2.3.15): (a) it was found that particle stabilization during polymerization with the rather short PVP10 is limited and therefore bigger sized particles possess slightly worse monodispersity; (b) PVP160 is commercially available only as 25% aqueous solution which makes handling difficult and (c) for PVP with MW > 40 (including PVP160 and PVP360), bigger-sized particles are difficult to obtain due to the strong stabilization of the cores during the polymerization.

Table 22. *Summary of CS particle architectures and corresonding particle properties such as adressable diameter, roughness and density.*

sketch				
SEM image	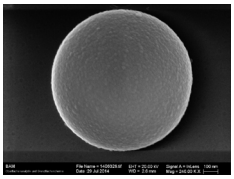	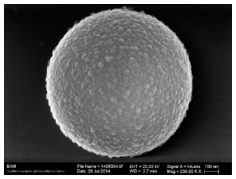	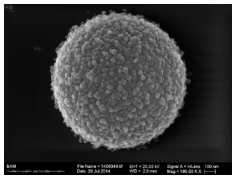	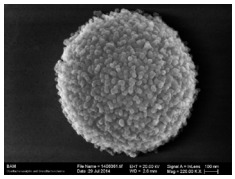
diameter / ecd	>1.0 µm	0.5 µm–2.5 µm	<1.0 µm	<1.0 µm
roughness / R_Q	~ 1.0 nm	~ 2.0 nm	~ 6.0 nm	~ 8.0 nm
density	ρ = 1.146	1.12 < ρ < 1.26[a]	n.d.	ρ = 1.205

[a] Density range addressable with the smallest particles. Larger particles will tend to have lower densities due to smaller ratio of SiO_2 to PS.

In fact, also for PVP40, the upper limit of addressable sizes with acceptable monodispersity lies at ca. 2.5 µm. Many synthesis parameters were tested to further increase the particles size (including different solvent polarity, varying ACVA concentration, higher styrene content, different PVP content; 25 syntheses were performed in total for these studies). However, no clear correlation was found and resulting particle sizes never exceeded the size of PS30-PVP40. Probably ACVA as the initiator limits further growing, either due to additional stabilization effect or decreased solubility of the growing polymer chain.

To this end, allowing highest modularity in a very interesting range of size, architecture density, and surface topology, the PVP40-mediated CS particles were chosen for the development of a multiplexed bead-based immunoassay in the third phase. Through encoding with two hydrophobic BODIPY dyes each, one green emitting and one red emitting organic fluorophore in different concentrations, two 5-plex arrays were created. The preparation of a non-fouling surface using PEG silane and APTES in a simple modification procedure highlights the

chemical tunability of the surface. An indirect assay to detect the psychoactive compound caffeine in beverages was realized successfully. The foundation for the multiplexed detection of four analytes was laid in a feasibility study by proving the specific capturing of anti-analyte-AB on the respective hapten-coupled CS bead. The application of the CS array in multiplexed wastewater analysis is currently under investigation.

5.1 SWOT analysis

A SWOT (strength, weakness, opportunity and thread) analysis (Figure 78) critically evaluates the potential of the CS platform.

The hybrid particles are promising candidates for commercial applications in SAT with superior technical features (strength), because

- they have ideal materials properties for SAT including controlled access to a range of surface topologies with different analytical features (e.g. small molecules on SiO_2@PS-PVP360, larger molecules on SiO_2@PS-PVP10 and 40) and density tuning for easy particle handling,
- stable entrapment of hydrophobic dyes (e.g. BODIPYs) in the core of the CS hybrid can be done via a swelling method which allows easy optical encoding and critical-to-success synthetic routes for shell functionalization (e.g. binary mixed surfaces show good anti-fouling properties only when prepared in ethanol),
- chemical flexibility enables the preparation of either unary surfaces with -COOH or -NH_2 groups for receptor coupling (e.g., DNA or haptens) or binary mixed surfaces with multifunctional properties such as anti-fouling with PEG-silane in a simple protocol.

For successful implementation in the field and enough industrial acceptance, other aspects from the end-user perspective must be considered. In this regard, especially the weaknesses and threads must be analyzed because these represent the most relevant technical barriers for a broad application.

Looking at synthetic weaknesses, the major drawback is the three-step procedure including the synthesis of the core, coating and functionalization. These additional steps (functionalized PS particles can be prepared in a single step) can also be regarded as having better process control toward uniformly tailored particles. From a single batch of PS core particles, for instance,

differently coded and differently surface-functionalized particles can be prepared in a branching preparation workflow, splitting the respective parent objects only before last modification step, and guaranteeing best possible homogeneity. When only a single, uncolored particle batch with unary functionalization is required, plain PS particles might be the better choice.

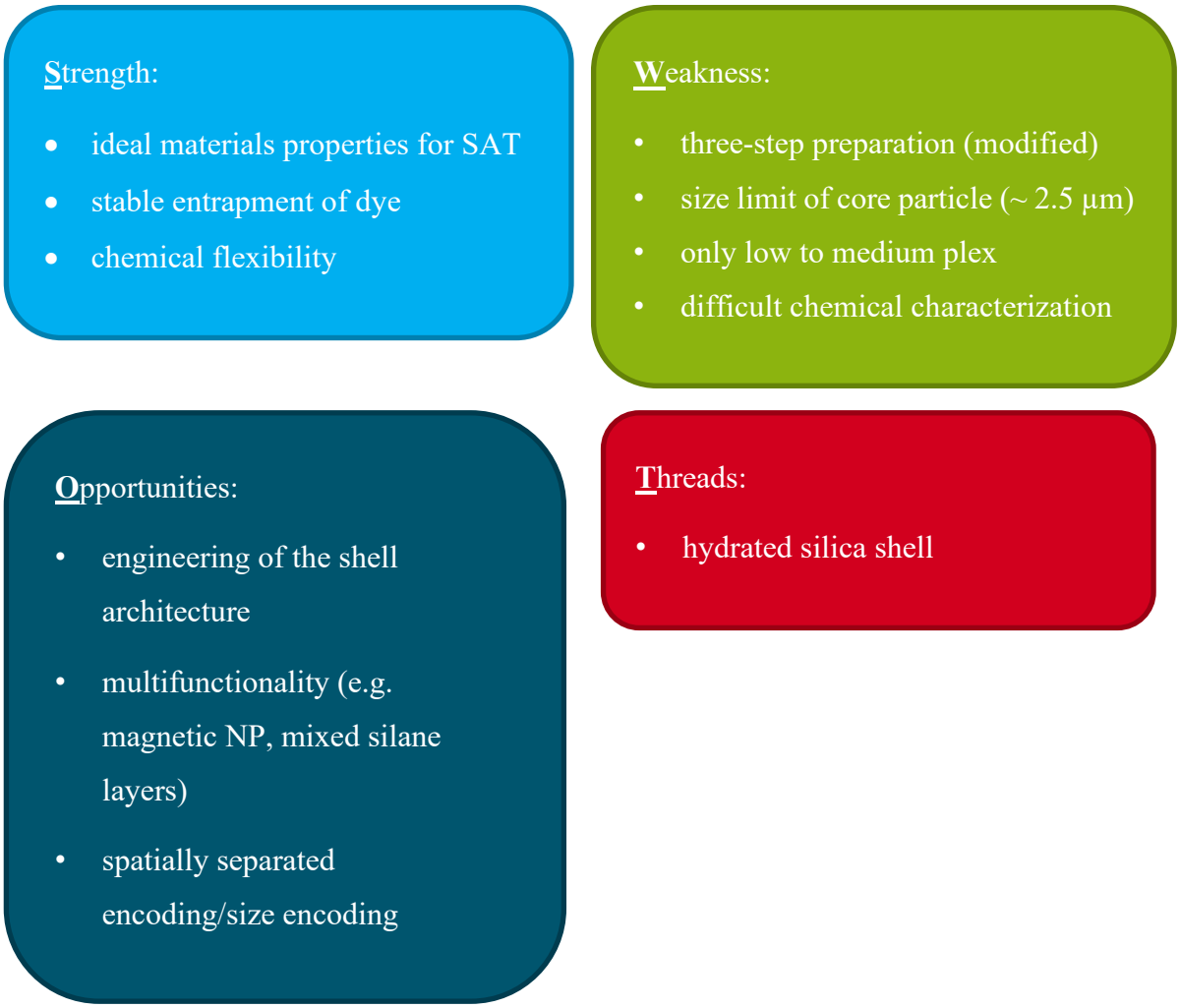

Figure 78. *SWOT-analysis of CS bead platform for SAT applications.*

Using the convergent approach with PVP and ACVA, a limitation of the addressable size range with a maximum of 2.5 µm for monodisperse particles was identified. Looking at beads which are commercially available, particles with sizes larger than 3 µm are typically employed because of the low densities, higher functionalization density "per particle" and higher loading capacities for dye-encoding. With CS particles the density is tuned in a way that these particles

can be nicely handled using centrifugation while being light-weighted enough for long-term measurements. Thus, the herein presented CS particles can potentially be applied in both SATs: cytometric and microscopic read-out, rendering the final application flexible. The performance in terms of sensitivity turned out to be adequate for the envisaged assay applications.

Regarding the encoding capacity, the smaller size will limit the color codes to low or medium plex arrays, which is yet often sufficient in quantitative assays in food, agricultural and environmental analysis, yet rather often also in medical or veterinary diagnostics. Nevertheless, further studies to determine the maximum number of codes must be done. It can be assumed, that the hybrid construction of the beads in this size range enable additional opportunities for encoding (cf. section 5.2)

Size also represents another key advantage: when batch scales are compared, ca. 75-times more analytical single-bead reporters result for the 1.3 µm CS beads compared with, for instance, BDs cytometric array and its 5.5 µm-sized PS particles. Because colored particles in SAT are commonly sold in number quantities (e.g., batches with typically 10^6–10^7 particles mL^{-1})—one particle providing one analytical result—and not in mass quantities, the substantial economic advantages of the smaller beads are obvious.

Characterization of chemically modified CS beads is challenging because of the architecture which consists of a polymeric core, a PVP macromolecule containing oxygen and nitrogen as well as the native yet not fully condensed SiO_2 shell. This hybrid composite renders element-specific characterization quasi-impossible. Elemental analysis, for example, is commonly used to determine coupling efficiency's on calcined silica materials.[189] The carbon content acts as a measure for functional silanes here. Due to the polymeric carbon-rich core, this method is not suitable for CS particles. XPS as a surface sensitive characterization method is another way to determine functional group densities on surfaces.[165] PVP which is potentially located at the surface contains nitrogen and will probably perturb signals from amino groups. FT-IR studies were performed which showed no relevant signals for amino or PEG groups. The low mass amount of the functional silane in relation to the bulk mass of polymeric core and SiO_2 shell is probably too low for reliable detection. For much smaller silica shells on magnetic NPs for example, the functional groups of APTES could only be detected with very low signals.[190] Accordingly, characterization of the particles relies on functionality-based methods (e.g. Ninhydrin test, immunochemical detection of PEG) or fit-to-purpose characterization as was

shown by the example of direct and indirect signaling with targeted and non-targeted receptors, i.e. primary antibodies, in chapter 4.

One key threat to the platform is the nature of the silica shell. The shell will consist of a hydrated and not fully condensed silica network. Thus, the shell might undergo permanent rearrangement and changes at the molecular level, especially when stored in aqueous dispersion media. However, neither were significant changes in assay performance noticed over time periods of roughly six months nor were morphological changes observed from a macroscopic perspective. For reliable and routine applications, nevertheless, long-term studies would have to be performed to stress the robustness of the material.

5.2 Opportunities

The opportunities within the SWOT analysis point toward interesting developments to be addressed in the future.

From a particle engineering perspective, further studying the effects of coating reaction parameters should complement the portfolio of addressable CS particle architectures. Multiparameter investigations would be required to investigate the interplay of various conditions and different PVP.

A more in-depth investigation of the structure-reactivity relationship of such particles would be promising. While the roughness of the particles can now be determined using the silhouette tool, more real application examples are required which put these values in direct correlation to analytical performance parameter. For retrospective analysis and/or future investigations on structurally controlled silica shells, with emphasis on PVP-mediated effects, the method to determine the R_Q value provides a standardized protocol to increase comparability of results between labs.

The concept of a hybrid composite could also be exploited further by introducing magnetic properties to facilitate handling and automation. This could be done by the integration of paramagnetic NPs into the core or shell domain.

Variations of the mixed silane composition could open new opportunities for assay optimization for example further tuning the APTES/PEGS ratio or introduction of other functional silanes with thiol-, epoxy-, or aldehyde-groups to add more functionality to the beads.

The generation of larger numbers of codes for the CS platform might be achieved when the shell domain is covalently doped for instance with silane derivatives of organic dyes. Because core and shell are sufficiently spatially separated to avoid energy transfer processes between single embedded dyes, any optical interference can be ruled out. Next to dyes, other entities such as noble metal NPs or QD can also be doped in either the core or the shell domain to increase functionality – the latter potentially providing additional stability features for the NPs.

Another interesting encoding feature is correlated to the herein employed size ranges of CS particles. Due to the increased detection sensitivity in FACS towards lower scattering intensities, even small changes in size can be used for encoding. In a proof-of-principle study during the work, the particle size was varied between approximately 1.0 and 1.3 µm in two steps creating three size-encoded beads. In combination with five dye-encodings with green dye **1**, a 15-plex array was easily constructed (cf. Annex 6.9).

Lastly, the practical application of the CS bead array is currently under investigation including the benchmarking against conventional single analyte ELISA assays. To this end, a multiplexed immunochemical assay will be developed for the detection of drug residues (CBZ, DCF, and CAF) and bile acids (ILA), all serving as markers for wastewater contamination of surface waters.

5.3 Concluding remarks

In the introduction, several requested attributes to an analytical sensing tool were carved out from the effects of global megatrends. First, a cheap and robust assay platform is of interest to make analytical testing affordable also for poorer regions where some of the megatrends have the biggest impact. This work has shown that CS particles can easily be prepared with typical lab equipment. Using typical benchtop cytometers, particle characterization for development and manufacturing as well as assay read-out can be performed with a single instrument.

Label-free sensing platforms also represent potentially cheap and portable analytical tools. These techniques have in common, however, that the sensor design inherently requires the complementary and precise adjustment of materials properties, functionalization, and system integration. This limits the modularity, simplicity of preparation and use, and finally results in long development cycles to target new analytes. Moreover, multiplexing is a major challenge because each probe/spot requires individual detectors. A recent review on portable optical

assays sheds further light on the current state-of-the-art in the field.[191] Despite the grand variety of emerging technologies presented therein, the authors conclude that "while academic labs utilize a wide variety of tools from optical, chemical, mechanical, and electrical operation principles, companies mostly leverage relatively straightforward methods with bead assays and protein arrays with fluorescent and chemiluminescent detection modalities".

The possibility for multiplexed testing – another required attribute – of small molecules was shown in a proof-of-principle study. The development of other assays simply relies on the respective functionalization of the beads in simple protocols. The transduction pathway (e.g. labeled complementary biomolecule), the platform itself (e.g. coded bead), the instrumentation for read-out (e.g. cytometer) all remains unchanged. New small-molecule probes using other pAB – hapten pairs can be quickly and, most important, modularly developed – of course given that the respective antibodies are available in good quality. Another route would comprise the direct attachment of small molecule indicators to transfer classical solution-phase assays to single particle-based assays.

This easy and fast access to a wide range of targets (from larger biomolecules like DNA to small molecules) in a multiplexed manner using this platform is a major benefit in comparison to other assay platforms which are either costly to produce (flat array assays), limited in high-throughput capacities (solution and dispersion phase assay including typical lab-on-chip or lab-on-paper devices) or still immature regarding their industry penetration (integrated sensors).

The remaining attribute is miniaturization. Even though the principles of cytometric read-out are simple, cytometers still have benchtop-dimensions and analysis is performed routinely within a lab environment. Accordingly, there is a technology gap between matured and high-performing bead-assays on the one side and portable FACS-technologies for single particle-based methods on the other side that still needs to be closed.

6 Annex

6.1 Nitrogen adsorption of PS-PVP360

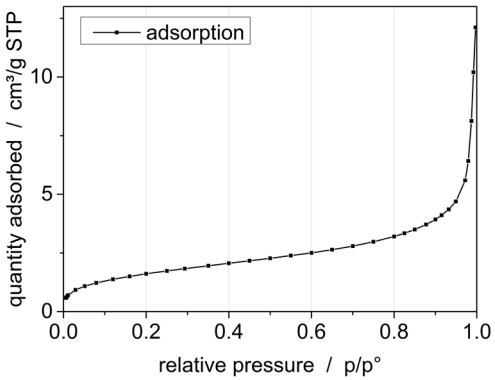

Figure 79. *Nitrogen adsorption isotherm of the PS-PVP360 particles after heating at 60°C for 4 hours.*

Table 23. *Report results obtained from the built-in software calculation of the BET surface area from adsorption data using an ASAP 2010 instrument form Micromertrics.*

BET Surface Area Report

BET Surface Area	6.0470 ± 0.0275 m²/g
Slope	0.705723 ± 0.003233 cm³/g STP
Y-Intercept	0.014167 ± 0.000431 cm³/g STP
C	50.81496
Qm	1.3891 cm³/g STP
Correlation Coefficient	0.9999685
Molecular Cross-Sectional Area	0.162 nm²

6.2 Dry mass and size distribution from RMM

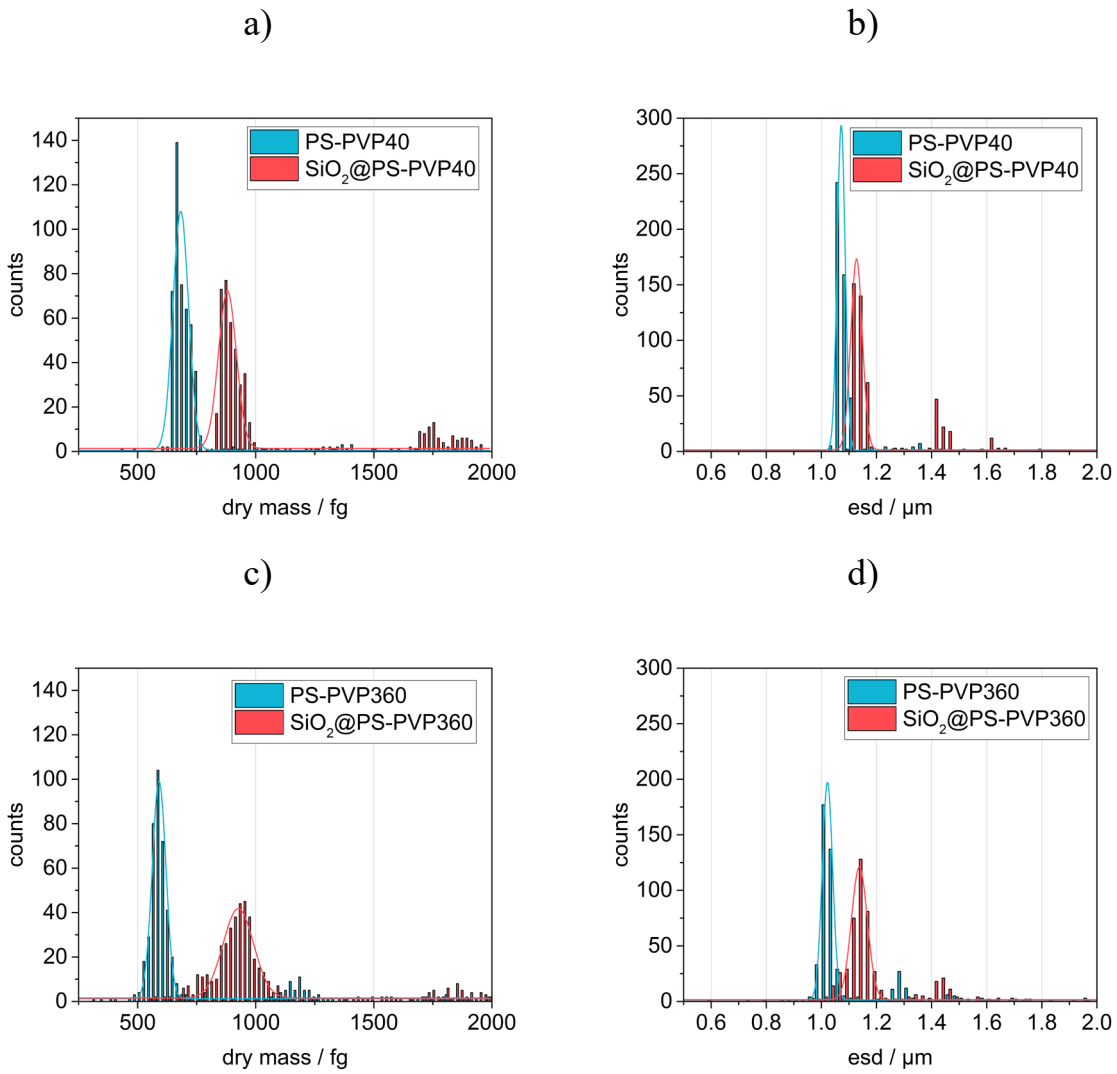

Figure 80. *Dry mass and size distribution of PS-PVP40 and SiO_2@PS-PVP40 (a, b) as well as PS-PVP360 and SiO_2@PS-PVP360 (c, d).*

6.3 Size of core particles prepared in isopropanol

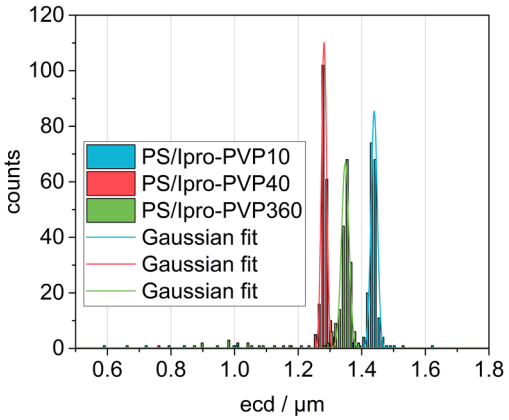

name	*ecd* / nm	c_{υ}
PS/IPro-PVP10	1439.1	10.2
PS/IPro-PVP40	1282.6	3.3
PS/IPro-PVP360	1347.9	7.1

Figure 81. *Size distribution of core particles prepared in isopropanol (left) and compiled size date (right).*

6.4 FACS correlation plot

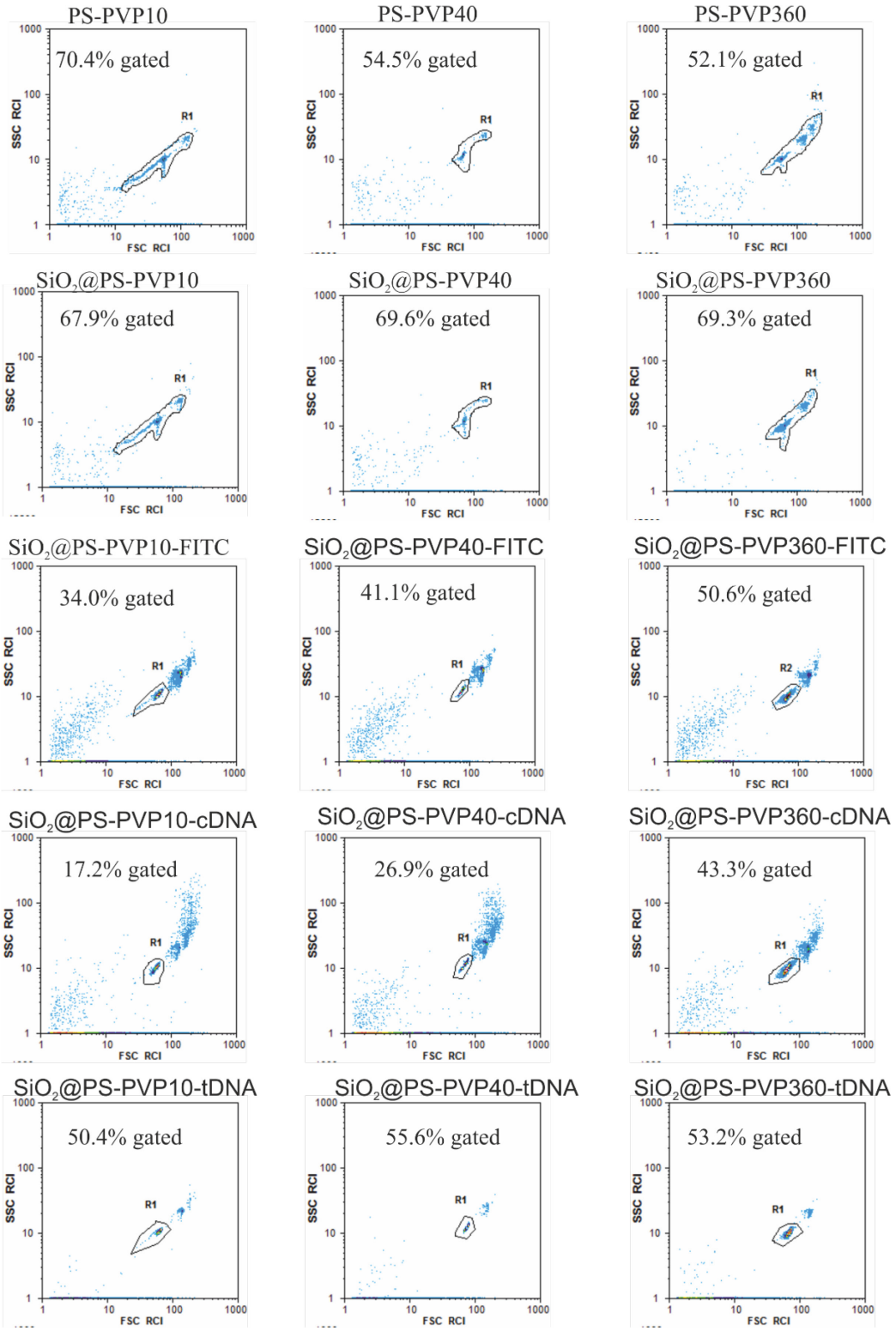

Figure 82. *Correlation plots obtained with FACS measurements. Gates (R1) were set to exclude secondary particles. Relative number of counted events are shown in percent.*

6.5 Size distribution of PS-PVP160 and SiO_2@PS-PVP160

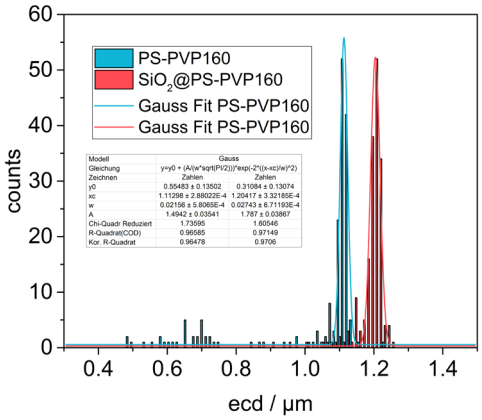

Figure 83. *Size distribution of core and CS particles prepared with PVP-160. Data form Gaussian fit are shown in the inset.*

6.6 TGA and nitrogen adsorption of SiO_2@PS-PVP160

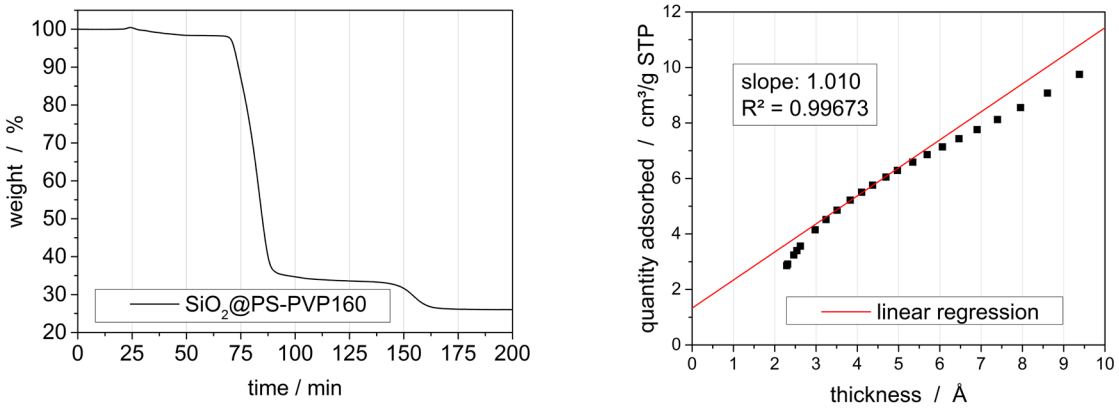

Figure 84. *Left – TGA curve for SiO_2@PS-PVP160. Right – t-plot analysis of SiO_2@PS-PVP160.*

6.7 Biochemical reagent list

biochemical reagent	Product Number, RRID[a], Presentation	c_{Stock} / mg mL^{-1}	c_{assay} / mg mL^{-1}	LOT number	supplier
Bovine IgG	G5009 Freeze-dried γ-Globulins from bovine blood, purity min. 99 % CAS: 9007-83-4	-	0.10	-	Sigma-Aldrich
Goat-anti-bovine IgG (H+L)-Alexa Fluor® 488 (polyclonal)	101-545-003, RRID: AB_2337323 “AffiniPure“	1.50	1.50	118210	Jackson ImmunoResearch
Goat-anti-mouse IgG (H+L)-Alexa Fluor® 488 (polyclonal)[b]	A-11029 RRID: AB_2534088 “highly cross adsorbed “	2.00	2.00	1745855	Thermo-Fisher Scientific
Goat-anti-mouse IgG (H+L)-Alexa Fluor® 647 (polyclonal)[b]	A-21236 RRID: AB_2535805 “highly cross adsorbed “	2.00	2.00	1705800	Thermo-Fisher Scientific
Goat-anti-rabbit-IgG (H+L) Alexa Fluor® 488 (polyclonal)[b]	A-11008 RRID: AB_143165 “highly cross adsorbed “	2.00	2.00	1745855	Thermo-Fisher Scientific
Mouse-anti-CAF (monoclonal)	C0110-06 IgG2b Clone: 1.BB.877	1.36	0.14	L2051502 M	US Biological
Rabbit-anti-PEG (monoclonal)	ab51257, RRID: AB_11155670 Clone: PEG-AB-47	0.91	0.18	GR173877-31	Abcam
Sheep-anti-BSA-FITC (polyclonal)	PA1-29252 RRID: AB_1957478	1.00	1.00	RC2170241J	Thermo-Fisher Scientific

[a] Research Resource Identifiers. [b] The immunogen was the whole IgG-molecule, consisting of heavy and light (H+L) chains.

6.8 Highlighted polystyrene core particles

sample	N	*ecd* / nm	c_{υ}	experimental	employed in
PS-PVP10	180	893.0	4.7	2.5.2	chapter 2
PS-PVP40	180	945.4	1.0	2.5.2	chapter 2
PS-PVP360	180	896.2	1.9	2.5.2	chapter 2
PS/Ipro-PVP10	200	1439.1	10.2	3.5.2	chapter 2
PS/Ipro-PVP40	200	1282.6	3.3	3.5.2	chapter 2 and 4
PS/Ipro-PVP360	200	1347.9	7.1	3.5.2	chapter 2
PS5-PVP40	250	550.2	1.7	2.5.2	chapter 3
PS20-PVP40	250	1254.2	2.2	2.5.2	chapter 3 and 4
PS30-PVP40	250	2449.3	12.9	2.5.2	chapter 3

6.9 Size encoding

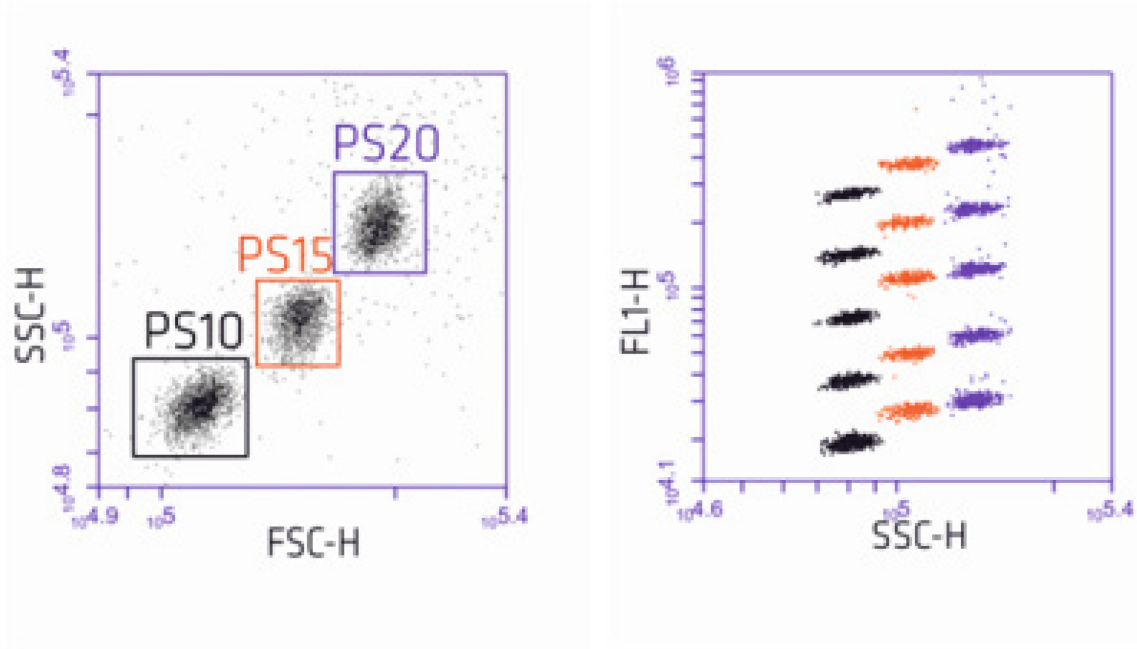

Figure 85. *Scattering plots of size-encoded beads: FSC-H vs. SSC-H (left) and SSC-H vs. FL1-H (right). The particles were prepared according to the method described in section 3.5.2 using the reaction station from Radleys®. PS20 corresponds to PS20-PVP40, PS15 and PS10 were prepared using 1.5 and 1 mL Styrene during polymerization.*

7 Abbreviations

AB ..... *antibody*
ACPA ..... *4,4'-azobis(4-4,4'-azobis(4-cyanopentanoic acid)*
AFM ..... *atomic force microscopy*
AIBN ..... *azobisisobutyronitrile*
APTES *3-aminopropyltriethoxysilane*
A_s ..... *surface area*
BODIPY *4,4-difluoro-4-bora-3a,4a-diaza-s-indacene*
BPO ..... *dibenzoyl peroxide*
BSA ..... *bovine serum albumin*
CAF ..... *caffeine*
CAFH ..... *caffein hapten*
CBZ ..... *carbamazepine*
c-DNA ..... *capture DNA*
CS ..... *core-shell*
c_υ ..... *coefficient of variation*
DCF ..... *diclofenac*
DF ..... *degrees of freedom*
DFT ..... *density functional theory*
DLS ..... dynamic light scattering
DMF ..... *dimethylformamide*
DNA ..... *deoxyribonucleic acid*, *desoxyribonucleic acid*
dsDNA ..... *double-strand DNA*
EC ..... *effective concentration*
ecd ..... *equivalent circular diameter*
EDC ..... *1-ethyl-3-(3-dimethylaminopropyl)carbodiimide*
EDX ..... *energy dispersive x-ray*
ELISA ..... *enzyme-linked immunosorbent assay*
EM ..... *electron microscopy*
esd ..... *equivalent spherical diameter*
EtOH ..... *ethanol*
FACS ..... *fluorescence-activated cell sorting*
FAM *6-carboxyfluorescein*
FDA ..... *food and drug administration*
FITC ..... *fluorescein isothiocyanate*
FL ..... *fluorescence channel*
FOA ..... *field of analysis*
FOV ..... field of view
FSC ..... *forward scattering*
GMT ..... *global megatrends*
GX ..... *green code*
HCl ..... *hydrochloric acid*
IgG ..... *immunoglobulin G*
ILA ..... *isolithocholic acid*
IPro ..... *isopropanol*
LbL ..... *layer-by-layer*

LED ..... *light-emitting diode*
LOD ..... *limit of detection*
LOQ ..... *limit of quantification*
MCI ..... *mean channel intensity*
MEF ..... *molecules of equivalent fluorochrome*
MES ..... *2-(N-morpholino)ethanesulfonic acid*
MW ..... *molecular weight*
N ..... *number*
n.d. ..... *not determined*
NM ..... *noble metal*
NP ..... *nanoparticle*
pAB ..... *primary antibody*
PB ..... *phosphate buffer*
PEG ..... *polyethylene glycol*, *polyethylene glycol*
PEGS ..... *polyethylene glycol silane*
POCT ..... *point of care testing*
PS ..... *polystyrene*
PVP ..... *polyvinylpyrrolidone*
QD ..... *quantum dot*
R_h ..... *hydrodynamic radius*
RMM ..... *resonant mass measurement*
RMS ..... *root mean square*
RNA ..... *ribonucleic acid*
R_Q ..... *profile roughness*
RX ..... *red code*
R_Z ..... *peak-to-valley height*
S/N ..... *signal-to-noise*
sAB ..... *secondary antibody*
SAT ..... *suspension array technology*
SD ..... *standard deviation*
SDS ..... *sodium dodecyl sulfate*
SEM ..... *scanning electron microscopy*
SERS ..... *surface enhanced Raman scattering*
SHM ..... *silica hollow microspheres*
SiO_2 ..... *silica*
S-NHS ..... *sulfo N-hydroxysuccinimid*
*S*Q ..... *surface roughness*
SSC ..... *sideward scattering*
SWOT ..... *strength, weakness, opportunity and thread*
T ..... *roughness threshold*
TBS ..... *tris-buffered saline*
t-DNA ..... *target DNA*
TE ..... *ethylenediaminetetraacetic acid*
TEM ..... *transmission electron microscopy*
TEOS ..... *tetraethoxysilane*
TGA ..... *thermogravimetric analysis*
THF ..... *tetrahydrofuran*
TMAC ..... *tetramethyl ammonium chloride*

TMOS ..... *tetramethyl orthosilicate*
TRIS ..... *tris(hydroxymethyl)aminomethane*
TSEM ..... *transmission scanning electron microscopy*
UC ..... *up-conversion*
V ..... *volume*
wt.-% ..... *weight percent*
x_m ..... *peak maximum*
ZP ..... *zeta potential*

8 Literature

1. *Future State 2030: The Global Megatrends Shaping Governments*; KPMG International: 2014.
2. Lung, T.; Wugt Larson, F. *Accelerating Technological Change*; European Environment Agency: 2013.
3. de Silva, A. P.; Gunaratne, H. Q.; Gunnlaugsson, T.; Huxley, A. J.; McCoy, C. P.; Rademacher, J. T.; Rice, T. E., Signaling recognition events with fluorescent sensors and switches. *Chem Rev* **1997,** *97*, 1515-1566.
4. McDonagh, C.; Burke, C. S.; MacCraith, B. D., Optical chemical sensors. *Chem Rev* **2008,** *108*, 400-422.
5. Descalzo, A. B.; Zhu, S.; Fischer, T.; Rurack, K., Optimization of the coupling of target recognition and signal generation. In *Advanced Fluorescence Reporters in Chemistry and Biology II: Molecular Constructions, Polymers and Nanoparticles*, Demchenko, A. P., Ed., Springer: Berlin, Heidelberg, 2010; pp 41-106.
6. Ros-Lis, J. V.; Marcos, M. D.; Martinez-Manez, R.; Rurack, K.; Soto, J., A regenerative chemodosimeter based on metal-induced dye formation for the highly selective and sensitive optical determination of Hg2+ ions. *Angew Chem Int Ed Engl* **2005,** *44*, 4405-4407.
7. Syahir, A.; Usui, K.; Tomizaki, K.-Y.; Kajikawa, K.; Mihara, H., Label and label-free detection techniques for protein microarrays. *Microarrays* **2015,** *4*, 228-244.
8. Epstein, J. R.; Biran, I.; Walt, D. R., Fluorescence-based nucleic acid detection and microarrays. *Anal Chim Acta* **2002,** *469*, 3-36.
9. Saha, K.; Agasti, S. S.; Kim, C.; Li, X.; Rotello, V. M., Gold nanoparticles in chemical and biological sensing. *Chem Rev* **2012,** *112*, 2739-2779.
10. Huang, C.-C.; Chang, H.-T., Selective gold-nanoparticle-based “turn-on” fluorescent sensors for detection of mercury(II) in aqueous solution. *Anal Chem* **2006,** *78*, 8332-8338.
11. Sepúlveda, B.; Angelomé, P. C.; Lechuga, L. M.; Liz-Marzán, L. M., LSPR-based nanobiosensors. *Nano Today* **2009,** *4*, 244-251.
12. Doria, G.; Conde, J.; Veigas, B.; Giestas, L.; Almeida, C.; Assuncao, M.; Rosa, J.; Baptista, P. V., Noble metal nanoparticles for biosensing applications. *Sensors* **2012,** *12*, 1657-1687.
13. Knopp, D.; Tang, D.; Niessner, R., Review: bioanalytical applications of biomolecule-functionalized nanometer-sized doped silica particles. *Anal Chim Acta* **2009,** *647*, 14-30.
14. Medintz, I. L.; Uyeda, H. T.; Goldman, E. R.; Mattoussi, H., Quantum dot bioconjugates for imaging, labelling and sensing. *Nat Mater* **2005,** *4*, 435-446.
15. Wang, L.; Yan, R.; Huo, Z.; Wang, L.; Zeng, J.; Bao, J.; Wang, X.; Peng, Q.; Li, Y., Fluorescence resonant energy transfer biosensor based on upconversion-luminescent nanoparticles. *Angew Chem Int Ed Engl* **2005,** *44*, 6054-6057.
16. Wu, S.; Duan, N.; Shi, Z.; Fang, C.; Wang, Z., Simultaneous aptasensor for multiplex pathogenic bacteria detection based on multicolor upconversion nanoparticles labels. *Anal Chem* **2014,** *86*, 3100-3107.

17. Yu, C.; Irudayaraj, J., Multiplex biosensor using gold nanorods. *Anal Chem* **2007,** *79*, 572-579.

18. Vet, J. A. M.; Majithia, A. R.; Marras, S. A. E.; Tyagi, S.; Dube, S.; Poiesz, B. J.; Kramer, F. R., Multiplex detection of four pathogenic retroviruses using molecular beacons. *Proc Natl Acad Sci USA* **1999,** *96*, 6394-6399.

19. Kuswandi, B.; Nuriman; Huskens, J.; Verboom, W., Optical sensing systems for microfluidic devices: A review. *Anal Chim Acta* **2007,** *601*, 141-155.

20. Marks, H.; Schechinger, M.; Garza, J.; Locke, A.; Coté, G., Surface enhanced Raman spectroscopy (SERS) for in vitro diagnostic testing at the point of care. *Nanophotonics* **2017,** *6*, 681-701.

21. Lian, D.-S.; Zhao, S.-J., Capillary electrophoresis based on nucleic acid detection for diagnosing human infectious disease. *Clin Chem Lab Med* **2016,** *54*, 707-738.

22. Ge, L.; Yu, J.; Ge, S.; Yan, M., Lab-on-paper-based devices using chemiluminescence and electrogenerated chemiluminescence detection. *Anal Bioanal Chem* **2014,** *406*, 5613-5630.

23. Windmiller, J. R.; Wang, J., Wearable electrochemical sensors and biosensors: A review. *Electroanalysis* **2013,** *25*, 29-46.

24. Länge, K.; Rapp, B. E.; Rapp, M. J. A.; Chemistry, B., Surface acoustic wave biosensors: a review. *Anal Bioanal Chem* **2008,** *391*, 1509-1519.

25. Carvajal Ahumada, L. A.; Herrera Sandoval, O. L.; Peña Perez, N.; Silva Gómez, F. A.; García-Vellisca, M. A.; Serrano Olmedo, J. J., Quartz crystal resonator for real-time characterization of nanoscale phenomena relevant for biomedical applications. In *In-situ Characterization Techniques for Nanomaterials*, Kumar, C. S. S. R., Ed. Springer: Berlin, Heidelberg, 2018; pp 289-350.

26. Putzbach, W.; Ronkainen, N. J., Immobilization techniques in the fabrication of nanomaterial-based electrochemical biosensors: A review. *Sensors* **2013,** *13*, 4811-4840.

27. Bañuls, M.-J.; Puchades, R.; Maquieira, Á., Chemical surface modifications for the development of silicon-based label-free integrated optical (IO) biosensors: A review. *Anal Chim Acta* **2013,** *777*, 1-16.

28. Dandy, D. S.; Wu, P.; Grainger, D. W., Array feature size influences nucleic acid surface capture in DNA microarrays. *Proc Natl Acad Sci USA* **2007,** *104*, 8223-8228.

29. Nolan, J. P.; Sklar, L. A., Suspension array technology: evolution of the flat-array paradigm. *Trends Biotechnol* **2002,** *20*, 9-12.

30. Romanov, V.; Davidoff, S. N.; Miles, A. R.; Grainger, D. W.; Gale, B. K.; Brooks, B. D., A critical comparison of protein microarray fabrication technologies. *Analyst* **2014,** *139*, 1303-1326.

31. Chandler, D. P., Bead-based flow systems: From centralized laboratories to genetic testing in the field. In *Nucleic Acid Testing for Human Disease*, Lorincz, A., Ed., Taylor&Francis: 2016; pp 93-113.

32. Derveaux, S.; Stubbe, B. G.; Braeckmans, K.; Roelant, C.; Sato, K.; Demeester, J.; De Smedt, S. C., Synergism between particle-based multiplexing and microfluidics technologies may bring diagnostics closer to the patient. *Anal Bioanal Chem* **2008,** *391*, 2453-2467.

33. Cho, S. H.; Godin, J. M.; Chen, C.-H.; Qiao, W.; Lee, H.; Lo, Y.-H., Review Article: Recent advancements in optofluidic flow cytometer. *Biomicrofluidics* **2010,** *4*, Art No 43001.

34. Lok, K. P.; Ober, C. K., Particle size control in dispersion polymerization of polystyrene. *Can J Chem* **1985,** *63*, 209-216.

35. Stöber, W.; Fink, A.; Bohn, E., Controlled growth of monodisperse silica spheres in the micron size range. *J Colloid Interface Sci* **1968,** *26*, 62-69.

36. Dunbar, S. A., Applications of Luminex xMAP technology for rapid, high-throughput multiplexed nucleic acid detection. *Clin Chim Acta* **2006,** *363*, 71-82.

37. Morgan, E.; Varro, R.; Sepulveda, H.; Ember, J. A.; Apgar, J.; Wilson, J.; Lowe, L.; Chen, R.; Shivraj, L.; Agadir, A.; Campos, R.; Ernst, D.; Gaur, A., Cytometric bead array: a multiplexed assay platform with applications in various areas of biology. *Clin Immunol* **2004,** *110*, 252-266.

38. Vargas-Sansalvador, I. M. P. d.; Canfrotta, F.; Piletsky, S. A., Synthesis of monodisperse polymeric nano- and microparticles and their application in bioanalysis. In *Advances in Chemical Bioanalysis*, Matysik, F.-M., Ed. Springer: 2014; pp 131-154.

39. Wilson, R.; Cossins, A. R.; Spiller, D. G., Encoded microcarriers for high-throughput multiplexed detection. *Angew Chem Int Ed Engl* **2006,** *45*, 6104-6117.

40. Yan, J.; Estévez, M. C.; Smith, J. E.; Wang, K.; He, X.; Wang, L.; Tan, W., Dye-doped nanoparticles for bioanalysis. *Nano Today* **2007,** *2*, 44-50.

41. Van Blaaderen, A.; Vrij, A., Synthesis and characterization of colloidal dispersions of fluorescent, monodisperse silica spheres. *Langmuir* **1992,** *8*, 2921-2931.

42. Guerrero-Martinez, A.; Perez-Juste, J.; Liz-Marzan, L. M., Recent progress on silica coating of nanoparticles and related nanomaterials. *Adv Mater* **2010,** *22*, 1182-1195.

43. Liu, Y.-Y.; Cheng, S.-L.; Chen, H., Architecture of micron-scale hollow spheres composed of silica nanoparticles and approach to luminescent spheres. *Colloid Polym Sci* **2012,** *290*, 1777-1784.

44. Li, L.; Ding, J.; Xue, J., Macroporous silica hollow microspheres as nanoparticle collectors. *Chem Mater* **2009,** *21*, 3629-3637.

45. Bamnolker, H.; Nitzan, B.; Gura, S.; Margel, S., New solid and hollow, magnetic and non-magnetic, organic-inorganic monodispersed hybrid microspheres: synthesis and characterization. *J Mater Sci Lett* **1997,** *16*, 1412-1415.

46. Graf, C.; Vossen, D. L. J.; Imhof, A.; van Blaaderen, A., A general method to coat colloidal particles with silica. *Langmuir* **2003,** *19*, 6693-6700.

47. Caruso, F.; Möhwald, H., Preparation and characterization of ordered nanoparticle and polymer composite multilayers on colloids. *Langmuir* **1999,** *15*, 8276-8281.

48. Sarma, D.; Gawlitza, K.; Rurack, K., Polystyrene core-silica shell particles with defined nanoarchitectures as a versatile platform for suspension array technology. *Langmuir* **2016,** *32*, 3717-3727.

49. Jiang, Q.; Zhong, J.; Hu, X.; Song, F.; Ren, K.; Wei, H.; Yi, L., Fabrication and optical properties of silica shell photonic crystals. *Colloids Surf A* **2012,** *415*, 202-208.

50. D'Acunzi, M.; Mammen, L.; Singh, M.; Deng, X.; Roth, M.; Auernhammer, G. K.; Butt, H. J.; Vollmer, D., Superhydrophobic surfaces by hybrid raspberry-like particles. *Faraday Discuss* **2010,** *146*, 35-48.

51. Du, X.; Liu, X.; Chen, H.; He, J., Facile fabrication of raspberry-like composite nanoparticles and their application as building blocks for constructing superhydrophilic coatings. *J Phys Chem C* **2009,** *113*, 9063-9070.

52. Gao, T.; Jelle, B. P.; Gustavsen, A., Antireflection properties of monodisperse hollow silica nanospheres. *Appl Phys A-Mater* **2012,** *110*, 65-70.

53. Li, X.; He, J., In situ assembly of raspberry- and mulberry-like silica nanospheres toward antireflective and antifogging coatings. *ACS Appl Mater Interfaces* **2012,** *4*, 2204-2211.

54. Zhang, L.; Wang, H.; Zhang, Z.; Qin, F.; Liu, W.; Song, Z., Preparation of monodisperse polystyrene/silica core–shell nano-composite abrasive with controllable size and its chemical mechanical polishing performance on copper. *Appl Surf Sci* **2011,** *258*, 1217-1224.

55. Nandiyanto, A. B.; Iwaki, T.; Ogi, T.; Okuyama, K., Mesopore-free silica shell with nanometer-scale thickness-controllable on cationic polystyrene core. *J Colloid Interface Sci* **2013,** *389*, 134-146.

56. Li, D.; Zhu, Y.; Mao, C., One-pot synthesis of surface roughness controlled hollow silica spheres with enhanced drug loading and release profile under ambient conditions in aqueous solutions. *J Mater Chem B* **2013,** *1*, 5515-5520.

57. Whitaker, K. A.; Furst, E. M., Layer-by-layer synthesis of mechanically robust solvent-permeable silica nanoshells. *Langmuir* **2014,** *30*, 584-591.

58. Wu, Y.; Li, Y.; Qin, L.; Yang, F.; Wu, D., Monodispersed or narrow-dispersed melamine–formaldehyde resin polymer colloidal spheres: preparation, size-control, modification, bioconjugation and particle formation mechanism. *J Mater Chem B* **2013,** *1*, 204-212.

59. Jun, B. H.; Noh, M. S.; Kim, G.; Kang, H.; Kim, J. H.; Chung, W. J.; Kim, M. S.; Kim, Y. K.; Cho, M. H.; Jeong, D. H.; Lee, Y. S., Protein separation and identification using magnetic beads encoded with surface-enhanced Raman spectroscopy. *Anal Biochem* **2009,** *391*, 24-30.

60. Li, Y.; Wu, Y.; Luo, C.; Wang, B.; Wu, D., Rewritable magnetic fluorescence-encoded microspheres: preparation, characterization, and recycling. *J Mater Chem C* **2015,** *3*, 8262-8271.

61. Wu, Y.; Li, Y.; Xu, J.; Wu, D., Incorporating fluorescent dyes into monodisperse melamine–formaldehyde resin microspheres via an organic sol–gel process: a pre-polymer doping strategy. *J Mater Chem B* **2014,** *2*, 5837-5846.

62. Wilson, R.; Spiller, D. G.; Prior, I. A.; Veltkamp, K. J.; Hutchinson, A., A simple method for preparing spectrally encoded magnetic beads for multiplexed detection. *ACS Nano* **2007,** *1*, 487-493.

63. Cao, Y. C.; Huang, Z. L.; Liu, T. C.; Wang, H. Q.; Zhu, X. X.; Wang, Z.; Zhao, Y. D.; Liu, M. X.; Luo, Q. M., Preparation of silica encapsulated quantum dot encoded beads for multiplex assay and its properties. *Anal Biochem* **2006,** *351*, 193-200.

64. Descalzo, A. B.; Xu, H. J.; Xue, Z. L.; Hoffmann, K.; Shen, Z.; Weller, M. G.; You, X. Z.; Rurack, K., Phenanthrene-fused boron−dipyrromethenes as bright long-wavelength fluorophores. *Org Lett* **2008,** *10*, 1581-1584.

65. Kato, N.; Ishii, T.; Koumoto, S., Synthesis of monodisperse mesoporous silica hollow microcapsules and their release of loaded materials. *Langmuir* **2010,** *26*, 14334-1444.

66. Zhu, Y.; Xu, H.; Chen, K.; Fu, J.; Gu, H., Encoding through the host-guest structure: construction of multiplexed fluorescent beads. *Chem Commun* **2014,** *50*, 14041-14044.

67. Schmid, A.; Fujii, S.; Armes, S. P., Polystyrene-silica nanocomposite particles via alcoholic dispersion polymerization using a cationic azo initiator. *Langmuir* **2006,** *22*, 4923-4927.

68. Leng, W.; Chen, M.; Zhou, S.; Wu, L., Capillary force induced formation of monodisperse polystyrene/silica organic-inorganic hybrid hollow spheres. *Langmuir* **2010,** *26*, 14271-14275.

69. Park, I., Monodisperse polystyrene-silica core-shell particles and silica hollow spheres prepared by the Stöber method. *J Nanosci Nanotechnol* **2009,** *9*, 7224-7228.

70. Chen, W.; Takai, C.; Khosroshahi, H. R.; Fuji, M.; Shirai, T., Surfactant-free fabrication of SiO2-coated negatively charged polymer beads and monodisperse hollow SiO2 particles. *Colloids Surf A* **2015,** *481*, 375-383.

71. Arshady, R., Suspension, emulsion, and dispersion polymerization: A methodological survey. *Colloid Polym Sci* **1992,** *270*, 717-732.

72. Lu, Y.; McLellan, J.; Xia, Y., Synthesis and crystallization of hybrid spherical colloids composed of polystyrene cores and silica shells. *Langmuir* **2004,** *20*, 3464-3470.

73. Lu, X.; Xin, Z., Synthesis of poly(styrene-co-3-trimethoxysilyl propyl methacrylate) microspheres coated with polysiloxane layer. *Colloid Polym Sci* **2006,** *285*, 599-604.

74. Hong, J.; Han, H.; Hong, C. K.; Shim, S. E., A direct preparation of silica shell on polystyrene microspheres prepared by dispersion polymerization with polyvinylpyrrolidone. *J Polym Sci Polym Chem* **2008,** *46*, 2884-2890.

75. Kobayashi, Y.; Misawa, K.; Kobayashi, M.; Takeda, M.; Konno, M.; Satake, M.; Kawazoe, Y.; Ohuchi, N.; Kasuya, A., Silica-coating of fluorescent polystyrene microspheres by a seeded polymerization technique and their photo-bleaching property. *Colloids Surf A* **2004,** *242*, 47-52.

76. Christopher-Hennings, J.; Araujo, K. P.; Souza, C. J.; Fang, Y.; Lawson, S.; Nelson, E. A.; Clement, T.; Dunn, M.; Lunney, J. K., Opportunities for bead-based multiplex assays in veterinary diagnostic laboratories. *J Vet Diagn Invest* **2013,** *25*, 671-691.

77. Peters, J.; Bienenmann-Ploum, M.; de Rijk, T.; Haasnoot, W., Development of a multiplex flow cytometric microsphere immunoassay for mycotoxins and evaluation of its application in feed. *Mycotoxin Res* **2011,** *27*, 63-72.

78. Sun, Z.; Peng, Y.; Zhang, M.; Wang, K.; Bai, J.; Li, X.; Ning, B.; Gao, Z., Simultaneous and highly sensitive detection of six different foodborne pathogens by high-throughput suspension array technology. *Food Control* **2014,** *40*, 300-309.

79. Birtwell, S.; Morgan, H., Microparticle encoding technologies for high-throughput multiplexed suspension assays. *Integr Biol* **2009,** *1*, 345-362.

80. Elshal, M. F.; McCoy, J. P., Multiplex bead array assays: performance evaluation and comparison of sensitivity to ELISA. *Methods* **2006,** *38*, 317-323.

81. Harich, R.; Roger, C.; Garnier, L.; Bienvenu, J.; Fabien, N., Comparison of anti-CCP autoantibodies measurement by ELISA and a bead-based assay in a large patient cohort. *Clin Biochem* **2014,** *47*, 485-488.

82. Zou, H.; Wu, S.; Ran, Q.; Shen, J., A simple and low-cost method for the preparation of monodisperse hollow silica spheres. *J Phys Chem C* **2008,** *112*, 11623-11629.

83. Toki, M.; Chow, T.; Ohnaka, T.; Samura, H.; Saegusa, T., Structure of poly(vinylpyrrolidone)-silica hybrid. *Polym Bull* **1992,** *29*, 653-660.

84. Paine, A. J.; Wayne, L.; McNulty, J., Dispersion polymerization of styrene in polar solvents. 6. Influence of reaction parameters on particle size and molecular weight in PVP-stabilized reactions. *Macromolecules* **1990,** *23*, 3104-3109.

85. Paine, A. J., Dispersion polymerization of styrene in polar solvents. 7. A simple mechanistic model to predict particle size. *Macromolecules* **1990,** *23*, 3109-3117.

86. Rasband, W. S. ImageJ, U. S. National Institutes of Health, Bethesda, Maryland, USA, http://imagej.nih.gov/ij/.

87. Hodoroaba, V. D.; Motzkus, C.; Mace, T.; Vaslin-Reimann, S., Performance of high-resolution SEM/EDX systems equipped with transmission mode (TSEM) for imaging and measurement of size and size distribution of spherical nanoparticles. *Microsc Microanal* **2014,** *20*, 602-612.

88. Corrie, S. R.; Lawrie, G. A.; Trau, M., Quantitative analysis and characterization of biofunctionalized fluorescent silica particles. *Langmuir* **2006,** *22*, 2731-2737.

89. Deslandes, Y.; Mitchell, D. F.; Paine, A. J., X-ray photoelectron spectroscopy and static time-of-flight secondary ion mass spectrometry study of dispersion polymerized polystyrene latexes. *Langmuir* **1993,** *9*, 1468-1472.

90. Rouquerol, F.; Rouquerol, J.; Sing, K., Adsorption by Active Carbons, In *Adsorption by Powders and Porous Solids*. Rouquerol, F., Rouquerol J., Sing, K., Eds., Academic Press: 1999; pp. 263.

91. Rollie, S.; Sundmacher, K., Determination of cluster composition in heteroaggregation of binary particle systems by flow cytometry. *Langmuir* **2008,** *24*, 13348-13358.

92. Song, X.; Gao, L., Fabrication of hollow hybrid microspheres coated with silica/titania via sol−gel process and enhanced photocatalytic activities. *J Phys Chem C* **2007,** *111*, 8180-8187.

93. Li, L.; He, S.; Song, Y.; Zhao, J.; Ji, W.; Au, C.-T., Fine-tunable Ni@porous silica core–shell nanocatalysts: Synthesis, characterization, and catalytic properties in partial oxidation of methane to syngas. *J Catal* **2012,** *288*, 54-64.

94. Chou, K.-S.; Chen, C.-C., Fabrication and characterization of silver core and porous silica shell nanocomposite particles. *Microporous Mesoporous Mater* **2007,** *98*, 208-213.

95. Kim, K. M.; Kim, H. M.; Lee, W. J.; Lee, C. W.; Kim, T. I.; Lee, J. K.; Jeong, J.; Paek, S. M.; Oh, J. M., Surface treatment of silica nanoparticles for stable and charge-controlled colloidal silica. *Int J Nanomed* **2014,** *9*, 29-40.

96. Barisik, M.; Atalay, S.; Beskok, A.; Qian, S., Size dependent surface charge properties of silica nanoparticles. *J Phys Chem C* **2014,** *118*, 1836-1842.

97. Kellaway, I. W.; Najib, N. M., The adsorption of hydrophilic polymers at the polystyrene-water interface. *Int J Pharm* **1980,** *6*, 285-294.

98. de Vos, W. M.; Cattoz, B.; Avery, M. P.; Cosgrove, T.; Prescott, S. W., Adsorption and surfactant-mediated desorption of poly(vinylpyrrolidone) on plasma- and piranha-cleaned silica surfaces. *Langmuir* **2014,** *30*, 8425-8431.

99. Burg, T. P.; Godin, M.; Knudsen, S. M.; Shen, W.; Carlson, G.; Foster, J. S.; Babcock, K.; Manalis, S. R., Weighing of biomolecules, single cells and single nanoparticles in fluid. *Nature* **2007,** *446*, 1066-1069.

100. Sarma, D.; Rurack, K.; Latunde-Dada, S.; Bott, R.; Jones, H. J., Determination of core-shell particle mass and size distribution, density and distinguishing shell thickness by resonant mass measurements. In *7th International Colloids Conference*, Sitges, Spain, 2017.

101. Masalov, V. M.; Sukhinina, N. S.; Kudrenko, E. A.; Emelchenko, G. A., Mechanism of formation and nanostructure of Stöber silica particles. *Nanotechnology* **2011,** *22*, 275718.

102. Sing, K., The use of nitrogen adsorption for the characterisation of porous materials. *Colloids Surf A* **2001,** *187*, 3-9.

103. Lippens, B., Studies on pore systems in catalysts V. The t method. *J Catal* **1965,** *4*, 319-323.

104. Chen, Z.; Greaves, T. L.; Caruso, R. A.; Drummond, C. J., Long-range ordered lyotropic liquid crystals in intermediate-range ordered protic ionic liquid used as templates for hierarchically porous silica. *J Mater Chem* **2012,** *22*, 10069-10076

105. Bogatyrev, V. M.; Borisenko, N. V.; Pokrovskii, V. A., Thermal degradation of polyvinylpyrrolidone on the surface of pyrogenic silica. *Russ J Appl Chem* **2001,** *74*, 839-844.

106. Szczerba, M.; Środoń, J.; Skiba, M.; Derkowski, A., One-dimensional structure of exfoliated polymer-layered silicate nanocomposites: A polyvinylpyrrolidone (PVP) case study. *Appl Clay Sci* **2010,** *47*, 235-241.

107. Smith, J. N.; Meadows, J.; Williams, P. A., Adsorption of polyvinylpyrrolidone onto polystyrene. *Langmuir* **1996,** *12*, 3773-3778.

108. Thibaut, A.; Misselyn-Bauduin, A. M.; Broze, G.; Jérôme, R., Adsorption of poly(vinylpyrrolidone)/surfactant(s) mixtures at the silica/water interface: a calorimetric investigation. *Langmuir* **2000,** *16*, 9841-9849.

109. Surawski, P. P.; Battersby, B. J.; Vogel, R.; Lawrie, G.; Trau, M., Modification and optimization of organosilica microspheres for peptide synthesis and microsphere-based immunoassays. *Mol Biosyst* **2009,** *5*, 826-831.

110. Blitz, J. P.; Gun'ko, V. M.; Samala, R.; Lawrence, B. A., Mixed bifunctional surface-modified silicas using tethered aminofunctional silane catalysts. *Colloids Surf A* **2014,** *462*, 1-8.

111. Saal, K.; Tätte, T.; Tulp, I.; Kink, I.; Kurg, A.; Mäeorg, U.; Rinken, A.; Lõhmus, A., Sol–gel films for DNA microarray applications. *Mater Lett* **2006,** *60*, 1833-1838.

112. Bagwe, R. P.; Hilliard, L. R.; Tan, W., Surface modification of silica nanoparticles to reduce aggregation and nonspecific binding. *Langmuir* **2006,** *22*, 4357-4362.

113. Soto-Cantu, E.; Cueto, R.; Koch, J.; Russo, P. S., Synthesis and rapid characterization of amine-functionalized silica. *Langmuir* **2012,** *28*, 5562-5569.

114. Kallury, K. M. R.; Macdonald, P. M.; Thompson, M., Effect of surface water and base catalysis on the silanization of silica by (aminopropyl)alkoxysilanes studied by X-ray photoelectron spectroscopy and 13C cross-polarization/magic angle spinning nuclear magnetic resonance. *Langmuir* **1994,** *10*, 492-499.

115. An, Y.; Chen, M.; Xue, Q.; Liu, W., Preparation and self-assembly of carboxylic acid-functionalized silica. *J Colloid Interface Sci* **2007,** *311*, 507-513.

116. Etienne, M.; Walcarius, A., Analytical investigation of the chemical reactivity and stability of aminopropyl-grafted silica in aqueous medium. *Talanta* **2003,** *59*, 1173-1188.

117. Tison, C. K.; Milam, V. T., Reversing DNA-mediated adhesion at a fixed temperature. *Langmuir* **2007,** *23*, 9728-9736.

118. Peterson, A. W.; Heaton, R. J.; Georgiadis, R. M., The effect of surface probe density on DNA hybridization. *Nucleic Acids Res* **2001,** *29*, 5163-5168.

119. Horejsh, D.; Martini, F.; Poccia, F.; Ippolito, G.; Di Caro, A.; Capobianchi, M. R., A molecular beacon, bead-based assay for the detection of nucleic acids by flow cytometry. *Nucleic Acids Res* **2005,** *33*, e13.

120. Thiollet, S.; Higson, S.; White, N.; Morgan, S. L., Investigation and development of quantum dot-encoded microsphere bioconjugates for DNA detection by flow cytometry. *J Fluoresc* **2012,** *22*, 685-697.

121. Sadasivan, S.; Dubey, A. K.; Li, Y.; Rasmussen, D. H. J. J. o. S.-G. S.; Technology, Alcoholic solvent effect on silica synthesis—NMR and DLS investigation. *J Sol-Gel Sci Techn* **1998,** *12*, 5-14.

122. Zhang, L.; D'Acunzi, M.; Kappl, M.; Auernhammer, G. K.; Vollmer, D.; van Kats, C. M.; van Blaaderen, A., Hollow silica spheres: synthesis and mechanical properties. *Langmuir* **2009,** *25*, 2711-2717.

123. He, Q.; Cui, X.; Cui, F.; Guo, L.; Shi, J., Size-controlled synthesis of monodispersed mesoporous silica nano-spheres under a neutral condition. *Micropor Mesopor Mater* **2009,** *117*, 609-616.

124. Tseng, C. M.; Lu, Y. Y.; El-Aasser, M. S.; Vanderhoff, J. W., Uniform polymer particles by dispersion polymerization in alcohol. *J Polym Sci Polym Chem* **1986,** *24*, 2995-3007.

125. Sarma, D.; Mielke, J.; Sahre, M.; Beck, U.; Hodoroaba, V.-D.; Rurack, K., TSEM-based contour analysis as a tool for the quantification of the profile roughness of silica shells on polystyrene core particles. *Appl Surf Sci* **2017,** *426*, 446-455.

126. Mammen, L.; Deng, X.; Untch, M.; Vijayshankar, D.; Papadopoulos, P.; Berger, R.; Riccardi, E.; Leroy, F.; Vollmer, D., Effect of nanoroughness on highly hydrophobic and superhydrophobic coatings. *Langmuir* **2012,** *28*, 15005-15014.

127. Jacobs, T. D. B.; Ryan, K. E.; Keating, P. L.; Grierson, D. S.; Lefever, J. A.; Turner, K. T.; Harrison, J. A.; Carpick, R. W., The effect of atomic-scale roughness on the adhesion of nanoscale asperities: A combined simulation and experimental investigation. *Tribol Lett* **2013,** *50*, 81-93.

128. Babick, F.; Mielke, J.; Wohlleben, W.; Weigel, S.; Hodoroaba, V. D., How reliably can a material be classified as a nanomaterial? Available particle-sizing techniques at work. *J Nanopart Res* **2016,** *18*, 158.

129. Hodoroaba, V. D.; Akcakayiran, D.; Grigoriev, D. O.; Shchukin, D. G., Characterization of micro- and nanocapsules for self-healing anti-corrosion coatings by high-resolution SEM with coupled transmission mode and EDX. *Analyst* **2014,** *139*, 2004-2410.

130. Ridler, T. W., and S. Calvard, Picture thresholding using an iterative selection method. *IEEE Trans Syst Man Cybern* **1978,** *8*, 630-632.

131. Zou, H.; Wu, S.; Shen, J., Preparation of silica-coated poly(styrene-co-4-vinylpyridine) particles and hollow particles. *Langmuir* **2008,** *24*, 10453-10461.

132. Xu, M.; Du, M.; Zhao, L.; Yin, Y.; Shao, X.; Li, W.; Pu, X., Facile preparation of monodisperse micrometer-sized hollow silica spheres with tunable size and commendable surface topography. *Mater Res Bull* **2010,** *45*, 1056-1063.

133. Standardization, I. O. f., Geometrical Product Specifications (GPS) - Surface Texture: Areal - Part 2: Terms, Definitions and Surface Texture Parameters, ISO 25178-2:2012. Geneva, 2012.

134. Chen, Y.; Qin, J.; Wang, Y.; Li, Z., Core/shell composites with polystyrene cores and meso-silica shells as abrasives for improved chemical mechanical polishing behavior. *J Nanopart Res* **2015,** *17*, 363.

135. Rades, S.; Hodoroaba, V.-D.; Salge, T.; Wirth, T.; Lobera, M. P.; Labrador, R. H.; Natte, K.; Behnke, T.; Gross, T.; Unger, W. E. S., High-resolution imaging with SEM/T-SEM, EDX and SAM as a combined methodical approach for morphological and elemental analyses of single engineered nanoparticles. *RSC Adv* **2014,** *4*, 49577-49587.

136. Hodoroaba, V. D.; Rades, S.; Salge, T.; Mielke, J.; Ortel, E.; Schmidt, R., Characterisation of nanoparticles by means of high-resolution SEM/EDS in transmission mode. *IOP Conf Ser: Mater Sci and Eng* **2016,** *109*, Art No 012006.

137. Sarma, D.; Carl, P.; Climent, E.; Schneider, R. J.; Rurack, K., Multifunctional polystyrene core/silica shell microparticles with antifouling properties for bead-based multiplexed and quantitative analysis. *ACS Appl Mater Interfaces* **2019,** *11*, 1321-1334.

138. Nolan, J. P.; Mandy, F., Multiplexed and microparticle-based analyses: quantitative tools for the large-scale analysis of biological systems. *Cytometry A* **2006,** *69*, 318-325.

139. de Jager, W.; Rijkers, G. T., Solid-phase and bead-based cytokine immunoassay: a comparison. *Methods* **2006,** *38*, 294-303.

140. Djoba Siawaya, J. F.; Roberts, T.; Babb, C.; Black, G.; Golakai, H. J.; Stanley, K.; Bapela, N. B.; Hoal, E.; Parida, S.; van Helden, P.; Walzl, G., An evaluation of commercial fluorescent bead-based luminex cytokine assays. *PLoS One* **2008,** *3*, e2535.

141. Maltais, A.; Boye, J. I., Bead-based arrays: Multiplex analyses. In *Green Technologies in Food Production and Processing*, Boye, J. I.; Arcand, Y., Eds., Springer: 2012; pp 495-518.

142. Hsu, H. Y.; Joos, T. O.; Koga, H., Multiplex microsphere-based flow cytometric platforms for protein analysis and their application in clinical proteomics - from assays to results. *Electrophoresis* **2009,** *30*, 4008-4019.

143. Yu, H. W.; Kim, I. S.; Niessner, R.; Knopp, D., Multiplex competitive microbead-based flow cytometric immunoassay using quantum dot fluorescent labels. *Anal Chim Acta* **2012,** *750*, 191-198.

144. Wang, Y.; Ning, B.; Peng, Y.; Bai, J.; Liu, M.; Fan, X.; Sun, Z.; Lv, Z.; Zhou, C.; Gao, Z., Application of suspension array for simultaneous detection of four different mycotoxins in corn and peanut. *Biosens Bioelectron* **2013,** *41*, 391-396.

145. Guo, Y.; Tian, J.; Liang, C.; Zhu, G.; Gui, W., Multiplex bead-array competitive immunoassay for simultaneous detection of three pesticides in vegetables. *Microchim Acta* **2013,** *180*, 387-395.

146. Luminex xMAP® Technology. https://www.luminexcorp.com/eu/research-xmap-technology/ (accessed 20.08.2018).

147. BDBiosciences Bead-Based Immunoassays. https://www.bdbiosciences.com/in/research/cytometricbeadarray/ (accessed 20.08.2018).

148. Leng, Y.; Sun, K.; Chen, X.; Li, W., Suspension arrays based on nanoparticle-encoded microspheres for high-throughput multiplexed detection. *Chem Soc Rev* **2015,** *44*, 5552-5595.

149. Waterboer, T.; Sehr, P.; Pawlita, M., Suppression of non-specific binding in serological Luminex assays. *J Immunol Methods* **2006,** *309*, 200-204.

150. Lu, S.; Zhang, D. S.; Wei, D.; Lin, Y.; Zhang, S.; He, H.; Wei, X.; Gu, H.; Xu, H., Three-dimensional barcodes with ultrahigh encoding capacities: a flexible, accurate, and reproducible encoding strategy for suspension arrays. *Chem Mater* **2017,** *29*, 10398-10408.

151. Lu, Y.; Lu, J.; Zhao, J.; Cusido, J.; Raymo, F. M.; Yuan, J.; Yang, S.; Leif, R. C.; Huo, Y.; Piper, J. A.; Paul Robinson, J.; Goldys, E. M.; Jin, D., On-the-fly decoding luminescence lifetimes in the microsecond region for lanthanide-encoded suspension arrays. *Nat Commun* **2014,** *5*, Art No 3741.

152. Han, M.; Gao, X.; Su, J. Z.; Nie, S., Quantum-dot-tagged microbeads for multiplexed optical coding of biomolecules. *Nat Biotechnol* **2001,** *19*, 631-635.

153. Bilan, R. S.; Krivenkov, V. A.; Berestovoy, M. A.; Efimov, A. E.; Agapov, II; Samokhvalov, P. S.; Nabiev, I.; Sukhanova, A., Engineering of optically encoded microbeads with FRET-free spatially separated quantum-dot layers for multiplexed assays. *ChemPhysChem* **2017,** *18*, 970-979.

154. Falconnet, D.; She, J.; Tornay, R.; Leimgruber, E.; Bernasconi, D.; Lagopoulos, L.; Renaud, P.; Demierre, N.; van den Bogaard, P., Rapid, sensitive and real-time multiplexing platform for the analysis of protein and nucleic-acid biomarkers. *Anal Chem* **2015,** *87*, 1582-1589.

155. Lee, H.; Kim, J.; Kim, H.; Kim, J.; Kwon, S., Colour-barcoded magnetic microparticles for multiplexed bioassays. *Nat Mater* **2010,** *9*, 745-749.

156. Lee, J.; Bisso, P. W.; Srinivas, R. L.; Kim, J. J.; Swiston, A. J.; Doyle, P. S., Universal process-inert encoding architecture for polymer microparticles. *Nat Mater* **2014,** *13*, 524-529.

157. Juncker, D.; Bergeron, S.; Laforte, V.; Li, H., Cross-reactivity in antibody microarrays and multiplexed sandwich assays: shedding light on the dark side of multiplexing. *Curr Opin Chem Biol* **2014,** *18*, 29-37.

158. Dobosz, P.; Morais, S.; Bonet, E.; Puchades, R.; Maquieira, A., Massive immuno multiresidue screening of water pollutants. *Anal Chem* **2015,** *87*, 9817-9824.

159. Pickering, J. W.; Larson, M. T.; Martins, T. B.; Copple, S. S.; Hill, H. R., Elimination of false-positive results in a luminex assay for pneumococcal antibodies. *Clin Vaccine Immunol* **2010,** *17*, 185-189.

160. Lowe, S.; O'Brien-Simpson, N. M.; Connal, L. A., Antibiofouling polymer interfaces: poly(ethylene glycol) and other promising candidates. *Polym Chem* **2015,** *6*, 198-212.

161. Kim, G.; Yoo, C. E.; Kim, M.; Kang, H. J.; Park, D.; Lee, M.; Huh, N., Noble polymeric surface conjugated with zwitterionic moieties and antibodies for the isolation of exosomes from human serum. *Bioconjug Chem* **2012,** *23*, 2114-2120.

162. Pochechueva, T.; Chinarev, A.; Bovin, N.; Fedier, A.; Jacob, F.; Heinzelmann-Schwarz, V., PEGylation of microbead surfaces reduces unspecific antibody binding in glycan-based suspension array. *J Immunol Methods* **2014,** *412*, 42-52.

163. Yuan, X.; Yoshimoto, K.; Nagasaki, Y., High-performance immunolatex possessing a mixed-PEG/antibody coimmobilized surface: highly sensitive ferritin immunodiagnostics. *Anal Chem* **2009,** *81*, 1549-1556.

164. Wattendorf, U.; Merkle, H. P., PEGylation as a tool for the biomedical engineering of surface modified microparticles. *J Pharm Sci* **2008,** *97*, 4655-4669.

165. Fischer, T.; Dietrich, P. M.; Streeck, C.; Ray, S.; Nutsch, A.; Shard, A.; Beckhoff, B.; Unger, W. E.; Rurack, K., Quantification of variable functional-group densities of mixed-silane monolayers on surfaces via a dual-mode fluorescence and XPS label. *Anal Chem* **2015,** *87*, 2685-2692.

166. Fischer, T.; Dietrich, P. M.; Unger, W. E.; Rurack, K., Multimode surface functional group determination: combining steady-state and time-resolved fluorescence with X-ray photoelectron spectroscopy and absorption measurements for absolute quantification. *Anal Chem* **2016,** *88*, 1210-1217.

167. Regulation (EU) No 1169/2011 of the European Parliament and of the Council on the provision of food information to consumers. European Parliament and Council of the European Union: Brussels, 2011.

168. Braeckmans, K.; De Smedt, S. C.; Leblans, M.; Pauwels, R.; Demeester, J., Encoding microcarriers: present and future technologies. *Nat Rev Drug Discov* **2002,** *1*, 447-456.

169. Kim, L. N.; Kim, M.; Jung, K.; Bae, H. J.; Jang, J.; Jung, Y.; Kim, J.; Kwon, S., Shape-encoded silica microparticles for multiplexed bioassays. *Chem Commun* **2015,** *51*, 12130-12133.

170. Behnke, T.; Wurth, C.; Hoffmann, K.; Hubner, M.; Panne, U.; Resch-Genger, U., Encapsulation of hydrophobic dyes in polystyrene micro- and nanoparticles via swelling procedures. *J Fluoresc* **2011,** *21*, 937-944.

171. Wittmershaus, B. P.; Baseler, T. T.; Beaumont, G. T.; Zhang, Y.-Z., Excitation energy transfer from polystyrene to dye in 40-nm diameter microspheres. *J Lumin* **2002,** *96*, 107-118.

172. Kollmannsberger, M.; Rurack, K.; Resch-Genger, U.; Daub, J., Ultrafast charge transfer in amino-substituted boron dipyrromethene dyes and Its inhibition by cation complexation: A new design concept for highly sensitive fluorescent probes. *J Phys Chem A* **1998,** *102*, 10211-10220.

173. Yu, Y. H.; Descalzo, A. B.; Shen, Z.; Rohr, H.; Liu, Q.; Wang, Y. W.; Spieles, M.; Li, Y. Z.; Rurack, K.; You, X. Z., Mono- and di(dimethylamino)styryl-substituted borondipyrromethene and borondiindomethene dyes with intense near-infrared fluorescence. *Chem Asian J* **2006,** *1*, 176-187.

174. Descalzo, A. B.; Xu, H.-J.; Shen, Z.; Rurack, K., Influence of the meso -substituent on strongly red emitting phenanthrene-fused boron–dipyrromethene (BODIPY) fluorophores with a propeller-like conformation. *J Photochem Photobiol A* **2018,** *352*, 98-105.

175. Anderson, A. S.; Dattelbaum, A. M.; Montano, G. A.; Price, D. N.; Schmidt, J. G.; Martinez, J. S.; Grace, W. K.; Grace, K. M.; Swanson, B. I., Functional PEG-modified thin films for biological detection. *Langmuir* **2008,** *24*, 2240-2247.

176. Karakoti, A. S.; Das, S.; Thevuthasan, S.; Seal, S., PEGylated inorganic nanoparticles. *Angew Chem Int Ed Engl* **2011,** *50*, 1980-1994.

177. Cras, J. J.; Rowe-Taitt, C. A.; Nivens, D. A.; Ligler, F. S., Comparison of chemical cleaning methods of glass in preparation for silanization. *Biosens Bioelectron* **1999,** *14*, 683-688.

178. Han, Y.; Mayer, D.; Offenhäusser, A.; Ingebrandt, S., Surface activation of thin silicon oxides by wet cleaning and silanization. *Thin Solid Films* **2006,** *510*, 175-180.

179. Goftman, V. V.; Aubert, T.; Ginste, D. V.; Van Deun, R.; Beloglazova, N. V.; Hens, Z.; De Saeger, S.; Goryacheva, I. Y., Synthesis, modification, bioconjugation of silica coated fluorescent quantum dots and their application for mycotoxin detection. *Biosens Bioelectron* **2016,** *79*, 476-481.

180. Hsu, J.-C.; Huang, C.-C.; Ou, K.-L.; Lu, N.; Mai, F.-D.; Chen, J.-K.; Chang, J.-Y., Silica nanohybrids integrated with CuInS2/ZnS quantum dots and magnetite nanocrystals: multifunctional agents for dual-modality imaging and drug delivery. *J Mater Chem* **2011,** *21*, 19257-19266.

181. Rabanel, J. M.; Hildgen, P.; Banquy, X., Assessment of PEG on polymeric particles surface, a key step in drug carrier translation. *J Controlled Release* **2014,** *185*, 71-87.

182. Kim, J.; Seidler, P.; Wan, L. S.; Fill, C., Formation, structure, and reactivity of amino-terminated organic films on silicon substrates. *J Colloid Interface Sci* **2009,** *329*, 114-119.

183. Tsoi, T.-H.; Wong, W.-T., A simple, highly sensitive, high throughput and organic solvent-free screening method for melamine by microsphere-based flow cytometry immunoassay. *Anal Methods* **2015,** *7*, 5989-5995.

184. Jiang, X.; Zhu, Z.; Sun, Z.; Wang, L.; Zhou, L.; Miao, H.; Zhang, Z.; Shi, F.; Zhu, C., The development of an indirect competitive immunomagnetic-proximity ligation assay for small-molecule detection. *Analyst* **2013,** *138*, 438-442.

185. Fraga, M.; Vilarino, N.; Louzao, M. C.; Rodriguez, P.; Campbell, K.; Elliott, C. T.; Botana, L. M., Multidetection of paralytic, diarrheic, and amnesic shellfish toxins by an inhibition immunoassay using a microsphere-flow cytometry system. *Anal Chem* **2013,** *85*, 7794-802.

186. Loudet, A.; Burgess, K., BODIPY dyes and their derivatives: syntheses and spectroscopic properties. *Chem Rev* **2007,** *107*, 4891-4932.

187. Qin, W.; Baruah, M.; Van der Auweraer, M.; De Schryver, F. C.; Boens, N., Photophysical properties of borondipyrromethene analogues in solution. *J Phys Chem A* **2005,** *109*, 7371-7384.

188. Carvalho, J. J.; Weller, M. G.; Panne, U.; Schneider, R. J., A highly sensitive caffeine immunoassay based on a monoclonal antibody. *Anal Bioanal Chem* **2010,** *396*, 2617-2628.

189. Climent, E.; Bernardos, A.; Martínez-Máñez, R.; Maquieira, A.; Marcos, M. D.; Pastor-Navarro, N.; Puchades, R.; Sancenón, F.; Soto, J.; Amorós, P., Controlled delivery systems using antibody-capped mesoporous nanocontainers. *J Am Chem Soc* **2009,** *131*, 14075-14080.

190. Bruce, I. J.; Sen, T., Surface modification of magnetic nanoparticles with alkoxysilanes and their application in magnetic bioseparations. *Langmuir* **2005,** *21*, 7029-7035.

191. Coskun, A. F.; Topkaya, S. N.; Yetisen, A. K.; Cetin, A. E., Portable multiplex optical assays. *Adv Opt Mater* **2019,** *7*, 1801109.

Acknowledgements

I feel deeply thankful for and enriched by the support of my project supervisor Dr. Knut Rurack - for welcoming me in his workgroup after my return from Spain in 2009, the guidance during my chemistry studies till 2012 and of course for the supervision during this doctoral thesis until today. He is and has been a mentor for me, not only in science, but also for my personal and professional development in life.

I gratefully thank Prof. Stefan Hecht – my doctoral supervisor – for giving me the chance to do my thesis at the Humboldt-University of Berlin at the Chemistry Department. Thank you for supporting me throughout these years and for allowing me to pursue my professional career next to the finalization of this work.

Special thanks go to Peter Carl. He became my scientific partner and friend from the moment in 2015 when we first spoke about synergies between his and my work at the 9th German Biosensor Symposium in Munich. This work benefited a lot due to his support for the immunochemical studies and simply because he was a reliable and fruitful partner for scientific discussions.

My deep gratitude is also dedicated to Dr. Vasile-Dan Hodoroaba, Ms. Benemann and Dr. Johannes Mielke from (BAM, Div. 6.1) for supporting me with SEM image acquisition and analysis as well as the development of the roughness tool. Their help implied more than just results for this work: The possibility to visualize the herein presented particles using SEM/TSEM throughout the whole project term was key to understand the nature of the beads and helped to find the right adjustments for the overall direction of this work.

Many thanks go to Ms. Annette Zimathies and Dr. Carsten Prinz (BAM, Div. 1.3) for the nitrogen adsorption studies; Mr. Feldmann (BAM, Div. 4.2) for the acquisition of SEM images; Dr. Uwe Beck and Dr. Mario Sahre (BAM, Div. 6.7) for conducting the AFM-studies; Dr. Stefan Reinsch (BAM, Div. 5.6) for the TGA data acquisition; and all the former and current co-workers in my lab for your support.

Lastly, the loves of my life: my girlfriend Miriam, my daughter Aurélie, my family, my friends – thank you all for being with me. You make me the person who I am.

Publications

Journal Articles

1. D. Sarma, K. Gawlitza, K. Rurack,

   Langmuir, **2016**, 32, 3717 – 3727

   Polystyrene core–silica shell particles with defined nanoarchitectures as a versatile platform for suspension array technology

   DOI: 10.1021/acs.langmuir.6b00373

2. D. Sarma, J. Mielke, M. Sahre, U. Beck, V.-D. Hodoroaba, K. Rurack,

   Applied Surface Science, **2017**, 426, 446 – 455

   TSEM-based contour analysis as a tool for the quantification of the profile roughness of silica shells on polystyrene core particles

   DOI: 10.1016/j.apsusc.2017.07.099

3. D. Sarma, P. Carl, E. Climent, R. J. Schneider, K. Rurack,

   ACS Applied Materials & Interfaces, **2019**, 11, 1321 – 1334

   Multifunctional polystyrene core/silica shell microparticles with antifouling properties for bead-based multiplexed and quantitative analysis

   DOI: 10.1021/acsami.8b10306

Patent

1. D. Sarma, K. Rurack,

   WO 2017158175 A1, published on 21st September **2017**.

   Verfahren zur Synthese hybrider Kern-Schale-Mikropartikel umfassend einen Polymerkern und eine Siliziumdioxidschale mit kontrollierter Struktur und Oberfläche

Talk

1. D. Sarma, K. Rurack,

   Functional Nanomaterials in Industrial Applications, Preston (UK), 30th March **2016.**

   Hybrid core-shell particles in diagnostic applications - a versatile platform for multiplexed cytometric bead assays

Posters

1. D. Sarma, K. Rurack, U. Panne,

   ANAKON 2013, Essen (Germany), 4th – 7th March **2013**. (winner of the poster prize)

   Preparation of hybrid particle architectures for single microparticle-based detection in suspension arrays using FRET

2. D. Sarma, K. Rurack,

   8. Deutsches BioSensor Symposium. Wildau (Germany), 10th – 13th March **2013**.

   Preparation of core-shell microparticles for single particle detection in suspension arrays

3. D. Sarma, K. Rurack,

   4th International Colloids Conference: Surface Design & Engineering, Madrid (Spain), 15th – 18th June **2014**.

   Preparation of polystyrene@silica core-shell particles for suspension arrays

4. D. Sarma, K. Rurack,

   9. Deutsches BioSensor Symposium, München (Germany), 11th – 13th March **2015**.

   Core-shell particles: Novel platforms for suspension array technologies (SAT)

5. D. Sarma, K. Rurack, S. L.-D. Dada, R. Bott, H. J. Jones,

   7th International Colloids Conference, Barcelona (Spain), 18th – 21th June **2017**.

   Determination of core-shell particle mass and size distribution, density and distinguishing shell thickness by resonant mass measurements

6. D. Sarma, K. Rurack, S. L.-D. Dada, R. Bott, H. J. Jones,

   UK Colloids 2017, Manchester (UK), 10th – 12th September **2017**.

   Determination of core-shell particle mass and size distribution, density and distinguishing shell thickness by resonant mass measurements

Journal Article, submitted

1. P. Carl, D. Sarma, B. J. R. Gregório, K. Hoffmann, A. Lehmann, K. Rurack, R. Schneider,

   A wash-free multiplex mix-and-read suspension array fluorescence immunoassay for anthropogenic markers in wastewater.

Talks and posters as co-author

1. P. Carl, D. Sarma, K. Rurack, R. J. Schneider,

   Innovations Forum Senftenberg, 2016 - Enabling Technologies for Multiparameter Analytics, Senftenberg (Germany), 1st – 2nd June **2016.**

   A bead suspension array for measuring emerging pollutants and anthropogenic markers in wastewater (poster)

2. P. Carl, R. J. Schneider, D. Sarma, K. Rurack,

   EBS 2017, Potsdam (Germany), 20th – 23th March **2017**.

   A wash-free, multiplex microbead assay for determination of emerging bioactive compounds in wastewater (poster)

3. P. Carl, R. J. Schneider, D. Sarma, K. Rurack, Pittcon 2017, Chicago (USA), 5th – 9th March **2017**.

   Determination of pharmacologically active compounds in wastewater by a bead-based flow-cytometric immunoarray (talk)

Declaration of the author

I declare that I have completed the thesis independently using only the aids and tools specified. I have not applied for a doctor's degree in the doctoral subject elsewhere and do not hold a corresponding doctor's degree. I have taken due note of the Faculty of Mathematics and Natural Sciences PhD Regulations, published in the Official Gazette of Humboldt-Universität zu Berlin no. 17/2012 on 27/06/2012.